Ministry of Science and Higher Education of the Russian Federation
ITMO University

ISSN 2220-8054

NANOSYSTEMS:

PHYSICS, CHEMISTRY, MATHEMATICS

2025, volume 16(1)

Наносистемы: физика, химия, математика
2025, том 16, № 1

NANOSYSTEMS:

PHYSICS, CHEMISTRY, MATHEMATICS

ADVISORY BOARD MEMBERS

Chairman: V.N. Vasiliev *(St. Petersburg, Russia)*,
V.M. Buznik *(Moscow, Russia)*; V.M. Ievlev *(Voronezh, Russia)*, P.S. Kop'ev*(St. Petersburg, Russia)*, V.N. Parmon *(Novosibirsk, Russia)*, A.I. Rusanov *(St. Petersburg, Russia)*,

EDITORIAL BOARD

Editor-in-Chief: I.Yu. Popov *(St. Petersburg, Russia)*

Section Co-Editors:
Physics – V.M. Uzdin *(St. Petersburg, Russia)*,
Material science – V.V. Gusarov *(St. Petersburg, Russia);* O.V. Al'myasheva *(St. Petersburg, Russia)*;
Chemistry – V.K. Ivanov *(Moscow, Russia)*,
Mathematics – I.Yu. Popov *(St. Petersburg, Russia)*.

Editorial Board Members:
V.M. Adamyan *(Odessa, Ukraine)*; A.P. Alodjants *(St. Petersburg, Russia)*; S. Bechta *(Stockholm, Sweden)*; J. Behrndt *(Graz, Austria)*; A. Chatterjee (*Hyderabad, India)*; A.V. Chizhov *(Dubna, Russia)*; A.N. Enyashin *(Ekaterinburg, Russia)*, P.P. Fedorov *(Moscow, Russia)*; E.A. Gudilin *(Moscow, Russia)*; H. Jónsson *(Reykjavik, Iceland)*; A.R. Kaul *(Moscow, Russia)*; A.A. Kiselev *(Durham, USA)*; Yu.S. Kivshar *(Canberra, Australia)*; S.A. Kozlov *(St. Petersburg, Russia)*; P.A. Kurasov *(Stockholm, Sweden)*; A.V. Lukashin *(Moscow, Russia)*; G.P. Miroshnichenko *(St. Petersburg, Russia)*; I.Ya. Mittova *(Voronezh, Russia)*; H. Najar *(Monastir, Tunisia),* Nguyen Anh Tien *(Ho Chi Minh, Vietnam)*; V.V. Pankov *(Minsk, Belarus)*; K. Pankrashkin *(Oldenburg, Germany)*; A.V. Ragulya *(Kiev, Ukraine)*; V. Rajendran *(Tamil Nadu, India)*; A.A. Rempel *(Ekaterinburg, Russia)*; A.A. Rogachev *(Minsk, Belarus)*; V.Ya. Rudyak *(Novosibirsk, Russia)*; H.M. Sedighi (*Ahvaz, Iran*); D Shoikhet *(Karmiel, Israel)*; M.N.Smirnova *(Moscow, Russia)*; P. Stovicek *(Prague, Czech Republic)*; V.M. Talanov *(Novocherkassk, Russia)*; A.Ya. Vul' *(St. Petersburg, Russia)*; A.V. Yakimansky (*St. Petersburg, Russia*), V.A. Zagrebnov *(Marseille, France)*.

Editors:
I.V. Blinova; A.I. Popov; A.I. Trifanov; E.S. Trifanova *(St. Petersburg, Russia),*
R. Simoneaux *(Philadelphia, Pennsylvania, USA)*.

Address: ITMO University, Kronverkskiy pr., 49, St. Petersburg 197101, Russia.
Phone: +7(812)607-02-54, **Journal site:** http://nanojournal.ifmo.ru/,
E-mail: nanojournal.ifmo@gmail.com

AIM AND SCOPE

The scope of the journal includes all areas of nano-sciences. Papers devoted to basic problems of physics, chemistry, material science and mathematics inspired by nanosystems investigations are welcomed. Both theoretical and experimental works concerning the properties and behavior of nanosystems, problems of its creation and application, mathematical methods of nanosystem studies are considered.
The journal publishes scientific reviews (up to 30 journal pages), research papers (up to 15 pages) and letters (up to 5 pages). All manuscripts are peer-reviewed. Authors are informed about the referee opinion and the Editorial decision.

CONTENT

NANOSYSTEMS:
PHYSICS, CHEMISTRY, MATHEMATICS

Original article

Manushkin A.A., et al. *Nanosystems: Phys. Chem. Math.*, 2025, **16** (1), 5–13.
http://nanojournal.ifmo.ru
DOI 10.17586/2220-8054-2025-16-1-5-13

Phase-contrast method for determining the size of the effective focal spot of a nanofocus X-ray tube

Alexey A. Manushkin[1,a], Nikolay N. Potrakhov[2], Dmitrii K. Kostrin[2,b], Karina K. Guk[2]

[1]"Diagnostika-M" LLC, Moscow, Russia

[2]Saint Petersburg Electrotechnical University "LETI", St. Petersburg, Russia

[a]manushkinaa@mail.ru, [b]dkkostrin@mail.ru

Corresponding author: A.A. Manushkin, manushkinaa@mail.ru

PACS 07.85.-m, 52.38.Ph

ABSTRACT The work is devoted to the development of a method for testing the focal spot size of nanofocus and microfocus X-ray tubes based on phase contrast radiography of test objects. The method is based on the comparison of the interference X-ray image with the calculated values obtained by the exact numerical solution of the wave equation. The high sensitivity of the method to the size of the source is ensured by the fusion of interference fringes with contrast of different signs. The formation of X-ray phase contrast images of test objects is analyzed on the basis of the wave equation using numerical modeling of the intensity profile. An analytical expression has been obtained to estimate the size of the X-ray tube focus. The results of calculations of phase contrast profiles for a nylon fishing line and a reference nanofocus test are presented.

KEYWORDS X-rays, phase contrast, interference, non-destructive testing, test object

ACKNOWLEDGEMENTS The work was carried out with the financial support of the Ministry of Education and Science of the Russian Federation (by Agreement dated February 09, 2023, No. 075-11-2023-006, state contract identifier 000000S407523Q6V0002).

FOR CITATION Manushkin A.A., Potrakhov N.N., Kostrin D.K., Guk K.K. Phase-contrast method for determining the size of the effective focal spot of a nanofocus X-ray tube. *Nanosystems: Phys. Chem. Math.*, 2025, **16** (1), 5–13.

1. Introduction

Currently, nanofocus radiography is increasingly being used in various fields of science, technology and medicine [1, 2]. In relation to the problems of flaw detection and control of electronic products with integrated circuits, it is important to use X-ray tubes with an anode voltage above 150 kV with nanometer and micrometer focus sizes. The development of nanofocus radiography in relation to the study of high-tech nanoelectronics devices and new materials requires the development of new X-ray source testing tools.

The size of the focal spot is the most important parameter determining the amount of geometric blurring and, consequently, the image quality of the objects under control. In the countries of the European Union, the EN 12543 standard "Non-destructive testing. Characteristics of focal spots in industrial X-ray systems for use in non-destructive testing" is in force. The generalized data of numerous measurements of nanofocus spots given in [1] and the results of relevant experimental studies obtained by the authors of the present work showed that the reliability and dispersion of the obtained measurement values performed in accordance with the above standards are unsatisfactory.

The standard methods for measuring the size of the effective focal spot of nanometer-sized X-ray tubes are based on the absorption of X-ray radiation in test objects made of materials that strongly absorb X-ray radiation. In addition to absorption, X-rays, when interacting with an object, experience refraction at its boundaries, which leads to the formation of a phase contrast [3, 4]. This refraction can be detected using highly coherent synchrotron X-ray sources [5, 6] or nanofocus X-ray tubes [7, 8] in the form of interference patterns at some distance from objects. The magnitude of the phase contrast critically depends on the size of the X-ray tube focus [9–12].

Numerous studies in the field of phase contrast have established a strong dependence of phase contrast on the size of the X-ray focal spot. However, as far as we know, no systematic studies have been conducted on the use of phase contrast imaging to determine the focal spot, while advanced methods of absorption contrast have been developed in a wide range of focal spot sizes up to the nanofocus region.

The formation of a two-dimensional absorption X-ray image $f(x, y)$ from an ideal point source is described within the framework of projection ray geometric optics, and the effect of size and shape on the final recorded image $g(x, y)$

© Manushkin A.A., Potrakhov N.N., Kostrin D.K., Guk K.K., 2025

is described as a convolution of the ray projection of an object with a two-dimensional distribution $h(x, y)$ of X-ray brightness along the focal spot:

$$g(x, y) = f(x, y) * h(x, y), \tag{1}$$

where the $*$ sign indicates a convolution operation.

With a high signal-to-noise ratio, reliable information not only about the size of the focus, but also its shape makes it possible to improve spatial resolution by deconvolution of the image. For example, in [13], the possibility of improving the image of bone tissues was demonstrated by taking into account the intensity distribution on the double focal spot due to the extended spiral structure of the tungsten anode.

For two-dimensional deconvolution, the two-dimensional Fourier transform can be used, as a result of which the original object can be formally restored in the domain of spatial frequencies:

$$F(u, v) = \frac{G(u, v)}{H(u, v)}, \tag{2}$$

where F, G, H are the Fourier transforms of the functions f, g, h.

In practice, in the presence of noise, it is necessary to make a more complex search for the optimal solution using a priori data on the desired distribution of $f(x, y)$ and on the nature of noise based on a reasonable balance between image sharpness and noise level.

It is shown in [14] that the two-dimensional deconvolution problem is reduced to one-dimensional deconvolution of radial profiles $I(x, y)$ of circular aperture images, resulting in a synogram of the Radon transformation of the focal spot with subsequent tomographic reconstruction. This procedure was applied to distribution of a focal spot with a diameter of 0.3 mm of a mammography tube.

In another work [15], the circular aperture method was scaled to focal spots with micron and submicron sizes. When working with nanofocus sources, test objects closely approach the focal spot at a distance of no more than a millimeter, and this makes it possible to provide a 1000× magnification when the detector is removed at a distance of about 1 m.

The low power of the nanofocus tubes, the large distance to the detector and the weak absorption contrast of the test objects cause a high level of image noise and a long signal accumulation time. For example, in [16] radiographic images of the JIMA test were obtained, with a test strip period of 150 nm. The images were obtained on a nano-CT laboratory setup at source voltages of 60 and 40 keV. The accumulation time was 10 and 20 min, respectively.

The purpose of this work is to explore the possibilities of a phase-contrast method for testing nanofocus tubes within the framework of classical principles of wave optics in order to provide practical recommendations for the development of test objects, methods of their use and the development of related software.

2. Materials and methods

To numerically calculate the phase-contrast image of a model object, Fourier optics methods based on the decomposition of the wave field into planar components were used [17]. Let's consider the wave equation for the amplitude $A(r, t)$ of a monochromatic wave propagating freely in space:

$$\Delta A - \frac{1}{v^2}\frac{\partial^2 A}{\partial t^2} = 0, \tag{3}$$

where Δ is the Laplace operator, $A(\mathbf{r}, t)$ is a function of spatial coordinates and time describing the wave field, v is the propagation velocity of the wave field. For a stationary field of monochromatic radiation

$$A(\mathbf{r}, t) = A(\mathbf{r})e^{i\omega t} \tag{4}$$

and the wave equation is simplified to a linear homogeneous Helmholtz equation:

$$\Delta A + k^2 A = 0, \tag{5}$$

where $k = \omega/v$. In vacuum, $v = c$ and $k = 2\pi/\lambda$, where λ is the wavelength of the propagating radiation. Plane waves of the form

$$A_{\mathbf{k}}(\mathbf{r}) = e^{i(\mathbf{k}\cdot\mathbf{r})}, \tag{6}$$

where $\mathbf{k}$ is the wave vector, are exact solutions of the wave equation and form the basis of functions from which the desired solution of the Helmholtz equation can be constructed:

$$A(\mathbf{r}) = \int a(\mathbf{k})e^{i(\mathbf{k}\cdot\mathbf{r})}dS_{\mathbf{k}}, \tag{7}$$

where $dS_{\mathbf{k}}$ is an element of the surface area of a sphere of radius $\mathbf{k}$, in which the wave vectors of plane waves are concentrated. Provided that $|\mathbf{k}| = k$, each possible direction $\mathbf{k} = (k_x, k_y, k_z)$ of propagation of a plane wave is given by its projections k_x and k_y onto the xy plane. Let's put $z = 0$ in formula (7), then this formula will be rewritten in the following form:

$$A(x, y, z = 0) = \int a(k_x, k_y)e^{i(k_x x + k_y y)}dk_x dk_y. \tag{8}$$

Thus, the wave field in free space is represented as a sum of plane-wave components, with expansion coefficients $a(k_x, k_y)$ determined by the Fourier expansion of the field in the plane. When a plane wave falls on an object, the phase shift of the wavefront and the curvature of the wave front are observed, and the appearance of plane-wave components of the scattered wave propagating paraxially at different angles of coherent scattering occurs.

When radiation propagates from the $z = 0$ plane to the z plane of image detection, each plane-wave component receives an additional phase multiplier $\exp(ik_z z)$, where

$$k_z = \sqrt{k^2 - k_x^2} \approx k\left(1 - \frac{k_x^2}{2k^2}\right) \approx k\left(1 - \frac{\alpha^2}{2}\right). \tag{9}$$

The interference of the incident wave and the wave scattered at an angle α forms interference fringes of size dx:

$$dx = \frac{\lambda}{2\sin\alpha}. \tag{10}$$

The angular spectrum of a coherently scattered plane wave is dominated by plane-wave components with small scattering angles. Components with large scattering angles and having smaller amplitude are formed at the edges of the object, where the phase shift in the object becomes small. Accordingly, at the final resolution of the detector, in order to observe a strong phase contrast with wider interference fringes, the detector should be removed from the object if the geometric blurriness is small. As the detector approaches the object, narrower interference fringes with less contrast are formed. The geometry of shooting a test object using the phase-contrast method is shown in Fig. 1.

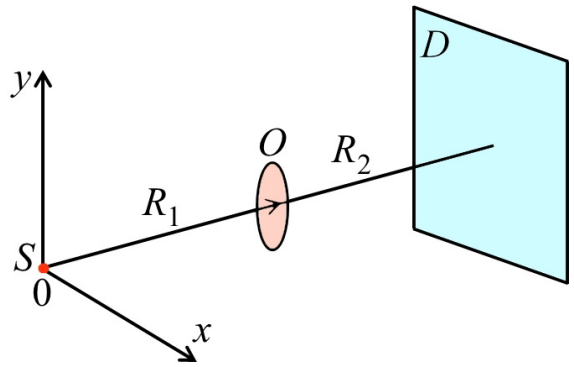

FIG. 1. Geometry of the phase-contrast shooting of the test object: S is a nanofocus source, O is a test object, D is a two-dimensional detector

In the coordinate representation, the paraxial propagation of a wave in free space from an object with a coordinate $z = 0$ to a detector with $z = R$ is expressed as a convolution of the amplitude of the initial $A(x', z = 0)$ with a Fresnel propagator:

$$A\,(x, z = R) = \int A\,(x', z = 0) \exp\left(-\frac{i\,(x - x')^2}{2R}\right) dx'. \tag{11}$$

The dx' integration regions can be divided into Fresnel zones with m indices. In the case of an incident plane wave, the radii d_m of the first Fresnel zones with small indices for the distance R from the object to the observation point are expressed by the well-known formula:

$$d_m \approx \sqrt{\lambda R m}, \quad m = 1,\, 2,\, 3\ldots \tag{12}$$

For a spherical wave on an object with distances of R_1 and R_2, the same formula with an effective diffraction distance R (lens formula) is valid:

$$\frac{1}{R_1} + \frac{1}{R_2} = \frac{1}{R}. \tag{13}$$

Thus, in the paraxial approximation, the calculation of the diffraction of an object on a spherical wave from a point source with geometric parameters R_1 and R_2 is equivalent to the calculation of the diffraction of an object on a plane wave [18]. Bringing the contrast calculation from a point source to a plane-wave case simplifies and significantly speeds up calculations and makes it possible to implement them on mobile platforms.

For $R_2 \to \infty$ the increase in R reaches the maximum value of R_1. Accordingly, the size of the first Fresnel zone and the magnitude of the phase contrast reach the limit values, which depend mainly on the difference in phase shift at the edges of this zone.

Let's determine the maximum size of the focal spot, which for a cylinder gives about 50 % of the maximum contrast from a point source. If R_1 and R_2 are the distances from the source to the object and from the object to the detector (see Fig. 1), then the factor of increasing the size of the source $f = 1 + R_2/R_1$ gives us a geometric blurriness $S = r(1 + R_2/R_1)$.

The possibility of geometrically increasing interference fringes without loss of contrast makes it possible to use amplifying screens and electronic recording devices instead of X-ray films. In order to observe a strong phase contrast, it is necessary that the width of the interference fringe $dx = \lambda/\sin\alpha$ be commensurate with the geometric blurriness. The condition of the opposite phases of the direct and scattered waves is expressed by the formula:

$$k\alpha^2 R = \pi. \tag{14}$$

From equations (11) and (14), taking into account $R \cong R_1$ at $R_2/R_1 \gg 1$, the maximum diameter d of the focal spot of the source is obtained, at which the contrast is close to half the contrast from the point source:

$$d \approx \sqrt{2}\, dx = \sqrt{\lambda R_1}. \tag{15}$$

3. Results and discussion

The numerical calculation of the phase contrast image from a point source according to the formula (11) in rectangular coordinates presents certain difficulties due to the need to represent the high-frequency modulation of a spherical wave field at a large aperture. The program used in this work to calculate the one-dimensional profile of images of model objects based on the fast Fourier transform used large amounts of RAM, and the calculation on a desktop computer with an NVIDIA GeForce RTX 2080 GPU lasted about a minute.

Figure 2 shows the intensity profiles for an ideal point source and a source with a finite size, which demonstrate the condition of strong contrast according to the formula (15).

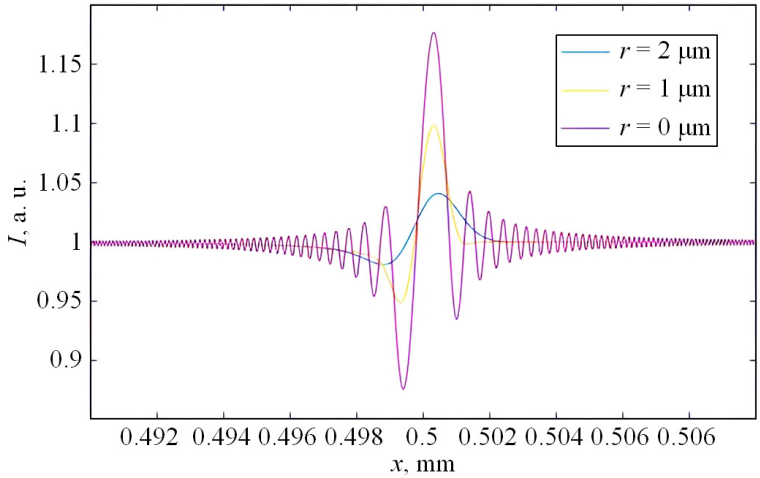

FIG. 2. Calculated intensity profiles of the phase-contrast image of the edge of a nylon fishing line with a diameter of 1 mm at a radiation energy of 60 keV for a point source and for focal spots of 1 and 2 micrometers in size ($R_1 = 50$ mm, $R_2 = 500$ mm)

Formula (15) corresponds to a focal spot diameter of 1 μm, at which the phase contrast value reaches 50 % of the contrast for a source with a zero focal spot size. When using X-ray optical transducers with a limited dynamic range or films with a nonlinear response, it is difficult to quantify the amount of contrast. The size of the focus is easier to estimate by measuring the width of the main interference maximum, which for the focal length $d = 2$ μm will double (Fig. 2). Model calculations for aluminum wire, with a refractive index about 2.7 times higher than that of nylon, show the possibility of increasing the phase contrast by 2 times and, accordingly, the possibility of increasing the signal-to-noise ratio by 4 times.

If it is necessary to check the estimated value r of the focal spot of the X-ray source, then for this purpose the minimum distance R_1 from the source to the test object should be selected according to formula (15). For example, for a spot diameter of 1 μm and energy of 60 keV, it is necessary to select a distance R_1 of the order of 50 mm. The distance R_2 is selected based on the choice of geometric magnification for a given detector resolution.

Let's consider the formation of nanofocus images on phase-modulating diffraction gratings, which are a set of periodic structures of several tungsten strips with different widths from 400 nm and thicknesses up to 10 μm, sufficient for deep phase modulation of X-ray radiation. These gratings are similar to the JIMA RT RU-02B tests designed to determine the size of the focus of X-ray tubes. The test manufacturer describes the strips as X-ray absorbing tungsten strips with a thickness of 1 μm. The calculated absorption attenuation per 1 μm of tungsten for energies from 60 to 30 keV is from 1 to 4 %. Tests of a similar design were used to obtain the resolution of scintillators [19].

It is convenient to analyze the formation of diffraction grating images in a pulsed representation based on equation (13) and formula (12), in which dx denotes the half-period of the diffraction grating. From formula (15), it is possible

to obtain the nearest effective distance R at which Fourier images of a diffraction grating with maximum contrast from a plane incident wave are formed (Talbot effect) [17]:

$$R = \frac{dx^2}{2\lambda} n, \quad n = 1,\ 2,\ 3\ldots \tag{16}$$

In the geometry of a point source, the Fourier images will be magnified by $(1 + R_2/R_1)$ times and will be observed at distances determined by the ratio [17]:

$$\frac{1}{R_1} + \frac{1}{R_2} = \frac{2\lambda}{dx^2 n}. \tag{17}$$

The Fourier images are obtained at consistently increasing intervals up to the maximum positive value of n, after which the value $(dx^2 n)/(2\lambda)$ will be greater than R_1. For $\lambda = 0.021$ nm ($E = 60$ keV) and $dx = 1$ μm, it turns out $dx^2/(2\lambda) = 23.8$ mm. This value determines the maximum distance R_1 at which condition (17) is satisfied.

Figures 3 and 4 show the calculated profiles of phase grating images for conditions of strong (far-focus mode) and weak (near-focus mode) contrast at a phase modulation depth on the diffraction grating $\pi/2$ and a focus diameter of 1 μm.

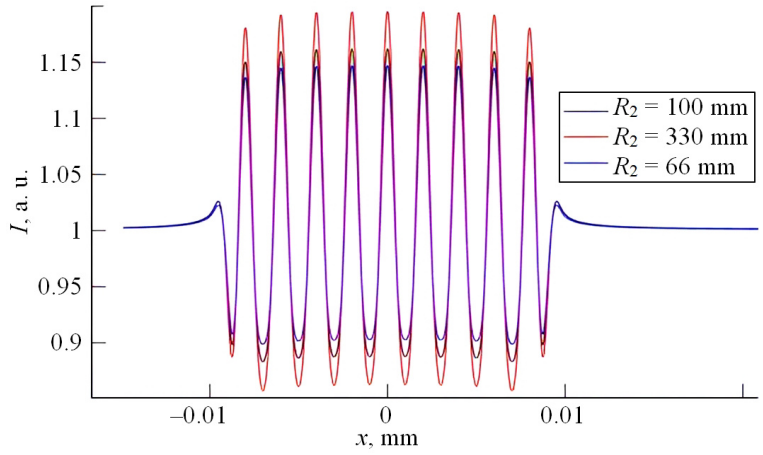

FIG. 3. Calculated contrast profiles of the test with a phase-modulating grating period of 1 μm for a radiation energy of 60 keV under shooting conditions with strong contrast ($R_1 = 33$ mm). The focus size is 1 μm

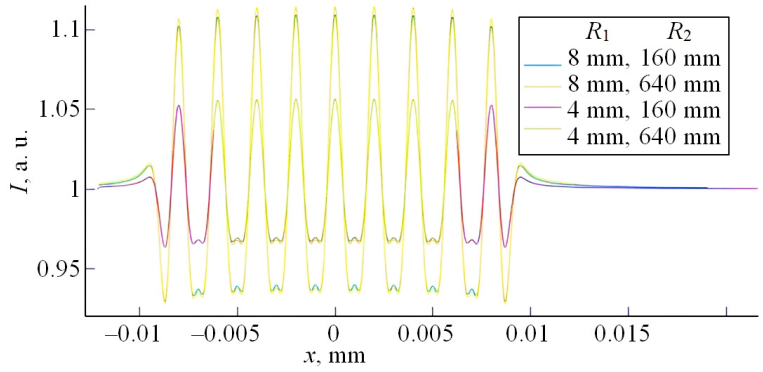

FIG. 4. Calculated contrast profiles of the test with a grating period of 1 μm for a radiation energy of 60 keV in the near-focus shooting mode. The focus size is 1 μm. The graphs are scaled along the x axis without taking into account geometric magnification

With a limited resolution of a digital matrix detector with a pixel size of more than 100 μm, it becomes necessary to bring the test closer to the focus of the source. At the same time, as shown in Fig. 4, the phase contrast determined by the difference between the maximum and minimum intensity values decreases, but remains even greater than the calculated absorption value of 4 %. Fig. 5 shows profiles for several focal spot sizes, with similar parameters $R_1 = 8$ mm, $R_2 = 640$ mm and $dx = 1$ μm.

From the above, it can be concluded that the contrast of the test image depends on the size of the focus and on the degree of transformation of the phase modulation of the grid into an amplitude one, determined by the geometry of the shooting. When the R_1 parameter is properly selected in the mode of limiting the conversion of phase modulation to amplitude, the contrast mainly depends on the size of the focus.

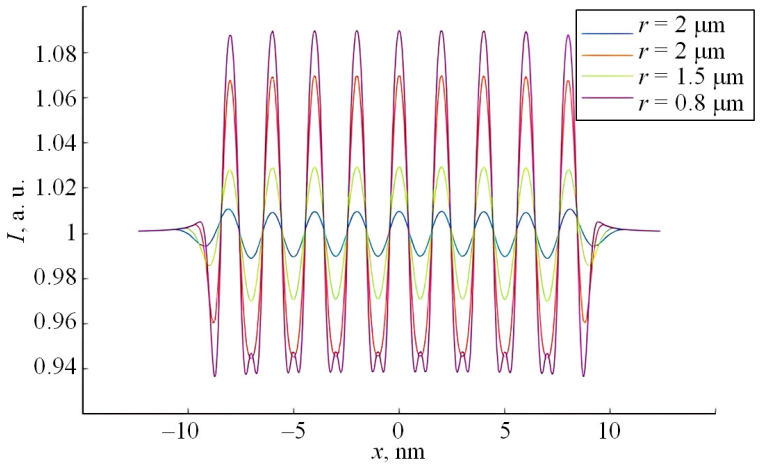

FIG. 5. Calculated diffraction grating images for different focal spot sizes. Radiation energy $E = 60$ keV, modulation depth of the lattice phase is $\pi/2$

Let's now consider the formation of a phase contrast in the braking radiation (bremsstrahlung) of an X-ray tube. The depth of phase modulation $\delta\varphi$ in the X-ray diffraction grating is determined by the phase shift, which is determined by the decrement of the refractive index δn and the thickness of the modulating layer t:

$$\delta\varphi = \frac{2\pi\delta n t}{\lambda}. \tag{18}$$

In the X-ray region of the electromagnetic spectrum, the decrement of the refractive index of a single-element substance is determined by the cross section of elastic X-ray scattering on an atom and the density of the substance:

$$\delta n = \frac{N r_e}{2\pi}\lambda^2, \tag{19}$$

where N is the electron density, r_e is the classical electron radius.

For tungsten, the refractive index decrement is $8.59 \cdot 10^{-7}$ for 60 keV. Thus, in order to obtain a phase shift of $\pi/2$, 6 micrometers of tungsten layer are needed.

To obtain deep phase modulation with a spatial frequency of 1 μm, high-tech methods for the formation of high-aspect microstructures based on liquid or plasma-chemical etching of silicon, currently used to create X-ray optical elements of Talbot–Laue interferometers, can be used [20].

The phase contrast distribution differs significantly for different values of the Fresnel number $NF = a^2/(\lambda R)$, where a is the size of the structure in the depicted object, $R \approx R_1$ (at $R_2 \gg R_1$) is the effective diffraction distance. The regions of the far (Fraunhofer diffraction region) and near fields (field of geometric optics) and the intermediate region (Fresnel diffraction region) are determined by the corresponding NF values: $NF \ll 1$, $NF > 1$, $NF \approx 1$. Diffraction effects occur not only with phase modulation of the wavefront, but also with amplitude modulation of radiation by X-ray absorbing objects.

The width of the diffraction blur on the detector at magnification M is determined by the expression:

$$\sigma = M\sqrt{\lambda R} \approx M\sqrt{\lambda R_1}. \tag{20}$$

To reduce the diffraction blurring of the image of the test object edges smaller than the size of the nanofocus spot, it is necessary to bring the object close to the source. For example, for an energy of 60 keV ($\lambda = 0.021$ nm) and a distance R_1, according to formula (20), this distance should be less than 0.5 mm.

The results of numerical calculation of diffraction blurring of an X-ray absorbing test periodic structure with a period of 100 nm are shown in Fig. 6. The normalized amplitude $A(x)$ of the test object was calculated using the formula $A(x) = 1 - cf(x)$, where $c = 0.02$ is the absorption amplitude decrease expressed as a percentage, and $f(x)$ is the normalized amplitude modulation profile after an X-ray mask with a strip width of 100 nm. The calculation results show a diffraction reduction in the contrast of the nanoobject.

In support of the conclusion about diffraction blurring of strip images, Fig. 7 shows radiographic absorption images of the JIMA test, with a period of 150 nm test strips, adapted from [16]. It is noteworthy that with a greater contrast of the wide boundaries of the test, the distinguishability of 150 nm strips for 40 kVp is worse than for 60 kVp, despite the lower noise level.

In our opinion, the authors of this work, performed at a high experimental level, mistakenly explained this difference by a different choice of the digital range of image representation. In fact, with the high accuracy of nanoscopy and the lower rigidity of X-ray radiation, the diffraction envelope of nanoscale obstacles by X-ray radiation manifested itself, which reduced the modulation amplitude.

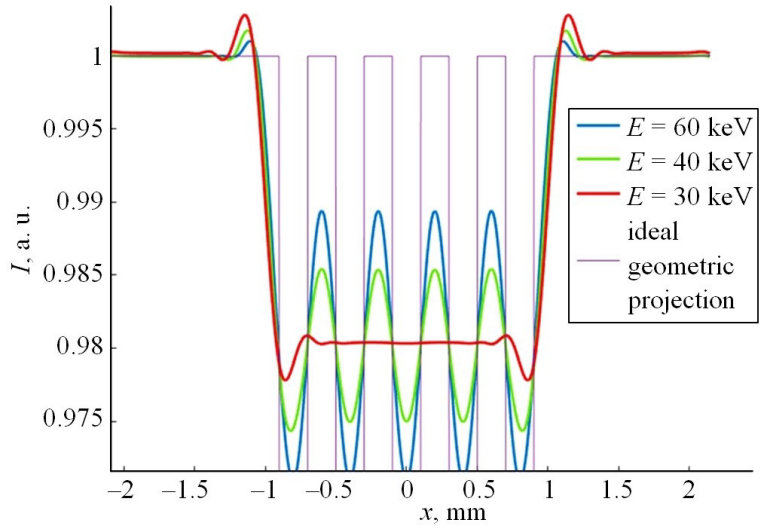

FIG. 6. Calculated profile of the normalized intensity modulation on the detector for different energies. $R_1 = 0.5$ mm, $R_2 = 1000$ mm, the focal spot size is 100 nm

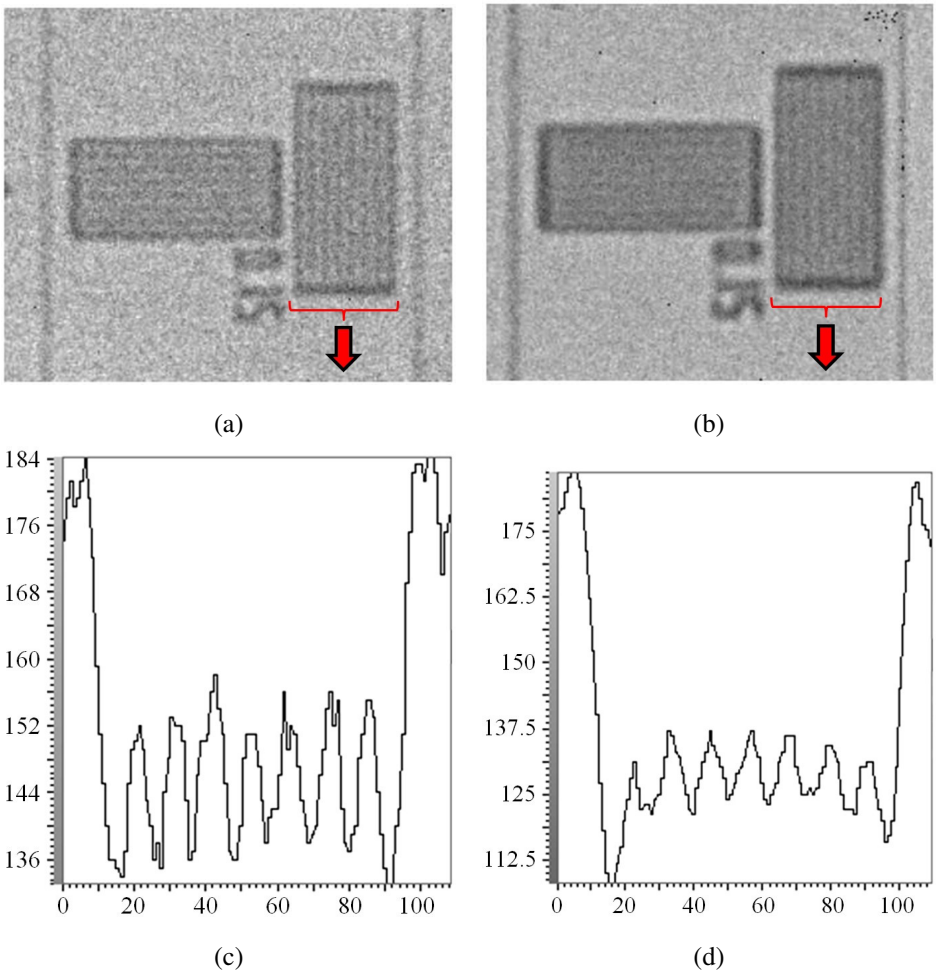

FIG. 7. Images of the test object (a), (b) and cross-section profiles of vertical test images after processing with a median filter of size 1×201 (c), (d): (a), (c) – 60 kVp, 1.15 μA, 10 min; (b), (d) – 40 kVp, 0.7 μA, 20 min

Let's turn now to the use of cylindrical test objects. Since the phase incursion at the line boundary will be small at nanofocus distances, and the resulting phase contrast is very weak, it is advisable to use high-density materials such as mercury or gold (Fig. 8).

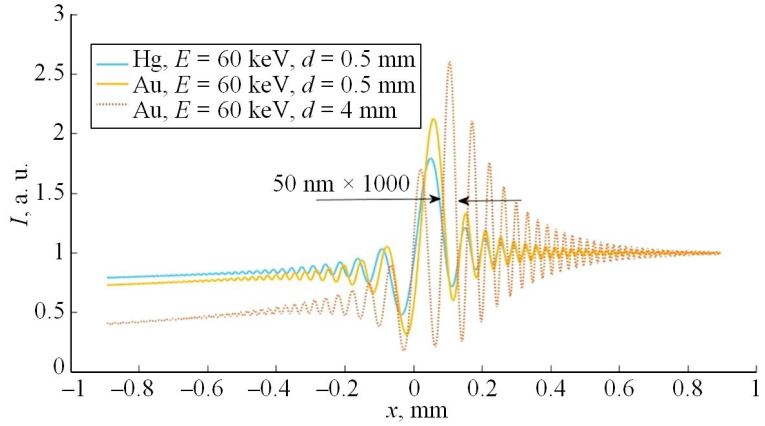

FIG. 8. Results of the model calculation of the phase profile at the boundaries of test cylindrical objects from a point source at $R_1 = 0.5$ mm, $R_2 = 500$ mm

As can be seen from the above result, the use of test objects of high-density materials with a high refraction index makes it possible to obtain from a point source a phase-contrast picture of edge diffraction with a spatial resolution of up to 50 μm with a magnification factor of $\times 1000$. The high level of phase contrast opens up potential possibilities for monitoring the size and position of the focal spot in real time and its corresponding correction during data collection.

4. Conclusion

The considered phase-contrast method for determining the focal spot of nanofocus and microfocus X-ray tubes using simple macroscopic test objects and reference phase-modulating periodic microstructures is characterized by high sensitivity to the parameters of nanofocus tubes in the size range from hundreds of nanometers to several micrometers. To determine the optimal shooting geometry and the correct interpretation of images of test objects, it is advisable to use the accompanying software.

It can also be noted that not only the focal spot itself can be adjusted by affecting the focusing system, but also the image itself can be corrected. In the continuation of the ongoing research, it is planned to conduct experiments on a wide range of real X-ray tubes for a more detailed comparison of experimental data and simulation results.

References

[1] Staroverov N.E. A method for automated control of electronic components on microfocus X-ray images. *J. of the Russian Universities. Radioelectronics*, 2021, **24** (4), P. 27–36.
[2] Potrakhov N.N., Gryaznov A.Yu., Zhamova K.K., Bessonov V.B., Obodovsky A.V., Staroverov N.E., Kholopova E.D. Microfocus radiography in medicine: physical and technical features and modern means of X-ray diagnostics. *Biotechnosphere*, 2015, **5** (41), P. 55–63.
[3] Lider V.V. X-ray methods of axial phase contrast and axial holography. *Industrial Laboratory. Diagnostics of Materials*, 2015, **81** (12), P. 32–40.
[4] Nugent K.A., Paganin D., Gureyev T.E. A phase odyssey. *Physics Today*, 2001, **54** (8), P. 27–32.
[5] Snigirev A., Snigireva I., Kohn V., Kuznetsov S., Schelokov I. On the possibilities of X-ray phase contrast microimaging by coherent high-energy synchrotron radiation. *Review of Scientific Instruments*, 1995, **66** (12), P. 5486–5492.
[6] Cloetens P., Barrett R., Baruchel J., Guigay J.P., Schlenker M. Phase objects in synchrotron radiation hard X-ray imaging. *J. of Physics D: Applied Physics*, 1996, **29** (1), P. 133–146.
[7] Davis T.J., Gao D., Gureyev T.E., Stevenson A.W., Wilkins S.W. Phase-contrast imaging of weakly absorbing materials using hard X-rays. *Nature*, 1995, **373**, P. 595–598.
[8] Gryaznov A.Yu. On the possibility of obtaining phase-contrast images on microfocus X-ray sources. *Biotechnosphere*, 2010, **1** (7), P. 30–32.
[9] Shovkun V.Ya., Kumakhov M.A. Phase contrast imaging with micro focus X-ray tube. *Proceedings of SPIE*, 2006, **5943**, 594315.
[10] Shovkun V.Ya. Development of a phase-contrast mammograph in the "in-line holography" scheme. *Medical physics*, 2007, **2** (34), P. 25–34.
[11] Hertz H.M., Bertilson M., Chubarova E., Ewald J., Gleber S.-C., Hemberg O., Henriksson M., Hofsten O., Holmberg A., Lindblom M., Mudry E., Otendal M., Reinspach J., Schlie M., Skoglund P., Takman P., Thieme J., Sedlmair J., Tjornhammar R., Tuohimaa T., Vita M., Vogt U. Laboratory X-ray micro imaging: Sources, optics, systems and applications. *J. of Physics: Conference Series*, 2009, **186** (1), 012027.
[12] Bavendiek K., Ewert U., Riedo A., Heike U., Zscherpel U. New measurement methods of focal spot size and shape of X-ray tubes in digital radiological applications in comparison to current standards. *Proceedings of the "18th World Conference on Nondestructive Testing"*, Durban, South Africa, 2012, **346**.
[13] Dougherty G., Kawaf Z. The point spread function revisited: image restoration using 2-D deconvolution. *Radiography*, 2001, **7** (4), P. 255–262.
[14] Di Domenico G., Cardarelli P., Contillo A., Talbi A., Gambaccini M. X-ray focal spot reconstruction by circular penumbra analysis – Application to digital radiography systems. *Medical Physics*, 2016, **43** (1), P. 294–302.
[15] Bicher B.A., Meli F., Kung A., Sofiienko A. Traceable x-ray focal spot reconstruction by circular edge analysis: from sum-microfocus to mesofocus. *Measurement Science and Technology*, 2022, **33** (7), 074005.

[16] Nachtrab F., Firsching M., Uhlmann N., Speier C., Takman P., Tuohimaa T., Heinzl C., Kastner J., Larsson D.H., Holmberg A., Berti G., Krumm M., Sauerwein C. NanoXCT: development of a laboratory nano-CT system. *Proceedings of SPIE*, 2014, **9212**, 92120L.
[17] Goodman J.W. *Introduction to Fourier optics*. Roberts and Company Publishers, Greenwood Village, 2005, 491 p.
[18] Cowley J.M. *Diffraction physics*. North Holland Publishing, Amsterdam, 1995, 488 p.
[19] Shao W., He T., Wang L., Wang J.X., Zhou Y., Shao B., Ugur E., Wu W., Zhang Z., Liang H., de Wolf S., Bakr O.M., Mohammed O.F. Capillary manganese halide needle-like array scintillator with isolated light crosstalk for micro-X-ray imaging. *Advanced Materials*, 2024, **36** (21), e2312053.
[20] Pfeiffer F., Bech M., Bunk O., Donath T., Henrich B., Kraft P., David C. X-ray dark-field and phase-contrast imaging using a grating interferometer. *J. of Applied Physics*, 2009, **105** (10), 102006.

Submitted 2 October 2024; revised 20 November 2024; accepted 28 November 2024

Information about the authors:

Alexey A. Manushkin – "Diagnostika-M" LLC, Volgogradskiy, 42, Moscow, 109316, Russia; ORCID 0009-0009-8428-9588; manushkinaa@mail.ru

Nikolay N. Potrakhov – Saint Petersburg Electrotechnical University "LETI", Professora Popova, 5, St. Petersburg, 197022, Russia; ORCID 0000-0001-8806-0603; nnpotrahov@etu.ru

Dmitrii K. Kostrin – Saint Petersburg Electrotechnical University "LETI", Professora Popova, 5, St. Petersburg, 197022, Russia; ORCID 0000-0002-6284-0246; dkkostrin@mail.ru

Karina K. Guk – Saint Petersburg Electrotechnical University "LETI", Professora Popova, 5, St. Petersburg, 197022, Russia; ORCID 0000-0002-4968-7857; kkguk@etu.ru

Conflict of interest: the authors declare no conflict of interest.

NANOSYSTEMS:
PHYSICS, CHEMISTRY, MATHEMATICS

Kadet V.V., et al. *Nanosystems: Phys. Chem. Math.*, 2025, **16** (1), 14–21.
http://nanojournal.ifmo.ru
DOI 10.17586/2220-8054-2025-16-1-14-21

Original article

Effectiveness of the use of nanoaggregates for polymer treatment in oil fields with hard-to-recover reserves

Valeriy V. Kadet[1,a], Ivan V. Vasilev[1,b], Andrei V. Tiutiaev[1,c]

[1]Gubkin University, 119991 Moscow

[a]kadet.v@gubkin.ru, [b]vas.ivn@mail.ru, [c]tyutyaev@mail.ru

Corresponding author: V. V. Kadet, kadet.v@gubkin.ru

PACS 47.56.+r

ABSTRACT The study presents the results of comprehensive research on the efficiency of using polymer systems with nanoaggregates as oil displacement agents. Laboratory tests included experiments to determine the oil displacement coefficient on linear core models, as well as experiments to determine the oil recovery factor using parallel flow tubes of varying permeability, simulating the implementation of polymer flooding technology in stratified-heterogeneous oil-saturated reservoirs. The results of hydrodynamic studies using parallel flow tubes with polymer systems containing nanoaggregates demonstrated a significantly greater redistribution effect of filtration flows compared to traditional polymer solutions. The theoretical modeling of the polymer flooding process was conducted based on a percolation-hydrodynamic model, accounting for the specific flow characteristics of polymer systems with nanoaggregates in a porous medium. A comparison of the theoretical results with laboratory test outcomes showed good agreement.

KEYWORDS oil displacement by polymer solutions, polymer systems with nanoaggregates, oil recovery factor, percolation-hydrodynamic model, linear core models, parallel flow tubes.

FOR CITATION Kadet V.V., Vasilev I.V., Tiutiaev A.V. Effectiveness of the use of nanoaggregates for polymer treatment in oil fields with hard-to-recover reserves. *Nanosystems: Phys. Chem. Math.*, 2025, **16** (1), 14–21.

1. Introduction

Polymer flooding is one of the most widely applied chemical methods for enhancing oil recovery from reservoirs [1,2]. It increases the sweep efficiency of the reservoir treatment and significantly improves the oil recovery factor (ORF). Additionally, its broad applicability enables its implementation in reservoirs with diverse characteristics [2–5].

The primary mechanisms for improving oil recovery when polymer solutions are applied to reservoirs include:

1. *Increasing the viscosity of the displacing agent.* Adding a high-molecular-weight chemical reagent to the injected water, even at low concentrations, significantly increases the viscosity of the displacing agent. This leads to a reduction in the mobility ratio between water and oil and a more uniform displacement front.

2. *Blocking water-conducting channels.* The adsorption of polymer molecules on the surface of the pore space leads to a complete or partial blocking of conducting capillary cross-sections. Notably, the positive role of adsorption is evident in water-swept reservoirs, as it reduces water permeability and correspondingly increases oil production [1,6].

With the growing demand for developing fields with hard-to-recover reserves, the creation of new polymer systems that expand the applicability of this technology has become increasingly relevant. In recent years, significant advancements have been made in polymer composite systems with nanoaggregates, such as polymers with hyperbranched nanoaggregates (Fig. 1) [6–10]. These polymers, through the selection of functional monomers tailored to the filtration and capacitive properties (FCP) of specific reservoirs and the physicochemical properties of the fluids saturating them, provide the potential for more effective control of micro-level processes occurring during the movement of polymer systems through porous media.

The addition of nanoaggregates provides significant advantages in using such composites, including enhanced resistance to thermal and chemical degradation, more substantial viscosity increases at the same polymer concentrations, and higher oil recovery factors (ORF) compared to classical reagents (polyacrylamide and its modifications, xanthan gum, polysaccharides, etc.) [11–14].

Various modifications of crosslinked polymer gels can also serve as such composite reagents [8]. Conceptually, they can be divided into two main groups: “in situ” gel systems and preformed gels. The primary difference between these lies in the location of the gel’s three-dimensional structure formation: on the surface before injection or within the reservoir after injection. Depending on particle size, preformed gels can be categorized as macrogels (from 100 μm) or microgels (from 0.1 to 30 μm).

There are several types of microgels, including standard crosslinked, thermosensitive (Bright Water), and pH-sensitive microgels. The polymer particles of Bright Water microgel, in dry form, range in size from 0.1–1 μm and exhibit high

© Kadet V.V., Vasilev I.V., Tiutiaev A.V., 2025

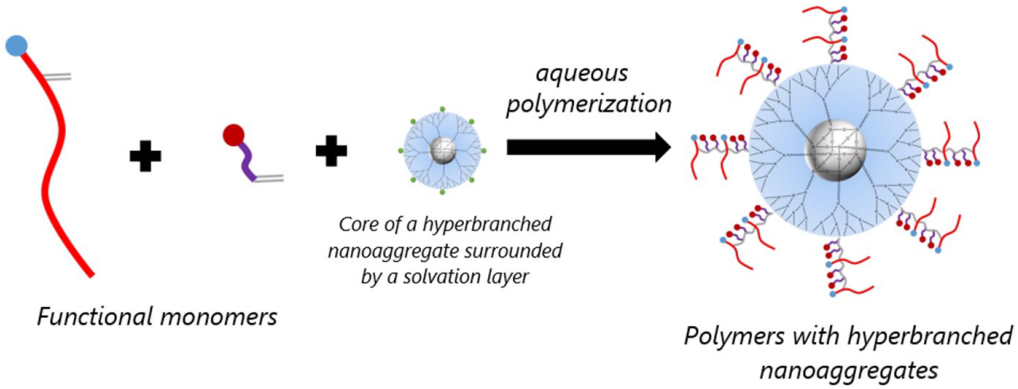

FIG. 1. Schematic of hyperbranched nanomaterial synthesis

penetration capability. Reservoir temperature triggers the process of abrupt and irreversible swelling of the particles, significantly reducing reservoir permeability. The size of the swollen particles must correspond to the characteristic pore size of the reservoir.

2. Theoretical calculation of the effect of using various polymer types

To determine the optimal parameters for implementing polymer flooding technology in oil-saturated reservoirs, the modeling process varied the FCP of the reservoir, the viscosity of the reservoir oil, and the concentration of the injected polymer solution.

To assess the effect of pore structure on the ORF, oil-saturated reservoirs with varying structures were considered: low-permeability (m_0 = 11 %, K_0 = 50 mD), medium-permeability (m_0 = 12 %, K_0 = 120 mD), and high-permeability (m_0 = 14 %, K_0 = 202 mD). The density distribution functions (DDF) of the capillaries' radii in these formations were assumed to follow a log-normal distribution (Fig. 2).

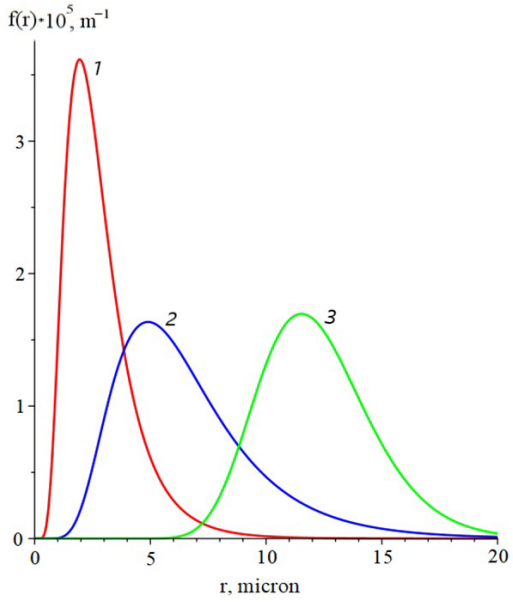

FIG. 2. Lognormal distribution density functions of capillaries by radii $f(r)$ for: 1 – Low permeability reservoir (m_0 = 11 %, K_0 = 50 mD); 2 – Medium permeability reservoir (m_0 = 12 %, K_0 = 120 mD); 3 – High permeability reservoir (m_0 = 14 %, K_0 = 202 mD)

When constructing relative phase permeability (RPP) curves based on the corresponding DDF, a percolation approach was employed [15].

The relative phase permeability curves for polymer flooding using classical polymer solutions and polymer systems with nanoaggregates are shown in Fig. 3 as solid blue lines and solid green lines, respectively. The calculated initial relative phase permeability curves for traditional flooding (without polymer addition) are presented as red dashed lines in Fig. 3.

The reduction in water-phase RPP (at water saturation S, equal to the reservoir's residual water saturation S^*) is 6 % to 16 % when using classical polymer solutions and 8 % to 21 % with polymer systems containing nanoaggregates. Notably, the greatest reduction in relative phase permeability is observed when using polymer systems with nanoaggregates in low-permeability reservoirs, reaching approximately 21 %.

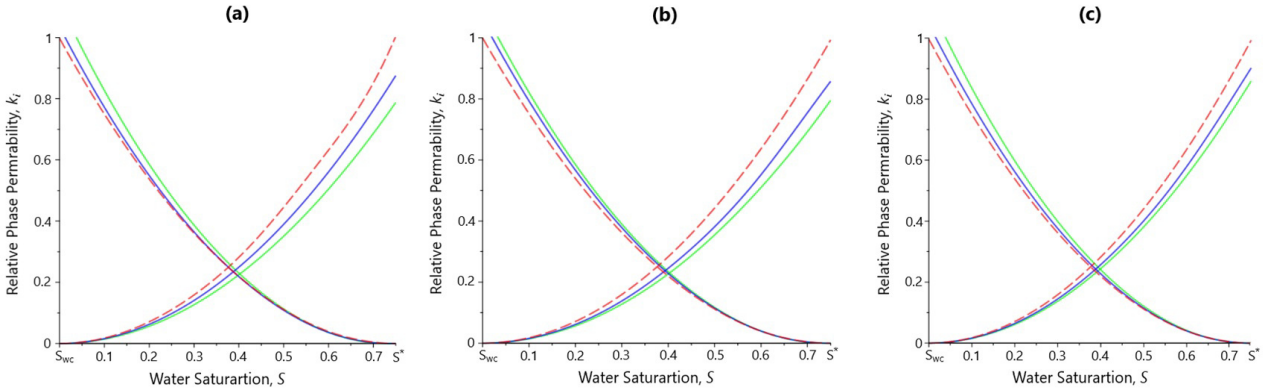

FIG. 3. Relative phase permeability curves for: (a) – high permeability reservoir; (b) – medium permeability reservoir; (c) – low permeability reservoir. Red dashed lines: basic flooding (without adding polymer); Blue solid lines: after injection of classical polymer; Green solid lines: after injection of polymer with hyperbranched nanoaggregates

The calculation of the dependence of the ORF increment relative to the baseline flooding scenario (without polymer addition) was performed by varying the concentration of the injected agent. This calculation was conducted for the case where the water cut of the produced fluid reached 99 % (Fig. 4).

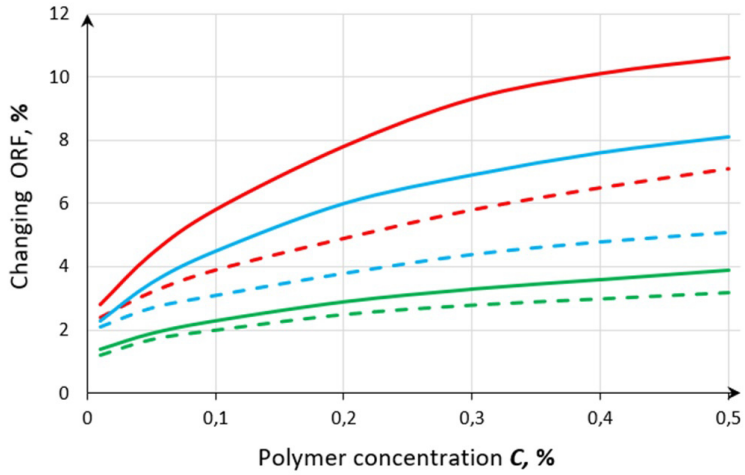

FIG. 4. Dependence of the increase in oil recovery factor relative to the basic flooding option on the concentration of the injected reagent (oil viscosity μ_0 = 50 cP) when using: polymers with hyperbranched nanoaggregates (solid lines) and classical polymer solutions (dashed lines): Red lines – Low permeability reservoir; Blue lines – Medium permeability reservoir; Green lines – High permeability reservoir

The relative increases in the oil recovery factor in various reservoirs when using polymer solutions of different types, for the most representative values of concentration and reservoir oil viscosity, are presented in Table 1.

From Table 1, it is evident that the use of polymer systems with nanoaggregates is particularly advantageous in fields with low-permeability reservoirs.

3. Laboratory Studies

Experimental research on the rheological and filtration properties of polymer systems with nanoaggregates was conducted in several stages.

For the laboratory tests, the following reagents were selected: polyacrylamide FP-107 (manufactured by SNF-CHINA) and a nanoscale reagent, chromium acetate. During polymer dissolution in water, the polyacrylamide and nanoscale additive interact at an intermolecular (nano) level, forming a crosslinked polymer system.

TABLE 1. Growth of oil recovery factor relative to the basic flooding option (without addition of polymer) at the concentration of the injected chemical reagent of 0.4 % and the viscosity of reservoir oil of 50 cP

Collector type	Increase in ORF when using classic polymer solutions, %	Increase in ORF when using polymer systems with nanoaggregates, %
Low permeability	6.5	10.1
Medium permeability	4.8	7.6
High permeability	3.1	3.5

Stage I: Solubility Study. The first stage of the research focused on the solubility of the polymer sample. Solubility is a critical parameter to consider when developing programs and plans for implementing permeability profile control technologies at specific oil fields. The solubility of a polymer in water is characterized by the rate and completeness of dissolution, which primarily depends on its molecular structure and the dispersity of the reagent powder. Achieving constant viscosity indicates the complete dissolution of the polymer.

The solubility of polymer samples was studied using a water model prepared with a specific component ionic composition. The component composition is provided in Table 2.

TABLE 2. Component composition of water

Component	HCO^{-3}	Cl^{-}	SO_4^{2-}	Ca^{2+}	Mg^{2+}	K^{+} + Na^{+}	Total concentration
Dimension	g/l	g/l	g/l	g/l	g/l	g/l	g/l
Concentration	0,204	107,262	1,008	5,127	2,164	62,789	178,550

Fig. 5 presents graphs showing the dependence of the effective viscosity of polymer solutions ($C = 0.4$ % and $C = 1$ %) on their dissolution time. The graphs indicate that the dissolution time for the majority of the reagent is 2.5 hours at $C = 0.4$ % and 3.3 hours at $C = 1$ %.

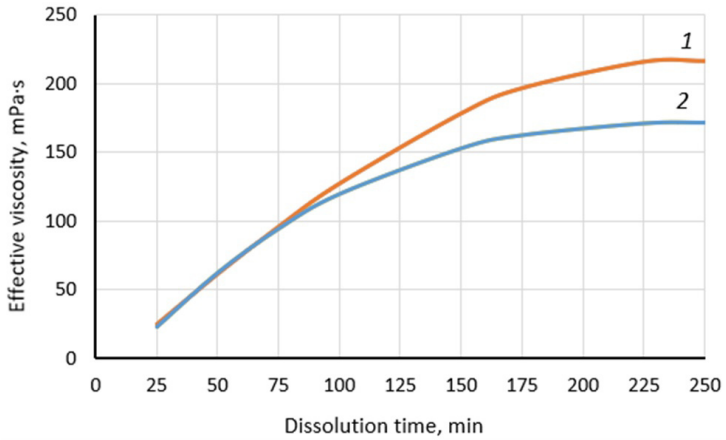

FIG. 5. Dependence of effective viscosity on dissolution time: Orange curve 1 – for polymer concentration $C = 1$ %; Blue curve 2 – for polymer concentration $C = 0.4$ %

It should be noted that under actual field conditions, the polymer dissolution time would be even shorter due to the existing pressure gradient.

Stage II: Rheological Properties Investigation. At the second stage, the rheological properties of the prepared solutions were studied using a Brookfield viscometer at a temperature of $T = 38$ ∘C, corresponding to the reservoir temperature. The investigation was conducted across a range of shear rates (0.122 – 6.12) s^{-1} (Fig. 6).

It is evident that these solutions exhibit pseudoplastic flow behavior, meaning that as the shear rate increases, the viscosity of the polymer solution decreases.

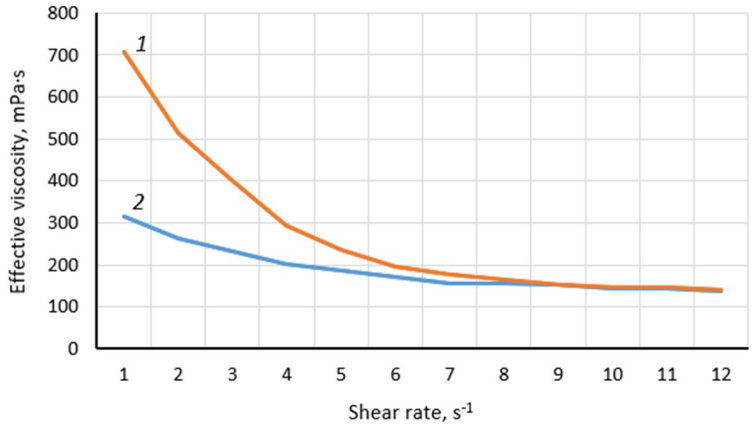

FIG. 6. Dependence of the effective viscosity of polymer solutions on the shear rate: Orange curve 1 – for polymer concentration C = 1 %; Blue curve 2 – for polymer concentration C = 0.4 %

Stage III of the experiment involved studying the kinetics of crosslinked structure formation, which is characterized by three sequential stages. In the first (initial) stage, there is a slow increase in viscosity due to the formation of microgel particles. In the second stage, the microgel particles grow larger, resulting in a more rapid increase in viscosity. Finally, in the third (final) stage, a continuous system forms throughout the volume, leading to an almost instantaneous increase in viscosity. The tested polymer, in combination with chromium acetate, demonstrated excellent structure-forming properties.

Stage IV of the experiment assessed the potential for gel formation in a porous medium through a filtration study using a single core sample. A natural core sample from the reservoir was used for this purpose (Table 3).

TABLE 3. Filtration-capacity characteristics and geometric parameters of the core sample

Rock type	Porosity, unit fraction	Absolute permeability, μm^2	Core sample length, cm	Core sample diameter, cm	Core sample volume, cm^3	Pore volume, cm^3
Sand	0.15	0.622	3.14	2.81	19.47	3.44

TABLE 4. The results of the experimental determination of the values of the displacement factor and residual oil saturation

Parameter / Experiment No.	Exp. No 1	Exp. No 2	Exp. No 3	**Exp. No 4**	**Exp. No 5**
Residual oil saturation, unit fraction.	0.318	0.312	0.288	**0.252**	**0.247**
Displacement factor, unit fraction.	0.665	0.672	0.702	**0.735**	**0.742**

The study was conducted using the automated core filtration unit UIK-4. At the beginning of the experiment, the core was saturated with injection water at a temperature of 38 ∘C, followed by the determination of water permeability. Next, a composition of 0.4 % FP-107 and 0.04 % nanoscale reagent was injected through the water-saturated core in a volume of 2 pore volumes at a filtration rate of 0.5 cm^3/min. After the injection of the composition, the core was maintained at reservoir temperature for 24 hours to enable the gel formation process. Subsequently, water was injected through the core sample again at the same volumetric rate.

Based on the experimental results, the residual resistance factor (RRF) created by the composition in the porous medium was calculated. RRF is one of the key parameters characterizing the effectiveness of the polymer flooding technology. It determines the degree of blockage of the most water-permeable filtration channels. After implementing the polymer composition with the nanosystem, the RRF was determined to be 57.3.

Stage V of the Experiment. The completeness of oil displacement by water was determined under laboratory conditions in accordance with the requirements of OST 39-195-86 [16]. The experiment was carried out using a core study setup similar to the one described in [17].

TABLE 5. Collector properties of low-permeability and high-permeability core samples during an experiment on parallel flow tubes (average values are highlighted in red)

Porosity, unit fraction	Gas permeability, μm^2	Residual oil saturation, unit fraction
Low permeability reservoir element model current tube		
0.096	0.0382	0.327
0.119	0.0429	0.321
0.097	0.043	0.310
0.111	0.0469	0.306
0.107	0.0492	0.293
0.11	0.052	0.301
0.114	0.0551	0.313
0.107	0.0557	0.279
0.125	0.0659	0.229
0.1095	**0.0486**	**0.298**
High permeability reservoir element model current tube		
0.137	0.1728	0.337
0.13	0.1738	0.335
0.133	0.1741	0.306
0.134	0.2013	0.282
0.138	0.2045	0.275
0.137	0.2124	0.275
0.136	0.2183	0.274
0.143	0.2201	0.274
0.133	0.2253	0.227
0.1355	**0.1986**	**0.287**

TABLE 6. Redistribution of filtration flows and changes in residual oil saturation after the implementation of the proposed technology

Current tube type	Ratio of volume velocities in parallel current tubes when creating residual oil saturation with produced water, unit fraction.	Ratio of volume velocities in parallel current tubes during flooding with produced water after the implementation of the proposed technology, unit fraction.	Increase in oil displacement factor, %
High permeability reservoir element model current tube	2.2	0.353	1.8
Low permeability reservoir element model current tube			9.2

The process of oil displacement by water was modeled on a composite core model assembled from 10 standard core samples obtained from the same reservoir.

Before testing, the core samples were extracted using an ethanol-benzene mixture and dried to constant weight. Then the samples were vacuum-saturated with highly mineralized formation water from the same reservoir (Table 2) and held for two days. Residual water saturation was then established in the samples by centrifugation.

The samples were subsequently saturated with kerosene and assembled into a composite reservoir model so that each subsequent sample in the displacement direction had lower permeability. The composite sample was placed in a rubber sleeve and installed in a core holder.

Next, kerosene was filtered through the linear reservoir model in a volume of about 10 pore volumes, followed by an equal amount of formation oil (a sample of which was collected from the well) at T_{res}=80 ∘C. Upon completing the oil injection, the model was held for 16 hours under thermobaric conditions corresponding to the reservoir. The initial oil saturation of the reservoir element model K_{ios} was 0.95.

The same reservoir water was used as the displacing agent. Displacement was performed at reservoir temperature (T_{res}=80 ∘C) at a constant rate until complete water breakthrough in the effluent fluid. As a result, the residual oil saturation K_{ros} was 0.318, and the displacement efficiency K_{displ} was 0.665.

After establishing residual oil saturation in the composite reservoir element model, the developed composite polymer flooding technology was implemented according to the following scheme:

(1) Oil displacement by water (without polymer addition);
(2) Injection of a well-mixed 0.4 % polymer solution;
(3) Injection of a well-mixed 1 % polymer solution;
(4) Injection of a well-mixed solution of 0.4 % polymer and 0.04 % nanoscale reagent;
(5) Injection of a well-mixed solution of 1 % polymer and 0.04 % nanoscale reagent.

Table 4 presents comparative data on the determination of residual oil saturations and displacement efficiencies for the specified scenarios.

Stage VI of the Experiment. Experiments were conducted on parallel flow tubes to study the redistribution of filtration flows and the intensification of production from low-permeability interlayers during oil recovery.

The flow tubes were composite models of reservoir elements with two interlayers differing in permeability. The displacing agent used was the formation water model specified in Table 2. Displacement was performed at reservoir temperature (T_{res}=80 ∘C) at a constant rate until the effluent fluid from the high-permeability section of the reservoir element model reached full water breakthrough.

The characteristics of the individual core samples for the low-permeability and high-permeability flow tubes are presented in Table 5.

Based on the laboratory tests, the oil displacement efficiency in the low-permeability flow tube (K_{ios} = 0.93 and K_{ros} = 0.298) was 0.679.

The oil displacement efficiency in the high-permeability reservoir element model (K_{ios} = 0.95 and K_{ros} = 0.287) was 0.698.

It is evident that the difference in displacement efficiencies between the high-permeability and low-permeability reservoir element models is negligible.

After establishing residual oil saturation in the composite reservoir element model, a thoroughly mixed 0.4 % polymer solution with the addition of 0.04 % nanoaggregate was injected. Changes in the oil volume collected in test tubes from each flow tube and the ratio of volumetric flow rates through the parallel flow tubes were recorded. The results obtained are presented in Table 6.

As shown in Table 6, the total increase in oil displacement efficiency in the parallel flow tube experiment was 11 %. This result is explained by the significant improvement in the displacement efficiency of the low-permeability flow tube due to the redistribution of filtration flows between the two flow tubes. This effect is a result of the substantial reduction in water-phase relative phase permeability in the low-permeability flow tube of the reservoir element model when polymer systems with nanoaggregates are used.

The theoretical results obtained using the percolation-hydrodynamic model (Table 1) align well with the experimental data (Table 6). Obviously, this is a consequence of the fact that the developed model fully takes into account the features of the flow of polymer solutions with included nanoaggregates, including the nature of their adsorption interaction with the surface of the pore space. At the same time, the parameters of polymer systems directly used in experiments were taken into account in the calculations. In general, this indicates a high degree of adequacy and accuracy of the constructed percolation-hydrodynamic model.

4. Conclusions

1. Experimental studies on the solubility and rheological properties of polymer composite systems were conducted. The characteristic dissolution time of the polymer composition and the establishment of a stable effective viscosity were determined. For polymer concentrations of 0.4 % and 1 % (with the addition of 0.04 % nanoaggregate in both cases),

the dissolution times were 2.5 hours and 3.5 hours, respectively. Rheological studies under varying shear rates confirmed pseudoplastic flow behavior.

2. Filtration studies were conducted on a single core sample from the selected reservoir to determine the residual resistance factor during the injection of the polymer composition (0.4 % FP-107 + 0.04 % nanoscale reagent). High RRF values indicated the formation of a stable, branched structure.

Filtration experiments on the single sample demonstrated an increase in oil recovery efficiency by (1.1–5.6) % when classical polymer solutions were used at polymer concentrations ranging from 0.4 % to 1 %. In contrast, polymer systems with nanoaggregates achieved a (10.5–11.6) % increase under the same conditions.

3. Experiments on parallel flow tubes were conducted to evaluate the efficiency of polymer flooding in oil-saturated reservoirs with stratified heterogeneity. Following the injection of a polymer composition (0.4 % FP-107 + 0.04 % nanoscale reagent), the oil displacement efficiency in the low-permeability flow tube of the reservoir element model increased by 9.2 %, while the overall model efficiency improved by 11 % relative to the baseline flooding scenario (without polymer addition).

4. Numerical studies of various polymer flooding scenarios in reservoirs of different types (considering variations in pore structure, reservoir oil viscosity, polymer type, and concentration) demonstrated a potential increase in oil recovery factor by approximately 10 % compared to the baseline flooding scenario when polymer systems with nanoaggregates were used. This estimate is consistent with the results of laboratory experiments on parallel flow tubes with different reservoir properties (low-permeability and high-permeability reservoirs).

References

[1] Zheltov Yu.P. *Development of Oil Fields: A Textbook for Universities*. Moscow, Nedra, 1986, 332 p.

[2] Zolotukhin A.B., Pyatibratov P.V., Nazarova L.N., et al. EOR methods applicability evaluation. Proceedings of the Gubkin I.M. Russian State University of Oil and Gas, 2016, **2**(283), P. 58–70.

[3] Silin M.A., Magadova L.A., Davletshina L.F., et al. Application experience and major trends in polymer flooding technology worldwide. *Territory of Oil and Gas*, 2021, **9–10**, P. 46–52.

[4] Telkov V.P., Kim S.V., Mostadjeren M. New Opportunities for Using Polymer Solutions for the Development of Heavy Oil and High-Viscosity Oil Fields. Achievements, Challenges, and Prospects for the Development of the Oil and Gas Industry: Proceedings of the International Scientific and Practical Conference Dedicated to the 60th Anniversary of Higher Oil and Gas Education in the Republic of Tatarstan, Almetyevsk, October 28–29, 2016. Almetyevsk: Almetyevsk State Oil Institute, 2016, **1**, P. 454–461.

[5] Pribylev, E. M. Analysis of world implementation experience polymer filling technologies. *Problems of the Development of Hydrocarbon and Ore Deposits*, 2020, **2**, P. 332.

[6] Kadet V.V., Vasiliev I.V. Use of hyperbranched nanocomplexes to improve the efficiency of polymer flooding. Theoretical Foundations of Chemical Engineering, 2023, **57**(6), P. 1385–1393.

[7] Grigorashchenko G.I., Zaitsev Yu.V., Kukin V.V., et al. *The Use of Polymers in Oil Recovery*. Moscow, Nedra, 1978.

[8] Ketova Iu.A., Galkin S.V., Votinov A.S., Kang W., Yang H. Analysis of the international practice in application of conformance control technologies based on cross-linked polymer gels. *Perm Journal of Petroleum and Mining Engineering*, 2020, **20**(2), P. 150–161.

[9] Tereshchenko T.A. Synthesis and application of polyhedral oligosilsesquioxanes and spherosilicates, T. A. Tereshchenko. *Polymer Science, Series B*, 2008, **50**(9-10), P. 249–262.

[10] Khavkin A.Ya. Nanophenomena and Nanotechnologies in Oil and Gas Recovery. Moscow, Izhevsk, NIC "Regular and Chaotic Dynamics", Institute for Computer Studies, 2010.

[11] Podoprigora D.G., Byazrov R.R., Khristich E.A. The current level and prospects for the development of large-volume injection technologies using polymers to increase oil recovery. *The Eurasian Scientific Journal*, 2022, **14**(2), P. 34.

[12] Seright R.S., Campbell A.R., Mozley P.S., Han P. Hydrolyzed Polyacrylamides at Elevated Temperatures in the Absence of Divalent Cations. *SPE Journal*, 2010, **15**(02), P. 341–348.

[13] Murzina L.A., Zakharova E.M., Zakharov V.P. Associative polymers to improve oil recovery. Practical Aspects of Oilfield Chemistry: Abstracts of the 4th All-Russian Scientific and Practical Conference, Ufa, May, 27–28, 2014. Ufa: OAO "BashNIPIneft", 2014, P. 17–19.

[14] Raupov I.R., Kondrasheva N.K., Raupov R.R. Development polymeric compositions for in-situ water shutoff of terrigenous deposits of oil field development. Oil and Gas Engineering, 2016, **14**(1), P. 80–87.

[15] Kadet V.V. *Percolation analysis of hydrodynamic and electrokinetic processes in porous media*. Moscow, INFRA-M, 2013, P. 139–155.

[16] OST 39-195-86. Oil. Method for Determining the Oil Displacement Factor by Water Under Laboratory Conditions.

[17] Petrov I.V., Tyutyaev A.V., Dolzhikova I.S. Program development for experimental evaluation of oil reservoir alkaline-sas floodind efficiency. *Advances in current natural sciences*, 2016, **11**, P. 182–185.

Submitted 26 December 2024; revised 16 January 2025; accepted 17 January 2025

Information about the authors:

Valeriy V. Kadet – Gubkin University, 119991 Moscow; ORCID 0000-0003-2981-5310; kadet.v@gubkin.ru

Ivan V. Vasilev – Gubkin University, 119991 Moscow; vas.ivn@mail.ru

Andrei V. Tiutiaev – Gubkin University, 119991 Moscow; tyutyaev@mail.ru

Conflict of interest: the authors declare no conflict of interest.

NANOSYSTEMS:
PHYSICS, CHEMISTRY, MATHEMATICS

Popkov M.A., et al. *Nanosystems: Phys. Chem. Math.*, 2025, **16** (1), 22–29.
http://nanojournal.ifmo.ru
DOI 10.17586/2220-8054-2025-16-1-22-29

Original article

Peroxidase-like activity of photochromic PVP-stabilized tungsten oxide nanoparticles: assessment by independent chemiluminescent and colorimetric assays

Matvei A. Popkov[1,a], Ekaterina D. Sheichenko[1,2,b], Arina D. Filippova[1,c], Ilya V. Tronev[1,2,d], Kristina N. Novoselova[1,2,e], Evelina A. Trufanova[1,2,f], Darya N. Vasilyeva[1,2,g], Maria R. Protsenko[1,2,h], Madina M. Sozarukova[1,j], Alexander E. Baranchikov[1,2,k], Vladimir K. Ivanov[1,2,l]

[1]Kurnakov Institute of General and Inorganic Chemistry, Russian Academy of Sciences, Moscow, Russia
[2]HSE University, Moscow, Russia

[a]ma_popkov@igic.ras.ru, [b]edsheychenko@edu.hse.ru, [c]arifilippova@yandex.ru, [d]ivtronev@edu.hse.ru, [e]knnovoselova@edu.hse.ru, [f]eatrufanova_1@edu.hse.ru, [g]Dnvasileva_1@edu.hse.ru, [h]mrprotsenko@edu.hse.ru,[j]s_madinam@bk.ru, [k]a.baranchikov@yandex.ru, [l]van@igic.ras.ru

Corresponding author: M. A. Popkov, ma_popkov@igic.ras.ru

PACS 68.65.-k, 78.67.-n, 82.65.+r

ABSTRACT In this work, peroxidase-like activity of ultrasmall tungsten oxide nanoparticles including those stabilized with polyvinylpyrrolidone (PVP) was assessed using two independent approaches: the colorimetric method, which is based on the analysis of 3,3',5,5'-tetramethylbenzidine (TMB) oxidation, and the luminol-enhanced chemiluminescence method. It was demonstrated that bare tungsten oxide nanoparticles effectively catalyze the decomposition of hydrogen peroxide. In turn, the PVP-stabilized nanoparticles possess lower catalytic activity, which can be attributed to a decrease in the number of available active centres on the nanoparticle surface.

KEYWORDS nanomaterials, nanozymes, sols, photochromic materials, chemiluminescence, TMB, peroxidase-like activity.

ACKNOWLEDGEMENTS The publication was prepared within the framework of the Academic Fund Program at HSE University (grant 24-00-036, Enzyme-like activity of nanodispersed inorganic materials). The studies were carried out on the equipment of the Joint Scientific Center for Physical Research Methods of the Kurnakov Institute of General and Inorganic Chemistry of the Russian Academy of Sciences, Moscow, Russia.

FOR CITATION Popkov M.A., Sheichenko E.D., Filippova A.D., Tronev I.V., Novoselova K.N., Trufanov E.A., Vasilyeva D.N., Protsenko M.R., Sozarukova M.M., Baranchikov A.E., Ivanov V.K. Peroxidase-like activity of photochromic PVP-stabilized tungsten oxide nanoparticles: assessment by independent chemiluminescent and colorimetric assays. *Nanosystems: Phys. Chem. Math.*, 2025, **16** (1), 22–29.

1. Introduction

In recent years, it has been demonstrated that certain inorganic nanomaterials are capable of participating in biochemical processes, performing functions analogous to those of natural enzymes [1, 2]. Such materials have been identified as a distinct class called nanozymes. Among them, nanoparticles of transition and rare earth metal oxides with switchable redox state are of particular interest. A number of studies have demonstrated that nanoscale oxide nanoparticles, including Fe_3O_4 [3, 4], CeO_2 [5–7], MnO_2 [8], and TiO_2 [9], exhibit oxidoreductase-like activity rendering them perspective regulators of free-radical reactions or even redox-metabolism in cells. Extended insights into enzyme-mimetic properties of inorganic nanoparticles could facilitate their application in both medical and ecological contexts.

One of the materials exhibiting high redox activity is tungsten oxide nanoparticles [10]. WO_3 is a semiconductor material demonstrating photochromic, electrochromic and photocatalytic properties [11–14]. Tungsten oxide nanoparticles effectively absorb ultraviolet radiation being able to show reversible coloring-bleaching cycles as a result of partial reduction of W^{+6} and oxidation of W^{+4}/W^{+5} states [15, 16]. Oxidants, such as NO_2 or H_2O_2, can also facilitate the redox transitions of tungsten ions, thus tungsten oxides can act as probes for these species [17, 18]. The coordination of WO_3 nanoparticles with OH- or NH_2-groups of certain organic stabilizers has been demonstrated to enhance the rate of the redox transitions, to intensify the color changes and to facilitate the cycling of coloration-decoloration processes [19].

WO_3-based materials have gained considerable attention as coatings for electrochemical sensors used for the detection of gases [14, 20] and biomolecules [21, 22]. It has been demonstrated that tungsten oxide possesses antibacterial and antifungal properties, being selectively toxic to human cancer cells [23–25]. This issue paves the way for new applications of tungsten oxide nanomaterials in medicine, including healing and disinfecting of wounds.

© Popkov M.A., Sheichenko E.D., Filippova A.D., Tronev I.V., Novoselova K.N., Trufanov E.A., Vasilyeva D.N., Protsenko M.R., Sozarukova M.M., Baranchikov A.E., Ivanov V.K., 2025

Recent research has demonstrated that nanoscale tungsten oxide is able to catalyze the decomposition of hydrogen peroxide, thus performing similar to the natural enzyme –peroxidase [26, 27]. This fact broadens the understanding of the biochemical activity of tungsten oxide nanoparticles, facilitating their consideration as a potential theranostic agent. However, the recent criticism on the probing the enzyme-like activities of inorganic nanoparticles [28,29] challenges their extended analysis by independent analytical methods including the use of classic enzyme kinetic modeling for the correct assessment of the biocatalytic characteristics of nanomaterials.

Our previous report demonstrated that photochromic tungsten oxide nanoparticles, obtained by ion exchange from sodium tungstate, probably catalyze the decomposition of hydrogen peroxide [19]. In this study, we focused on this effect and investigated the possible peroxidase-like activity of ultrasmall WO_x particles by two independent assays: colorimetric assay using 3,3',5,5'-tetramethylbenzidine; and chemiluminescence analysis of luminol oxidation by hydrogen peroxide.

2. Materials and methods

2.1. Synthesis and characterization of tungsten oxide nanoparticles

Ultrasmall tungsten oxide nanoparticles were prepared by ion-exchange method [11] using Na_2WO_4 (Rushim, CAS 10213-10-2) solution and strongly acidic cation exchange resin (Amberlite, IR120). Briefly, the ion exchange resin in protonated form was placed in a separating funnel (filling volume 100 mL), then 50 mL of 20 mM sodium tungstate solution was passed through this column. The obtained colloid solution was divided into two parts. To the first, 0.67 g of polyvinylpyrrolidone (PVP k-30, Sigma, CAS 9003-39-8) was added, the sol was transferred to a flask and stirred for 4 h at 90 ∘C. After stabilization, a clear colloidal solution of WO_x was obtained. The second part was used as synthesized.

To determine the possible effect of the stabilizer (PVP) on the peroxidase-like activity, we prepared 40 mM PVP aqueous solution (control).

Powder X-ray diffraction (XRD) patterns were collected using Bruker D8 Advance diffractometer (USA) with CuKα-radiation in the 2θ range of 5–50° with a step of 0.02° and counting time at least of 0.2 s per step.

Analysis of particle size distribution by dynamic light scattering (DLS) and ζ-potential measurements were carried out using a Photocor Compact-Z analyzer (Russia) equipped with a 636.65 nm laser at 20 ∘C. The correlation function for each sample was obtained by averaging 10 curves, each of which was accumulated for 20 s. The hydrodynamic radius of aggregates was determined by the regularization method using DynalS software.

FTIR-spectra were recorded in the wavenumber range of 400–4,000 cm^{-1} with a spectral resolution of 2 cm^{-1} using an InfraLUM FT-08 infrared spectrometer (Russia).

The optical absorption spectra were recorded using quartz cuvettes (10.0 mm optical path length) in a 200–600 nm range, at 0.1 nm steps, on an SF-2000 spectrophotometer (Russia) with a deuterium-halogen light source.

2.2. Analysis of peroxidase-like property by luminol-enhanced chemiluminescence method

The peroxidase-like activity of the WO_x sols was investigated using the chemiluminescent method which is based on the registration of luminol oxidation by hydrogen peroxide in a phosphate buffer solution (100 mM, pH 7.4) at 37 ∘C. Luminol (5-amino-1,2,3,3,4-tetrahydro-1,4-phthalazindione, Sigma 123072) and hydrogen peroxide (Aldosa, CAS 7722-84-1) were added to the buffer solution sequentially until concentrations of 50 μM and 10 mM were reached, respectively. Chemiluminescence signal was recorded in 2 ml plastic cuvettes using a 12-channel chemiluminometer DISoft Lum-1200 (Russia) and analyzed using the PowerGraph software v.3.3 (Russia).

2.3. Analysis of peroxidase-like property by colorimetric method

Peroxidase-like activity was investigated by the reaction of TMB (3,3',5,5'-tetramethylbenzidine hydrochloride, Sigma 87750) oxidation by hydrogen peroxide in an acetate buffer (0.2 M, pH 4.00) at 37 ∘C.

A solution of TMB (40 mM, 0–150 μl) in an aqueous solution of 6M acetic acid, and hydrogen peroxide (2 M, 37.5 μl) were added sequentially to the buffer solution. The mixture was incubated at 37 ∘C for 2 min, then WO_x sol (20 mM, 75 μl) was added. The total volume of the mixture was 1.5 ml. The coloration (from colorless to blue) kinetics of the obtained solution was recorded every 2 sec for 5 min in the wavelength range of 450–800 nm with a step of 1 nm using an Ocean Optics QE65000 spectrometer (USA) using an HPX-2000 xenon lamp equipped with a 450 nm UV-filter.

3. Results and discussion

Transparent sols of tungsten oxide nanoparticles with or without polyvinylpyrrolidone (PVP) as a stabilizing agent were obtained using an ion exchange technique. The concentration of the sols was measured gravimetrically to be 20.4 and 19.6 mM, respectively.

The particle size distribution was determined using dynamic light scattering (Fig. 1a). The unstabilized WO_x nanoparticles demonstrated a monodisperse size distribution, with an average hydrodynamic diameter of 4.8 nm and a ζ-potential of –20 mV. The solution of bare WO_x possessed low aggregation stability and precipitated within 72 h. Thus, all the experiments with this material were performed in few hours after the synthesis (freshly prepared samples). In the WO_x@PVP

sol, three fractions of particles were present with average hydrodynamic diameters of 1.6, 7.3 and 52 nm. The zeta potential of the sol was about –2 mV, while the sol exhibited excellent colloidal stability (more than several months) indicating the steric stabilization by a polymer layer.

Fig. 1b shows the diffraction pattern of the dried tungsten oxide sol stabilized by PVP. The material is mostly amorphous, the observed broad peak in the small angle region ($2\theta < 10^{\circ}$) can be attributed to the scattering on ultrasmall WO_x nanoparticles according to the previous reports [11, 30].

The IR spectra of the PVP powder and the dried WO_x@PVP sol are shown in Fig. 1c-d. Both spectra show absorption bands related to characteristic vibrations of polyvinylpyrrolidone. The absorption bands of O–H stretching vibrations overlap with the absorption band of N–H stretching vibrations of PVP, forming a wide band in the region of 3,500–3,100 cm^{-1}. The bands corresponding to stretching and bending vibrations of CH_2 group are observed in the regions of 2,900 cm^{-1} and 1,300–1,200 cm^{-1}, respectively. Bands in the region 1,480–1,390 cm^{-1} were attributed to the N-C stretching vibrations. The absorption bands in the region of 500–1,000 cm^{-1}refer to skeletal vibrations of PVP: (C–C) 933 cm^{-1}, $\delta(CH_2)$ 843 cm^{-1}, δ(N–C=O) 648 cm^{-1}, 574 cm^{-1}. The IR spectrum of the dried WO_x@PVP sol also shows absorption bands related to the valence vibrations of WO_3 bonds (W=O) 955 cm^{-1}, (O–W–O) 820 cm^{-1}, 795 cm^{-1}, which agrees well with the recently reported data [30, 31].

The WO_x@PVP sols exhibit a rapid change in color from transparent to blue under UV irradiation, due to the reduction of W^{+6} by PVP [32]. Such a reduction mechanism was also observed in heteropolynuclear molybdenum complexes with PVP under UV irradiation [33]. Fig. 2 shows photographs and UV-visible spectra of the WO_x@PVP sol before and after 30 sec of UV irradiation at 365 nm. The UV-vis spectrum of the irradiated sol shows a broad absorption band with a maximum at 630 nm, corresponding to reduced tungsten oxide species. The mechanism of reduction was discussed recently [11, 19]. It should be noted that the unstabilized sol does not demonstrate any coloration even after prolonged irradiation (more than 20 min). It can be concluded that upon interaction of tungsten oxide nanoparticles with PVP, a complex with charge transfer is formed which promotes the reduction of tungsten ions and slows down their further oxidation in aqueous solution.

The peroxidase-like activity of both tungsten oxide sols was investigated using chemiluminescence method, with luminol as a probe molecule. The experiments were carried out in a 0.1 M phosphate buffer solution (pH 7.4) at 37 ∘C. The decomposition of hydrogen peroxide results in the formation of hydroxyl radicals, which are capable of oxidizing luminol, thereby yielding luminescence signal. The nanoparticles can affect the decomposition process thus enhancing the chemiluminescence, which could be used to assess their catalytic activity.

Fig. 3(a–c) shows the chemiluminescence curves after the addition of WO_x@PVP or the bare WO_x sol or PVP solution to luminol-hydrogen peroxide mixture. As can be seen from the Fig. 3a, the addition of WO_x@PVP sol at concentrations of 10.2–510 μM to the solution increases the luminescence intensity in a dose-dependent manner. It can be concluded that upon the increase in the concentration of the catalyst, the rate of ROS generation increases, too.

In turn, the addition of bare WO_x nanoparticles to the reaction mixture results in a short increase in the intensity of the luminescence, which can be attributed to the very fast generation of hydroxyl radicals (Fig. 3b). After an initial flash-like stage, the luminescence intensity descends to a stationary level in approximately three minutes. It is reasonable to assume that the observed burst of luminescence is due to the high amount of the reaction centres on the nanoparticles' surface.

To confirm that it is the WO_x nanoparticles that exhibit peroxidase-like activity, the luminescence kinetics of luminol was recorded upon addition of a PVP solution in the concentration range 10 μM–8 mM. Fig. 3c shows that the addition of PVP results only in a slight increase in luminol-associated luminescence intensity, which indicates the absence of any catalytic activity inherent in the polymer.

The integral chemiluminescence intensity (Fig. 3d) shows a dose-dependent correlation of the rate of hydrogen peroxide decomposition in the presence of the tungsten oxide nanoparticles in the concentration range of 10.2–510 μM. In addition, the integral luminol luminescence intensity upon addition of the bare WO_x sol is nearly 10 times higher compared to the PVP-stabilized WO_x sol.

The peroxidase-like activity of nanoparticles is often determined by the colorimetric method using standard substrates such as hydrogen peroxide and 3,3',5,5'-tetramethylbenzidine (TMB) [34]. The catalyst accelerates the homolytic fission of the O–O bond in hydrogen peroxide, resulting in the generation of free hydroxyl radicals. The rate of radical generation is directly proportional to the rate of oxidation of TMB, which is converted to the colored (absorption at 652 nm) cation-radical form by a one-electron process. The corresponding reaction is typically conducted in a buffer solution at pH 3–6. The optimal pH value is approximately 4, and the ionic strength of the buffer is 0.1–0.2 M [35]. Here, we should emphasize that, in our experiments, the chemiluminescence and colorimetric measurements were conducted at different pH, $\sim$7 for chemiluminescence and $\sim$4 for colorimetric. This difference is due to very low luminescence intensity of luminol oxidation product (aminophthalic acid) at pH <6 and low rate of TMB coloration at pH >6. The rate of decomposition of hydrogen peroxide varies with pH [36, 37], but the underlying reaction mechanism is pH-independent, thereby permitting a qualitative comparison of the two analytical methods.

The colorimetric experiments were carried out in a 0.2 M acetate buffer solution (pH 4.00) at a temperature of 37 ∘C. The decomposition of hydrogen peroxide results in the formation of hydroxyl radicals, which are capable of oxidizing

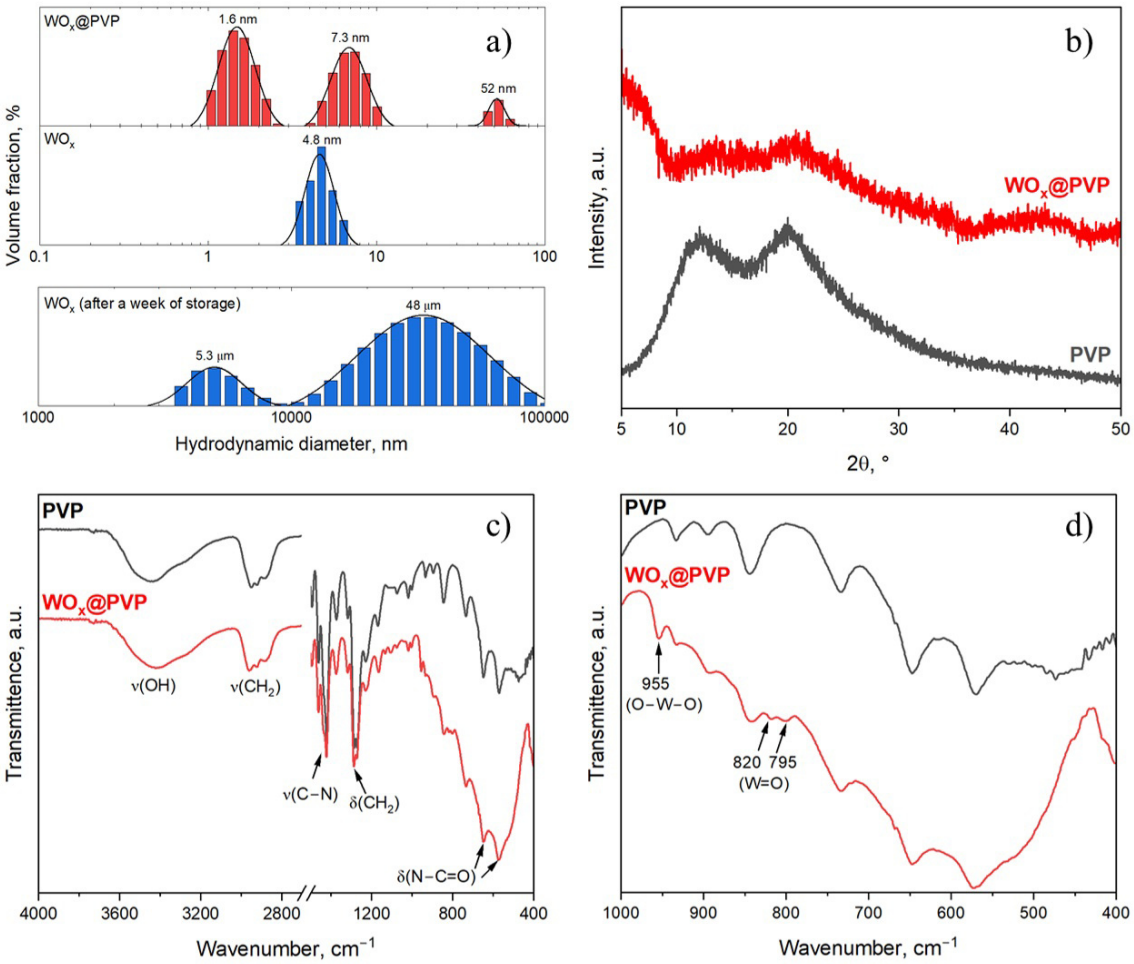

FIG. 1. (a) Hydrodynamic diameter distributions for the WO_x@PVP sol, bare WO_x sol immediately after the synthesis and after a week of storage under ambient conditions; (b) X-ray diffraction patterns of the dried WO_x@PVP sol and PVP powder; (c–d) FTIR spectra of PVP and WO_x@PVP powders

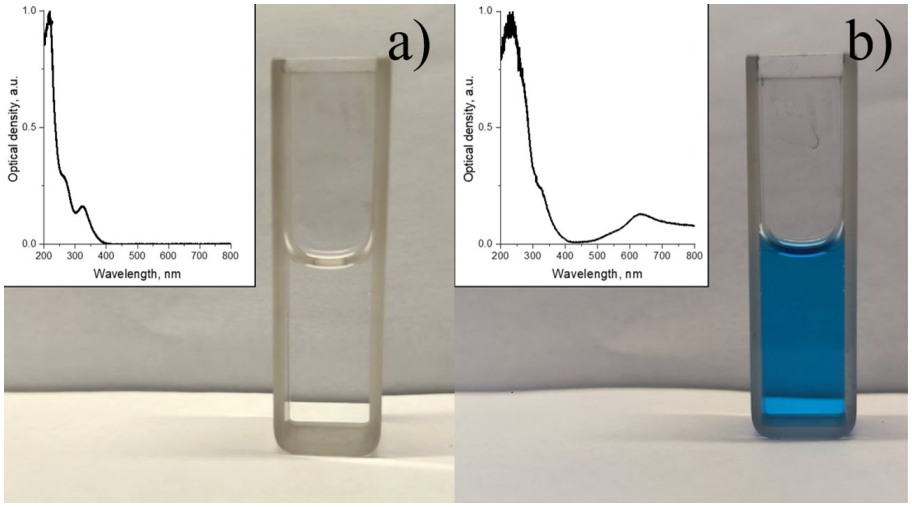

FIG. 2. Photographs and UV-vis spectra of WO_x@PVP sols (a) before and (b) after 30 s of the UV-irradiation (λ = 365 nm)

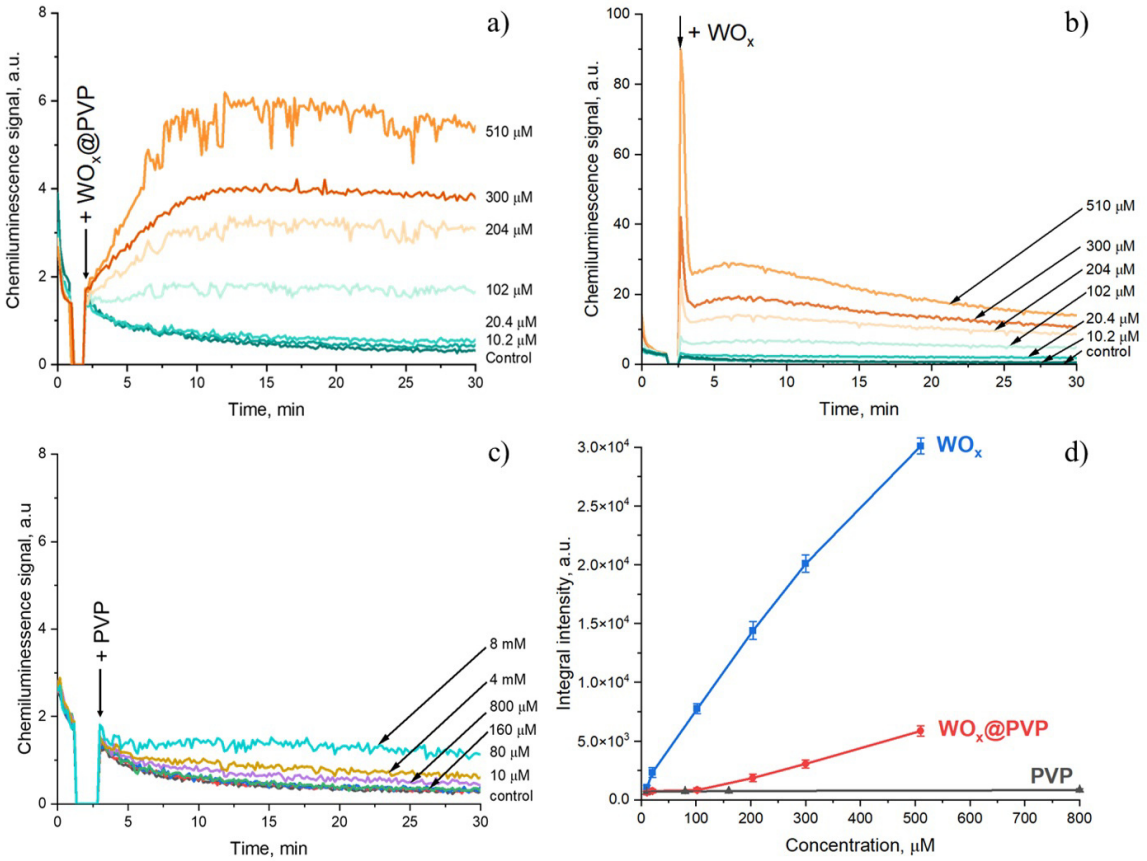

FIG. 3. Chemiluminescence kinetic curves for the H_2O_2/luminol solutions upon addition of (a) WO_x@PVP sol (10.2 – 510 μM), (b) bare WO_x sol (10.2 – 510 μM) and (c) PVP aqueous solution (10 μM – 8 mM). The experimental data were obtained via direct chemiluminescent measurements. Control: luminol and H_2O_2 in a phosphate-buffered solution without WO_x and/or PVP. (d) The integral luminescence intensities of the reaction mixtures measured within 20 min after the addition of a tested material

TMB, thereby causing its coloration. The incorporation of nanoparticles into the mixture may result in an enhancement of coloration, which would demonstrate their catalytic activity. The UV-visible absorption spectra of the reaction mixture were recorded at 2-second intervals, and the time dependence of the absorption intensity at 652 nm (the wavelength of maximum absorption of the colored oxidation product of TMB) was determined (Fig. 4). To eliminate the influence of ultraviolet radiation on redox processes at the surface of tungsten oxide nanoparticles, a light filter was installed in front of the reaction mixture to block radiation with a wavelength shorter than 450 nm.

Bare WO_x nanoparticles demonstrated dose-dependent catalytic activity in the hydrogen peroxide decomposition reaction. In turn, the activity of WO_x@PVP sols at the same concentration range is approximately 10–20 times lower than the catalytic activity of the bare nanoparticles. These data are in good accordance with the results of the chemiluminescence analysis.

The time dependencies of the optical density of the reaction mixture (proportional to the concentration of the oxidized form of TMB) containing the bare WO_x nanoparticles (Fig. 5) were found to be fitted well to the Michaelis-Menten equation

$$\nu = \frac{V_{MAX} \cdot [S]}{K_M + [S]}$$

where ν is the initial reaction rate, V_{MAX} is the maximum reaction rate, and K_M is the Michaelis constant, which reflects the affinity of a catalyst for the substrate, and [S] is the substrate (TMB) concentration. The correspondence of the kinetics of substrate oxidation in the presence of inorganic nanoparticles to the Michaelis-Menten model confirms their enzyme-like activity.

The following kinetic parameters were determined from the Michaelis-Menten equation ($R^2 > 0.99$). The Michaelis constant was found to be $(3.9 \pm 0.5) \times 10^{-3}$ M, the maximum reaction rate was determined to be $(1.5 \pm 0.2) \times 10^{-7}$ M·s^{-1}. The catalytic constant (k_{cat}) is the rate constant defining the maximum number of substrate molecules undergoing transformation per time unit. The k_{cat} for the WO_x nanocatalyst amounted to $1.5 \cdot 10^{-4}$ s^{-1}. These kinetic parameters are in line with those typically reported for various inorganic nanoparticles [38–40].

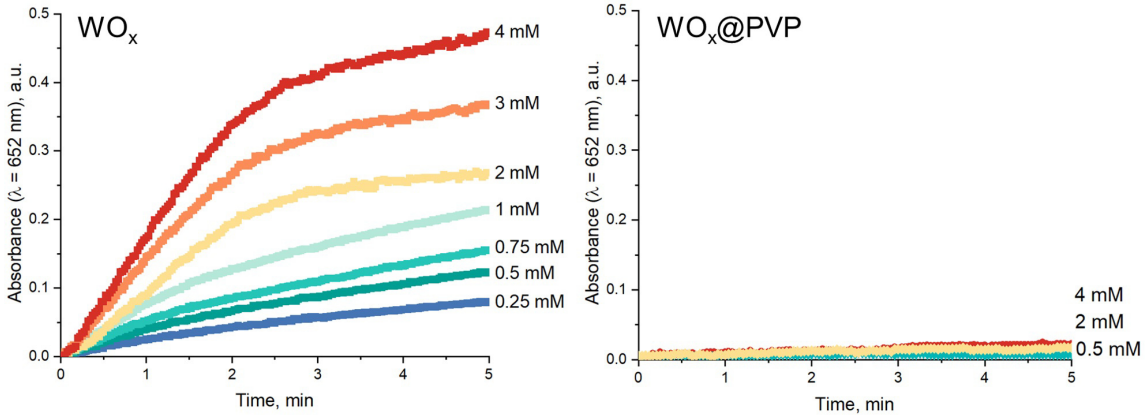

FIG. 4. The kinetics of TMB oxidation by hydrogen peroxide in the presence of (a) bare WO_x (0.25–4 mM) and (b) WO_x@PVP (0.5–4 mM) nanoparticles as determined from the absorption at 652 nm.

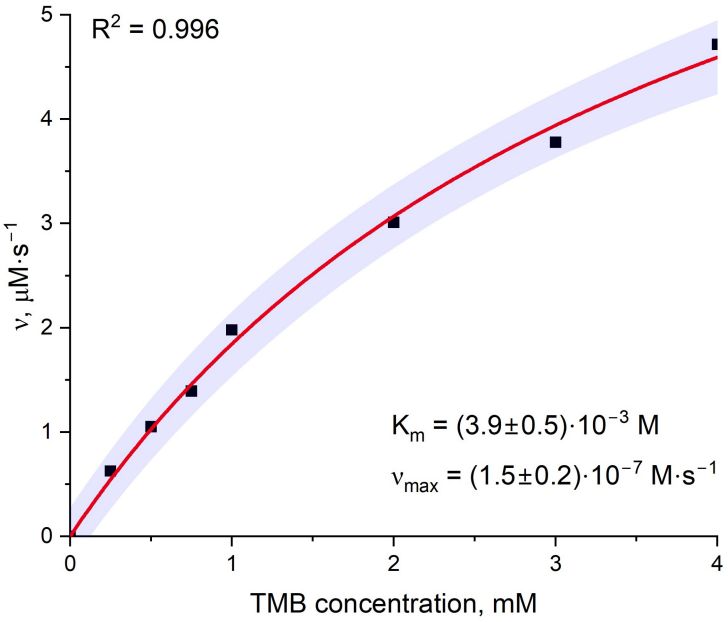

FIG. 5. The kinetics of TMB oxidation by hydrogen peroxide in the presence of bare WO_x sols and its fitting to the Michaelis-Menten model. The light-purple band shows 95 % coincidence interval

A quantitative comparison of the results obtained by chemiluminescent and colorimetric methods is challenging due to the impossibility of constructing a calibration curve which would correlate the rate of hydrogen peroxide decomposition and the chemiluminescence intensity. Additionally, the analytical signal is significantly dependent on the pH of the buffer solution. However, despite these limitations, the both methods demonstrate a high qualitative agreement.

4. Conclusions

Ultra-small non-stabilized and PVP-stabilized tungsten oxide nanoparticles were synthesized by the ion exchange method and their peroxidase-like activity was evaluated using two independent assays: colorimetric and chemiluminescent. The results obtained demonstrate that the bare tungsten oxide nanoparticles exhibited a dose-dependent catalytic activity. The oxidation of 3,3',5,5'-tetramethylbenzidine (TMB) by hydrogen peroxide in the presence of the nanoparticles is described by the Michaelis-Menten model. The calculated kinetic parameters were $K_S = (3.9 \pm 0.5) \times 10^{-3}$ M, $V_{MAX} = (1.5 \pm 0.2) \times 10^{-7}$ M·s^{-1} M·s^{-1} and $k_{cat} = 1.5 \cdot 10^{-4}$ s^{-1}.

The stabilization of the WO_x nanoparticles with PVP substantially decreases their peroxidase-like activity, which is 10–20 times lower than the catalytic activity of the bare WO_x nanoparticles. This behavior may be attributed to a shielding of the available active sites on the nanoparticles surface.

References

[1] Kang T., Kim Y.G., Kim D., Hyeon T. Inorganic nanoparticles with enzyme-mimetic activities for biomedical applications. *Coord. Chem. Rev.*, 2020, **403**, P. 213092.

[2] Liang X., Han L. White Peroxidase-Mimicking Nanozymes: Colorimetric Pesticide Assay without Interferences of O_2 and Color. *Adv. Funct. Mater.*, 2020, **30**(28), P. 2001933.

[3] Gao L., Zhuang J., Nie L., et al. Intrinsic peroxidase-like activity of ferromagnetic nanoparticles. *Nat. Nanotechnol.*, 2007, **2**(9), P. 577–583.

[4] Gao L. Enzyme-Like Property (Nanozyme) of Iron Oxide Nanoparticles. In: *Iron Oxide Nanoparticles*, IntechOpen, 2022.

[5] Yang Y., Mao Z., Huang W., et al. Redox enzyme-mimicking activities of CeO_2 nanostructures: Intrinsic influence of exposed facets. *Sci. Rep.*, 2016, **6**(1), P. 35344.

[6] Filippova A.D., Baranchikov A.E., Ivanov V.K. Enzyme-Like Activity of Cerium Dioxide Colloidal Solutions Stabilized with L-Malic Acid. *Colloid. J.*, 2023, **85**(5), P. 782–794.

[7] Filippova A.D., Sozarukova M.M., Baranchikov A.E., Kottsov S.Y., Cherednichenko K.A., Ivanov V.K. Peroxidase-like Activity of CeO_2 Nanozymes: Particle Size and Chemical Environment Matter. *Molecules*, 2023, **28**(9), P. 3811.

[8] Zhao M., Tao Y., Huang W., He Y. Reversible pH switchable oxidase-like activities of MnO_2 nanosheets for a visual molecular majority logic gate. *Phys. Chem. Chem. Phys.*, 2018, **20**(45), P. 28644–28648.

[9] Lin S., Tan W., Han P., et al. A photonanozyme with light-empowered specific peroxidase-mimicking activity. *Nano. Res.*, 2022, **15**(10), P. 9073–9081.

[10] Deng Z., Gong Y., Luo Y., Tian Y. WO_3 nanostructures facilitate electron transfer of enzyme: Application to detection of H_2O_2 with high selectivity. *Biosens. Bioelectron.*, 2009, **24**(8), P. 2465–2469.

[11] Kozlov D.A., Shcherbakov A.B., Kozlova T.O., et al. Photochromic and Photocatalytic Properties of Ultra-Small PVP-Stabilized WO_3 Nanoparticles. *Molecules*, 2019, **25**(1), P. 154.

[12] Lee S.-H., Deshpande R., Parilla P.A., et al. Crystalline WO_3 Nanoparticles for Highly Improved Electrochromic Applications. *Adv. Mater.*, 2006, **18**(6), P. 763–766.

[13] Aliannezhadi M., Abbaspoor M., Shariatmadar Tehrani F., Jamali M. High photocatalytic WO_3 nanoparticles synthesized using Sol-gel method at different stirring times. *Opt. Quantum Electron.*, 2023, **55**(3), P. 250.

[14] Huang Z., Song J., Pan L., Zhang X., Wang L., Zou J. Tungsten Oxides for Photocatalysis, Electrochemistry, and Phototherapy. *Adv. Mater.*, 2015, **27**(36), P. 5309–5327.

[15] Dong X., Lu Y., Liu X., Zhang L., Tong Y. Nanostructured tungsten oxide as photochromic material for smart devices, energy conversion, and environmental remediation. *J. Photochem. Photobiol. C Photochem. Rev.*, 2022, **53**, P. 100555.

[16] Zeb S., Sun G., Nie Y., Xu H., Cui Y., Jiang X. Advanced developments in nonstoichiometric tungsten oxides for electrochromic applications. *Mater. Adv.*, 2021, **2**(21), P. 6839–6884.

[17] George J.M., Antony A., Mathew B. Metal oxide nanoparticles in electrochemical sensing and biosensing: a review. *Microchim. Acta*, 2018, **185**(7), P. 358.

[18] Can F., Courtois X., Duprez D. Tungsten-Based Catalysts for Environmental Applications. *Catalysts*, 2021, **11**(6), P. 703.

[19] Kameneva S.V., Popkov M.A., Tronev I.V., Kottsov S.Y., Sozarukova M.M., Ivanov V.K. Photochromic aerogels based on cellulose and chitosan modified with WO_3 nanoparticles. *Nanosyst. Physics., Chem., Math*, 2022, **13**(4), P. 404–413.

[20] Staerz A., Somacescu S., Epifani M., Russ T., Weimar U., Barsan N. WO_3 Based Gas Sensors. In: *EUROSENSORS 2018*. MDPI, 2019, P. 826.

[21] Zhou Y., She X., Wu Q., Xiao J., Peng T. Monoclinic WO_3 nanosheets-carbon nanotubes nanocomposite based electrochemical sensor for sensitive detection of bisphenol A. *J. Electroanal. Chem.*, 2022, **915**, P. 116355.

[22] Anithaa A.C., Lavanya N., Asokan K., Sekar C. WO_3 nanoparticles based direct electrochemical dopamine sensor in the presence of ascorbic acid. *Electrochim. Acta*, 2015, **167**, P. 294–302.

[23] Sharma A., Saini A.K., Kumar N., et al. Methods of preparation of metal-doped and hybrid tungsten oxide nanoparticles for anticancer, antibacterial, and biosensing applications. *Surfaces and Interfaces*, 2022, **28**, P. 101641.

[24] Bashir A., Khan S.R., Aqib A.I., Shafique L., Ataya F.S. Multifunctional integration of tungsten oxide (WO_3) coating: A versatile approach for enhanced performance of antibiotics against single mixed bacterial infections. *Microb. Pathog.*, 2024, **189**, P. 106571.

[25] Popov A.L., Han B., Ermakov A.M., et al. PVP-stabilized tungsten oxide nanoparticles: pH sensitive anti-cancer platform with high cytotoxicity. *Mater. Sci. Eng. C*, 2020, **108**, P. 110494.

[26] Jiang X., Liu W., Li Y., et al. WO_3 nanosheets with peroxidase-like activity and carbon dots based ratiometric fluorescent strategy for xanthine oxidase activity sensing and inhibitor screening. *Talanta*, 2024, **267**, P. 125129.

[27] Sadashivanna R.H., Krishna H., Shivakumar A., Gangadhara N.Y., Mahesh Lohith K.S., Krishnegowda A. Oxalic acid capped tungsten oxide nanozyme mimicking peroxidase activity, its synthesis characterization, and kinetic data validation via spectrophotometric studies. *Nano-Structures & Nano-Objects*, 2024, **40**, P. 101340.

[28] Robert A., Meunier B. How to Define a Nanozyme. *ACS Nano*, 2022, **16**(5), P. 6956–6959.

[29] Zandieh M., Liu J. Nanozymes: Definition, Activity, and Mechanisms. *Adv. Mater.*, 2024, **36**(10), P. 2211041.

[30] Popov A.L., Savintseva I.V., Popova N.R., et al. PVP-stabilized tungsten oxide nanoparticles (WO_3) nanoparticles cause hemolysis of human erythrocytes in a dose-dependent manner. *Nanosyst. Physics., Chem., Math*, 2019, **10**(2), P. 199–205.

[31] Basha M.A.F. Magnetic and optical studies on polyvinylpyrrolidone thin films doped with rare earth metal salts. *Polym. J.*., 2010, **42**(9), P. 728–734.

[32] Pacheco M.L., Pinto T.V., Sousa C.M., et al. Tuning the Photochromic Properties of WO_3 -Based Materials toward High-Performance Light-Responsive Textiles. *ACS Appl. Opt. Mater.*, 2023, **1**(8), P. 1434–1451.

[33] Hussain M., Kalulu M., Ahmad Z., Ejeromedoghene O., Fu G. Rapid fabrication of polyoxometalate-enhanced photo responsive films from ethyl cellulose (EC) and polyvinylpyrrolidone (PVP). *Int. J. Biol. Macromol.*, 2024, **280**, P. 136051.

[34] Jiang B., Duan D., Gao L., et al. Standardized assays for determining the catalytic activity and kinetics of peroxidase-like nanozymes. *Nat. Protoc.*, 2018, **13**(7), P. 1506–1520.

[35] Zheng J.J., Zhu F., Song N., et al. Optimizing the standardized assays for determining the catalytic activity and kinetics of peroxidase-like nanozymes. *Nat. Protoc.*, 2024, **19**, 3470–3488.

[36] Feng K., Wang G., Wang S., et al. Breaking the pH Limitation of Nanozymes: Mechanisms, Methods, and Applications. *Adv. Mater.*, 2024, **36**(31), P. 2401619.

[37] Eroi S.N., Ello A.S., Diabaté D., Ossonon D.B. Heterogeneous WO_3/H_2O_2 system for degradation of Indigo Carmin dye from aqueous solution. *South African J. Chem. Eng.*, 2021, **37**, P. 53–60.

[38] Shi R., Wei S., Cheng S., Zeng J., Wang Y., Shu X. Colorimetric Detection of Glucose Using WO_3 Nanosheets as Peroxidase-mimetic Enzyme. *Chem. Res. Chinese Univ.*, 2022, **38**(4), P. 985–990.

[39] Yang J., Cheng S.Q., Shi R., Ying Qin S., Huang L., Lin Wang Y. Spectrophotometric detection of uric acid with enzyme-like reaction mediated 3,3',5,5'-tetramethylbenzidine oxidation. *Bull. Chem. Soc. Ethiop.*, 2022, **37**(1), P. 11–21.

[40] Li Z., Liu X., Liang X.H., Zhong J., Guo L., Fu F. Colorimetric determination of xanthine in urine based on peroxidase-like activity of WO_3 nanosheets. *Talanta*, 2019, **204**, P. 278–284.

Submitted 25 October 2024; accepted 12 November 2024

Information about the authors:

Matvei A. Popkov – Kurnakov Institute of General and Inorganic Chemistry, Russian Academy of Sciences, Leninsky, 31, Moscow, 119991, Russia; ORCID 0000-0002-9811-6241; ma_popkov@igic.ras.ru

Ekaterina D. Sheichenko – Kurnakov Institute of General and Inorganic Chemistry, Russian Academy of Sciences, Leninsky, 31, Moscow, 119991, Russia; HSE University, Myasnitskaya, 20, Moscow, 101000, Russia; ORCID 0000-0003-3485-1842; edsheychenko@edu.hse.ru

Arina D. Filippova – Kurnakov Institute of General and Inorganic Chemistry, Russian Academy of Sciences, Leninsky, 31, Moscow, 119991, Russia; ORCID 0000-0002-2725-8891; arifilippova@yandex.ru

Ilya V. Tronev – Kurnakov Institute of General and Inorganic Chemistry, Russian Academy of Sciences, Leninsky, 31, Moscow, 119991, Russia; ORCID 0000-0002-0718-1911; ivtronev@edu.hse.ru

Kristina N. Novoselova – Kurnakov Institute of General and Inorganic Chemistry, Russian Academy of Sciences, Leninsky, 31, Moscow, 119991, Russia; HSE University, Myasnitskaya, 20, Moscow, 101000, Russia; ORCID 0009-0006-4139-1476; knnovoselova@edu.hse.ru

Evelina A. Trufanova – Kurnakov Institute of General and Inorganic Chemistry, Russian Academy of Sciences, Leninsky, 31, Moscow, 119991, Russia; HSE University, Myasnitskaya, 20, Moscow, 101000, Russia; ORCID 0009-0009-1645-5759; eatrufanova_1@edu.hse.ru

Darya N. Vasilyeva – Kurnakov Institute of General and Inorganic Chemistry, Russian Academy of Sciences, Leninsky, 31, Moscow, 119991, Russia; HSE University, Myasnitskaya, 20, Moscow, 101000, Russia; ORCID 0009-0004-3560-4178; dnvasileva_1@edu.hse.ru

Maria R. Protsenko – Kurnakov Institute of General and Inorganic Chemistry, Russian Academy of Sciences, Leninsky, 31, Moscow, 119991, Russia; HSE University, Myasnitskaya, 20, Moscow, 101000, Russia; ORCID 0009-0007-0738-4974; mrprotsenko@edu.hse.ru

Madina M. Sozarukova – Kurnakov Institute of General and Inorganic Chemistry, Russian Academy of Sciences, Leninsky, 31, Moscow, 119991, Russia; ORCID 0000-0002-5868-4746; s_madinam@bk.ru

Alexander E. Baranchikov – Kurnakov Institute of General and Inorganic Chemistry, Russian Academy of Sciences, Leninsky, 31, Moscow, 119991, Russia; HSE University, Myasnitskaya, 20, Moscow, 101000, Russia; ORCID 0000-0002-2378-7446; a.baranchikov@yandex.ru

Vladimir K. Ivanov – Kurnakov Institute of General and Inorganic Chemistry, Russian Academy of Sciences, Leninsky, 31, Moscow, 119991, Russia; HSE University, Myasnitskaya, 20, Moscow, 101000, Russia; ORCID 0000-0003-2343-2140; van@igic.ras.ru

Conflict of interest: the authors declare no conflict of interest.

NANOSYSTEMS:
PHYSICS, CHEMISTRY, MATHEMATICS

Original article

Shutilov A.A., et al. *Nanosystems: Phys. Chem. Math.*, 2025, **16** (1), 30–43.
http://nanojournal.ifmo.ru
DOI 10.17586/2220-8054-2025-16-1-30-43

Design of highly active $Ni_xCo_{1-x}Al_2O_4$ ($x = 0.1 – 0.5$) catalysts for the dry reforming of methane reaction

Alexey A. Shutilov[1,a], Mikhail N. Simonov[1,2,b], Valeria E. Fedorova[1,c], Alexander S. Marchuk[2,d], Igor P. Prosvirin[1,e], Galina A. Zenkovets[1,f]

[1]Boreskov Institute of Catalysis SB RAS, Novosibirsk, Russia
[2]Novosibirsk State University, Novosibirsk, Russia

[a]alshut@catalysis.ru, [b]smike@catalysis.ru, [c]valeria@catalysis.ru, [d]alexander.s.marchuk@gmail.com, [e]prosvirin@catalysis.ru, [f]zenk@catalysis.ru

Corresponding author: Alexey A. Shutilov, alshut@catalysis.ru

ABSTRACT On the first step using co-precipitation method from Ni-, Co-, Al-containing solution a precipitates with a general composition of $Ni_xCo_{1-x}Al_2O_4$ ($x = 0.1 – 0.5$) were prepared. Calcination the obtained precipitates at 700 °C in air makes the precursors of catalysts for DRM with a stable spinel-like framework in which nickel and cobalt species are homogeneously incorporated. Reduction of the precursors at 700 °C in H_2 and further work under reaction medium leads to formation of the active phase which represents by the ensembles of Ni–Co alloy nanoparticles located on the surface of nanostructured spinel. The effect of the catalysts composition on catalytic properties in DRM was investigated. The high and stable catalytic activity of representative samples in DRM conditions with extremely short contact time ($\tau = 30$ ms) due to the formation of 17 – 18 wt. % active phase which represents highly dispersed (3 – 4 nm) Ni–Co alloy nanoparticles stabilized on the spinel with nanocristalline structure.

KEYWORDS sustainable environment, CH_4 and CO_2 utilization, dry reforming of methane (DRM), Ni–Co nanoalloy, spinel-based catalysts

ACKNOWLEDGEMENTS The authors express their gratitude to Ph. D. Olga A. Stonkus for studying catalysts using the TEM method and Ph. D. Vladimir A. Rogov for studying catalysts using the TPR-H_2 method. The study was funded by Russian Science Foundation according to the research project No. 23-23-10054, https://rscf.ru/project/23-23-10054/, and by the Government of Novosibirsk region contract 000000540699599823512080 2/ No. p-72.

FOR CITATION Shutilov A.A., Simonov M.N., Fedorova V.E., Marchuk A.S., Prosvirin I.P., Zenkovets G.A. Design of highly active $Ni_xCo_{1-x}Al_2O_4$ ($x = 0.1 – 0.5$) catalysts for the dry reforming of methane reaction. *Nanosystems: Phys. Chem. Math.*, 2025, **16** (1), 30–43.

1. Introduction

Today the dependence of humanity on fossil fuels has resulted in detrimental effects of growing emission of greenhouse gases, such as CO_2 and CH_4 [1], major contributors to climate change and resulting increase to the global temperature. Therefore, there is an urgency to control these emissions. Dry reforming of methane (DRM) is environmentally friendly catalytic transformation methane and carbon dioxide to syngas (1):

$$CH_4 + CO_2 = 2CO + 2H_2 \quad (\Delta_r H^o = 247.3\ \mathrm{kJ/mol}) \tag{1}$$

Due to a molar ratio of H_2/CO is close to 1, this is suitable for the synthesis of oxygenated chemicals and long chain hydrocarbons via Fisher–Tropsch synthesis [1–7]. Reaction (1) is also an attractive way to catalytically generate hydrogen-containing gas and can be used for hydrogen production [8]. In light of the energy applications, DRM formed H_2 + CO mixture is a very suitable fuel for intermediate and high temperatures solid oxide fuel cells for electricity production [9].

Among a large number of investigated catalysts for DRM, supported noble metals (Rh, Ru, Pd, Pt, Ir) can provide high and stable catalytic properties without sintering and coking of the catalysts during the reaction conditions [7, 10–13]. However, from an industrial standpoint, they are unsuitable for commercial use due to their high cost and limited availability. Therefore, it is more practical to develop non-noble metal-based catalysts [1, 2, 11]. It was shown that transitions metals Ni, Co, Fe, Cu and Mo supported on common supports such as γ-Al_2O_3, MgO, SiO_2, CeO_2 and ZrO_2 are alternatives to the catalysts for DRM, containing noble metals. Among that Ni containing catalysts are the most studded due to their high activity closed to noble metals [1, 2, 14, 15]. Thanks to the easy availability and low cost of γ-Al_2O_3, MgO, SiO_2, CeO_2 and ZrO_2, they have been widely studied for the DRM catalysts. Supports are not catalytically active

© Shutilov A.A., Simonov M.N., Fedorova V.E., Marchuk A.S., Prosvirin I.P., Zenkovets G.A., 2025

but interact with the active site to facilitate dispersion of metal, strengthen the metal-support interaction, limit sintering, accelerate reduction of the catalyst, and decrease or eliminate carbonaceous species development [12]. Due to low price, affordability and very good activity Ni-based catalysts may be used for the DRM reaction. However, these catalysts are prone to deactivation due to carbon deposition, as well as sintering of Ni nanoparticles under DRM conditions, that is the major drawback in the development of stable Ni-based catalysts [16–27].

To increase the activity and stability of supported Ni-based catalysts Co often has been used as an additive in these catalysts [11, 28–38]. Today, Ni–Co bimetallic catalysts have been widely explored as potential catalysts for use in DRM due to their advantages in activity and low cost [1, 33–37]. Thus, highly active and stable Ni–Co/Al_2O_3 catalyst for DRM reaction was reported by Wu et al.in [36]. The high catalytic performance they attribute to the formation of Ni–Co alloy under reaction conditions. Due to the similar Co and Ni electronic configuration, bimetallic Ni–Co alloyed nanoparticles are easily formed during the DRM reaction. Investigation of these catalysts by EXAFS and microscopic analysis revealed the lattice-strained configuration for the Ni–Co alloy and confirmed the strong interaction between Ni and Co atoms. The average bond lengths between the metal atoms in the bimetallic catalysts are some different compared to those in the parent metals, resulting in changes of the chemisorption properties [39]. Ni and Co easily form alloyed nanoparticles, and thus exhibiting a synergistic effect on one another. In literature extensive investigations of combinations between Ni and Co have been carried out for DRM. It has been reported that incorporation of Co into Ni catalysts inhibits the agglomeration of the nickel particles due to the formation of Ni–Co alloy and leads to an increased dispersion of the Ni particles [1, 11, 27].

In continuous efforts to develop Ni-based catalysts with the lowest carbon deposition and sustainable catalytic activity, the catalyst preparation process, including the metal loading percentage, calcination temperature, and reduction temperature on the catalytic properties are investigated today. It was shown [1, 2, 11, 12, 40, 41] that catalysts synthesis methods significantly affect catalysts activity in DRM. Impregnation, precipitation and co-precipitation, sol-gel, hydrothermal method, solvothermal method, microwave method, atomic layer deposition (ALT), sonochemical method, solution combustion are discussed. It was reported that catalysts prepared by a simple impregnation method have lower surface area compared to catalysts synthesized with sol-gel method due to pore blockage of the support by metal particles. Similar results were obtained in [11, 12] for catalysts prepared with sol-gel method in which Ni was highly dispersed on support with the strong metal-support interaction. The importance of the synthesis method was also reported by Wu et al. [36] who investigated the simultaneous and consecutive impregnation of the active phases (Ni and Co) on Al_2O_3 support for the DRM reaction. The authors concluded that the second method resulted in stronger Co-Ni interactions, which favored carbon gasification.

Our work proposed promising directions for the development of highly active and coke resistant catalysts for stable work in DRM. It was carried out a comprehensive investigation of the stage formation the structure of precursor of catalysts for DRM with a general composition of $Ni_xCo_{1-x}Al_2O_4$ ($x = 0.1 - 0.5$) prepared by using co-precipitation method after calcination at 700 °C in air. Also it was studied that the reduction of the precursors at 700 °C in H_2 and under reaction conditions which leads to formation of the active phase which represents by the ensembles of Ni–Co alloy nanoparticles of 3 – 4 nm in size located on the surface of nanostructured spinel. The effect of the catalysts composition on catalytic properties in DRM with extremely short contact time (τ) was investigated

2. Experimental

2.1. Catalyst preparation

Catalysts with a general composition of $Ni_xCo_{1-x}Al_2O_4$ ($x = 0.1 - 0.5$) were prepared by co-precipitation method. For comparison, $Co_1Al_2O_4$ sample was prepared too. Metal nitrate salts ($Ni(NO_3)_2 \cdot 6H_2O$, $Co(NO_3)_2 \cdot 6H_2O$ and $Al(NO_3)_3 \cdot 9H_2O$ (Vekton, Russia) were used as Ni, Co and Al precursors respectively. All reagents were used without additional purification. The required amounts of metal salts was dissolved in deionized water and then all individual solutions were mixed together to obtain the resulting solution, which was precipitated with 12.5 % solution of NH_4OH at pH = 7.5 and temperature of 75 °C. The precipitate was filtered, washed with deionized water and dried at room temperature and then dried overnight in air at 110 °C. The dried catalysts were calcined in static air at 700 °C for 4 h in a muffle furnace with a temperature ramp of 5 °C/min.

2.2. Catalyst characterization

Bulk chemical composition of the calcined catalyst was determined using a Perkin Elmer ISP OPTIMA 4300DV atomic emission spectrometer (Perkin Elmer, USA).

The specific surface area (S_{BET}) of the samples was determined by BET method using argon thermal desorption with a sorbtometr Sorby-M adsorption analyzer (META, Russia).

X-ray powder diffraction (XRD) analysis was carried out with Tongda TD3700 (Tongda, China) diffractometer using CuK_α-radiation and a Mythen2R 1D (Dectris, Switzerland) multistrip detector. Scanning was made over an angular range of 2θ = 5 – 70° at a 0.03° step and counting time of 3 s. Phase analysis, refinement of unite cell parameters and estimation of the quantitative content were performed by the full profile modeling of X-ray patterns by the Rietveld

method. The calculations were made using the TOPAS v.4.2 software package [42], structural parameters were taken from ICSD database [43]. Coherent scattering region (CSR) size was estimated by Rietveld method too.

In situ XRD analysis with H_2 atmosphere was made by using a Bruker D8 Advance diffractometer (Bruker, Germany), over an angular range of 2θ = 5 – 70° at a 0.03° step and counting time of 3 s. at each point using a LynxEye (1D) line detector. The monochromatic CuK_α-radiation ($\lambda = 1.5418$ Å) was used. The measurements were carried out using an XRK-900 high-temperature reactor chamber (Anton Paar, Austria). The 10 % H_2/ 90 % He mixture at a flow rate of 90 ml/min was passed through the chamber during heating or cooling to room temperature with a heating rate of 10 °C/min. The lattice parameters and phase relationships were refined with the Rietveld method.

The reducibility of the catalysts was studied by TPR-H_2 (temperature-programmed reduction) by 10 vol. % H_2 in Ar feed at flow rate of 40 ml/min during a linear temperature increase (10 °/min) in the range of 25 – 800 °C. Hydrogen consumption was determined by the heat conductivity detector of a Tsvet 500 chromatograph (Tsvet, Russia). Water was removed from the product by freezing at 77 K. The total H_2 consumption was calculated by integrating the area under the curve.

TEM (transmission electron microscopy) investigation was carried out using a JEM-2200FS transmission electron microscopy (JEOL Ltd., Japan, accelerating voltage 200 kV, lattice resolution $\sim$ 1 Å) equipped with a Cs-corrector. Dark-field images were obtained in a scanning mode using HAADF (High-Angle Annular Dark-Field) detector. The microscope is equipped with an EDX spectrometer (JEOL Ltd., Japan) for local elemental analysis (locality up to 1 nm, energy resolution -130 eV). Samples for the TEM study were prepared by ultrasonic dispersing in ethanol and subsequent deposition of the suspension upon a "holey" carbon film supported on a copper grid.

X-ray photoelectron spectra (XPS) were recorded on a SPECS spectrometer (SPECS, Germany) equipped with a PHOIBOS-150-MCD-9 analyzer and a FOCUS-500 monochromatic (MgK_α radiation, $h\nu = 1253.6$ eV, 150 W). The binding energy scale was calibrated using the levels of positions of the Au4$f_{7/2}$ ($E_b = 84.0$ eV) and Cu2$p_{3/2}$ peaks ($E_b = 932.67$ eV). Binding energy was calibrated against the position of the C1s peak ($E_b = 284.8$ eV), which corresponds to hydrocarbon deposits on the sample surface [44]. A sample in the form of a powder was deposited on a conductive double-sided copper adhesive tape. The survey spectrum and individual spectra of the elements were recorded at pass energy of the analyzer of 20 eV. The atomic ratios of the elements were calculated from the integral intensities of photoelectron peaks, which were corrected using appropriate sensitivity factors in terms of the Scofield photoionization cross sections [45]. The processing and analysis of the spectral data were conducted using the XPS Peak 4.1 software [46].

2.3. Catalytic tests

Catalytic tests were performed with 0.06 – 0.1 mm catalysts fraction in tubular quartz with an inner diameter of 4 mm which was installed in a furnace, where a thermocouple was placed into the annular space between the reactor and the furnace. Before the reaction, the catalysts were pretreated in a 10 vol % O_2/N_2 medium at 600 °C for 30 min with further reduction at 700 °C for 1 h in a 5 vol % H_2/He medium. In all cases, the DRM reaction was performed at a reaction mixture composition of (15 vol % CH_4 + 15 vol % CO_2) in N_2, the volumetric flow rate was 8 l/h, the volume of the loaded catalyst was 0.07 ml, a contact time (τ) was 30 ms, and temperatures of 500, 550, 600, 650 and 700 °C with exposure of the catalyst at each temperature for 30 min. The concentrations of the reagents and products were measured in the real-time regime on a Test-201 gas analyzer (Boner, Russia) equipped with IR optical, electrochemical, and polarographic sensors.

The catalyst performance was characterized by CH_4 conversion (X_{CH_4}, %), CO_2 conversion (X_{CO_2}, %), yield of H_2 (Y_{H_2}, %), and yield of CO (Y_{CO}, %), which were as follow:

$$X_{CH_4},\ \% = \frac{C^0_{CH_4} - C_{CH_4}}{C^0_{CH_4}} \cdot 100,$$

$$X_{CO_2},\ \% = \frac{C^0_{CO_2} - C_{CO_2}}{C^0_{CO_2}} \cdot 100,$$

$$Y_{H_2},\ \% = \frac{C_{H_2}}{2C^0_{CH_4}} \cdot 100,$$

$$Y_{CO},\ \% = \frac{C_{CO}}{C^0_{CO_2} + C^0_{CH_4}} \cdot 100,$$

where C^0_i , [vol. %] is the concentration of reagent at the inlet and C_i, [vol. %] – at the outlet of the reactor.

Due to the change in volume during the reaction, the conversion values calculated from volume concentrations are overestimated, which leads to a systematic error. In the conversion range from 10 % to 40 %, the relative error in determining the conversion is from 26.2 to 16.1 %. With increasing of conversion, the relative error decreases and at $X = 80$ % does not exceed 4.8 %.

Long-term tests for all investigated catalysts were carried out at 700 °C for 20 hours under DRM medium.

3. Results and discussion

3.1. Catalytic properties

The catalytic properties of obtained catalysts $Ni_xCo_{1-x}Al_2O_4$ ($x = 0.1 – 0.5$) and comparison sample $Co_1Al_2O_4$ were investigated in dry reforming of methane reaction under the identical reaction conditions. In Fig. 1 the influence of the reaction temperature on the methane (X_{CH_4}) and carbon dioxide (X_{CO_2}) conversion, on the hydrogen yield (Y_{H_2}) and on the molar ratio of H_2/CO are presented for all catalysts under investigation. It can be seen that activity of all catalyst as well as hydrogen production are increased with increasing reaction temperature from 500 to 700 °C, which is in accordance with the strong endothermic character of the dry reforming of methane reaction [2].

It can be seen that the monometallic $Co_1Al_2O_4$ catalyst is less active compare to bimetallic $Ni_xCo_{1-x}Al_2O_4$ catalysts. In the case of $Co_1Al_2O_4$ catalyst at 700 °C $X_{CH_4} = 61$ %, $X_{CO_2} = 62$ %, and the hydrogen yield $Y_{H_2} = 32$ %, H_2/CO = 0.62. A comparison of the bimetallic samples with each other shows that catalytic activity is increased with increasing the nickel content in the catalysts. At the reaction temperature of 700 °C increase the x value in catalyst $Ni_xCo_{1-x}Al_2O_4$ from 0.1 to 0.5 leads to increase in the X_{CH_4} from 64 to 77 %, the X_{CO_2} from 65 to 76 %, the Y_{H_2} from 32 to 42 % and H_2/CO ratio from 0.63 to 0.69.

The rather low the values of H_2/CO due to the reverse water gas shift reaction [2]:

$$CO_2 + H_2 = CO + H_2O. \tag{2}$$

According to the eq. (2), hydrogen reacts with CO_2 and CO and H_2O are formed. It leads to decrease in H_2/CO ratio in the reaction product compared to theoretical value H_2/CO = 1.

All investigated catalysts passed the long-term tests for study of stability in DRM medium without loss of catalytic activity (Table 1). Fig. 1(f) presents the results obtained during 20 hours of DRM reaction at 700 °C for the representative samples $Ni_{0.35}Co_{0.75}Al_2O_4$ and $Ni_{0.1}Co_{0.9}Al_2O_4$ catalysts.

TABLE 1. Catalytic properties of $Ni_xCo_{1-x}Al_2O_4$ samples ($x = 0.1 – 0.5$) and the comparison sample $Co_1Al_2O_4$ after 20 hours in the dry reforming of methane reaction at 700 °C

Sample	X_{CH_4}, %	X_{CO_2}, %	Y_{H_2}, %	Y_{CO}, %	H_2/CO, mole/mole	Result of long-term test
$Co_1Al_2O_4$	61	62	32	49	0.62	passed
$Ni_{0.1}Co_{0.9}Al_2O_4$	64	65	34	52	0.63	passed
$Ni_{0.25}Co_{0.75}Al_2O_4$	71	70	38	57	0.67	passed
$Ni_{0.35}Co_{0.65}Al_2O_4$	76	73	40	59	0.68	passed
$Ni_{0.5}Co_{0.5}Al_2O_4$	77	76	42	61	0.69	passed

3.2. Structural features

According to X-ray fluorescence analysis, the chemical composition of the prepared catalysts corresponds to the calculated one.

The structural properties of the obtained catalysts heated at 700 °C in air presented in Table 2 and Fig. 2. Based on the X-ray diffraction data, it may be seen that the phase composition of $Ni_xCo_{1-x}Al_2O_4$ (with $x = 0.1 – 0.5$) samples are the same. The main peaks located at $2\theta = 18.96$, 31.20, 36.76, 38.46, 48.97, 55.52, 59.22, 65.08° correspond to (111), (220), (311), (222), (331), (422), (511), (440) crystallographic planers of spinel structure Fm3m (ICSD-78407).

Unit cell parameter of spinel lattice is practically the same in all samples. It may be due to a very close values of ionic radius of Ni^{2+} and Co^{2+} (Ni^{2+} = 0.74 Å, Co^{2+} = 0.72 Å). But average size of a coherent scattering region (CSR) is some decreased from 12.69 to 9.54 nm with increasing the Ni concentration in spinel structure. The specific surface area of investigated samples is some increased from 109 to 128 m^2/g when the mole fraction of Ni varies within (0.1 – 0.5). It may be the reason of some reducing of particle size in the spinel structure when the mole fraction of Ni is increased, which is in a good agreement with XRD data.

Figure 3 shows electron microscopy images of a $Ni_{0.35}Co_{0.65}Al_2O_4$ catalyst calcined in air at a temperature of 700 °C. It can be seen that the sample consists of agglomerated particles of similar morphology with the size of 5 – 10 nm. EDX-element mapping analysis indicated the complete incorporation of Ni and Co in to the spinel lattice. That is in agreement with XRD investigations.

The structural characteristics of the catalysts after reaction presented in Table 3 and Fig. 4. In the $CoAl_2O_4$ catalyst spinel and pure metallic Co^0 phases were registered by XRD method. One can see the presence of spinel in comparison

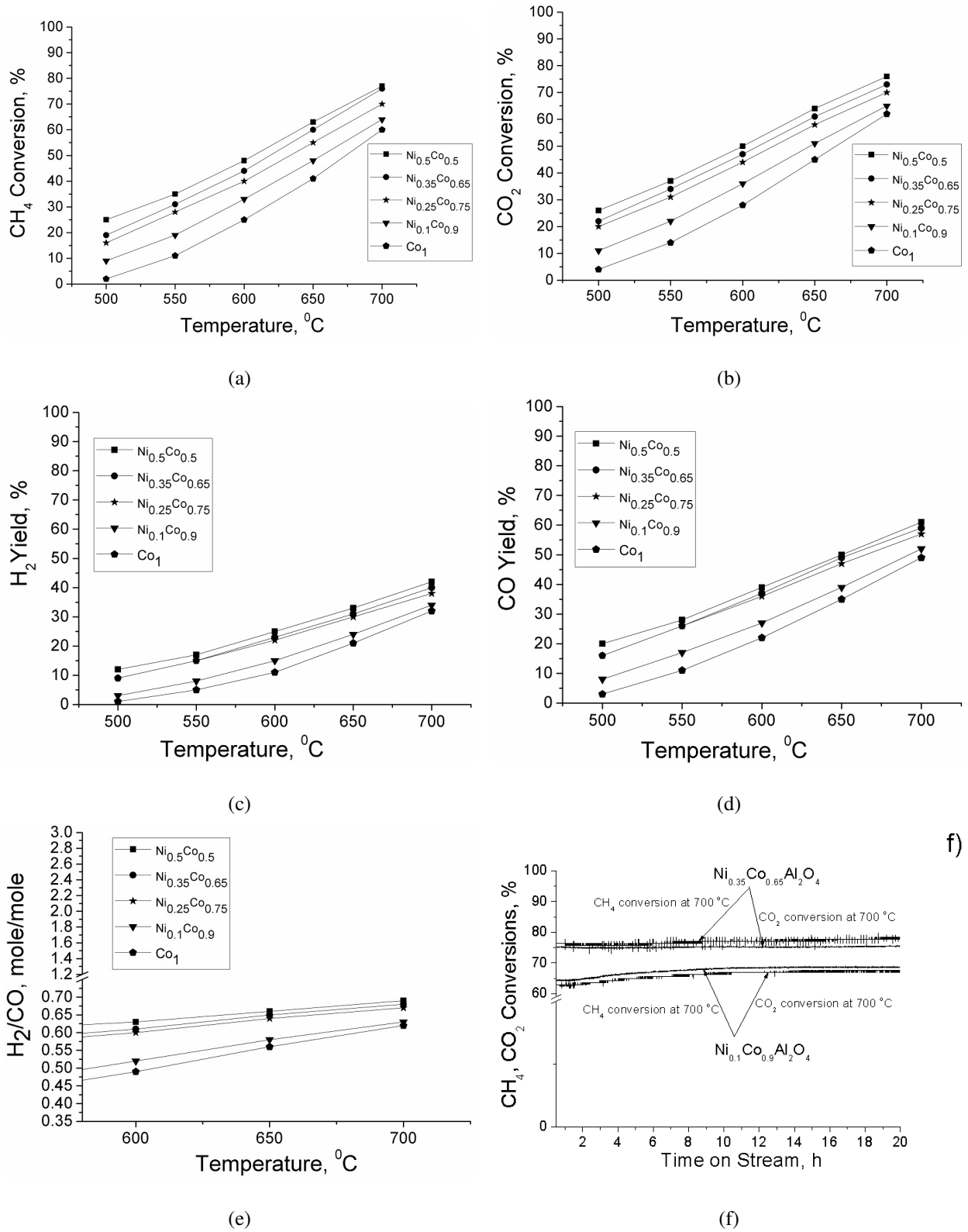

FIG. 1. CH_4 (a) and CO_2 (b) conversions, hydrogen yield (c), CO yield (d), molar ratio H_2/CO (e) and their corresponding equilibriums curves as a function of temperature in DRM over $Co_1Al_2O_4$, $Ni_{0.1}Co_{0.9}Al_2O_4$, $Ni_{0.25}Co_{0.75}Al_2O_4$, $Ni_{0.35}Co_{0.65}Al_2O_4$, $Ni_{0.5}Co_{0.5}Al_2O_4$ catalysts. And time on stream stability of DRM (f) over representative $Ni_{0.35}Co_{0.65}Al_2O_4$ and $Ni_{0.1}Co_{0.9}Al_2O_4$ catalysts

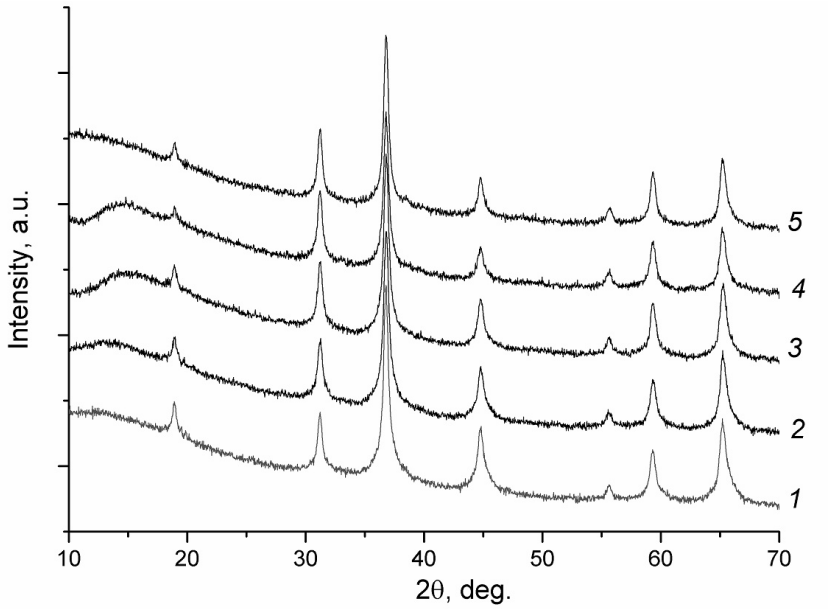

FIG. 2. X-ray patterns of $CoAl_2O_4$ (1), $Ni_{0.1}Co_{0.9}Al_2O_4$ (2), $Ni_{0.25}Co_{0.75}Al_2O_4$ (3), $Ni_{0.35}Co_{0.65}Al_2O_4$ (4), $Ni_{0.5}Co_{0.5}Al_2O_4$ (5) samples, heated in air at 700 °C

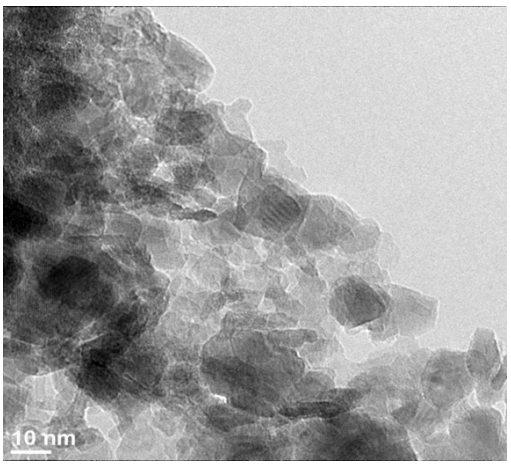

(a)

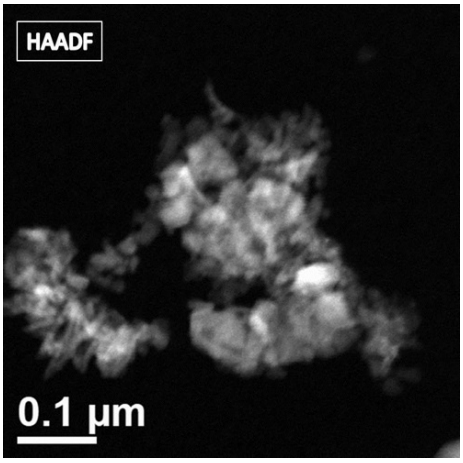

(b)

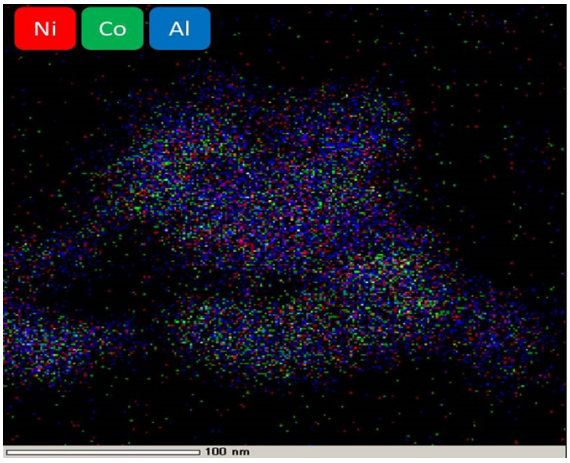

(c)

FIG. 3. TEM image (a), HAADF-STEM (b) image and corresponding EDX elemental mapping (c) of the representative $Ni_{0.35}Co_{0.65}Al_2O_4$ sample calcined in air at 700 °C

TABLE 2. Phase composition and structural properties of fresh catalysts $Ni_xCo_{1-x}Al_2O_4$ ($x = 0.1$ – 0.5) and the comparison sample $Co_1Al_2O_4$ heated at 700 °C in air

#	Sample	Phase	Lattice parameter, Å	CSR, nm	S_{BET}, m^2/g
1	$Co_1Al_2O_4$	Spinel	8.0939	12.69	116
2	$Ni_{0.1}Co_{0.9}Al_2O_4$	Spinel	8.0947	11.90	108.2
3	$Ni_{0.25}Co_{0.75}Al_2O_4$	Spinel	8.0914	11.48	108.8
4	$Ni_{0.35}Co_{0.65}Al_2O_4$	Spinel	8.0908	10.18	123.7
5	$Ni_{0.5}Co_{0.5}Al_2O_4$	Spinel	8.0943	9.54	127.6

TABLE 3. Phase composition and structural characteristics of $Ni_xCo_{1-x}Al_2O_4$ ($x = 0.1 – 0.5$) catalysts and the comparison sample $Co_1Al_2O_4$ after work in DRM media

#	Sample	Phase	Lattice parameter, Å	CSR, nm
1	$Co_1Al_2O_4$	Spinel (62 %) Co^0 (38 %)	8.042 3.540	3.62 3.99
2	$Ni_{0.1}Co_{0.9}Al_2O_4$	Spinel (83.5 %) (0.33Ni–0.77Co) alloy (16.5 %)	8.031 3.537	3.69 3.90
3	$Ni_{0.25}Co_{0.75}Al_2O_4$	Spinel (82.9 %) (0.3Ni–0.7Co) alloy (17.1 %)	8.049 3.539	3.06 3.67
4	$Ni_{0.35}Co_{0.65}Al_2O_4$	Spinel (82.3 %) (0.29Ni–0.71Co) alloy (17.7 %)	8.041 3.540	2.93 3.04
5	$Ni_{0.5}Co_{0.5}Al_2O_4$	Spinel (81.7 %) (0.42Ni–0.58Co) alloy (18.3 %)	8.039 3.530	3.89 3.75

sample $Co_1Al_2O_4$ and bimetallic Ni–Co alloy phase in $Ni_xCo_{1-x}Al_2O_4$ ($x = 0.1 – 0.5$) due to the shift of characteristics of the diffraction peaks at 2θ: 44.26 – 44.52°. The X-ray diffraction patterns of the Ni–Co alloy shows the diffraction peaks at 2θ: 44.26 – 44.52°, 51.57 – 51.58°, 75.92 – 76.44° which were attributed to the (111), (200), and (220) crystal planes of the Ni–Co alloy (ICSD-76632, ICSD-646088).

X-ray patterns of $Ni_{0.35}Co_{0.65}Al_2O_4$ catalyst at first heated in air at 700 °C and then in situ reduced in 10 % H_2/ 90 % He mixture in the temperature range of 200 – 700 °C presented in Fig. 5. It may be seen that the phase of intermetallic Ni–Co alloy is formed under the reduction at 620 °C and higher.

It is visible from the data presented in Table 3 that in $Co_1Al_2O_4$ sample the concentration of Co^0 metal phase is 38 %. In $Ni_xCo_{1-x}Al_2O_4$ samples the concentration of Ni–Co alloy metal phase is increased from 16.5 % to 18.3 % as x value increased from 0.1 to 0.5. At the same time Ni/Co ratio in bimetallic alloy does not change significantly (0.33/0.77; 0.3/0.7; 0.29/0.71) with x value increasing from 0.1 to 0.35. In a sample with $x = 0.5$ this value is increased to ratio $0.42/0.58$.

Despite the high reaction temperature, the rather high dispersion of catalysts particles are observed in investigated catalysts (Table 3). By comparison of data in Tables 2 and 3, one can see that the CSR value of spinel structure decreases from 10 – 11 to 3.0 – 3.5 nm. Simultaneously, the highly dispersed particles of Ni–Co nanoalloy with the average size of 3 – 4 nm are formed.

As can be seen from the HAADF-STEM image of $Ni_{0.35}Co_{0.65}Al_2O_4$ catalyst after work in the reaction mixture (Fig. 6a), the agglomerates of metal particles about 10 – 20 nm in size are observed on the surface of the spinel structure. This fact is inconsistent with the XRD data in (Table 3). According to element mapping data (Fig. 6b) the Ni–Co bimetallic alloy are formed. The formation of individual cobalt and nickel particles smaller than 1 nm on the surface cannot be ruled out. Fig. 6c show that under reaction condition cobalt and nickel leave the spinel structure, stabilized as nanodispersed Ni–Co alloy particles about 5 nm in size, collected in bigger aggregates on the outer surface, whereby the spinel structure becomes nanocrystalline. It consists of incoherently fused small spinel particles of 3 – 4 nm in size. In this case, the spinel CSR size decreases, but it lattice parameter does not change. This explanation agrees to the XRD results presented above. Due to the extraction of nickel and cobalt cations from the spinel structure under reducing conditions, their content in areas not containing metal particles decreases by about 1.5 times comparing to the initial catalyst.

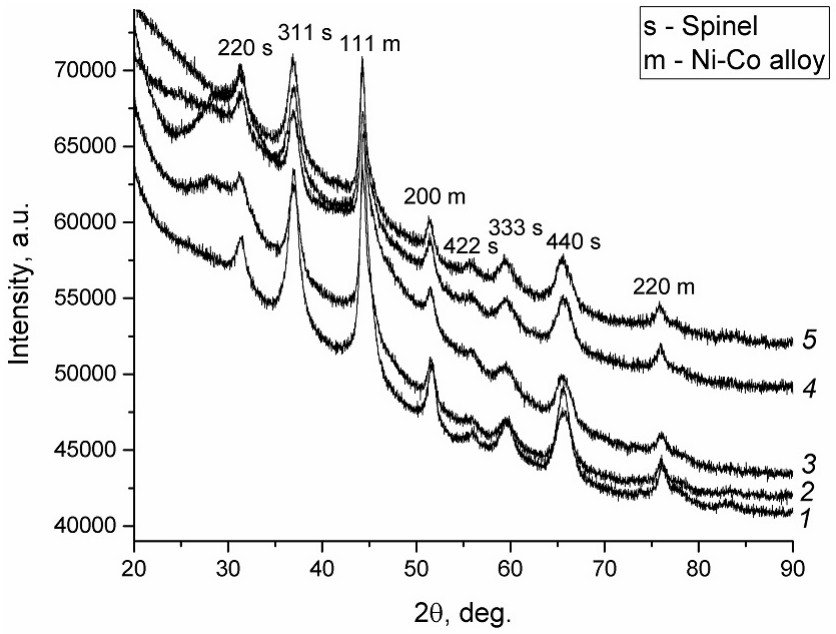

FIG. 4. X-ray patterns of $CoAl_2O_4$ (1), $Ni_{0.1}Co_{0.9}Al_2O_4$ (2), $Ni_{0.25}Co_{0.75}Al_2O_4$ (3), $Ni_{0.35}Co_{0.65}Al_2O_4$ (4), $Ni_{0.5}Co_{0.5}Al_2O_4$ (5) used catalysts with previous activation in hydrogen at 700 °C

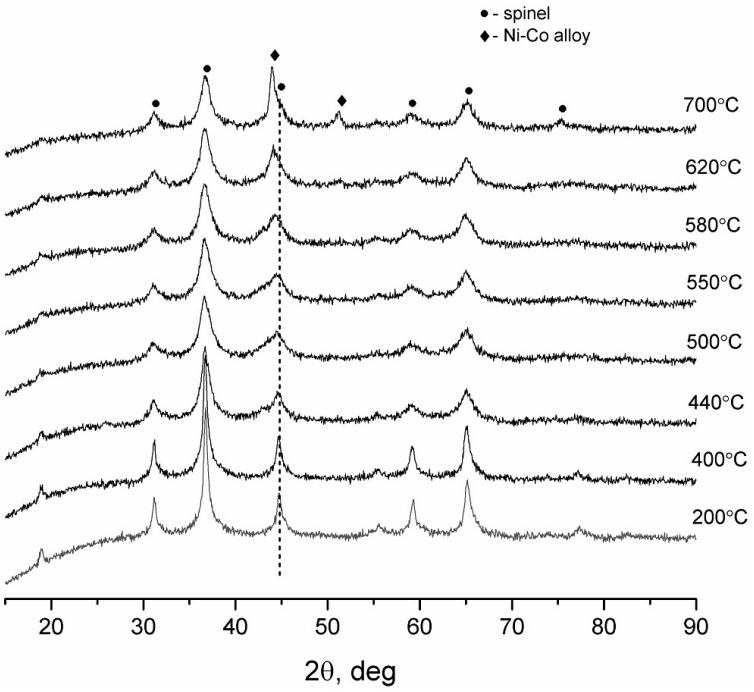

FIG. 5. X-ray patterns recorded during *in situ* reduction of representative $Ni_{0.35}Co_{0.65}Al_2O_4$ catalyst, previously heated at 700 °C in air

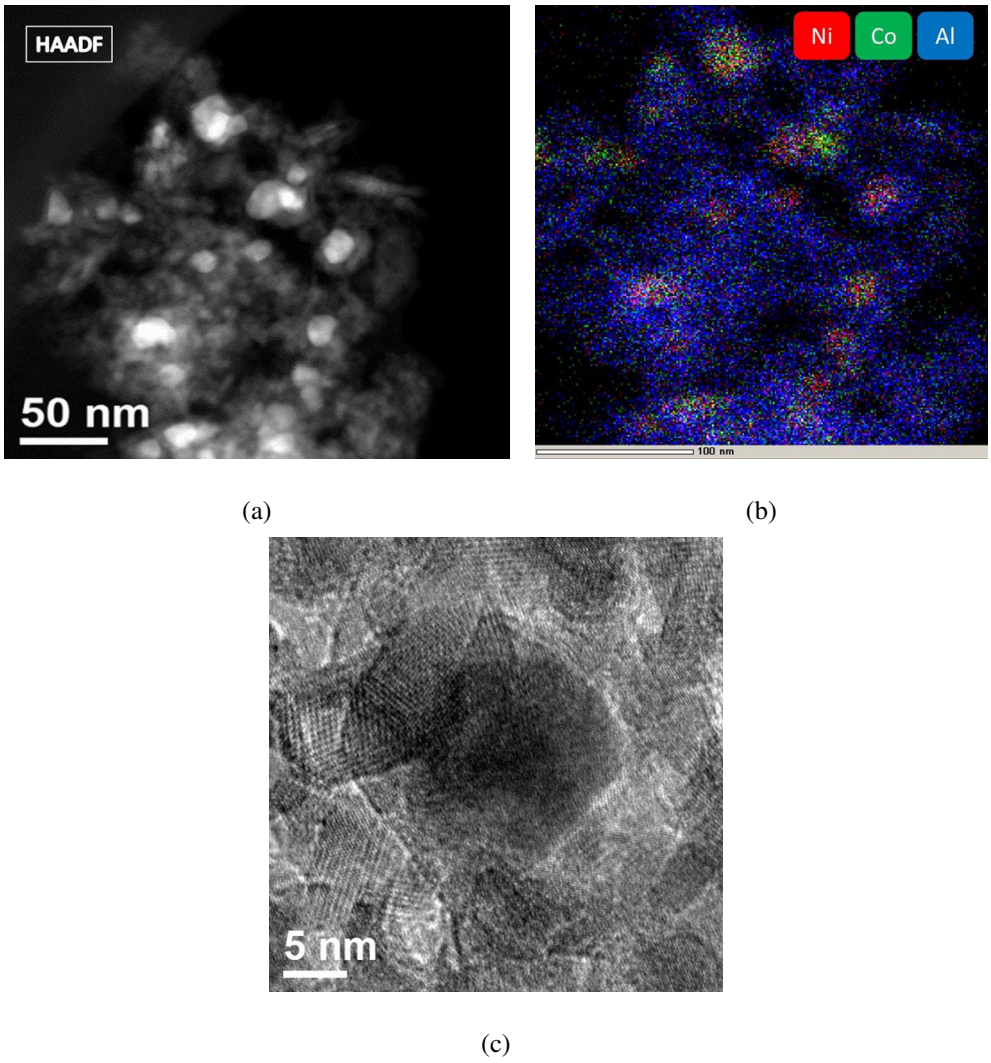

FIG. 6. HAADF-STEM image (a), EDX elemental mapping (b) and HRTEM (c) of the representative $Ni_{0.35}Co_{0.65}Al_2O_4$ sample after reaction

It was shown in the literature that formation of Ni–Co alloy configuration may exert a significant influence on the electronic properties of Ni–Co and thus benefit the catalytic properties [2, 36]. Certainly Ni–Co alloy is the active phase in DRM reaction. In our case, it is visible that increasing the concentration of Ni–Co alloy in $Ni_xCo_{1-x}Al_2O_4$ catalysts lead to increasing their catalytic activity in DRM.

3.3. Catalysts reducibility (TPR–H_2)

Before the reaction $Ni_xCo_{1-x}Al_2O_4$ ($x = 0.1 - 0.5$) catalysts and the comparison sample $Co_1Al_2O_4$ previously calcined at 700 °C in air, were activated by reduction of 5 vol. % H_2/He mixture at 700 °C for 1 h. In order to study the features of this activation, method of temperature-programed hydrogen reduction (TPR–H_2) was applied. Obtained TPR–H_2 profilers for all catalysts are shown in Fig. 7. For $CoAl_2O_4$ sample hydrogen consumption peaks can be distinguished at the temperature of 527, 670 and 774 °C. According to the literature [31, 47, 48] and XRD data in situ, the first peak at 527 °C can be identified as the reduction of surface Co^{3+} to Co^{2+}. The peak at 670 °C may be identified with the reduction of the part of Co^{3+} ions to Co^0 with formation of metal compound. The high temperature reduction peak at 774 °C may be associated with the reduction of some part of $Co^{(2,3)+}$ ions localized in strong interaction in the volume of the spinel structure.

For $Ni_xCo_{1-x}Al_2O_4$ ($x = 0.1 - 0.5$) series, in all samples also three regions of hydrogen consumption can be observed: 512 – 409 °C (I region), 631 – 587 °C (II region), and 784 – 812 °C (III region), whose positions are dependent on the Ni content. With increasing x value from 0.1 to 0.5 peaks observed in I and II regions slightly shift towards lower temperature ranges and peaks observed in region III some shift to higher temperature range. The value of H_2 consumption increases from 4.9 to 5.6 mlmol H_2/g with an increase in the nickel content in the samples from $x = 0$ to $x = 0.5$.

Based on the analysis of literature data [2, 28, 31, 47, 48] and the results of studying samples by XRD method, the H_2 consumption in the I temperature region may indicate the reducibility of Ni^{2+} to Ni^0 in (Ni–O–Co, Ni–O–Al) structures

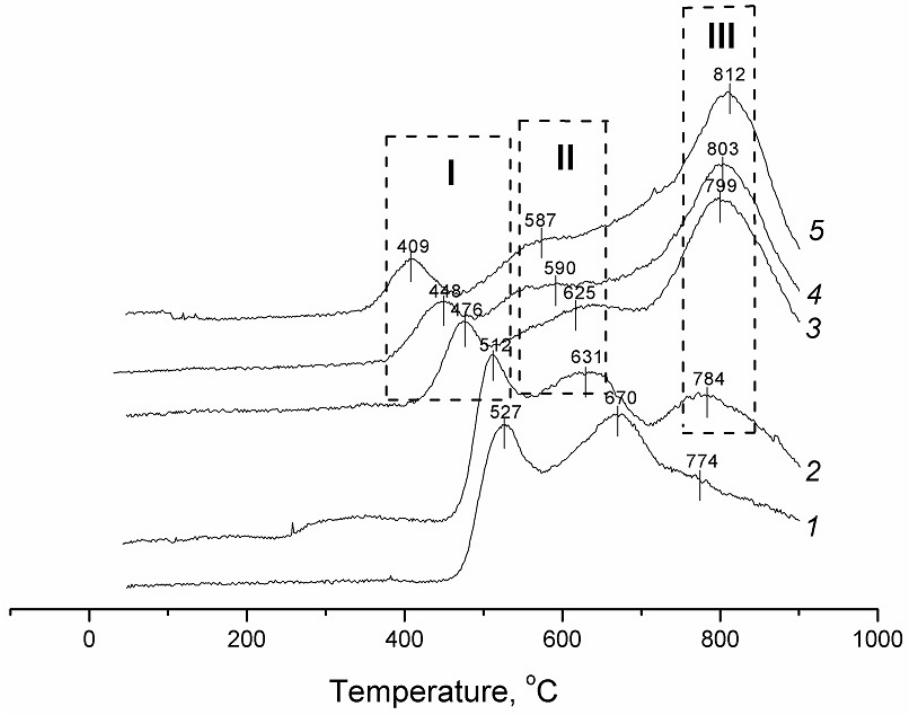

FIG. 7. TPR-H_2 profiles of $CoAl_2O_4$ (1), $Ni_{0.1}Co_{0.9}Al_2O_4$ (2), $Ni_{0.25}Co_{0.75}Al_2O_4$ (3), $Ni_{0.35}Co_{0.75}Al_2O_4$ (4), $Ni_{0.5}Co_{0.5}Al_2O_4$ (5) samples

localized on the surface of the spinel structure. Decreasing in Co^{3+} reduction temperature from 527 to 512 °C under addition of Ni to $CoAl_2O_4$ indicates the decreasing strength of the metal-support interaction in these catalysts [36]. This region of hydrogen uptake is associated with the reduction of Co^{3+} cations localized on the surface of spinel structure. The peaks in the region II may be due to the formation of Ni–Co alloy. This process becomes easier as the x value increases. According to [1, 2, 36], this shift indicates ease of reduction of the metallic oxides to the metallic forms. The high temperature reduction peak localized in III region may be associated with the reduction of some part of Co and Ni ions localized in strong interaction in the volume of the spinel structure [47].

Hence, the introduction of Ni into $CoAl_2O_4$ greatly changes their reducing properties. Thus, in the $Ni_xCo_{1-x}Al_2O_4$ samples, as a result of activation, reduction of Ni^{2+} and Co^{3+} cations on the surface of spinel structure lead to their exsolution and bimetallic alloyed Ni–Co nanoparticles are formed.

3.4. XPS study

Figure 8 presents the survey X-ray photoelectron spectrum of $Ni_{0.35}Co_{0.65}Al_2O_4$ sample heated in air at 700 °C. The surface composition of this sample corresponds to the declared one because no additional elements and contamination were detected. To investigate the valance states of individual elements the narrow spectral regions were analyzed. These spectra are presented in Fig. 9(a – d). One can see that binding energy (BE) of $Ni2p_{3/2}$ peak is 854.8 eV which corresponds to Ni^{2+} state [49, 50]. In Co2p spectrum peak position is 781.2 eV corresponding to Co^{2+} state [51, 52].

After reaction in the spectra of investigated sample in the spectral region of Ni2p additional shoulder with BE = 852.6 eV is appeared, which corresponds to Ni^0 state [44]. Simultaneous, in Co2p spectrum additional shoulder with BE = 778.2 eV is appeared. Such value of BE indicates the presence of Co^0 state [53]. The chemical state of alumina was carried out from Al2p peak position. In both samples (fresh and after reaction), the value of the BE of this peak is 74.3 eV and is characteristic of Al^{3+} state [54, 55]. XP spectra recorded in O1s region (Fig. 9d) indicate the peak at ∼531 eV due to O^- in the Al_2O_3 lattice.

Obtained results indicate that in fresh catalyst nickel is predominantly in the Ni^{2+} state and cobalt in Co^{2+} state, alumina in Al^{3+} state. In the catalyst after reaction nickel in Ni^0 state, cobalt in Co^0 state are appeared. In both samples Al^{3+} state is observed.

4. Conclusions

Highly active bimetallic Ni–Co catalysts supported on spinel-based structure with a general composition of $Ni_xCo_{1-x}Al_2O_4$ ($x = 0.1 - 0.5$) for DRM reaction were prepared by co-precipitation method. Preparation of the catalysts by precipitation method allow on the first stage to obtained precursors containing homogeneously distributed Ni and Co species in its volume, which on the further calcination at 700 °C in air spinel structure with homogeneous distribution of

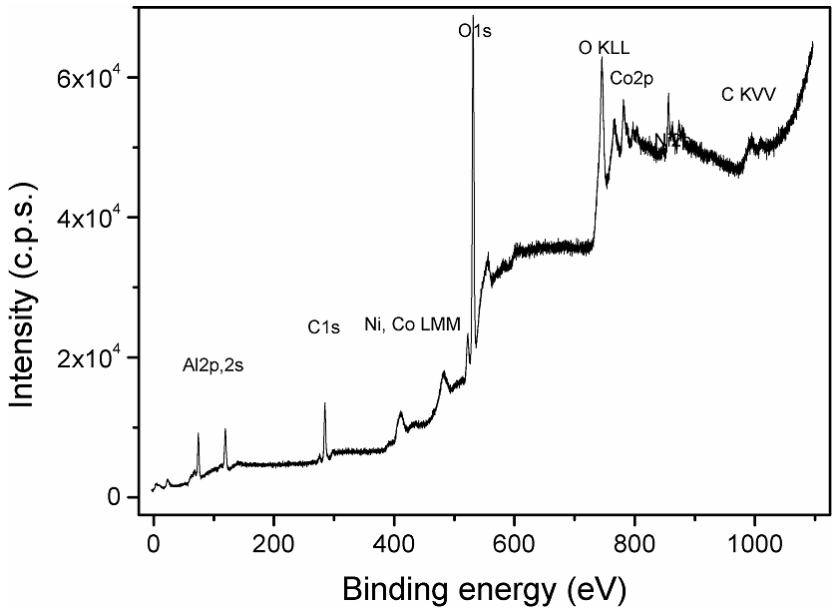

FIG. 8. Survey XP spectrum of the $Ni_{0.35}Co_{0.65}Al_2O_4$ catalyst before the reaction

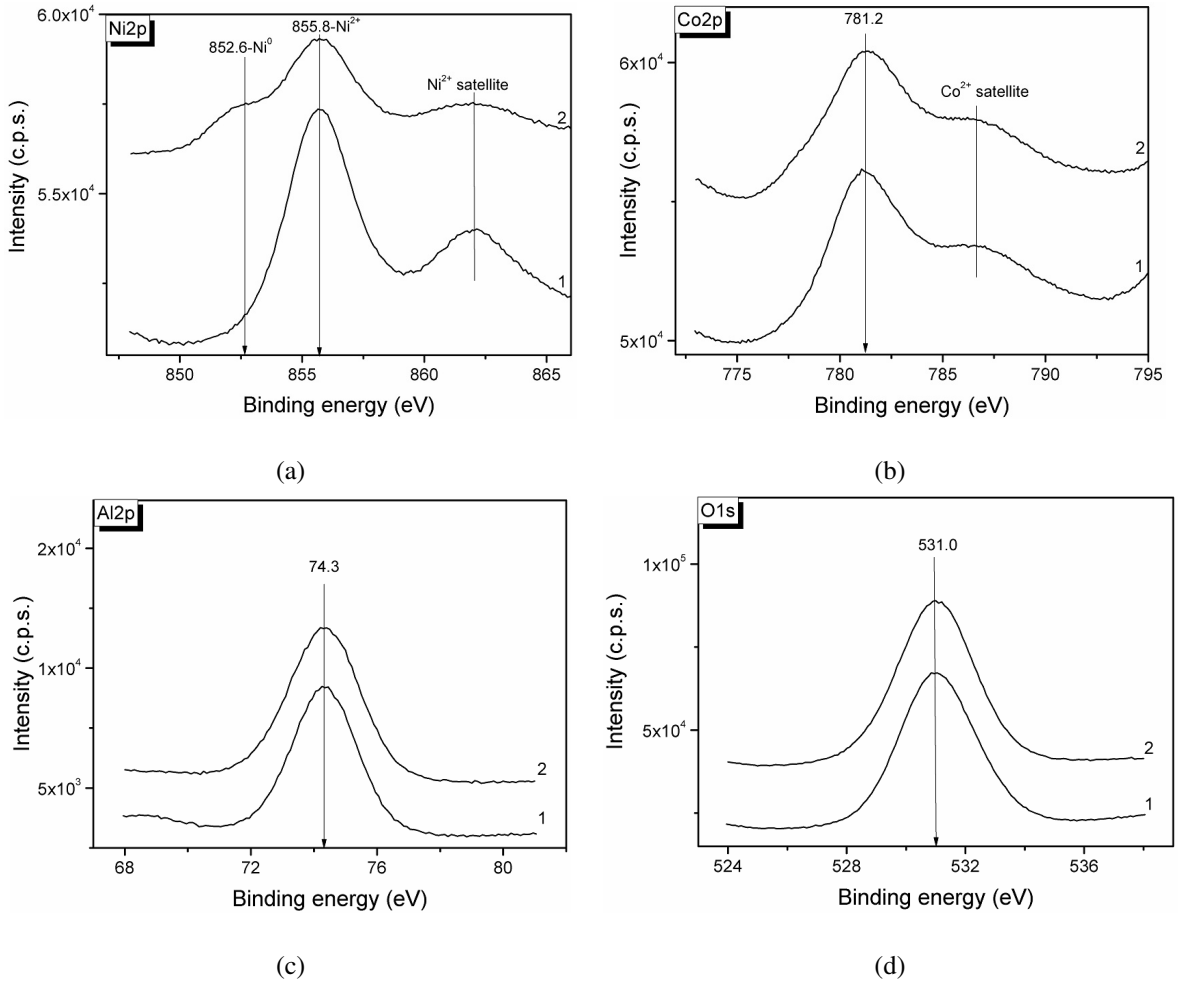

FIG. 9. Ni2p (a), Co2p (b), Al2p (c), O1s (d) spectra of representative $Ni_{0.35}Co_{0.65}Al_2O_4$ catalyst before (1) and after (2) reaction

Ni^{2+} and Co^{2+} ions in the spinel structure. During the reduction in H_2 or *in situ* reaction condition Ni^0 and Co^0 formed by the reduction can no longer stay in the spinel lattice, resulting in the migration to the surface to form the highly dispersed Ni–Co bimetallic alloy particles. It should be noted that under these catalytic conditions, not all nickel and cobalt are completely reduced to the metallic state in the spinel structure. The content of metal Ni–Co alloy particles is about 17 – 18 wt. %. The rest part of the nickel and cobalt remains stabilized in the spinel structure. According to the obtained and some literature data, it may be concluded that the high activity of this catalysts are due to the highly dispersed and stable Ni–Co alloy particles (3 – 4 nm in size) on the surface of spinel structure, from which the nickel and cobalt species partly evolve from the cations homogeneously distributed in spinel matrix. The synergy of Ni and Co in alloy bimetallic catalysts provides high activity with extremely short contact time ($\tau = 30$ ms) and high stability during time on steam in DRM reaction.

A comparison of experimental data obtained in this work for catalytic activity in the DRM reaction with literature analogues (Table 4) indicates the significant potential of the our catalysts among catalysts described in the literature.

TABLE 4. A comparison of experimental data obtained in this work for catalytic activity in the DRM reaction with literature analogues

#	Catalyst	Preparation method	DRM reaction conditions	Best performance achievements	Time of stream (TOS) stability	Ref.
1	3.37 % Co – 11.2 % $Ni/MgAl_2O_4$	Incipient wetness impregnation	18825 ml/g·h; CH_4:CO_2:N_2 = 1:1:3; 600 °C	X_{CH_4}= 9 %; X_{CO_2}=13 %; H_2/CO = 0.5	Only an initial slight drop of X_{CH_4}; X_{CO_2} after TOS 1.5 h	28
2	7.5 % Co – 7.5 % $Ni/MgAl_2O_4$	Incipient wetness impregnation	10000 ml/g·h; CH_4:CO_2:N_2 = 1:1:3; 600 °C	X_{CH_4}=16 %; H_2/CO = 0.45	A small decrease of X_{CH_4} in the first 90 min	38
3	8 % Co – 1 % Ni/Al_2O_3	Excess volume impregnation	22000 h^{-1} (GHSV); CH_4:CO_2 = 1:1 700 °C	X_{CH_4}=71 %; X_{CO_2}= 80 %	Deactivation after 6 h	37
4	$Ni_{0.375}Co_{0.375}Mg_{0.25}Al_2O_4$	Wet impregnation	60000 h^{-1} (GHSV) CH_4:CO_2:N_2 = 2.3:4.6:1 (20 ppm H_2S) 850 °C	X_{CH_4}=40 %; X_{CO_2}= 32 %	Performance decreases in the first 6 h	56
5	NiCoAlO	One pot evaporation-induced self-assembly	CH_4:CO_2 = 1; 700 °C	X_{CH_4}=52 %; X_{CO_2}= 60 %; H_2/CO = 0.82	—	57
6	Ni/Al_2O_3	Impregnation	12000 ml/g·h; 700 °C	X_{CH_4}=57 %; X_{CO_2}= 70 %	Performance decreases in the first 3 h	58
7	$Ni_{0.5}Co_{0.5}Al_2O_4$ (a); $Ni_{0.35}Co_{0.65}Al_2O_4$ (b)	Co-precipitation	120000 h^{-1} (GHSV) (15 % CH_4 + 15 % CO_2)/N_2 700 °C	X_{CH_4} =77 %; X_{CO_2} =76 %; H_2/CO = 0.69 (a); X_{CH_4} = 76 %; X_{CO_2} = 73 %; H_2/CO = 0.68 (b)	Stable performance for 20 h	This work

References

[1] Alipour Z., Borugadda V.B., Wang H., Dalai A.K. Syngas production through dry reforming: A review on catalysts and their materials, preparation methods and reactor type. *Chemical Engineering J.*, 2023, **452**, 139416.

[2] Yentekakis I.V., Panagiotopoulou P., Artemakis G. A review of recent efforts to promote dry reforming of methane (DRM) to syngas production via bimetallic catalyst formulations. *Appl. Catal. B: Environ.*, 2021, **296**, 120210.

[3] Zhang G., Liu J., Xu Y., Sun Y. A review of CH_4 CO_2 reforming to synthesis gas over Ni-based catalysts in recent years (2010–2017). *Int. J. Hydrogen Energy*, 2018, **43**, P. 15030–15054.

[4] Yentekakis I.V., Goula G., Hatzisymeon M., Betsi-Argyropoulou I., Botzolaki G., Kousi K., Kondarides D.I., Taylor M.J., Parlett C.M.A., Osatiashtiani A., Kyriakou G., Holgado J.P., Lambert R.M. Effect of support oxygen storage capacity on the catalytic performance of Rh nanoparticles for CO_2 reforming of methane. *Appl. Catal. B: Environ.*, 2019, **243**, P. 490–501.

[5] Abdulrasheed A., Jalil A.A., Gambo Y., Ibrahim M., Hambali H.U., Shahul Hamid M.Y. A review on catalyst development for dry reforming of methane to syngas: recent advances. *Renewable Sustainable Energy Rev.*, 2019, **108**, P. 175–193.

[6] Song Y., Ozdemir E., Ramesh S., Adishev A., Subramanian S., Harale A., Albuali M., Fadhel B.A., Jamal A., Moon D., Choi S.H., Yavuz C.T. Dry reforming of methane by stable Ni–Mo nanocatalysts on single-crystalline MgO. *Science*, 2020, **367**, P. 777–781.

[7] Pakhare D., Spivey J. A review of dry (CO_2) reforming of methane over noble metal catalysts. *Chem. Soc. Rev.*, 2014, **43**, P. 7813–7837.

[8] Su B., Wang Y., Xu Z., Han W., Jin H., Wang H. Novel ways for hydrogen production based on methane steam and dry reforming integrated with carbon capture. *Energy Convers. Manag.*, 2022, **270**, 116199.

[9] Yentekakis I.V., Goula G. Biogas management: advanced Utilization for Production of renewable energy and added-value chemicals. *Front. Environ. Sci.*, 2017, **5**, P. 7–18.

[10] Tsoukalou A., Imtiaze Q., Kim S.M., Abdala P.-M., Yoon S., Muller C.-R. Dry-reforming of methane over bimetallic Ni–M/La_2O_3 (M = Co, Fe): The effect of the rate of $La_2O_2CO_3$ formation and phase stability on the catalytic activity and stability. *J. Catal.*, 2016, **343**, P. 208–214.

[11] Bitters J.S., He T., Nestler E., Senanayake S.D., Chen J.G., Zhang C. Utilizing bimetallic catalysts to mitigate coke formation in dry reforming of methane. *J. of Energy Chemistry*, 2022, **68**, P. 124–142.

[12] Sharifianjazi F., Esmaeilkhanian A., Bazli L., Eskandarinezhad S., Khaksar S., Shafiee P., Yusuf M., Abdullah B., Salahshour P., Sadeghi F. A review on recent advances in dry reforming of methane over Ni- and Co-based nanocatalysts. *Int. J. Hydrog. Energy*, 2022, **47**, P. 42213–42233

[13] Rezaei M., Alavi S.M., Sahebdelfar S., Yan Z.F. Syngas production by methane reforming with carbon dioxide on noble metal catalysts. *J. Nat. Gas. Chem.*, 2006, **15**, P. 327–334.

[14] Barama S., Dupeyrat-Batiot C., Capron M., Bordes-Richard E., Bakhti-Mohammedi O., Catalytic properties of Rh, Ni, Pd and Ce supported on Al-pillared montmorillonites in dry reforming of methane. *Catal. Today*, 2009, **141**, P. 385–392.

[15] Ferreira-Aparicio P., Guerrero-Ruiz A., Rodriquez-Ramos I. Comparative study at low and medium reaction temperatures of syngas production by methane reforming with carbon dioxide over silica and alumina supported catalysts. *Appl. Catal. A: Gen.*, 1998, **170**, P. 177–187.

[16] Goula M.A., Charisiou N.D., Siakavelas G., Tzounis L., Tsiaoussis I., Panagiotopoulou P., Goula G., Yentekakis I.V. Syngas production via the biogas dry reforming reaction over Ni supported on zirconia modified with CeO_2 or La_2O_3 catalysts. *Int. J. Hydrog. Energy*, **42**, P. 13724–13740.

[17] Le Sach´e E., Pastor-P´erez L., Watson D., Sepúlveda-Escribano A., Reina T.R. Ni stabilised on inorganic complex structures: superior catalysts for chemical CO_2 recycling via dry reforming of methane. *Appl. Catal. B: Environ.*, 2018, **236**, P. 458–465.

[18] Serrano-Lotina A., Daza L. Long-term stability test of Ni-based catalyst in carbon dioxide reforming of methane. *Appl. Catal. A Gen.*, 2014, **474**, P. 107–113.

[19] Li X., Li D., Tian H., Zeng L., Zhao Z.-J., Gong J. Dry reforming of methane over Ni/La_2O_3 nanorod catalysts with stabilized Ni nanoparticles. *Appl. Catal. B: Environ.*, 2017, **202**, P. 683–694.

[20] Stroud T., Smith T.J., Le Sach´e E., Santos J.L., Centeno M.A., Arellano-Garcia H., Odriozola J.A., Reina T.R. Chemical CO_2 recycling via dry and bi reforming of methane using Ni-Sn/Al_2O_3 and Ni-Sn/CeO_2-Al_2O_3 catalysts. *Appl. Catal. B: Environ.*, 2018, **224**, P. 125–135.

[21] Makri M.M., Vasiliades M.A., Petallidou K.C., Efstathiou A.M., Effect of support composition on the origin and reactivity of carbon formed during dry reforming of methane over 5 wt % Ni/$Ce_{1-x}MxO_{2-\delta}$ (M = Zr^{4+}, Pr^{3+}) catalysts. *Catal. Today*, 2015, **259**, P. 150–164.

[22] Zhang W.D., Liu B.S., Tian Y.L. CO_2 reforming of methane over Ni/Sm_2O_3-CaO catalyst prepared by a sol–gel technique. *Catal. Comm.*, 2007, **8**, P. 661–667.

[23] Amin M.H., Mantri K., Newnham J., Tardio J., Bhargava S.K. Highly stable ytterbium promoted Ni/γ-Al_2O_3 catalysts for carbon dioxide reforming of methane. *Appl. Catal. B: Environ.*, 2012, **119**, P. 217–226.

[24] Zhang F., Liu Z., Zhang S., Akter N., Palomino R.M., Vovchok D., Orozco I., Salazar D., Rodriguez J.A., Llorca J., Lee J., Kim D., Xu W., Frenkel A.I., Li Y., Kim T., Senanayake S.D. In situ elucidation of the active state of Co–CeO_x catalysts in the dry reforming of methane: the important role of the reducible oxide support and interactions with cobalt. *ACS Catal.*, 2018, **8**, P. 3550–3560.

[25] Fakeeha A.H., Al Fatesh A.S., Ibrahim A.A., Kurdi A.N., Abasaeed A.E. Yttria modified ZrO_2 supported Ni catalysts for CO_2 reforming of methane: the role of Ce promoter. *ACS Omega*, 2021, **6**, P. 1280–1288.

[26] Kim S.M., Abdala P.M., Margossian T., Hosseini D., Foppa L., Armutlulu A., van Beek W., Comas-Vives A., Cop´eret C., Müller C. Cooperativity and dynamics increase the performance of NiFe dry reforming catalysts. *J. Am. Chem. Soc.*, 2017, **139**, P. 1937–1949.

[27] Kurlov A., Deeva E.B., Abdala P.M., Lebedev D., Tsoukalou A., Comas-Vives A., Fedorov A., Muller C.R. Exploiting two-dimensional morphology of molybdenum oxycarbide to enable efficient catalytic dry reforming of methane. *Nat. Comm.*, 2020, **11**, 4920.

[28] Sengupta S., Ray K., Deo G. Effects of modifying Ni/Al_2O_3 catalyst with cobalt on the reforming of CH_4 with CO_2 and cracking of CH_4 reactions. *Int. J. Hydrog. Energy*, 2014, **39**, P. 11462–11472.

[29] Gonzalez-delaCruz V.M., Pereniguez R., Ternero F., Holgado J.P., Caballero A. In situ XAS study of synergic effects on Ni–Co/ZrO_2 methane reforming catalysts. *J. Phys. Chem. C.*, 2012, **116**, P. 2919–2926.

[30] Son I.H., Lee S.J., Roh H-S. Hydrogen production from carbon dioxide reforming of methane over highly active and stable MgO promoted Co-Ni/α-Al_2O_3 catalyst. *Int. J. Hydrog. Energy*, 2014, **39**, P. 3762–3770.

[31] Xu J., Zhou W., Li Z., Wang J., Ma J. Biogas reforming for hydrogen production over nickel and cobalt bimetallic catalysts. *Int. J. Hydrog. Energy*, 2009, **34**, P. 6646–6654.

[32] Foo S.Y., Cheng C.K., Nguyen T-H., Adesina A.A. Oxidative CO_2 reforming of methane on alumina-supported Co–Ni catalyst. *Ind. Eng. Chem. Res.*, 2010, **49**, P. 10450–10458.

[33] Fan M-S., Abdullah A.Z., Bhatia S. Utilization of greenhouse gases through carbon dioxide reforming of methane over Ni–Co/MgO-ZrO_2: preparation, characterization and activity studies. *Appl. Catal. B: Environ.*, 2010, **100**, P. 365–377.

[34] Halliche D., Bouarab R., Cherifi O., Bettahar M.M. Carbon dioxide reforming of methane on modified Ni/α-Al_2O_3 catalysts. *Catal. Today*, 1996, **29**, P. 373–377.

[35] San-Jose-Alonso D., Illan-Gomez M.J., Roman-Martınez M.C. Low metal content Co and Ni alumina supported catalysts for the CO_2 reforming of methane. *Int. J. Hydrog. Energy*, 2013, **38**, P. 2230–2239.
[36] Wu Z., Yang B., Miao S., Liu W., Xie J., Lee S.,. Pellin M.J, Xiao D., Su D., Ma D. Lattice strained Ni–Co alloy as a high-performance catalyst for catalytic dry reforming of methane. *ACS Catal.*, 2019, **9**, P. 2693–2700.
[37] San-Joze-Alonso D., Juan-Juan J., Illan-Gomez M.J., Roman-Martinez M.C. Ni, Co and bimetallic Ni–Co catalysts for the dry reforming of methane. *Appl. Catal. A: Gen.*, 2009, **371**, P. 54–59.
[38] Kumari R., Sengupta S. Catalytic CO_2 reforming of CH_4 over $MgAl_2O_4$ supported Ni–Co catalysts for the syngas production. *Int. J. Hydrog. Energy*, 2020, **45**, P. 22775–22787.
[39] Li H., Shin K., Henkelman G. Effects of ensembles, ligand, and strain on adsorbate binding to alloy surfaces. *J. Chem. Phys.*, 2018, **149**, 174705.
[40] Khairudin N.F., Mohammadi M., Mohamed A.R. An investigation on the relationship between physicochemical characteristics of alumina-supported cobalt catalysts and its performance in dry reforming of methane. *Environ. Sci. Pollut. Control Ser.*, 2021, **28** (23), P. 29157–29176.
[41] Dekkar S., Tezkratt S., Sellam D., Ikkour K., Parkhomenko K., Martinez-Martin A., Roger A.C. Dry reforming of methane over Ni–Al_2O_3 and Ni–SiO_2 catalysts: role of preparation methods. *Catal. Lett.*, 2020, **150**, P. 2180–2199.
[42] *TOPAS V4.2: General Profile and Structure Analysis Software for Powder Diffraction Data – User's Manual*; Bruker AXS: Karlsruhe, Germany, 2008; Available online: (http://algol.fis.uc.pt/jap/TOPAS %204-2 %20Users %20Manual.pdf (accessed on 8 May 2020))
[43] Database: Inorganic Crystal Structure Database, ICSD. In Release 2008. Fashinformationszentrum Karsruhe D #8211 1754 Eggenstein #8211 Leopoldshafen, Germany, 2008.
[44] Moudler J., Stickle W., Sobol P., Bomben K., *Handbook of X-ray Photoelectron Spectroscopy*, Perkin-Elmer Corp.: Eden. Prairie, MN, 1992.
[45] Scofield J.H., *J. Electron Spectrosc. Relat. Phenom.*, 1976, **8**, P. 129–137.
[46] Kwok R. Free, fully featured, software for the analysis of XPS spectra. November 25, 2023, http://xpspeak.software.informer.com/4.1/ .
[47] Ji Y., Zhao Z., Duan A., Jiang G., Liu J. Comparative study on the formation and reduction of bulk and Al_2O_3-supported cobalt oxides by H_2-TPR technique. *Phys. Chem. C*, 2009, **113**, P. 7186–7199.
[48] Andonova S., de Avila C.N., Arishtirova K., Bueno J.M.C., Damyanova S. Structure and redox properties of Co promoted Ni/Al_2O_3 catalysts for oxidative steam reforming of ethanol. *Appl. Catal. B: Environ.*, 2011, **105**, P. 346–360.
[49] Wang R., Li Y., Shi R., Yang M. Effect of metal-support interaction on the catalytic performance of Ni/Al_2O_3 for selective hydrogenation of isoprene. *J. Mol. Catal. A: Chem.*, 2011, **344**, P. 122–127.
[50] Zhang H.J., Chen Z.Q., Wang S.J. Spin conversion of positronium in NiO/Al_2O_3 catalysts observed by coincidence Doppler broadening technique. *Phys. Rev. B*, 2010, **82**, 035439.
[51] Gao Y., Qiao F., Hou W., Ma L., Li N., Shen C., Jin T., Xie K. Radiation effects on lithium metal batteries. *The Innovation*, 2024, **3**, 100468.
[52] Du J., Liu G., Li F., Zhu Y., Sun Iron–Salen L. Complex and Co^{2+} Ion-Derived Cobalt–Iron Hydroxide/Carbon Nanohybrid as an Efficient Oxygen Evolution. *Electrocatalyst. Adv. Sci.*, 2019, **6**, 1900117.
[53] Li C., Li S., Zhao J., Sun M., Wang W., Lu M., Qu A., Hao C., Chen C., Xu C., Kuang H., Xu L. Ultrasmall Magneto-chiral Cobalt Hydroxide Nanoparticles Enable Dynamic Detection of Reactive Oxygen Species in Vivo. *JACS*, 2022, **144**, P. 1580–1588.
[54] Cano A.M., Marquardt A.E., DuMont J.W., George S.M. Effect of HF Pressure on Thermal Al_2O_3 Atomic Layer Etch Rates and Al_2O_3 Fluorination. *J. Phys. Chem. C*, 2019, **123**, P. 10346–10355.
[55] Huang L., Xiong K., Wang X., He X., Yu L., Fu C., Zhu X., Feng W. The Mechanism of Oxide Growth on Pure Aluminum in Ultra-High-Temperature Steam. *Metals*, 2022, **12**, 1049
[56] Misture S.T., McDevitt K.M., Glass K.C., Edwards D.D., Howe J.Y., Rector K.D.,H. He, Vogel S.C., Sulfur-resistant and regenerable Ni/Co spinel-based catalysts for methane dry reforming. *Catal. Sci. Technol.*, 2015, **5**, P. 4565–4574.
[57] Li B., Luo Y., Li B., Yuan X., Wang X. Catalytic performance of iron-promoted nicel-based ordered mesoporous alumina FeNiAl catalysts in dry reforming of methane. *Fuel Process. Technol.*, 2019, **193**, P. 348–360.
[58] Alipour Z., Rezaei M., Meshkani F. Effects of support modifiers on the catalytic performance of Ni/Al_2O_3 catalyst in CO_2 reforming of methane. *Fuel*, 2014, **129**, P. 197–203.

Submitted 5 September 2024; revised 28 November 2024; accepted 5 December 2024

Information about the authors:

Alexey A. Shutilov – Boreskov Institute of Catalysis SB RAS, Lavrentieva 5, Novosibirsk 630090, Russia; ORCID 0009-0008-1682-1125; alshut@catalysis.ru

Mikhail N. Simonov – Boreskov Institute of Catalysis SB RAS, Lavrentieva 5, Novosibirsk 630090, Russia; Novosibirsk State University, Pirogova 2, Novosibirsk 630090, Russia; ORCID 0000-0002-5161-5684; smike@catalysis.ru

Valeria E. Fedorova – Boreskov Institute of Catalysis SB RAS, Lavrentieva 5, Novosibirsk 630090, Russia; ORCID 0000-0002-0551-1892; valeria@catalysis.ru

Alexander S. Marchuk – Novosibirsk State University, Pirogova 2, Novosibirsk 630090, Russia; ORCID 0000-0003-4063-5142; alexander.s.marchuk@gmail.com

Igor P. Prosvirin – Boreskov Institute of Catalysis SB RAS, Lavrentieva 5, Novosibirsk 630090, Russia; ORCID 0000-0002-0351-5128; prosvirin@catalysis.ru

Galina A. Zenkovets – Boreskov Institute of Catalysis SB RAS, Lavrentieva 5, Novosibirsk 630090, Russia; ORCID 0000-0002-3896-8071; zenk@catalysis.ru

Conflict of interest: the authors declare no conflict of interest.

NANOSYSTEMS:
PHYSICS, CHEMISTRY, MATHEMATICS

Boleiko G.M., et al. *Nanosystems: Phys. Chem. Math.*, 2025, **16** (1), 44–50.
http://nanojournal.ifmo.ru
DOI 10.17586/2220-8054-2025-16-1-44-50

Original article

Synthesis and characterization of $InGaZn_2O_5$ obtained by nitrate-tartrate complex decomposition method

Gelena M. Boleiko[1,a], Gleb M. Zirnik[1,b], Andrey I. Kovalev[1,2,c], Daniil A. Uchaev[2,d], Ibrohimi A. Solizoda[1,3,4,e], Alexander S. Chernukha[1,2,f], Svetlana A. Gudkova[1,3,g], Denis A. Vinnik[1,2,3,h]

[1]Moscow Institute of Physics and Technology Institutsky lane, 9, Dolgoprudny, 141701, Russia

[2]South Ural State University, Lenin Av., 76, Chelyabinsk, 454080, Russia

[3]St. Petersburg State University Universitetskaya embankment, 7-9, 199034, St. Petersburg

[4]Tajik National University Rudaki Av., 17, Dushanbe, 734025, Tajikistan

[a]boleiko.gm@mipt.ru, [b]glebanaz@mail.ru, [c]asp23kai165@susu.ru, [d]uchaevda@susu.ac.ru, [e]solizoda.ia@mipt.ru, [f]chernukha.as@mipt.ru, [g]svetlanagudkova@yandex.ru, [h]vinnik.da@mipt.ru

Corresponding author: D. A. Vinnik, vinnik.da@mipt.ru

ABSTRACT The study for the first time presents a method for producing indium-gallium-zinc oxide $InGaZn_2O_5$ using the nitrate-tartrate complex decomposition method. The material is characterized by X-ray diffraction, electron microscopy, IR- and UV-spectroscopy. It has been established that the use of tartaric acid as a precursor already at a temperature of 500 °C leads to the formation of a single-phase homogeneous material consisting of nanocrystalline particles in the form of micrometer agglomerates. The proposed method for producing nanoparticles can be used in the future to produce semiconductor inks based on IGZO.

KEYWORDS indium-gallium-zinc oxide, $InGaZn_2O_5$, IGZO, nanoparticles.

ACKNOWLEDGEMENTS The research is supported by the Ministry of Science and Higher Education of the Russian Federation, project No 075-15-2024-560.

FOR CITATION Boleiko G.M., Zirnik G.M., Kovalev A.I., Uchaev D.A., Solizoda I.A., Chernukha A.S., Gudkova S.A., Vinnik D.A. Synthesis and characterization of $InGaZn_2O_5$ obtained by nitrate-tartrate complex decomposition method. *Nanosystems: Phys. Chem. Math.*, 2025, **16** (1), 44–50.

1. Introduction

At present, several main areas of work can be distinguished for obtaining semiconductor materials for further use in semiconductor devices:

1) obtaining one-dimensional Si nanostructures [1];
2) obtaining nano-sized one-dimensional structures of GaAs [2], GaN [3], InAs [4] and others;
3) obtaining metal chalcogenides (MoS_2 [5], WSe_2 [6], etc.) with two-dimensional morphology;
4) obtaining semiconductor oxide materials (indium tin oxide ITO [7], indium zinc oxide IZO [8], etc.).

Each of these areas covers its own place in terms of material use in the final device. The creation of functional materials for use in electronics, with the aim of developing them towards miniaturisation, is a priority for many research teams around the world. In parallel, the development of printed and flexible electronics is progressing [9–12].

For practical applications, one of the promising oxide materials is amorphous indium gallium zinc oxide [13–15] (α–IGZO of various compositions). IGZO (in amorphous state) compares favorably with traditional amorphous silicon due to its higher properties (for example, charge mobility and optical transparency), which ensures both high electrical stability of the material and the flexibility of thin-film transistors based on it. Historically, the possibility of using IGZO as a component to create an electronic device was first demonstrated in the pioneering work of Japanese researchers Nomura and his colleagues [12]. However, in this work, a thin-film transistor was obtained using a single-crystal IGZO layer of the composition $InGaO_3ZnO_5$ on a substrate of single-crystal ZrO_2 (stabilized by Y_2O_3). Later, the amorphous state of IGZO was also studied. The most promising use of this material was found to be in the form of amorphous thin films [16, 17].

Thin film transistors are used in the new generation of flat panel displays [14, 16–19] and form the basis of devices in all digital systems. Their characteristics, such as carrier mobility (μ), threshold voltage (V_{th}), on/off current ratio (I_{on}/I_{off}) and subthreshold swing (SS) depend largely on the properties of the semiconductor channel and are determined by the chemical composition, crystallinity, film thickness and the method of obtaining the thin film.

Currently, organic structures are the most popular semiconductors for the production of flexible microelectronic devices. They have become widespread due to the use of high performance technological printing processes and the good quality of the inks produced for printing, the possibility of producing final devices at low temperatures and excellent

© Boleiko G.M., Zirnik G.M., Kovalev A.I., Uchaev D.A., Solizoda I.A., Chernukha A.S., Gudkova S.A., Vinnik D.A., 2025

compatibility with flexible substrates [20–27]. However, despite these undoubted advantages, the use of organic semiconductors as ink material is limited because final devices on such semiconductors have low technical characteristics, in particular, the mobility of charge carriers in devices using organic semiconductors does not usually exceed 1...2 $cm^2/V{\cdot}s$, which does not allow them to be used for high-power devices. The aspect described above leads to the use of other materials. One of them can be a group of amorphous oxides, for example the ternary oxide IGZO, which has a sufficient set of characteristics of the final device and can be obtained by printing methods. There are several approaches to obtaining materials that would be suitable for ink production. One of these approaches is to obtain "true" non-aggregated nanoparticles in solution and then stabilize them with surfactants to obtain semiconductor ink. For example, there are a number of papers [28, 29] in which the authors have succeeded in obtaining oxide nanoparticles $MeFe_2O_4$ (Me = Mn, Co, Fe) (8...12 nm) of different morphologies (in the form of cubes or hexagons) using Me-acetylacetonate surfactant-mediated decomposition method (the original article did not propose a short name for the method). Theoretically, the use of this synthesis method will potentially allow the stabilized colloidal solutions obtained to be used directly as an ink, without the step of adding surfactants. At the same time, to the best of our knowledge, the described method has not yet been used to obtain indium-gallium-zinc oxide nanoparticles. Despite the excellent results of the Me-acetylacetonate surfactant-mediated decomposition method, which allows obtaining monodisperse nanoparticles, it is poorly scalable, which will lead to difficulties in introducing it into the technological chains of production of these inks in industry.

Another approach is to synthesize nanoparticles using a scalable technology (including solid-phase synthesis [30]), convert the resulting particles to a powder state (in which the nanoparticles are aggregated into large agglomerates) and separate the resulting aggregates using ultrasound treatment or milling methods. This method is not without its drawbacks - during the final stage of milling, it is difficult to obtain a fraction of nanoparticles (their total mass in the final product after milling is about several percents), in addition, the particle size distribution at the final stage of milling becomes random. The above approach can be implemented using the method of decomposition of an organometallic complex (gel) (often called the sol-gel or "solution combustion" method; in the case of using citric acid as a complexing agent, the name "citrate-nitrate" method is common). The essence of the method is to prepare solutions of nitrates of the required metals, form a complex, heat the resulting mixture to remove water and initiate an exothermic self-sustaining oxidation reaction of the complex to yield the target product (called as self-combustion synthesis). The synthesis method is well scalable and relatively simple, allowing the production of agglomerates of IGZO nanoparticles in an amorphous (X-ray amorphous) state under low temperature conditions.

In the literature, works on obtaining thin films (using spin-coating technology with subsequent initiation of the spontaneous combustion reaction) are mostly presented, where 2-methoxyethanol [31] and urea [32] are used as complexing agents. However, it is also possible to use ready-made organometallic complexes - metal acetylacetonates [33]. The authors proposed an approach using a mixture of 3-nitroacetylacetone and acetylacetone to facilitate the spontaneous combustion reaction [34]. It is reported that the introduction of 3-nitroacetylacetone also improves the films quality. Mixtures of 2-methoxyethanol and acetylacetone with the addition of an aqueous ammonia solution have also been used to obtain IGZO films [[35] (by spraying a mixture of precursors followed by decomposition), as well as compounds "related" to this system [36] or other oxide materials [37]. The use of organic additives as co-fuels (sorbitol, sucrose and β-glucose) to obtain IGZO thin films [38] or polymer additives [39] has been reported.

As for the case of obtaining IGZO in the form of single nanoparticles, such works are extremely rare [40, 41]. Previously, our team published a series of papers demonstrating that the phase composition and final morphology of the material can be influenced by the choice of complexing agent used in the synthesis. It was found that ethylene glycol, glycerol and tartaric acid are suitable for obtaining IGZO - their use leads to the formation of a powder without any crystallite impurities [42, 43]. The use of many other organic complexing agents (citric and oxalic acid, urea, sucrose, fructose [42], EDTA and ascorbic acid – *unpublished data* of our group) led to the appearance of foreign crystalline impurities (indium oxide) in the final powders.

The aim of this work is synthesis of $InGaZn_2O_5$ using method previously successfully tested (see [43]), and to study the properties of the obtained material.

2. Preparation and characterization method

The following reagents were used in the work: indium nitrate hydrate [$In(NO_3)_3 \cdot xH_2O$ (chemically pure)], gallium nitrate hydrate [$Ga(NO_3)_3 \cdot xH_2O$ (chemically pure)], zinc nitrate hydrate [$Zn(NO_3)_2 \cdot xH_2O$ (chemically pure)] and tartaric acid (analytical grade). All salts were preliminarily determined gravimetrically. The masses of the precursor samples were calculated from the ratio of metal cations In^{3+}:Ga^{3+}:Zn^{2+} = 1:1:2 in the final ternary oxide. Samples were selected using a Joanlab FA2204N analytical balance. An IKA C-MAG HS7 magnetic stirrer with heating was used for stirring and evaporating the solutions of the mixture. The synthesis and thermal treatment of the xerogel obtained by evaporation of the initial mixture was carried out according to the method [44]. The samples were sintered in corundum crucibles at 700 °C and 900 °C for 12 hours. The samples were cooled in the furnace to 200 °C and then in air. The sintering temperatures are reflected in the names of the samples, which are discussed later.

X-ray diffraction (XRD) pattern of IGZO was collected on a Drawell DW-XRD-2700A powder diffractometer (Cu Kα, 40 kV, 30 mA, Ni filter) in the 2θ angle range from 5° to 90° at a rate of 1 deg/min at room temperature. The size and

morphology of the particles were studied using Jeol JSM 7001F scanning electron microscopy (SEM) with accelerating voltage = 20 kV), the distribution of the main elements of the batch was studied using an Oxford X-Max 80 energy dispersive analyzer (EDS method) combined with a SEM. The crystalline structure of the particles was studied by Jeol JSM-2100 transmission electron microscopy (TEM) with accelerating voltage = 160 kV. IR- spectroscopy was performed using a Shimadzu IRAffinity-1S FTIR spectrometer (from 4000 to 400 cm^{-1} in transmission mode). The background calibration was made for pure analytical grade KBr. The material was pressed into a tablet 13 mm in size and 1–1.5 mm thick. The content of indium gallium zinc oxide in the tablet was about 3...5 wt. %. A Shimadzu UV-2700 UV-Vis spectrophotometer was used to record diffuse reflectance spectra in the range from 250 to 800 nm at a recording rate of 1 nm/sec. The background calibration was performed for a pure barium sulfate $BaSO_4$ tablet. The sample was deposited on the barium sulfate tablet. The obtained diffuse reflectance spectra were used to calculate the band gap parameter (Kubelka-Munk transformation was applied under the assumption of a optically allowed direct bandgap).

3. Results and discussion

Fig. 1 shows the XRD patterns of the sample heat-treated at 500 °C, 700 °C and 900 °C. It can be seen from Fig. 1 that the general appearance of the diffraction pattern corresponds to the literature data for $InGaZn_2O_5$ [45, 46]. Over the entire range of sintering temperatures, the sample is single-phase and does not contain any extraneous reflections. Note that sintering at 900 °C is necessary to demonstrate the homogeneity of the material at lower temperatures, since the use of other complexing agents (e.g., urea) can lead to the formation of amorphous agglomerates of impurity phases that remain in the amorphous state up to temperatures of 900 °C [42]. At the same time, we do not exclude the possibility of a chemical reaction occurring at sintering temperatures of 700 and 900 °C if the sample is multiphase at a temperature of 500 °C. This will be discussed in the next section. It is easy to notice that the full width at half maximum of each individual reflex decreases with increasing processing temperature, which can be associated with an increase of crystallinity and grain growth. Thus, the sample obtained at 500 °C is X-ray amorphous, at 700 °C – weakly crystallized, at 900 °C – crystallized.

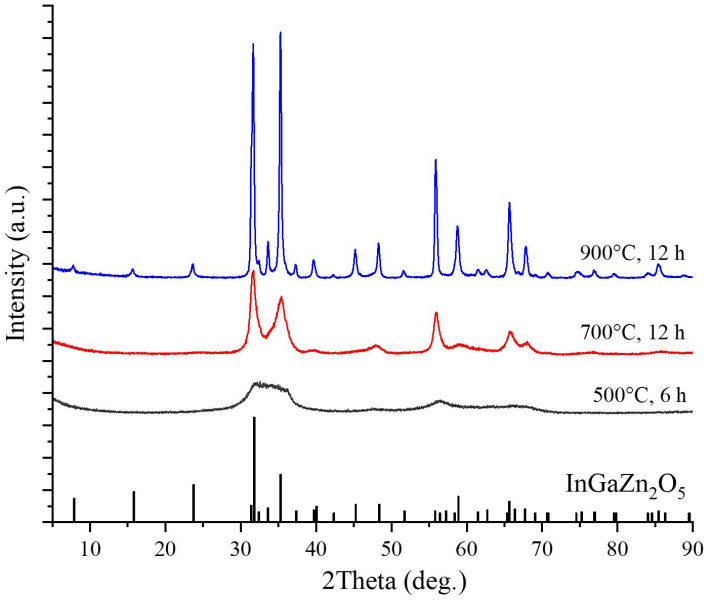

FIG. 1. XRD pattern of the $InGaZn_2O_5$ sample obtained at different temperatures, explanation in the legend

The morphology, size of agglomerates and particles of the $InGaZn_2O_5$ sample subjected to heat treatment at 500 °C for 6 hours were studied by SEM method in secondary electron contrast. In Fig. 1a, at x5000 magnification, particles from less than one to ten micrometres are visible. The shape of the particles is three dimensional, with distinct edges. The structure is non-uniform, with large structural elements and medium and small elements. At higher magnification, in Figs. 2(b-c), particles smaller than 100 nm are visible in the same area of the surface of large agglomerate. The structure of the agglomerate is very dense and uniform and the pores are not visible.

Fig. 3 shows the results of the EDS analysis. The chemical composition does not depend on the heat treatment temperature of the sample and shows a uniform distribution of the elements contained in the ternary oxide. The calculated formula of the compound indicates the proximity of the actual composition to the target, derived from the composition of the batch – $In_{1.01}Ga_{0.96}Zn_{2.03}O_5$. Thus, the chemical composition data are presented within the determined error limits and it can be stated that the sample corresponds to the specified composition.

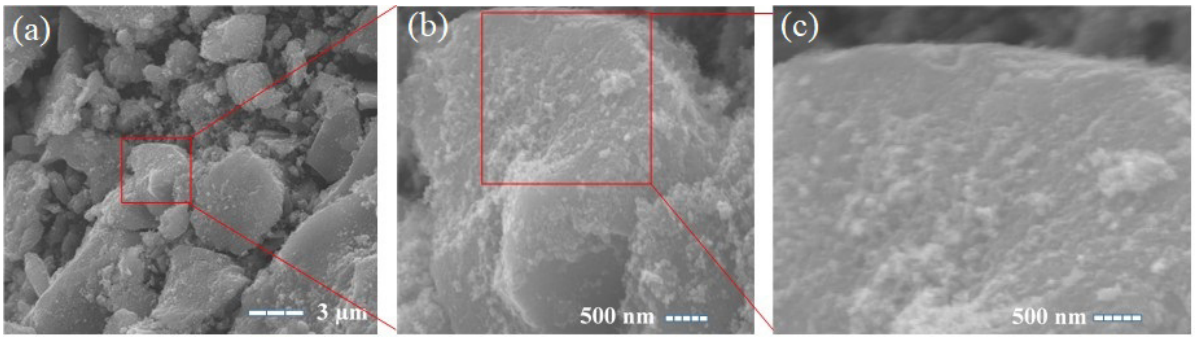

FIG. 2. SEM image of $InGaZn_2O_5$ sample sintered at 500 °C for 6 hours

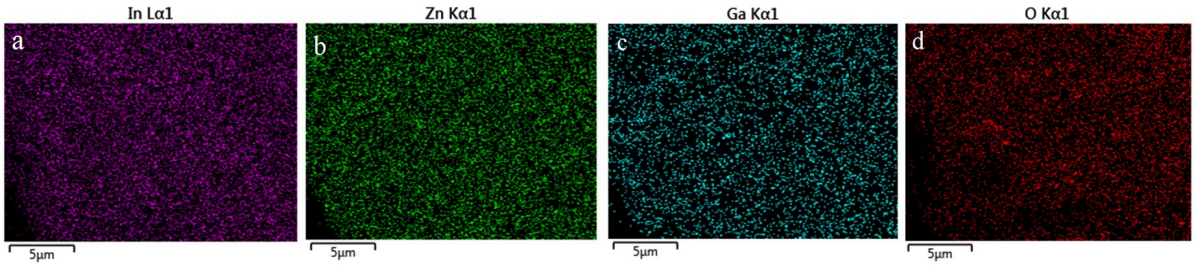

FIG. 3. EDS map of element distribution of In (a), Ga (b), Zn (c) and O (d)

Fig.4 and Fig. 5 show the results of transmission electron microscopy. As can be seen from Fig. 4, the sample is an agglomerate of small (approximately 4–8 nm) spherical-like nanoparticles. On a larger scale, in Fig. 5, it is clear that the particles are crystalline. Thus, it can be stated that a crystalline product is already formed at a temperature of 500 °C, with the degree of crystallinity increasing as the sintering temperature increases (according to X-ray diffraction data). At the same time, the coherent scattering region volume is low in the nanoparticles, so that the $InGaZn_2O_5$ sample sintered at 500 °C is X-ray amorphous.

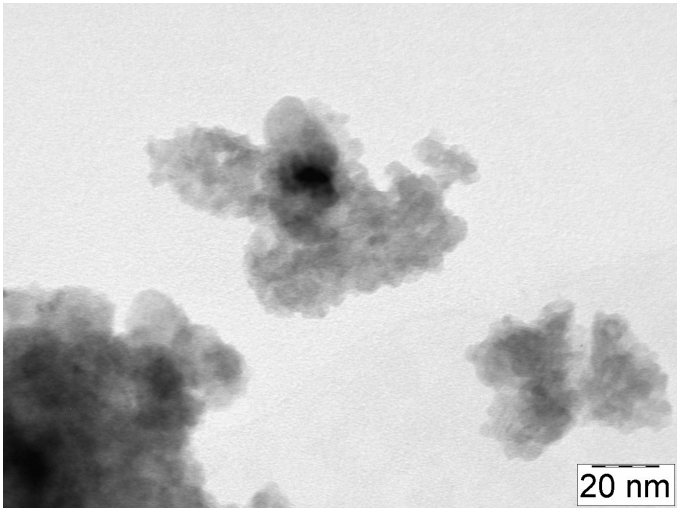

FIG. 4. TEM images of $InGaZn_2O_5$ sintered at 500 °C for 6 hours (low resolution)

The sample sintered at 500 °C was studied by IR-spectroscopy. The data is presented in the form of a detailed text description. A series of wavenumbers were recorded: from 3650 to 3000, 2900, 2700, 2400...2280, 1740...1280, 620, 430 cm^{-1}. A broad absorption peak in the region of 3650 to 3000 cm^{-1} corresponds to the stretching vibrations of the "–OH" bond, which may indicate either the presence of the presence of adsorbed water bound water in the material or the presence of oxyhydroxides in the material. Two low intensity absorption bands were found in the region of 2900 and 2700 cm^{-1}, apparently the region of the stretching vibrations of the "–CH" bond, most likely due to contamination of the samples with ethanol used for sample preparation. Absorption bands of carbon dioxide CO2 were recorded in the region from 2400 to 2280 cm^{-1}. The sample also had an absorption peak in the region of lower wave numbers from

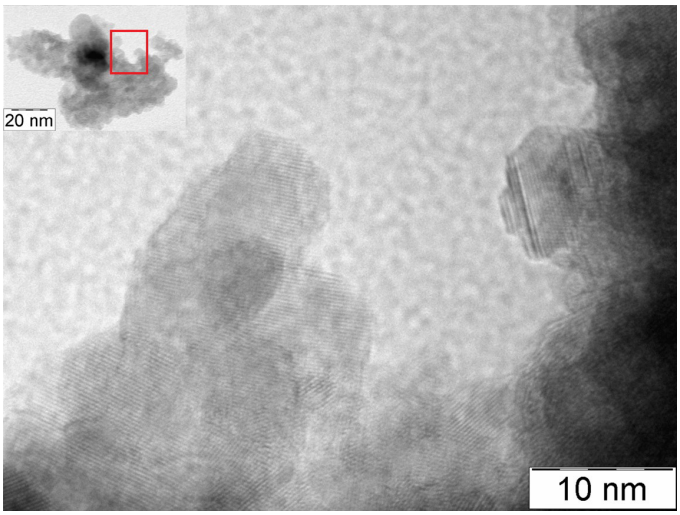

FIG. 5. TEM image of $InGaZn_2O_5$ sintered at 500 °C for 6 hours (high resolution)

1740 to 1280 cm^{-1}, which most likely corresponds to the "–C=O" bond, indicating the presence of tartaric acid oxidation products in the samples, which cannot be removed at a temperature of 500 °C and exposure of 6 hours. Alternatively, this peak may correspond to the "C–C" bond, which may indicate the same thing. The most informative part of the spectrum is the region from 600 to 300 cm^{-1}, as it contains information about the Me–O bonds. In our analysis, the 600 to 400 cm^{-1} region was examined only, due to hardware limitations. In this region, an absorption peak at ≈630 cm^{-1} is observed which can be attributed to the In–O or Ga–O bond. The peak at ≈420 cm^{-1} could not be clearly interpreted.

A diffuse reflectance UV-Vis spectrum was recorded for the sample sintered at 500 °C. As can be seen from the data (Fig. 6), no significant light absorption was detected in the near IR and visible range from 800 to 300 nm. This correlates with the appearance of the sample, which is presented as white powder with yellowish tinge. The data for the UV-Vis diffuse reflectance spectra obtained were used to calculate the optical band gap, which was found to be 3.10 eV, in little disagreement with data from previously published work on the same IGZO composition [47], with the difference about 0.15 eV.

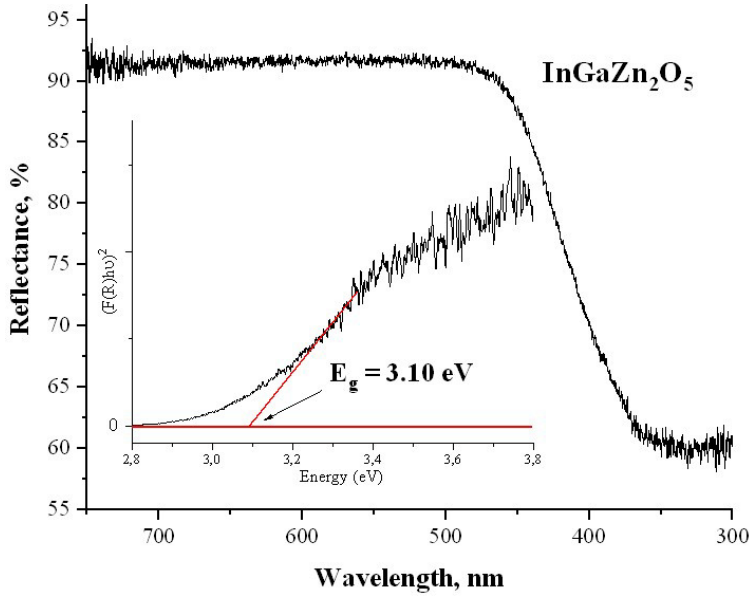

FIG. 6. UV-Vis spectrum and Tauc plot (insert) for determining the optical band gap of $InGaZn_2O_5$

4. Conclusion

The nitrate-tartrate complex decomposition method has been successfully applied to the process of obtaining $InGaZn_2O_5$. The use of tartaric acid as a chelating reagent in nitrate-organic complex decomposition method leads to the formation of a nanocrystalline material at a sintering temperature of 500 °C. Using electron microscopy (SEM and

TEM), it was found that the material sintered at 500 °C is an agglomerate of nanoparticles, the morphology of individual nanoparticles being close to spherical. As the sintering temperature increases, the degree of crystallinity of the material increases, at 900 °C the material is well crystallized according to the XRD data. The distribution of the main elements in the material is homogeneous according to EDS data. The IR-spectrum confirms the presence of Me–O bonds in the material. The band gap for the $InGaZn_2O_5$ sample sintered at 500 °C is 3.10 eV.

References

[1] Zhang Z., Zou R., Yu L., Hu J. Recent research on one-dimensional silicon-based semiconductor nanomaterials: Synthesis, structures, properties and applications. *Crit. Rev. Solid State Mater. Sci.*, 2011, **36**(3), P. 148–173.

[2] Balaghi L., Shan S., Fotev I., Moebus F., Rana R., Venanzi T., Hübner R., Mikolajick T., Schneider H., Helm M., Pashkin A., Dimakis E. High electron mobility in strained GaAs nanowires. *Nat. Commun.*, 2021, **12**, P. 6642.

[3] Khan M.A.H., Rao M.V. Gallium Nitride (GaN) Nanostructures and their gas sensing properties: A review. *Sensors.*, 2020, 20(14), P. 3889.

[4] Potts H., Morgan N.P., Tutuncuoglu G., Friedl M., Morral A.F.i. Tuning growth direction of catalyst-free InAs(Sb) nanowires with indium droplets. *Nanotechnology*., 2017, 28(5), P. 054001.

[5] Li X., Zhu H. Two-dimensional MoS2: Properties, preparation, and applications. *J. Materiomics.*, 2015, 1(1), P. 33–44.

[6] Patoary N.H., Xie J., Zhou G., Mamun F.Al., Sayyad M., Tongay S., Esqueda I.S. Improvements in 2D p-type WSe2 transistors towards ultimate CMOS scaling. *Sci. Rep.*, 2023, **13**, P. 3304.

[7] Yu Z., Perera I.R., Daeneke T., Makuta S., Tachibana Y., Jasieniak J.J., Mishra A., Bäuerle P., Spiccia L., Bach U. Indium tin oxide as a semiconductor material in efficient p-type dye-sensitized solar cells. *NPG Asia Mater.*, 2016, **8**(8), P. e305–e305.

[8] Cheng C.-H., Tsay C.-Y., Flexible a-IZO thin film transistors fabricated by solution processes. *J. Alloys Compd.*, 2010, **507**(1), P. L1–L3.

[9] Bastola A., He Y., Im J., Rivers G., Wang F., Worsley R., Austin J.S., Nelson-Dummett O., Wildman R.D., Hague R., Tuck C.J., Turyanska L. Formulation of functional materials for inkjet printing: A pathway towards fully 3D printed electronics. *Mater. Today Electron.*, 2023, **6**, P. 100058.

[10] Kaçar R., Serin R.B., Uçar E., Ülkü A. A review of high-end display technologies focusing on inkjet printed manufacturing. Mater. *Today Commun.*, 2023, **35**, P. 105534.

[11] Bhatti G., Agrawal Y., Palaparthy V., Kavicharan M., Agrawal M. Chapter 13 - Flexible Electronics: A Critical Review. In: Agrawal Y., Mummaneni K., Sathyakam P.U., editors. Interconnect Technologies for Integrated Circuits and Flexible Electronics. Springer Tracts in Electrical and Electronics Engineering. Springer, Singapore. 2024, P. 221–248.

[12] Bi S., Gao B., Han X., He Z.R., Metts J., Jiang C.M., Asare-Yeboah K. Recent progress in printing flexible electronics: A review. *Sci. China Technol. Sci.*, 2024, **67**(8), P. 2363–2386.

[13] Samanta S., Han K., Sun C., Wang C., Thean A.V.-Y., Gong X. Amorphous IGZO TFTs Featuring Extremely-Scaled Channel Thickness and 38 nm Channel Length: Achieving Record High Gm,max of 125 μS/μm at VDS of 1 V and ION of 350 μA/μm. In Proc. IEEE Symp. VLSI Technol., 2020, P. 1–2.

[14] Yin X., Ji X., Liu W., Li X., Wang M., Xin Q., Zhang J., Yan Z., Song A. Electrolyte-gated amorphous IGZO transistors with extended gates for prostate-specific antigen detection. *Lab. Chip.*, 2024, **24**, P. 3284–3293.

[15] Sheng J., Hong T., Lee H.-M., Kim K., Sasase M., Kim J., Hosono H., Park J.-S. Amorphous IGZO TFT with High Mobility of $\sim$70 cm2/(V s) via Vertical Dimension Control Using PEALD. ACS Appl. Mater. Interfaces., 2019, **11**(43), P. 40300–40309.

[16] Han Y., Lee D.H., Cho E.-S., Kwon S.J., Yoo H. Argon and Oxygen Gas Flow Rate Dependency of Sputtering-Based Indium-Gallium-Zinc Oxide Thin-Film Transistors. Micromachines, 2023, **14**(7), P. 1394.

[17] Nomura K., Ohta H., Takagi A., Kamiya T., Hirano M., Hosono H. Room-temperature fabrication of transparent flexible thin-film transistors using amorphous oxide semiconductors. *Nature*, 2004, **432**(7016), P. 488–492.

[18] Wager J.F., Yeh B., Hoffman R.L., Keszler D.A. An amorphous oxide semiconductor thin-film transistor route to oxide electronics. *Curr. Opin. Solid State Mater. Sci.*, 2014, **18**(2), P. 53–61.

[19] Chiang H.Q., Wager J.F., Hoffman R.L., Jeong J., Keszler D.A. High mobility transparent thin-film transistors with amorphous zinc tin oxide channel layer. *Appl. Phys. Lett.*, 2004, **86**(1), P. 13503.

[20] Venkateshvaran D., Nikolka M., Sadhanala A., Lemaur V., Zelazny M., Kepa M., Hurhangee M., Kronemeijer A.J., Pecunia V., Nasrallah I., Romanov I., Broch K., McCulloch I., Emin D., Olivier Y., Cornil J., Beljonne D., Sirringhaus H. Approaching disorder-free transport in high-mobility conjugated polymers. *Nature*, 2014, **515**(7527), P. 384–388.

[21] Fukuda K., Takeda Y., Yoshimura Y., Shiwaku R., Tran L.T., Sekine T., Mizukami M., Kumaki D., Tokito S. Fully-printed high-performance organic thin-film transistors and circuitry on one-micron-thick polymer films. *Nat. Commun.*, 2014, **5**(1), P. 4147.

[22] Giri G., DeLongchamp D.M., Reinspach J., Fischer D.A., Richter L.J., Xu J., Benight S., Ayzner A., He M., Fang L., Xue G., Toney M.F., Bao Z. Effect of solution shearing method on packing and disorder of organic semiconductor polymers. *Chem. Mater.*, 2015, **27**(7), P. 2350–2359.

[23] Yan H., Chen Z., Zheng Y., Newman C., Quinn J.R., Dötz F., Kastler M., Facchetti A. A high-mobility electron-transporting polymer for printed transistors. *Nature*, 2009, **457**(7230), P. 679–686.

[24] Takeda Y., Yoshimura Y., Shiwaku R., Hayasaka K., Sekine T., Okamoto T., Matsui H., Kumaki D., Katayama Y., Tokito S. Organic complementary inverter circuits fabricated with reverse offset printing. *Adv. Electron. Mater.*, 2018, **4**(1), P. 1700313.

[25] Shiwaku R., Takeda Y., Fukuda T., Fukuda K., Matsui H., Kumaki D., Tokito S. Printed 2 V-operating organic inverter arrays employing a small-molecule/polymer blend, Sci. Rep., 2016, **6**(1), P. 34723.

[26] Minemawari H., Yamada T., Matsui H., Tsutsumi J., Haas S., Chiba R., Kumai R., Hasegawa T. Inkjet printing of single-crystal films. *Nature*, 2011, **475**(7356), P. 364–367.

[27] Zhang W., Smith J., Watkins S.E., Gysel R., McGehee M., Salleo A., Kirkpatrick J., Ashraf S., Anthopoulos T., Heeney M., McCulloch I. Indacenodithiophene semiconducting polymers for high-performance, air-stable transistors. *J. Am. Chem. Soc.*, 2010, **132**(33), P. 11437–11439.

[28] Zeng H., Rice P.M., Wang S.X., Sun S. Shape-controlled synthesis and shape-induced texture of MnFe2O4 nanoparticles. *J. Am. Chem. Soc.*, 2004, **126**(37), P. 11458–11459.

[29] Sun S., Zeng H., Robinson D.B Raoux S., Rice P.M., Wang S.X., Li G. Monodisperse MFe_2O_4 (M=Fe, Co, Mn) Nanoparticles. *J. Am. Chem. Soc.*, 2004, **126**(1), P. 273–279.

[30] Vinnik, D.A., Kovalev, A.I., Sherstyuk, D., Zhivulin, D.E., Zirnik, G.M., Batmanova T. Development of a scalable method for synthesizing a promising oxide material for electronics In-Ga-Zn-O, RusMetal, 2024.

[31] Yoon S., Kim S.J., Tak Y.J., Kim H.J. A solution-processed quaternary oxide system obtained at low-temperature using a vertical diffusion technique. *Sci. Rep.*, 2017, **7**(1), P. 43216.

[32] Sanctis S., Hoffmann R.C., Koslowski N., Foro S., Bruns M., Schneider J.J. Aqueous Solution Processing of Combustible Precursor Compounds into Amorphous Indium Gallium Zinc Oxide (IGZO) Semiconductors for Thin Film Transistor Applications. *Chem. Asian J.*, 2018, **13**(24), P. 3912–3919.
[33] Xie Y., Wang D., Fong H.H. High-Performance Solution-Processed Amorphous InGaZnO Thin Film Transistors with a Metal–Organic Decomposition Method. *J. Nanomater.*, 2018, **2018**, P. 7423469.
[34] Chen Y., Wang B., Huang W., Zhang X., Wang G., Leonardi M.J., Huang Y., Lu Z., Marks T.J., Facchetti A. Nitroacetylacetone as a Cofuel for the Combustion Synthesis of High-Performance Indium–Gallium–Zinc Oxide Transistors. *Chem. Mater.*, 2018, **30**(10), P. 3323–3329.
[35] Wang B., Yu X., Guo P., Huang W., Zeng L., Zhou N., Chi L., Bedzyk M.J., Chang R.P.H., Marks T.J., Facchetti A. Solution-Processed All-Oxide Transparent High-Performance Transistors Fabricated by Spray-Combustion Synthesis. *Adv. Electron. Mater.*, 2016, **2**(4), P. 1500427.
[36] Kim M.-G., Kanatzidis M.G., Facchetti A., Marks T.J. Low-temperature fabrication of high-performance metal oxide thin-film electronics via combustion processing. Nat. Mater., 2011, **10**(5), P. 382–388.
[37] Hennek J.W., Kim M.-G.,, Kanatzidis M.G., Facchetti A., Marks T.J. Exploratory Combustion Synthesis: Amorphous Indium Yttrium Oxide for Thin-Film Transistors. *J. Am. Chem. Soc.*, 2012, **134**(23), P. 9593–9596.
[38] Wang B., Zeng L., Huang W., Melkonyan F.S., Sheets W.C., Chi L., Bedzyk M.J., Marks T.J., Facchetti A. Carbohydrate-Assisted Combustion Synthesis To Realize High-Performance Oxide Transistors. *J. Am. Chem. Soc.*, 2016, **138**(22), P. 7067–7074.
[39] Wang B., Huang W., Bedzyk M.J., Dravid V.P., Hu Y.Y., Marks T.J., Facchetti A. Combustion Synthesis and Polymer Doping of Metal Oxides for High-Performance Electronic Circuitry. *Acc. Chem. Res.*, 2022, **55**(3), P. 429–441.
[40] Fukuda N., Watanabe Y., Uemura S., Yoshida Y., Nakamura T., Ushijima H. In–Ga–Zn oxide nanoparticles acting as an oxide semiconductor material synthesized via a coprecipitation-based method. *J. Mater. Chem. C.*, 2014, **2**(13), P. 2448–2454.
[41] Wu M.-C., Hsiao K.-C., Lu H.-C. Synthesis of InGaZnO4 nanoparticles using low temperature multistep co-precipitation method. *Mater. Chem. Phys.*, 2015, **162**, P. 386–391.
[42] Zirnik G.M., Chernukha A.S., Uchaev D.A., Solizoda I.A., Gudkova S.A., Nekorysnova N.S., Vinnik D.A. Phase formation of nanosized InGaZnO4 obtained by the sol-gel method with different chelating agents. *Nanosyst. Physics, Chem. Math.*, 2024, **15**(4), P. 520–529.
[43] Zirnik G.M., Sozykin S.A., Uchaev D.A., Chernukha A.S., Solizoda I.A., Gudkova S.A., Vinnik D.A. Preparation and synthesis of polycrystalline InGaZnO4 via tartaric acid mediated sol-gel method. Russ. Metall, 2024.
[44] Zirnik G.M., Sozykin S.A., Chernukha A.S., Solizoda I.A., Gudkova S.A., Vinnik D.A. Indium gallium zinc oxide: Effect of complexing agent on structure. *Journal of Structural Chemistry*, 65(2024), P. 133998.
[45] Tien T.-C., Wu J.-S., Hsieh T.-E., Wu H.-J. The Fabrication of Indium–Gallium–Zinc Oxide Sputtering Targets with Various Gallium Contents and Their Applications to Top-Gate Thin-Film Transistors. *Coatings.*, 2022, **12**(8), P. 1217.
[46] Kimizuka N., Mohri T., Matsui Y., Siratori K. Homologous compounds, InFeO3(ZnO)m (m=1–9). *J. Solid State Chem.*, 1988, **74**(1), P. 98–109.
[47] Préaud S., Byl C., Brisset F., Berardan D. SPS-assisted synthesis of InGaO3(ZnO) ceramics, and influence of m on the band gap and the thermal conductivity. *J. Am. Ceram. Soc.*, 2020, **103**(5), P. 3030–3038.

Submitted 14 October 2024; accepted 11 February 2025

Information about the authors:

Gelena M. Boleiko – Moscow Institute of Physics and Technology Institutsky lane, 9, Dolgoprudny, 141701, Russia; ORCID 0009-0003-3438-5893; boleiko.gm@mipt.ru

Gleb M. Zirnik – Moscow Institute of Physics and Technology Institutsky lane, 9, Dolgoprudny, 141701, Russia; ORCID 0009-0008-4546-1368; glebanaz@mail.ru

Andrey I. Kovalev – Moscow Institute of Physics and Technology Institutsky lane, 9, Dolgoprudny, 141701, Russia; South Ural State University, Lenin Av., 76, Chelyabinsk, 454080, Russia; ORCID 0009-0003-4773-1687; asp23kai165@susu.ru

Daniil A. Uchaev – South Ural State University, Lenin Av., 76, Chelyabinsk, 454080, Russia; ORCID 0000-0002-8623-4769; uchaevda@susu.ac.ru

Ibrohimi A. Solizoda – Moscow Institute of Physics and Technology Institutsky lane, 9, Dolgoprudny, 141701, Russia; St. Petersburg State University Universitetskaya embankment, 7-9, 199034, St. Petersburg; Tajik National University Rudaki Av., 17, Dushanbe, 734025, Tajikistan; ORCID 0000-0001-6973-4633; solizoda.ia@mipt.ru

Alexander S. Chernukha – Moscow Institute of Physics and Technology Institutsky lane, 9, Dolgoprudny, 141701, Russia; South Ural State University, Lenin Av., 76, Chelyabinsk, 454080, Russia; ORCID 0000-0002-1272-1628; chernukha.as@mipt.ru

Svetlana A. Gudkova – Moscow Institute of Physics and Technology Institutsky lane, 9, Dolgoprudny, 141701, Russia; St. Petersburg State University Universitetskaya embankment, 7-9, 199034, St. Petersburg; ORCID 0000-0002-3028-947X; svetlanagudkova@yandex.ru

Denis A. Vinnik – Moscow Institute of Physics and Technology Institutsky lane, 9, Dolgoprudny, 141701, Russia; South Ural State University, Lenin Av., 76, Chelyabinsk, 454080, Russia; St. Petersburg State University Universitetskaya embankment, 7-9, 199034, St. Petersburg; ORCID 0000-0002-5190-9834; vinnik.da@mipt.ru

Conflict of interest: the authors declare no conflict of interest.

NANOSYSTEMS:
PHYSICS, CHEMISTRY, MATHEMATICS

Original article

Kapishnikov A.V., Gerasimov E.Yu. *Nanosystems: Phys. Chem. Math.*, 2025, **16** (1), 51–57.
http://nanojournal.ifmo.ru
DOI 10.17586/2220-8054-2025-16-1-51-57

Phase transformations in perovskites $La_{0.6}Ca_{0.4}Mn_{1-y}Co_yO_{3\pm\delta}$ under the action of hydrogen

Alexander V. Kapishnikov, Evgeny Yu. Gerasimov

Boreskov Institute of Catalysis SB RAS, Novosibirsk, Russia

Corresponding author: E. Yu. Gerasimov, gerasimov@catalysis.ru

PACS 81.30.Bx

ABSTRACT The structural and phase transformations of $La_{0.6}Ca_{0.4}Mn_{1-y}Co_yO_{3\pm\delta}$ ($y = 0.2 - 0.6$) solid solutions in a reducing atmosphere were studied using in situ XRD and HRTEM methods. Experiments have shown that heat treatment in a reducing atmosphere of H_2 leads to the partial decomposition of solid solutions, the nature of which differs from decomposition in an inert atmosphere. In the case of a system with a hydrogen-containing atmosphere, the heterogeneous reduction of the structure leads to the formation of an orthorhombic phase of $LaMnO_3$-based perovskite with disordered vacancies, an additional phase of ordered Rudlesden–Popper-type perovskite based on La_2CoO_4 and Co and Ca_2MnO_4 nanoparticles on the surface of perovskite. In an environment with excessive partial oxygen pressure for the reduced sample, the reverse phase transition of the Rudlesden–Popper phase into the perovskite phase occurs.

KEYWORDS Rudlesden–Popper-type perovskite, hydrogen reduction, lanthanum manganite, in situ XRD, phase transition

ACKNOWLEDGEMENTS This study was supported by Russian Science Foundation, project No. 23-23-00535. XRD and HRTEM measurements were performed using the equipment of the Shared Research Center "National Center of Investigation of Catalysts" at the Boreskov Institute of Catalysis Siberian Branch, Russian Academy of Sciences.

FOR CITATION Kapishnikov A.V., Gerasimov E.Yu. Phase transformations in perovskites $La_{0.6}Ca_{0.4}Mn_{1-y}Co_yO_{3\pm\delta}$ under the action of hydrogen. *Nanosystems: Phys. Chem. Math.*, 2025, **16** (1), 51–57.

1. Introduction

Complex oxides with a perovskite structure have great potential for the synthesis and research of new compounds of this type, due to their structural flexibility [1–3]. They are widely used as catalysts for various reactions, in particular, reactions of high-temperature oxidation of hydrocarbons [4–6], decomposition of nitrogen oxides [7–9], in the processes of photocatalytic production of hydrogen [10–12] or the disposal of antibiotics in wastewater [13, 14]. In many ways, these properties are provided by structural features, in particular, the presence and distribution of cationic and anionic vacancies [15, 16]. The most common method of influencing the perovskite structure is to obtain solid solutions by replacing part of the cations with a lower charge state [17,18]. This leads to a decrease in the energy of vacancy formation, an increase in the level of nonstoichiometry [19, 20] and, as a result, to an increase in the activity of catalysts in oxidation reactions [21, 22].

Another way to create the required level of nonstoichiometry may be heat treatment of a complex oxide under reducing conditions. In the presence of cations of variable valence [23, 24], a decrease in the degrees of oxidation (as a rule, in the B-sublattice) will lead to irreversible removal of lattice oxygen and the formation of vacancies. The initial structure during these processes can either be preserved, undergoing minor changes in structural parameters [25], or be partially destroyed [26] with the formation of new phases. In this case, nanoparticles of new phases can form on the surface of perovskite-like oxides, which also affect their catalytic activity [27]. Thus, the catalytic activity of perovskites can increase simultaneously due to an increase in the level of nonstoichiometry in the structure and mobility of lattice oxygen, as well as due to the formation of a "carrier-active component" type system on the surface with partial decomposition of the initial phase. On the other hand, additional temperature exposure in a reducing atmosphere can lead to partial decomposition of solid solutions and can lead to negative consequences, in particular, to a decreasing of catalytic activity.

In this regard, studies of phase transformations of mixed oxides (for example, La–Ca–Mn–Co–O) are of interest for understanding their mechanisms and possibilities of controlling the reduction process to obtain more active systems or to search for optimal conditions for impact on initial solid solutions.

© Kapishnikov A.V., Gerasimov E.Yu., 2025

2. Experimental section

$La_{0.6}Ca_{0.4}Mn_{1-y}Co_yO_3$ sample was synthesized by the polymerizable precursor method. Appropriate amounts of crystal hydrates of salts, including $La(NO_3)_3 \cdot 6H_2O$ (ZRM, > 99 %), $Ca(NO_3)_2 \cdot 4H_2O$ (Merck, > 99 %), $Mn(NO_3)_2 \cdot 4H_2O$ (Merck, > 99 %), $Co(NO_3)_2 \cdot 6H_2O$ (Merck, > 99 %), citric acid (ChimProm, > 99.5 %), ethylene glycol (ChimProm, > 99.5 %), and distilled water were mixed. An aqueous solution with appropriate cation ratio La:Ca:Mn:Co was prepared. The resulting reagent was evaporated at 70 – 80 °C until the formation of a resinous polymer. The precursor was calcined at 800 °C for four hours with a rise in temperature of 100 °C/h.

The microstructure of the photocatalysts was studied by HRTEM using a ThemisZ electron microscope (Thermo Fisher Scientific, Waltham, MA, USA) at an accelerating voltage of 200 kV. The microscope was equipped with a SuperX energy-dispersive spectrometer and a spherical aberration corrector. The maximum resolution of the microscope was 0.06 nm. For the HRTEM analysis, the samples were ultrasonically dispersed onto perforated carbon substrates attached to copper grids.

XRD patterns were obtained on a Bruker AXS D8 Advance diffractometer (Karlsruhe, Germany) equipped with a high temperature, supply of various gas mixtures, the use of CuKα radiation in scanning with a step of $2\theta = 0.05^\circ$ point by point, and an ac-cumulation time of 3 s at each point in a range of the angles $2\theta = 15 - 75^\circ$. Temperature measurements were performed according to the following conditions: temperature rate of 10 °C/min with 30 % H_2 + 70 % He flow and a mixture rate of 40 mL/min. Dif-fractograms were obtained at temperatures of 30, 300, 450, 600 and 750 °C. The crystallite sizes and chemical compositions were calculated in the X'Pert HighScore Plus (PANalytical B.V., Almelo, The Netherlands) software. The calculation and refinement of lattice parameters were performed in the IK (BIC SB RAN, Novosibirsk, Russia) software by the method of least squares.

Thermal analysis of the sample was performed using a synchronous thermal analysis device, STA 449C Jupiter (NETZSCH, Selb, Germany). This device combines the methods of differential thermal analysis (DTA) and thermogravimetric analysis (TGA) into one dimension. The weight of the sample was approximately 100 mg. The furnace temperature was increased from 40 to 900 °C at a rate of 10 °C/min with He flux of 30 mL/min. The sample weight was monitored continuously as a function of temperature.

3. Results and discussions

The samples of the $La_{0.6}Ca_{0.4}Mn_{1-y}Co_yO_{3\pm\delta}$ series, ($y = 0.2 - 0.6$) synthesized by the Pechini method, according to XRD, are well-crystallized solid solutions having ortho-rhombic symmetry with s.g. Pnma (see Fig. 1a). The volume of the unit cell of complex oxides varied from 224 to 227 Å^3 (see Table 1). With an increase in the degree of cobalt substitution, the volume of the unit cell showed a slight decrease, which can be explained by lower values of the radii of Co^{3+} cations (0.59 ± 0.05 Å for Co^{3+} and 0.62 ± 0.02 Å for Mn^{3+}), the number of which presumably increases with a growth in the pro-portion of cobalt in the solid solution. The electroneutrality in the structure is mainly provided by the formation of oxygen vacancies and Mn4+ cations, which has already been shown for $La_{1-x}Ca_xMnO_{3\pm\delta}$ [28], although the formation of Co^{2+} cations is also allowed, as in $LaMn_{1-y}Co_yO_{3\pm\delta}$ [29].

TABLE 1. Unit cell parameters of $La_{0.6}Ca_{0.4}Mn_{1-y}Co_yO_{3\pm\delta}$ in initial state

Sample	V, Å^3	D, Å	ε	S, m^2/g
$La_{0.6}Ca_{0.4}Mn_{0.8}Co_{0.2}O_3$	227.37	590	0.0017	7.7
$La_{0.6}Ca_{0.4}Mn_{0.7}Co_{0.3}O_3$	226.64	437	0.001	9.5
$La_{0.6}Ca_{0.4}Mn_{0.6}Co_{0.4}O_3$	225.69	470	0.003	11.5
$La_{0.6}Ca_{0.4}Mn_{0.5}Co_{0.5}O_3$	224.71	380	0.0035	11.8
$La_{0.6}Ca_{0.4}Mn_{0.4}Co_{0.6}O_3$	224.33	433	0.0026	13.7

According to XRD data, the particles of solid solutions consist of crystallites with sizes of 20 – 30 nm (see Table 1), correlating with the particle size, according to the HRTEM data, the average particle size is 40 – 50 nm (Fig. 1b). Based on calculations, the micro-distortion parameter increases slightly in samples with a high content of Co cations. The specific surface area increases with the cobalt content and correlates with a decrease in the size of crystallites and particles, respectively (Table 1). The performed mapping of chemical elements did not show significant deviations from the chemical composition (Fig. 1c). A more detailed study by the HRTEM method showed that the samples of this series are well crystallized and have a perovskite structure in orthorhombic modification (Fig. 1d).

In situ XRD experiments in hydrogen containing atmosphere have shown that partial decomposition is characteristic for perovskite-like oxides of these compositions, and the effect of a reducing medium leads to a decomposition mechanism different from that observed in an only He medium [26]. $La_{0.6}Ca_{0.4}Mn_{1-x}Co_xO_3$ samples similarly to

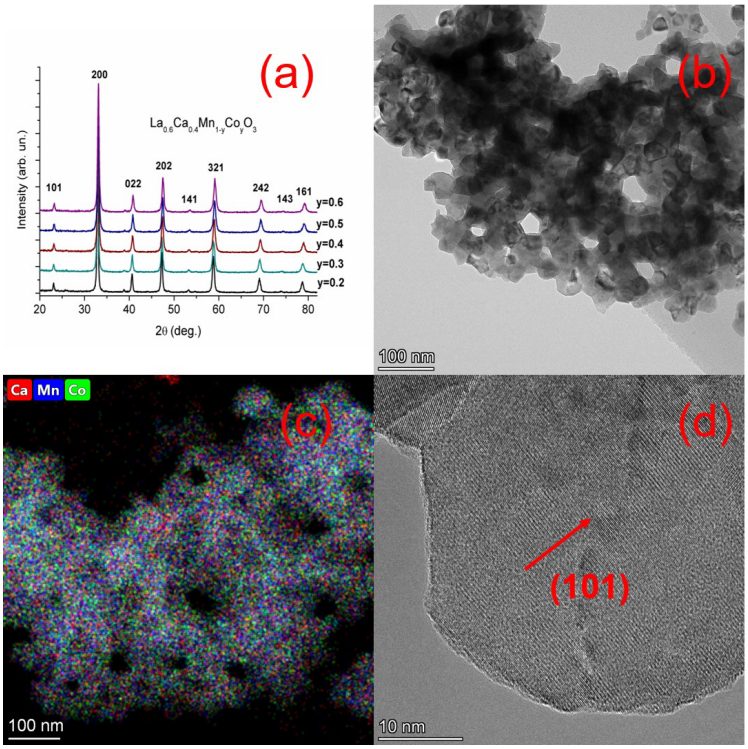

FIG. 1. XRD patterns of $La_{0.6}Ca_{0.4}Mn_{1-y}Co_yO_{3\pm\delta}$ in initial state (a). HRTEM images of sample morphology (b) and microstructure (c), EDX mapping for $La_{0.6}Ca_{0.4}Mn_{0.5}Co_{0.5}O_3$ sample (d)

$La_{0.5}Ca_{0.5}Mn_{0.5}Co_{0.5}O_3$ release lattice oxygen when heated to 600 °C in a helium environment, which leads to a visible increase in the cell parameters. Further heating to 750 °C leads to the decomposition of the complex oxide with the formation of CaO and CoO particles on the surface of the perovskite (Fig. 2a). At the same time, the structure of the perovskite type is quite stable with minor changes in chemical composition. The size of the crystallites also does not change significantly and remains around the same values (about 55 nm for $La_{0.6}Ca_{0.4}Mn_{0.8}Co_{0.2}O_3$).

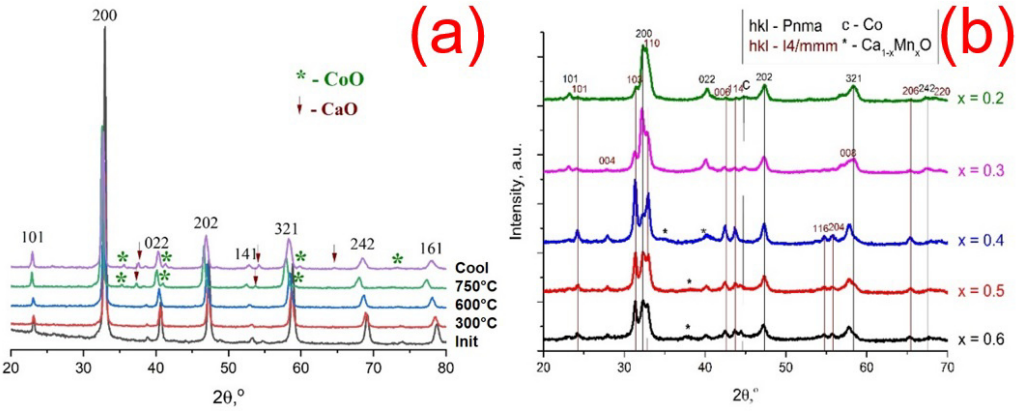

FIG. 2. In situ XRD patterns of $La_{0.6}Ca_{0.4}Mn_{0.8}Co_{0.2}O_3$ in He atmosphere (a), XRD patterns of $La_{0.6}Ca_{0.4}Mn_{1-y}Co_yO_3$ after treatments in hydrogen containing atmosphere (b)

At the same time, strong asymmetric broadenings of the perovskite phase reflexes are observed in the hydrogen medium (Fig. 2b), further splitting of which occurs at 550 – 600 °C. The phase composition of the system most likely includes perovskite-like solid solutions of orthorhombic symmetry, with different chemical compositions and, as a result, unit cell parameters. The differences in composition are primarily due to different oxygen content, while the formation of cobalt nanoparticles on the surface (S.g. Fm3m, PDF No. 15-806), as well as Ca_2MnO_4 (PDF No. 78-1031) and CaO (PDF No. 37-1497) shows that changes occur in the cationic sublattices. At 600 °C, the transformation of part of the initial solid solution into the phase of ordered perovskite (Raddlesden–Popper) of tetragonal symmetry (structural type La_2CoO_4, s.g. I4/mmm, PDF No. 34-1081) is also observed.

For the sample with the highest content of Mn cations – $La_{0.6}Ca_{0.4}Mn_{0.8}Co_{0.2}O_3$, a similar transformation is also observed, although it is expressed to a lesser extent (Fig. 2a). With a decrease in the proportion of manganese cations in the structure to 0.6 – 0.4, the intensity of the peaks of the ordered perovskite phase increases significantly and it becomes larger, which makes it possible to make conclusion about the key role of cobalt in this transformation. An increase in the cobalt content in the solid solution also reduces the temperature at which structural transformations begin: for example, in the case of $La_{0.6}Ca_{0.4}Mn_{0.4}Co_{0.6}O_3$ decomposition begins at 450 °C (Fig. 3a), while for $La_{0.6}Ca_{0.4}Mn_{0.6}Co_{0.4}O_3$ the process does not begin earlier than 550 °C (see Fig. 3b) for $La_{0.6}Ca_{0.4}Mn_{0.5}Co_{0.5}O_3$ it begins at 500 °C and for $La_{0.6}Ca_{0.4}Mn_{0.8}Co_{0.2}O_3$ – 600 °C.

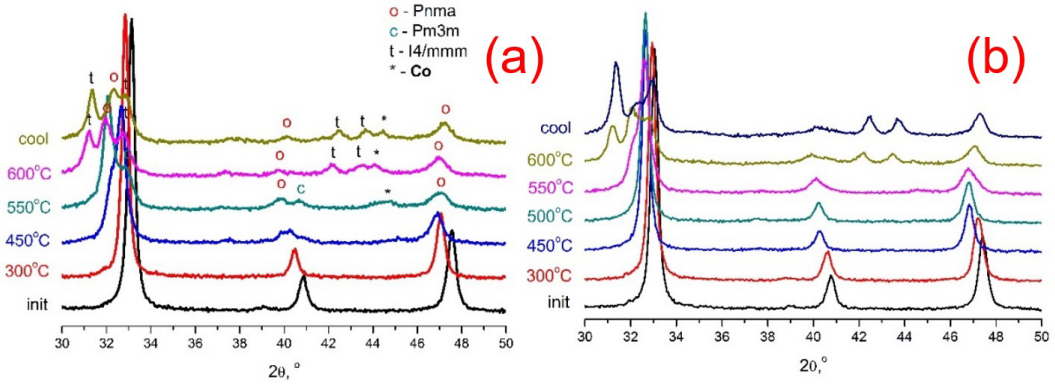

FIG. 3. In situ XRD patterns obtained in hydrogen containing atmosphere $La_{0.6}Ca_{0.4}Mn_{0.4}Co_{0.6}O_3$ (a) and $La_{0.6}Ca_{0.4}Mn_{0.6}Co_{0.4}O_3$ (b)

Table 2 shows the parameters of the unit cell (in the form of reduced volumes, for clarity) before and after heat treatment in a reducing medium. The parameters for one of the phases after reducing are closer to the initial values, which allows us to assert the heterogeneous layered nature of reducing medium. For the forming phase of an ordered perovskite, the cell parameter is slightly less than that for La_2CoO_4. Apparently, this is due to the formation of a solid solution, with the assumed composition of $La_{2-x}Ca_xCoO_{4-\delta}$. The difference of 1 Å^3 allows us to assert that the proportion of calcium in it is relatively small, however, the presence of manganese cations in it is not excluded, which increase the volume of the cell, and therefore it is difficult to judge the exact ratio of calcium in the structure. For the second phase based on perovskite, the parameters are close to those for $La_{0.85}Ca_{0.15}MnO_3$.

TABLE 2. The reduced volume of the unit cell of the initial and reduced samples

Sample	$V/Z_{\text{init.}}$, Å^3	$V/Z_{\text{tetr.}}$, Å^3	$V/Z_{\text{ort.}}$, Å^3
$La_{0.6}Ca_{0.4}Mn_{0.8}Co_{0.2}O_3$	56.84	94.42	58.04
$La_{0.6}Ca_{0.4}Mn_{0.7}Co_{0.3}O_3$	56.66	94.39	58.12
$La_{0.6}Ca_{0.4}Mn_{0.6}Co_{0.4}O_3$	56.34	94.36	59.33
$La_{0.6}Ca_{0.4}Mn_{0.5}Co_{0.5}O_3$	56.12	94.26	59.40
$La_{0.6}Ca_{0.4}Mn_{0.4}Co_{0.6}O_3$	55.93	94.50	59.79

Apparently, the observed change in the structure of perovskite occurs due to the reduction of cobalt and manganese cations, in particular, one of the key transformations here is $Co^{3+} \rightarrow Co^{2+}$. On the surface, under the influence of the medium, these cations are further reduced to a metallic state and migrate to the surface, forming surface defects and thereby promoting the process of H_2 diffusion and reduction of the complex oxide. Taking into account the XRD data and the possible heterogeneity of perovskite recovery, the phase of ordered perovskite based on La_2CoO_4 is located mainly in the near-surface layers of particles, since it is characterized by a high content of Co^{2+} in its composition, while the phase of disordered perovskite is located closer to the center of the particles.

At the same time, this process demonstrates partial reversibility in the case of repeated heat treatment in an oxygen-containing atmosphere, as previously shown [27]. A similar behaviour was shown by the $La_{0.6}Ca_{0.4}Mn_{1-y}Co_yO_3$ systems: for the phases, a decrease in cell parameters and an overlap of reflexes were observed, and only the perovskite phase with orthorhombic symmetry was observed relatively reliably in the phase composition, the volume of the cell of which was 2 – 3 Å^3 larger than the volume of the initial phase (see Table 2). The process of restoring the structure is mainly associated with the return of oxygen to the structure of the complex oxide, which is reflected in the thermogravimetry

curves (Fig. 4a). This process is also clearly visible on the diffractograms of the initial sample $La_{0.6}Ca_{0.4}Mn_{0.4}Co_{0.6}O_3$ in comparison with reduced in hydrogen and reoxidized in air (Fig. 4b). Thermogravimetric curves recorded for the corresponding states in the air atmosphere. For the initial sample of the reduced form, the presence of an oxygen release peak at 600 °C was noted. This process, as it was shown earlier [27], leads to destabilization of the structure of complex oxides. For the recovered sample, there is also an intense peak of oxygen absorption in the region of 300 °C, which is formed due to at least the contribution of two processes: oxidation of complex oxides with a perovskite structure and oxidation of cobalt metal nanoparticles to Co_3O_4.

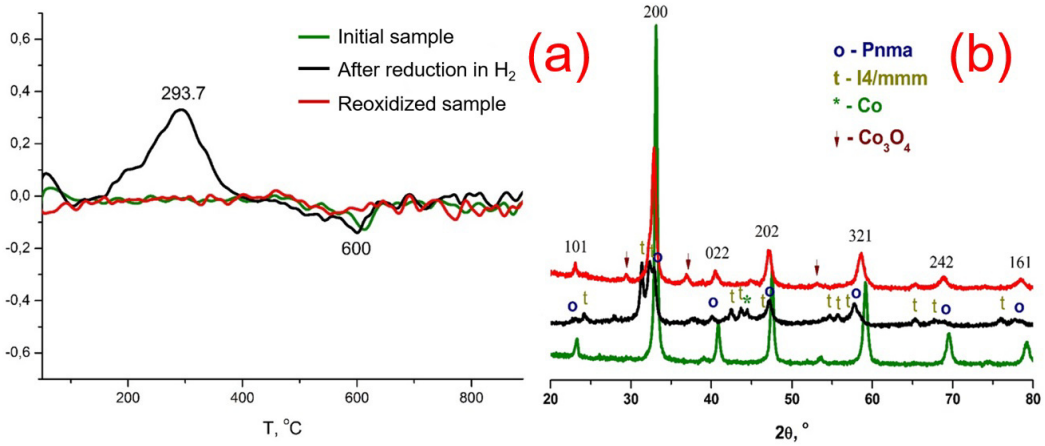

FIG. 4. TG curves for the initial, reduced and oxidized $La_{0.6}Ca_{0.4}Mn_{0.5}Co_{0.5}O_3$ in the air atmosphere (a) and comparative XRD patterns of $La_{0.6}Ca_{0.4}Mn_{0.4}Co_{0.6}O_3$, the green curve corresponds to the original sample, the black curve corresponds to the reduced one in hydrogen, the red curve corresponds to the reoxidized sample in the air stream (b)

In situ XRD studies show that upon reaching a temperature of 300 °C in air oxygen (Fig. 5b), the intensity of the tetragonal phase reflex 100 changes due to the contribution of the orthorhombic reflex 200 to the signal, and some of the other reflexes related to the orthorhombic phase shift towards large angles, which indicates a decrease in the cell parameter of this phase. With a further increase to 600 °C, the reflexes of the ordered perovskite disappear, while at a lower temperature (for example, 450 °C) this process is not carried out. This suggests that the mechanism of "reoxidation" of $La_{0.6}Ca_{0.4}Mn_{1-x}Co_xO_3$ proceeds in at least two stages: through oxygen saturation and "oxidation" of the structure of nonstoichiometric orthorhombic perovskite at 300 °C, and then through subsequent restructuring of the layer of ordered perovskite. Most likely, the transition to an unordered state requires a higher temperature, while the phase of an ordered perovskite can be saturated with oxygen to certain limits while maintaining this state, and also serve as an effective oxygen conductor for deeper layers, as a result of which their saturation and change occur. The La_2CoO_4-based phase may also hinder further reduction of perovskite, as it may impede the diffusion of cobalt cations to the surface, due to which the reduction in hydrogen proceeds inhomogeneously.

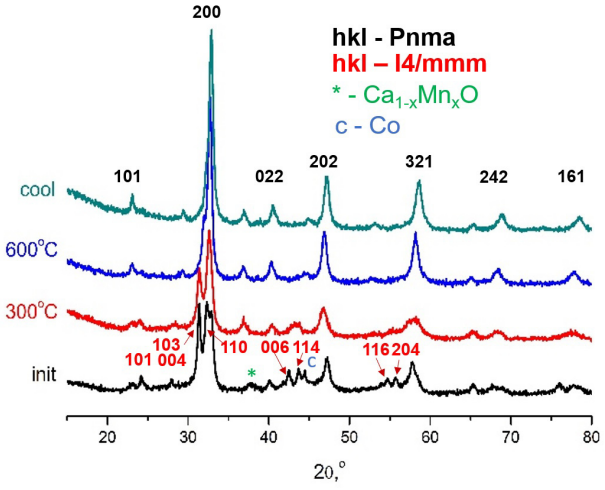

FIG. 5. In situ XRD patterns demonstrating the processes of reoxidation of solid solutions $La_{0.6}Ca_{0.4}Mn_{0.6}Co_{0.4}O_3$

Significant changes in the microstructure are clearly visible on EDX mapping (Fig. 6a). In the sample, after treatment in a reducing atmosphere, the release of cobalt particles on the surface of the perovskite phase is observed. These particles have approximately the same size on the order of 10 nm and a uniform distribution over the surface of the perovskite. Also, according to the EDX mapping data, it can be seen that there are zones of enrichment with calcium cations, which corresponds to the XRD data on the coexistence of two phases with different chemical compositions. The morphology of the sample after reoxidation to 600 °C changes significantly, the particles of both the perovskite phase and cobalt oxide particles are enlarged (Fig. 6b). At the same time, Ca cation enrichment zones are observed, which indicates that Ca does not fully return to the perovskite structure. It is worth noting that according to HRTEM data, calcium oxide forms a film coating (Fig. 6c) and therefore the signal from this phase is practically not observed on diffractograms. In general, the structure of perovskite undergoes significant changes, expressed in the presence of a large number of micro-distortions and a decrease in the degree of crystallinity (Fig. 6d).

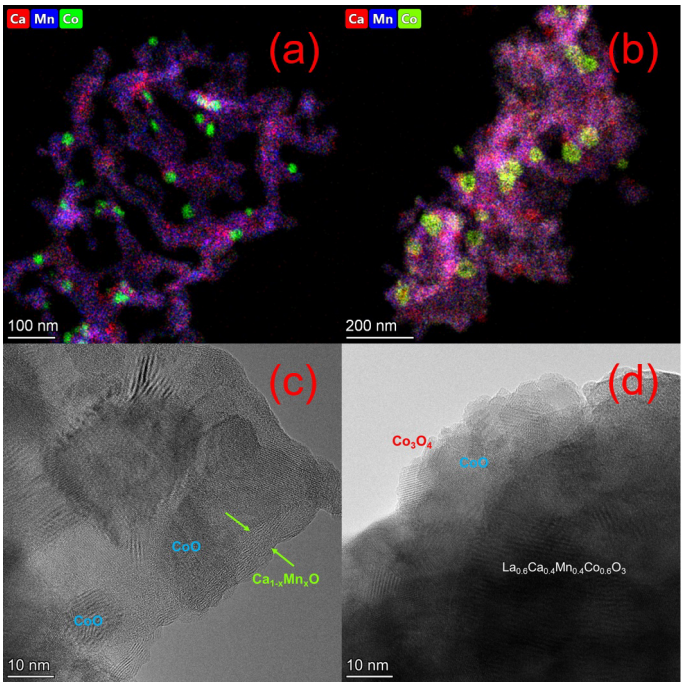

FIG. 6. EDX mappings and HRTEM images of $La_{0.6}Ca_{0.4}Mn_{0.4}Co_{0.6}O_3$ sample after treatments in hydrogen containing medium (a,c) and after subsequent oxidation at a temperature of 600 °C (b, d)

4. Conclusion

The effect of the reducing medium on the structure of complex oxides $La_{0.6}Ca_{0.4}Mn_{1-x}Co_xO_3$ was studied by in situ XRD and HRTEM methods. It is shown that the influence of the reducing medium at temperatures of 450 – 600 °C leads to the formation of ordered phases based on the Radlesdenne–Popper structure, while the content of this phase strongly depends on the initial composition of perovskite. In addition, the high content of Mn cations in the perovskite sublattice increases the temperature of such transitions.

The effect of oxygen treatment of the reduced samples at temperatures of 300 – 600 °C leads to a partial return of the multicomponent system to its original state. Thermogravimetry has shown that oxygen is absorbed by these systems in the temperature range 200 – 350 °C, which leads to a partial return to the perovskite structure. The study of the microstructure by the HRTEM method showed that during the treatment of solid solutions in hydrogen, cobalt particles and a $Ca_{1-x}Mn_xO$ layers coating are formed on the surface of the perovskite phase. After calcination in air, particles of the Co and Ca-containing phase remain on the surface of the perovskite phase, which also indicates an incomplete return of the structure of solid solutions to its initial state.

References

[1] Xia W., Pei Z., Leng K., Zhu X. Research Progress in Rare Earth-Doped Perovskite Manganite Oxide Nanostructures. *Nanoscale Research Letters*, 2020, **15** (1), 9.

[2] Zhu J., Li H., Zhong L., Xiao P., Xu X., Yang X., Zhao Z., Li J. Perovskite Oxides: Preparation, Characterizations, and Applications in Heterogeneous Catalysis. *ACS Catalysis*, 2014, **4** (9), P. 2917–2940.

[3] Grabowska E. Selected perovskite oxides: Characterization, preparation and photocatalytic properties-A review. *Applied Catalysis B: Environmental*, 2016, **186**, P. 97–126.

[4] Bashan V., Ust Y. Perovskite catalysts for methane combustion: applications, design, effects for reactivity and partial oxidation. *Int. J. of Energy Research*, 2019, **43** (14), P. 7755–7789.
[5] Najjar H., Batis H. Development of Mn-based perovskite materials: Chemical structure and applications. *Catalysis Reviews*, 2016, **58** (3), P. 371–438.
[6] Keav S., Matam S., Ferri D., Weidenkaff A., Keav S., Matam S.K., Ferri D., Weidenkaff A. Structured Perovskite-Based Catalysts and Their Application as Three-Way Catalytic Converters—A Review. *Catalysts*, 2014, **4** (3), P. 226–255.
[7] Khaledian H.R., Zolfaghari P., Nezhad P.D.K., Niaei A., Khorram S., Salari D. Surface modification of $LaMnO_3$ perovskite supported on CeO_2 using argon plasma for high-performance reduction of NO. *J. of Environmental Chemical Engineering*, 2021, **9** (1), 104581.
[8] Shen Q., Dong S., Li S., Yang G., Pan X. A Review on the Catalytic Decomposition of NO by Perovskite-Type Oxides. *Catalysts*, 2021, **11** (5), 622.
[9] Wu Y., Liu H., Li G., Jin L., Li X., Ou X., Dong L., Jin G., Li B. Tuning composition on B sites of $LaM_{0.5}Mn_{0.5}O_3$ (M = Cu, Co, Fe, Ni, Cr) perovskite catalysts in NOx efficient reduction. *Applied Surface Science*, 2020, **508**, 145158.
[10] Afify M.S., Faham M.M.E., Eldemerdash U., El-Dek S.I., Rouby W.M.A.E. Effects of Ag doping on $LaMnO_3$ photocatalysts for photoelectrochemical water splitting. *Applied Physics A: Materials Science and Processing*, 2022, **128** (10), P. 1–12.
[11] Jawhari A.H., Hasan N., Radini I.A., Narasimharao K., Malik M.A. Noble Metals Deposited $LaMnO_3$ Nanocomposites for Photocatalytic H_2 Production. *Nanomaterials*, 2022, **12** (17), 2985.
[12] Kida T., Guan G., Yoshida A. $LaMnO_3$/CdS nanocomposite: a new photocatalyst for hydrogen production from water under visible light irradiation. *Chemical Physics Letters*, 2003, **371** (5–6), P. 563–567.
[13] Garba Z.N., Zhou W., Zhang M., Yuan Z. A review on the preparation, characterization and potential application of perovskites as adsorbents for wastewater treatment. *Chemosphere*, 2020, **244**, 125474.
[14] Yiğiter İ.E., Pişkin B. Investigation into Ca-Doped $LaMnCoO_3$ Perovskite Oxides for Thermochemical Water Splitting. *JOM*, 2022, **74** (12), P. 4682–4694.
[15] Kwon O., Kim Y.I., Kim K., Kim J.C., Lee J.H., Park S.S., Han J.W., Kim Y.-M., Kim G., Jeong H.Y. Probing One-Dimensional Oxygen Vacancy Channels Driven by Cation–Anion Double Ordering in Perovskites. *Nano Letters*, 2020, **20** (11), P. 8353–8359.
[16] Gan L.-Y., Akande S.O., Schwingenschlögl U. Anisotropic O vacancy formation and diffusion in $LaMnO_3$. *J. Mater. Chem. A*, 2014, **2** (46),
[17] Zheng J., Zhao H., Guo X., Jin X., Wang L., Dong S., Chen J. Enhanced Electrochemical Performance of $LaMnO_3$ Nanoparticles by Ca/Sr Doping. *Coatings*, 2023, **14**, 20.
[18] Yin X., Zhang R., Zhang Y., Wang S., Shen L. Enhanced reactivity of methane partial oxidation of nickel doped $LaMnO_{3+\delta}$ perovskites for chemical looping process. *Int. J. of Hydrogen Energy*, 2024, **71**, P. 481–492.
[19] Politov B.V., Shalamova A.M., Shein I.R., Suntsov A.Y. Exploring oxygen non-stoichiometry in presumably stoichiometric double perovskites: the case study for $LaCu_{0.5}Mn_{0.5}O_{3-\delta}$. *Acta Materialia*, 2023, **250**, 118872.
[20] Vieten J., Bulfin B., Huck P., Horton M., Guban D., Zhu L., Lu Y., Persson K.A., Roeb M., Sattler C. Materials design of perovskite solid solutions for thermochemical applications. *Energy & Environmental Science*, 2019, **12** (4), P. 1369–1384.
[21] Liu X., Wang S., Liao Y., Lei M., Fang X., Xu X., Wang X. La/Mn molar ratio tuning the activity of La–Mn perovskites for CO and propane oxidation. *J. of the Energy Institute*, 2024, **114**, 101595.
[22] Zhao A., Ren Y., Wang H., Qu Z. Enhancement of toluene oxidation performance over La1-CoO3- perovskite by lanthanum non-stoichiometry. *J. of Environmental Sciences*, 2023, **127**, P. 811–823.
[23] Jiang Y., Li Z., Zhu T., Li D., Wang H., Zhu X. Oxygen Storage Characteristics and Redox Behaviors of Lanthanum Perovskite Oxides with Transition Metals in the B-Sites. *Energy & Fuels*, 2023, **37** (13), P. 9419–9433.
[24] Mantzavinos D. Oxygen stoichiometries in $La_{1-x}Sr_xCo_{1-y}Fe_yO_{3-\delta}$ perovskites at reduced oxygen partial pressures. *Solid State Ionics*, 2000, **134** (1–2), P. 103–109.
[25] Nadeev A.N., Tsybulya S.V., Gerasimov E.Y., Isupova L.A. High-temperature phase transitions in the $La_{0.25}Sr_{0.75}FeO_{3-\delta}$ solid solution with a perovskite structure. *J. of Structural Chemistry*, 2009, **50**, P. 108–113.
[26] Gerasimov E.Yu., Rogov V.A., Prosvirin I.P., Isupova L.A., Tsybulya S.V. Microstructural Changes in $La_{0.5}Ca_{0.5}Mn_{0.5}Fe_{0.5}O_3$ Solid Solutions under the Influence of Catalytic Reaction of Methane Combustion. *Catalysts*, 2019, **9**, 563.
[27] Kapishnikov A.M., Bespalko Yu.N., Shuvarakova E.I., Tsybulya S.M., Isupova L.A., Gerasimov E.Yu. Influence of Oxygen Nonstoichiometry on the Structural Stability of $La_{1-x}Ca_xMn_{0.5}Co_{0.5}O_3$ Complex Oxides ($x = 0.2 - 0.6$) Subjected to Heat Treatment in He. *J. of Structural Chemistry*, 2024, **65**, P. 107–116.
[28] Isupova L.A., Gerasimov E.Yu., Zaikovskii V.I., Tsybulya S.V. Effect of the reaction medium on the structure of the $La_{1-x}Ca_xMnO_3$ ($x = 0 - 1$) solid solutions prepared by the pechini method. *Kinetics and Catalysis*, 2011, **52**, P. 104–110.
[29] Flores-Lasluisa J.X., Huerta F., Cazorla-Amorys D., Morallyn E. Structural and morphological alterations induced by cobalt substitution in $LaMnO_3$ perovskites. *J. of Colloid and Interface Science*, 2019, **556**, P. 658–666.

Submitted 19 November 2024; accepted 12 December 2024

Information about the authors:

Alexander V. Kapishnikov – Boreskov Institute of Catalysis SB RAS, Lavrentieva Ave, 5, Novosibirsk, 630090, Russia; ORCID 0000-0002-3921-5629; avl97@mail.ru

Evgeny Yu. Gerasimov – Boreskov Institute of Catalysis SB RAS, Lavrentieva Ave, 5, Novosibirsk, 630090, Russia; ORCID 0000-0002-3230-3335; gerasimov@catalysis.ru

Conflict of interest: the authors declare no conflict of interest.

NANOSYSTEMS:
PHYSICS, CHEMISTRY, MATHEMATICS

Trukhanova K.A., et al. *Nanosystems: Phys. Chem. Math.*, 2025, **16** (1), 58–66.
http://nanojournal.ifmo.ru
DOI 10.17586/2220-8054-2025-16-1-58-66

Original article

Nanostructured transparent Fe^{2+}-doped lithium aluminosilicate glass-ceramics with tunable optical properties: effect of heat-treatment regimes on near-infrared absorption

Kristina A. Trukhanova[1,a], Olga S. Dymshits[2,3,b], Irina P. Alekseeva[3,c], Kirill V. Bogdanov[4,d], Svetlana S. Zapalova[3,e], Maksim I. Tenevich[2,f], Anastasia K. Bachina[2,g], Vadim I. Popkov[2,h], Aleksandr A. Zhilin[5,i]

[1]Nordwestlab LLC, St. Petersburg, Russia

[2]Ioffe Institute, St. Petersburg, Russia

[3]Vavilov State Optical Institute, St. Petersburg, Russia

[4]ITMO University, St. Petersburg, Russia

[5]D. V. Efremov Institute of Electrophysical Apparatus, pos. Metallostroi, St. Petersburg, Russia

[a]kristina.truhanova@gmail.com, [b]vodym1959@gmail.com, [c]vgolub19@gmail.com, [d]kirw.bog@gmail.com, [e]zenii99@yandex.ru, [f]mtenevich@gmail.com, [g]a.k.bachina@yandex.ru, [h]vip-07@yandex.ru, [i]zhilin1311@yandex.ru

Corresponding author: O.S. Dymshits, vodym1959@gmail.com

PACS 78.67.Bf, 61.46.Hk, 42.70.Ce, 64.75.Jk, 81.10.Aj, 78.20.Ci

ABSTRACT This study explores optical tuning of nanostructured transparent lithium aluminosilicate glass-ceramics nucleated by titania and doped with Fe^{2+} ions. The glass was melted at 1620 °C and heat-treated between 660 °C and 800 °C, yielding nanocrystals of γ-Al_2O_3 (2 – 23 nm) and β-quartz solid solutions (8 – 40 nm). Fe^{2+} ions in octahedral coordination in the initial glass are responsible for absorption in the 1000 – 1400 nm range. Tetrahedrally coordinated Fe^{2+} ions in γ-Al_2O_3 are responsible for absorption at 1550 – 2300 nm. Crystallization of β-quartz solid solutions leads to decreasing the γ-Al_2O_3 fraction and corresponding decrease of absorption at 1550 – 2300 nm. Differential scanning calorimetry, scanning electron microscopy, X-ray diffraction, Raman and optical spectroscopy reveal the relationship between heat-treatment regimes, crystalline phase development, and optical performance, highlighting the potential of Fe^{2+}-doped LAS glass-ceramics for advanced photonic applications. The glass-ceramics exhibit customizable optical properties, promising for saturable absorbers in passive Q-switching lasers.

KEYWORDS Nanophase glass-ceramics, γ-Al_2O_3 nanocrystals, nanocrystals of β-quartz solid solution, Fe^{2+} ions

ACKNOWLEDGEMENTS This work was partly supported by the Russian Science Foundation (Grant 23-23-00446).

FOR CITATION Trukhanova K.A., Dymshits O.S., Alekseeva I.P., Bogdanov K.V., Zapalova S.S., Tenevich M.I., Bachina A.K., Popkov V.I., Zhilin A.A. Nanostructured transparent Fe^{2+}-doped lithium aluminosilicate glass-ceramics with tunable optical properties: effect of heat-treatment regimes on near-infrared absorption. *Nanosystems: Phys. Chem. Math.*, 2025, **16** (1), 58–66.

1. Introduction

Transparent nanophase lithium aluminosilicate (LAS) glass-ceramics based on nanocrystals of lithium aluminosilicates with the structure of β-quartz were invented by Stookey more than sixty years ago [1], and they still remains the most commercially successful ones due to a combination of transparency, near zero thermal expansion coefficient, high mechanical strength and durability [2–5]. The LAS system remains the subject of numerous studies [6–25]. On the one hand, complex devices and new research methods are emerging, allowing one to reconsider previously formulated approaches to the development of these materials, their structure and the regularities of their formation [6–14]. On the other hand, even small changes in the basic composition, as well as the nature and concentration of nucleating agents, and the introduction of modifying, coloring, and luminescent ions make it possible to develop new transparent, heat-resistant and durable materials that meet new needs [15–20, 22, 22–25]. Precise control of the phase composition of glass-ceramics of

© Trukhanova K.A., Dymshits O.S., Alekseeva I.P., Bogdanov K.V., Zapalova S.S., Tenevich M.I., Bachina A.K., Popkov V.I., Zhilin A.A., 2025

the LAS system allowed us to develop transparent glass-ceramics based on spinel and β-quartz solid solutions (ss) and doped with Ni^{2+} and Co^{2+} ions intended for thermal shock resistant color filters and saturable absorbers of Er lasers [23]. The aim of the present study is the development of transparent spinel-based glass-ceramics with selective doping of ferrous ions into tetrahedral positions in the crystals with spinel structure ensuring broadband absorption in the spectral range of 2 μm, which is promising for saturable absorbers in the near IR spectral range.

2. Experimental

2.1. Preparation of glass and glass-ceramics

The reagent grade lithium carbonate, alumina, silica, titania, and ferrous oxide were thoroughly mixed to prepare the glass with the composition 12 Li_2O, 24 Al_2O_3, and 64 SiO_2 (mol%) [26] nucleated by 6 mol% TiO_2 and doped with 0.1 % FeO added on top of the main components. The batch to produce 400 g of glass was placed into a crucible made of quartz ceramics and melted in a laboratory electric furnace at a temperature of 1620 °C with stirring, cast onto a cold metal plate and annealed at 640 °C for 0.5 h. The pieces of transparent pale-yellow glass were heat-treated by single and two-stage schedules in the temperature range of 660 to 1200 °C for 6 h at each stage. The samples obtained by heat-treatments up to 1000 °C were transparent and brown-colored. The complex character of the color variation with heat-treatment temperature is in relation to precipitated crystalline phases and will be discussed elsewhere. The glass-ceramic obtained by heat-treatments at 1100 °C was translucent, and that obtained at 1200 °C was opaque, see Fig. 1.

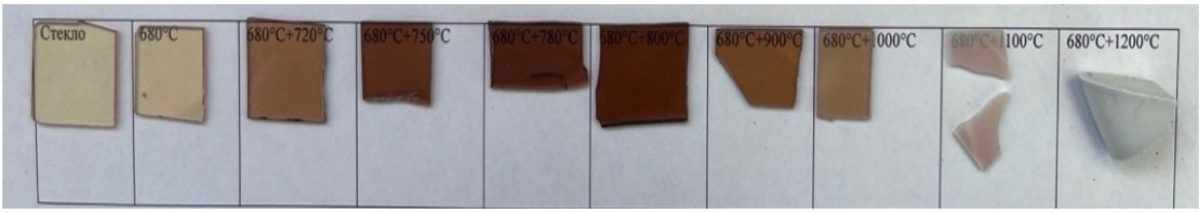

FIG. 1. Images of glasses and glass-ceramics. Transparent samples are polished plates with thickness of 1 mm.

2.2. Methods

Differential scanning calorimetry (DSC) of the initial as-quenched and heat-treated glasses with the weight of $\sim$ 15 mg was performed in a temperature range from 35 to 1300 °C in a flow of Ar using the simultaneous thermal analyzer NETZSCH STA 449 F3 Jupiter at a heating rate of 10 °C/min.

Raman spectra were recorded using a confocal InVia Renishaw Raman microscope equipped with a $\times$50 Leica objective (N.A. = 0.75), a TE cooled CCD camera and an edge filter. The spectra were excited by an Ar^+ ion laser line at 488 nm. The spectral resolution was 2 cm^{-1}. Every spectrum was averaged over 10 acquisitions with duration of 10 s.

The Tescan Vega 3 SBH scanning electron microscope was used to study the morphology of the materials. To obtain the scanning electron microscopy images, the surfaces of the samples were cleaned using isopropyl alcohol and benzene, then etched in a hydrofluoric acid for about 2 s and washed in distilled water. The particle size was estimated using ImageJ software [27].

The X-ray diffraction (XRD) experiments were performed on the Shimadzu XRD-6000 diffractometer operating with Cu Kα radiation and a Ni filter (λ = 1.5406 Å). The average crystal sizes were calculated from broadening of X-ray peaks according to Scherrer's equation [28]. The average size of γ-Al_2O_3 crystals was estimated from the peak with indices hkl (440); the size of tieilite crystals, Al_2TiO_5, from the peak with indices hkl (020). The average size of crystals of β-quartz ss was determined from the (220) peak, while the average size of crystals of β-spodumene ss was calculated using the (102) peak. The error in the estimation of the average crystal size is $\sim$ 5 – 10 %. The lattice parameter a of γ-Al_2O_3 nanocrystals was estimated from the position of the peak with Miller's indices hkl (440), those of Al_2TiO_5 from the peaks with indices (002), (020), (110), (023) and (200). The lattice parameters of β-quartz ss were estimated from the positions of the peaks with indices (110) and (211), while those of β-spodumene ss were estimated using the peaks with Miller's indices (111) and (102). The error is $\pm$0.003 Å.

Absorption spectra of polished flat-parallel plates with a thickness of $\sim$ 1 mm were measured using a Shimadzu UV-3600 spectrophotometer in the spectral range from 200 to 3300 nm.

Density was measured by the hydrostatic weighing in toluene at room temperature.

3. Results and discussion

The DSC traces of as-quenched and heat-treated glasses demonstrate a pronounced influence of preliminary heat-treatments on the character of phase transformations and the nature of crystalline phases, see Fig. 2. The DSC curve of the as-quenched glass is typical for glasses of the lithium aluminosilicate (LAS) system [29] nucleated by titanium

oxide. It shows the onset of the glass transition (T_g) at 698 °C. At higher temperatures, the DSC curve exhibits a strong exothermic peak with crystallization onset temperature $T_x = 852$ °C and crystallization peak temperature, $T_p = 873$ °C, which is explained by the crystallization of the lithium aluminosilicate with β-quartz structure [29]. Indeed, the XRD pattern of the as-quenched glass heated in the furnace of the DSC instrument up to 885 °C, which is the temperature at the end of the first exothermic peak, presents the lines of the β-quartz ss, the main crystalline phase characteristic of these glass-ceramics, see Fig. 3(a). There are also traces of tieilite, aluminum titanate, the crystalline phase of the nucleating agent [30]. Small peaks in the temperature range from ca. 950 to 1150 °C can be assigned to traces of minor phases and will not be discussed here. The second rather prominent peak also of low intensity is seen at $\sim$ 1177 °C, Fig. 2. This peak is usually attributed to the appearance of β-spodumene ss [29], the high-temperature crystalline phase characteristic of LAS glass-ceramics [1, 2]. The preliminary heat-treatment at 660 °C for 6 h predictably leads to a decrease in the crystallization peak temperature, T_p, by about 20 °C, see Fig. 2 and Table 1. The peak becomes broader and has a lower intensity at the maximum as compared with the exothermic peak of the as-quenched glass. The XRD pattern of this glass heated in the furnace of the thermal analyzer up to 900 °C, also demonstrates crystallization of β-quartz ss (not shown here). We observed the similar character of the gahnite crystallization peak behavior after preliminary heat-treatment in glasses of the zinc aluminosilicate system nucleated by titania [31]. The DSC curve of glass heat-treated at 680 °C for 6 h has quite a different shape. Instead of one sharp peak in the temperature range from 800 to 900 °C, it presents two peaks in the temperature range from ca. 800 to ca. 950 °C. The first peak with $T_p = 829$ °C is caused by crystallization of γ-Al_2O_3 with cubic spinel structure, see Fig. 3(b), while the second peak is assigned to β-quartz ss, see Fig. 3(a). An additional proof of the attribution of the first peak on the DSC curve of the sample preliminary heat-treated at 680 °C to spinel crystallization is the DSC trace of the sample, in which spinel has already crystallized. Fig. 3(b) shows the XRD pattern of the glass-ceramic obtained by the two-stage heat-treatment at 680 and 750 °C for 6 h at each stage, which demonstrates a distinct spinel peak at $2\theta = 66.7°$. The DSC thermograph of this sample is presented in Fig. 2. It shows all the DSC peaks with the exception of the low-temperature exothermal peak assigned to spinel crystallization. Thus, we unambiguously attribute the first prominent peak on the DSC curve of the sample preliminary heat-treated at 680 °C to spinel crystallization and the second intense peak to crystallization of β-quartz ss.

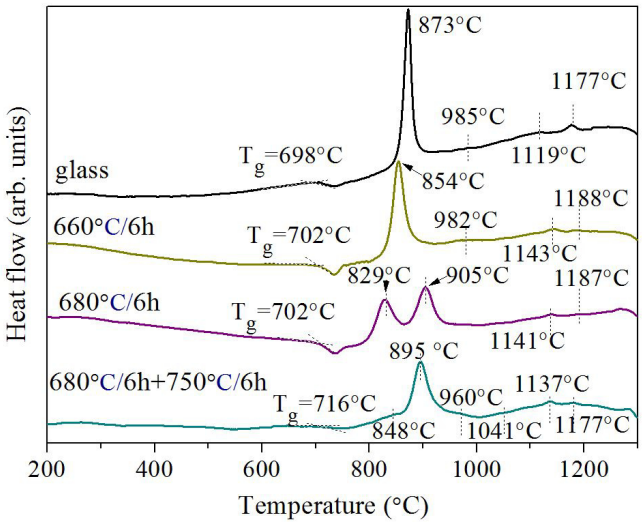

FIG. 2. DSC thermographs for the as-quenched and heat-treated glasses. The heat-treatment schedules are listed in figure. The curves are shifted for convenience of observation.

TABLE 1. Characteristic temperatures of the as-quenched and heat-treated glasses derived from DSC traces presented in Fig. 2.

Heat-treatment schedule, °C/h	T_g, °C	T_{p1}, °C	T_{p2}, °C
—	698±2	—	873±1
660/6	702±2	—	854±1
680/6	702±2	829±1	905±1
680/6+750/6	716±2	848±1	895±1

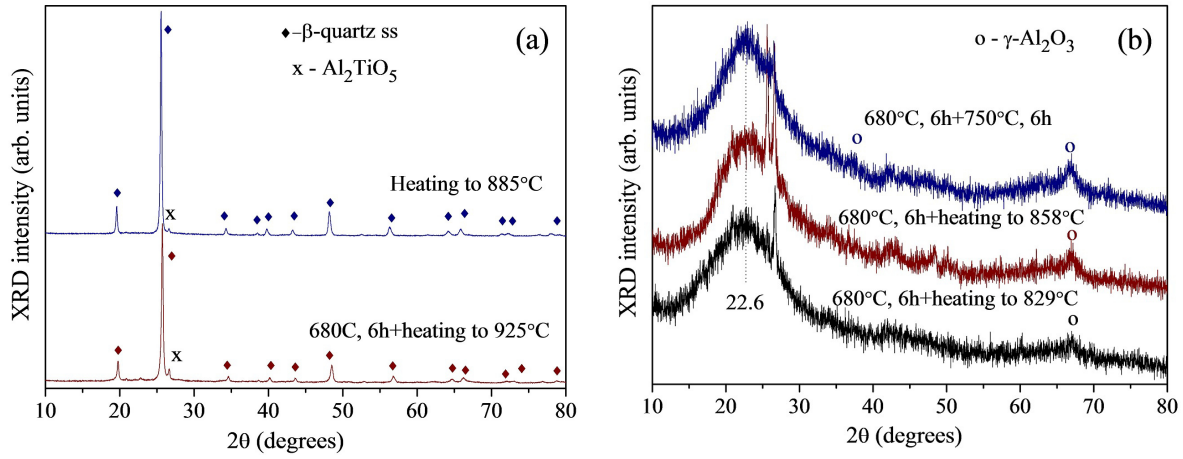

FIG. 3. XRD patterns of: (a) the as-quenched and heat-treated glasses heated in the furnace of the DSC instrument; (b) heat-treated glasses heated in the furnace of the DSC instrument and glass-ceramics obtained by the heat-treatment at 680 °C for 6 h and at 750 °C for 6 h added for comparison. The heat-treatment schedules are listed in figure. The curves are shifted for convenience of observation.

Taking into account the results of the DSC study, two-stage heat-treatments were conducted with the first stage at 680 °C for 6 h and the second stage in the temperature range of 720 to 800 °C for 6 h.

The Raman spectrum of the initial annealed glass shows a broad band with a maximum at 482 cm^{-1}, a band at 800 cm^{-1} and a broad band with maxima at ca. 917 cm^{-1} and ca. 1003 cm^{-1}, see Fig. 4. The wing of this band extends to 1200 cm^{-1}. The detailed arguments in favor of the attribution of the bands at 482 cm^{-1}, at 800 cm^{-1} and at 1003 cm^{-1} to the aluminosilicate glass network and the band located at ca. 917 cm^{-1} to titanium-oxygen tetrahedrons (TiO_4) built into this network can be found elsewhere [30]. Only minor changes are observed in the Raman spectrum of glass after its heat-treatment at 660 °C for 6 h. The peak in the range of wavenumbers from 850 to 1200 cm^{-1} becomes broader and has a flatter top, see Fig. 4.

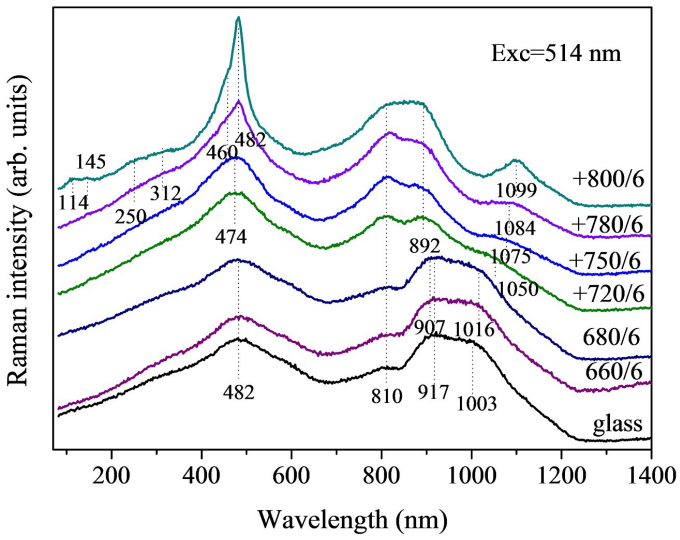

FIG. 4. Raman spectra of the initial and heat-treated glasses. $\lambda_{exc} = 514$ nm. The heat-treatment schedules (°C/h) are shown above the curves. The sign "+" designates the preliminary heat-treatment at 680 °C for 6 h. Numbers denote the position of the Raman peaks in cm^{-1}. The curves are shifted for the convenience of observation.

The maximum at 907 cm^{-1} becomes prominent in the Raman spectrum of the sample heat-treated at 680 °C for 6 h, and no other changes can be found in this spectrum as compared with the spectrum of the initial glass. The two-stage heat-treatment with the second stage at 720 °C results in significant modification of the Raman spectrum. The new band with two well-resolved maxima appears in the spectral range from 820 to 890 cm^{-1} and is assigned to (TiO_5) and (TiO_6) groups in aluminotitanate amorphous regions [30]. The high wavenumber wing of the broad band exhibits maximum at ca. 1050 cm^{-1}. The middle-range band becomes somewhat narrower, and its position slightly changes to 474 cm^{-1}.

These changes develop in spectra of the samples heat-treated at 750 and 780 °C at the second stage. The distinct feature of the Raman spectrum of the sample obtained by heat-treatment at 780 °C is a narrow band, which appears at 482 cm^{-1}. It is assigned to β-quartz ss [30]. In the Raman spectrum of the sample heat-treated at 800 °C at the second stage, there are bands with maxima at ca. 114, 482, and 1099 cm^{-1}, characteristic of solid solutions with β-quartz structure [32, 33]. A small peak at ca. 145 cm^{-1} is at the position of the strongest peak of metastable titania modification of anatase [32]. Two distinct maxima at 250 and 312 cm^{-1} are seen in a weak broad band located in the low wavenumber spectral range. Together with a strong and broad band with a maximum at ca. 890 cm^{-1}, they manifest crystallization of tieilite, Al_2TiO_5 [30].

The SEM images of all these samples demonstrate their inhomogeneous structure. This structure develops with an increase in the heat-treatment temperature, see Fig. 5. Fig. 5(a) shows that the annealed glass has a bimodal structure with smaller particle sizes of 5 – 10 nm and larger particle sizes of ca. 15 – 30 nm. The average particle size is 14 nm. The morphology of the glass heat-treated at 680 °C for 6 h demonstrates a broader particle size distribution with a somewhat smaller average particle size of 12 nm, see Fig. 5(b). The morphology of the sample obtained by a two-stage heat-treatment with a temperature of 720 °C at the second stage is composed of large particles with sizes ranging from 15 nm to ca. 60 nm and an average size of 31 nm, see Fig. 5(c). After heat-treatments at 750 °C, see Fig. 5(d), the particle sizes are similar to those in materials obtained by heat-treatments at 720 °C. Agglomerated particles are clearly seen in SEM images of samples obtained by heat-treatments at 780 °C, Fig. 5(e), and 800 °C, Fig. 5(f), at the second stage.

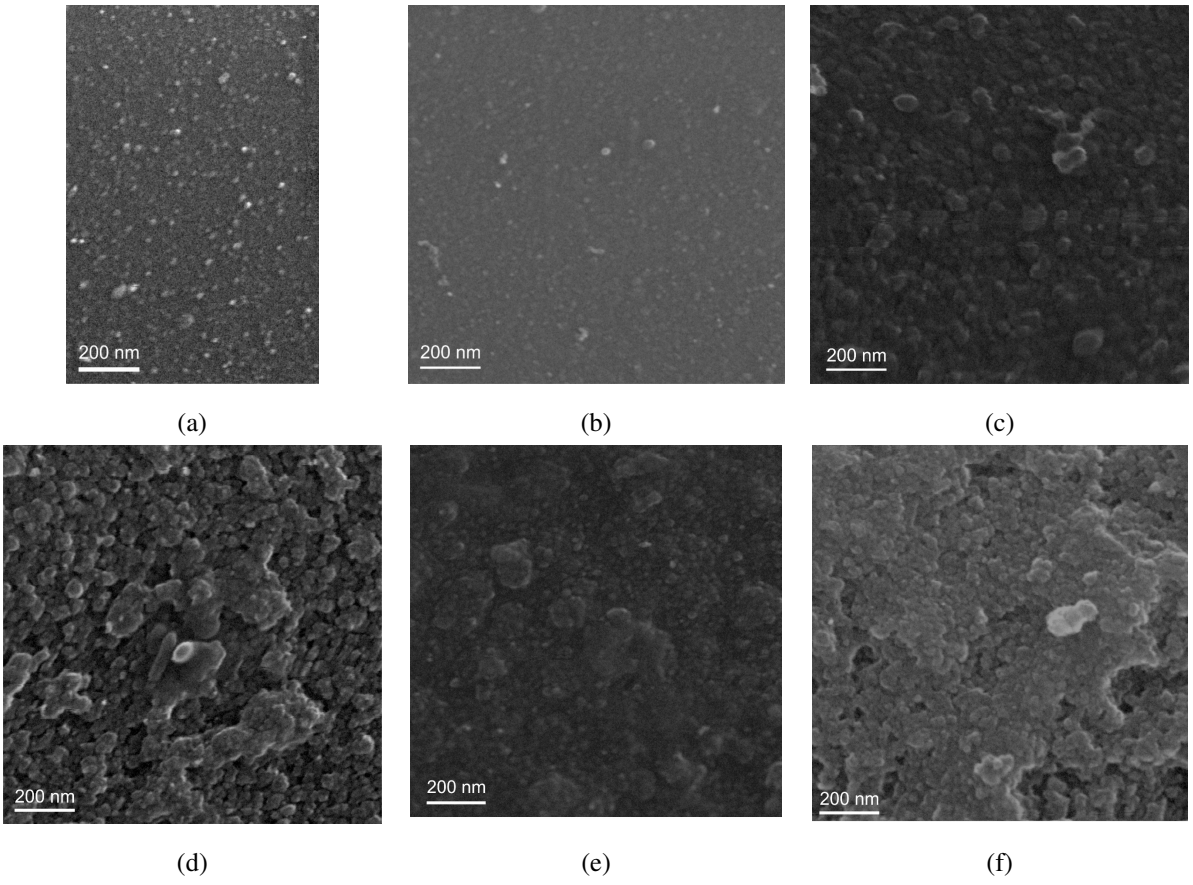

FIG. 5. SEM images of the samples under study: (a) the initial glass; (b) the glass after heat-treatment at 680 °C for 6 h; (c – f) the glasses ceramized at 680 °C for 6 h and at: (c) 720 °C for 6 h; (d) 750 °C for 6 h; (e) 780 °C for 6 h; (f) 800 °C for 6 h.

XRD patterns of glasses and glass-ceramics presented in Fig. 6(a,b) demonstrate that the initial glass and the glass heat-treated at 680 °C are X-ray amorphous. The nanocrystals with spinel structure evolve starting from the two-stage heat-treatment with a temperature at the second stage of 720 °C, while β-quartz ss and Al_2TiO_5 nanocrystals appear additionally during heat-treatments at 780 and 800 °C. The spinel lattice parameter a changes from 7.915 to 7.979 Å with an increase in the heat-treatment temperature at the second stage from 720 °C to 800 °C, while the crystal size increases more than ten times from ca. 2 to 23 nm, see Table 2. Note that according to ref. [34], the standard lattice parameter a for γ-Al_2O_3 is in the range of a = 7.900 – 7.908 Å. The lattice parameters and sizes of β-quartz ss are also presented in Table 2. The sizes increase from 29 to 39 nm with an increase of the heat-treatment temperature at the second stage from 720 to 800 °C. Table 3 shows the lattice parameters a, b, and c, and average sizes of Al_2TiO_5 crystals. The unit cell

of tieilite has three parameters. The XRD pattern of the glass-ceramic obtained by the heat-treatment at 780 °C for 6 h clearly shows only the line of Al_2TiO_5 with Miller's indices hkl (110). It is the evidence of a small fraction of Al_2TiO_5. Therefore, it is not possible to determine the lattice parameters. The lattice parameters b and c of Al_2TiO_5 crystals in the sample obtained by the heat-treatment at 780 °C for 6 h are lower than those listed in the standard ICDD card # 26-0040.

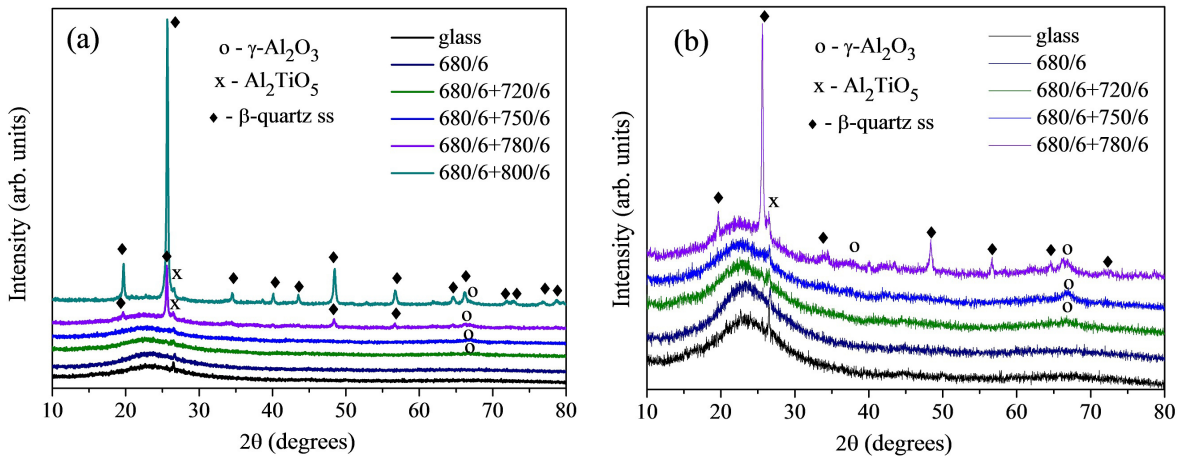

FIG. 6. XRD patterns of the initial and heat-treated glasses. Labels denote heat-treatment schedules (°C/h). The curves are shifted for the convenience of observation.

TABLE 2. Lattice parameters and average sizes of γ-Al_2O_3, and β-quartz ss crystals

Heat-treatment schedule	γ-Al_2O_3		β-quartz ss		
	a, Å	D, nm	a, Å	c, Å	D, nm
680 °C, 6 h + 720 °C, 6 h	7.915	< 2	—	—	
680 °C, 6 h + 750 °C, 6 h	7.905	5	—	—	
680 °C, 6 h + 780 °C, 6 h	7.949	8	5.220	5.439	29
680 °C, 6 h + 800 °C, 6 h	7.979	23	5.199	5.433	39

TABLE 3. Lattice parameters a, b, and c, and average sizes of Al_2TiO_5 crystals

Heat-treatment schedule	a	b	c	D, nm
680 °C, 6 h + 780 °C, 6 h	traces			20
680 °C, 6 h + 800 °C, 6 h	3.593	9.384	9.617	26

Density variation with the heat-treatment schedule presented in Fig. 7 shows that the densities of samples preliminarily heat-treated at 660 and 680 °C are only slightly higher than the density of the initial glass. The density increases rapidly when glasses are heat-treated by two-stage schedules with crystallization of dense spinel (at 720 °C and at 750 °C and then with spinel and β-quartz ss at 780 °C and at 800 °C).

Figure 8(a,b) shows absorption spectra of glasses and glass-ceramics under study. The detailed designation of absorption bands due to titanium and iron ions in different oxidation states and absorption bands assigned to interaction of these ions was performed in ref. [35] describing spectroscopy of Fe^{2+}:$MgAl_2O_4$ transparent ceramics and glass-ceramics. We will use the interpretation of absorption spectra developed in ref. [35] to explain the absorption spectra of our glasses and glass-ceramics.

The spectrum of the glass heat-treated at 680 °C for 6 h is similar to the spectrum of the initial glass, with the only exception that the position of the absorption edge shifts by about 20 nm to longer wavelengths, from 335 to 354 nm. We believe that the interaction of Fe^{3+} and Ti^{4+} ions is mainly responsible for the position of the absorption edge. The nature of the so-called ilmenite brown coloration in glasses of the LAS system nucleated solely by TiO_2 was discussed in [10] and assigned to an Fe^{3+}–O–Ti^{4+} charge transfer. The shift of the absorption edge after preliminary heat-treatment

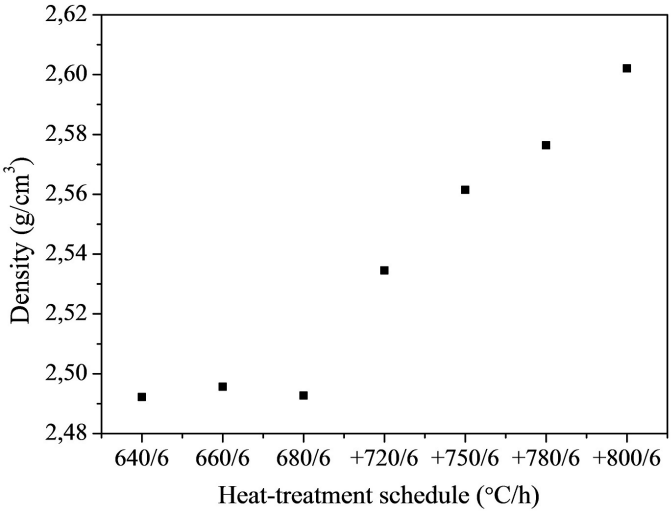

FIG. 7. Density of glasses and glass-ceramics obtained by heat-treatment schedules listed on the X-axis. The sign "+" designates the preliminary heat-treatment at 680 °C for 6 h.

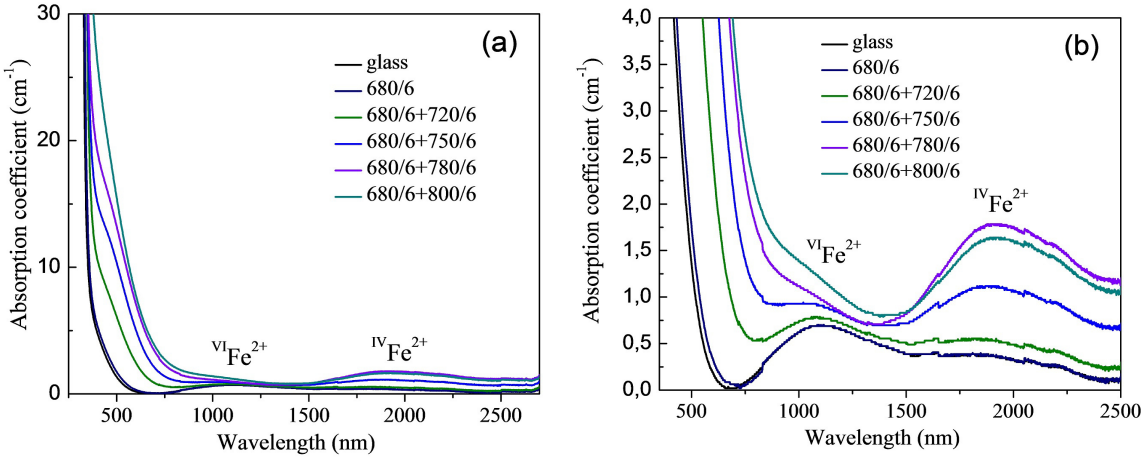

FIG. 8. (a) Absorption spectra of the initial and heat-treated glasses. (b) A closer look on spectra. Labels denote heat-treatment schedules (°C/h).

implies that Fe^{3+} ions together with titanium ions participate in the development of liquid-liquid phase separation and enter the aluminotitanate amorphous regions. The similarity of the absorption spectra of the initial glass and glass heat-treated at 680 °C testifies that Fe^{2+} ions in octahedral coordination, that are responsible for a broad absorption band with a maximum at about 1100 nm, do not participate in the development of liquid-liquid phase separation that occurs during heat-treatment at 680 °C. With an increase in the heat-treatment temperature at the second stage, there is a gradual shift of the absorption edge to longer wavelengths. In this case, absorption in the visible spectral range has multiple reasons. It is mainly caused by heterovalent charge transfer band between iron and titanium ions [10], as well as by homovalent charge transfer bands between Fe^{3+}/Fe^{2+} ions and Ti^{4+}/Ti^{3+} ions [35]. The gradual shift of this absorption edge to the visible and even near IR spectral range confirms that the iron and titanium ions participate in liquid-liquid phase separation and crystallization of the glass during two-stage heat-treatments. Raising the heat-treatment temperature at the second stage from 720 to 780 °C leads to a gradual increase in intensity of the absorption band with a maximum at ca. 1900 nm. The position of the maximum shifts from 1824 nm (the glass ceramized at 720 °C) to 1930 nm (the glass ceramized at 780 °C). The increase in the intensity of this band corresponds to the growth of the crystallinity fraction of γ-Al_2O_3. The heat-treatment at 800 °C at the second stage results in a decrease in the intensity of this absorption band, while the position of the maximum remains unchanged. Thus, based on XRD data, we may conclude that with crystallization of β-quartz ss the crystallinity fraction of γ-Al_2O_3 begins to decrease, which results in the decrease in the intensity of absorption band assigned to Fe^{2+} ions in crystals of γ-Al_2O_3. The iron ions begin to enter the structure of β-quartz ss.

4. Conclusions

The model glass and transparent glass-ceramics of the lithium aluminosilicate system nucleated by TiO_2 and doped with 0.1 % FeO were developed. The initial glass is structurally inhomogeneous yet X-ray amorphous. Fe^{2+} ions are octahedrally coordinated, which gives raise to the band with a maximum at about 1100 nm due to the $^5T_2 \rightarrow {}^5E$ (^5D) transition.

According to DSC data, the secondary heat-treatment at 660 °C for 6 h influences the glass structure but does not result in the development of three-phase immiscibility. The preliminary heat-treatment at 680 °C for 6 h significantly modifies the glass structure, which is clearly revealed in the DSC scan. It is interesting that the DSC method appears to be a powerful tool for studying the structural changes in liquid-liquid phase separated materials. It is more sensitive to structure variation than SEM, Raman, and absorption spectroscopy data for phase separated glasses of the LAS system.

Crystallization of γ-Al_2O_3 with spinel structure occurs from the phase separated amorphous regions. The average crystal sizes change from ca. 2 to 23 nm, while the lattice parameter a increases from 7.915 to 7.979 Å. Ferrous ions enter the structure of spinel crystals in tetrahedral position giving rise to a broad band absorption in the spectral range of 1930 nm due to the $^5E \rightarrow {}^5T_2$ (^5D) transition.

The precise control of the heat-treatment schedule allows tailoring the absorption properties of the developed transparent nanophase glass-ceramics.

References

[1] Method of Making Ceramics and Product Thereof. Method of Making Ceramics and Product Thereof: patent 2920971 U.S. Stookey, S.D. January 12, 1960.

[2] Bach H., Krause D. *Low Thermal Expansion Glass Ceramics*, Springer-Verlag Berlin Heidelberg, 2005, 246 p.

[3] Höland W., Beall G.H. *Glass-Ceramic Technology*, Wiley: Hoboken, NJ, USA, 2012, 414 p.

[4] Zanotto E.D. A bright future for glass-ceramic. *Am Ceram Soc Bull.,* 2010, **89** (8), P. 19–27.

[5] Venkateswaran C., Sreemoolanadhan H., Vaish R. Lithium aluminosilicate (LAS) glass-ceramics: a review of recent progress. *Int. Mater. Rev.,* 2022, **67** (6), P. 620–657.

[6] Zandona A., Patzig C., Rüdinger B., Hochrein O., Deubener J. TiO_2(B) nanocrystals in Ti-doped lithium aluminosilicate glasses. *J. Non-Cryst. Solids*, 2019, **2**, 100025.

[7] Fernandez-Martin C., Bruno G., Crochet A., Ovono D.O., Comte M., Hennet L. Nucleation and growth of nanocrystals in glass-ceramics: an in situ SANS perspective. *J. Am. Ceram. Soc.,* 2012, **95** (4), P. 1304–1312.

[8] Glatz P., Comte M., Montagne L., Doumert B., Cousin F., Cormier L. Structural evolution at short and medium range distances during crystallization of a P_2O_5–Li_2O–Al_2O_3–SiO_2 glass. *J. Am. Ceram. Soc.,* 2020, **103** (9), P. 4969–4982.

[9] Vigier M., Deniard P., Gautron E., Gautier N., Genevois C., Ory S., Allix M., Kacem I.B., Jobic S. Microstructural insights on lithium aluminum silicate (LAS) glass ceramics. *Ceram. Int.*, 2024, **50** (16), P. 29011–29015.

[10] Kleebusch E., Patzig C., Krause M., Hu Y., Höche T., Rüssel C. The effect of TiO_2 on nucleation and crystallization of a Li_2O–Al_2O_3–SiO_2 glass investigated by XANES and STEM. *Sci. Rep.,* 2018, **8**, 2929.

[11] Kleebusch E., Patzig C., Höche T., Rüssel C. The evidence of phase separation droplets in the crystallization process of a Li_2O–Al_2O_3–SiO_2 glass with TiO_2 as nucleating agent – An X-ray diffraction and (S)TEM-study supported by EDX-analysis. *Ceram. Int*., 2018, **44**, P. 2919–2926.

[12] Naumov A.S., Shakhgildyan G.Y., Golubev N.V., Lipatiev A.S., Fedotov S.S., Alekseev R.O., Ingat'eva E.S., Savinkov V.I., Sigaev V.N. Tuning the coefficient of thermal expansion of transparent lithium aluminosilicate glass-ceramics by a two-stage heat treatment. *Ceram.,* 2023, **7** (1), P. 1–14.

[13] Raghuwanshi V.S., Rüssel C., Hoell A., Crystallization of $ZrTiO_4$ nanocrystals in lithium-alumino-silicate glass ceramics: anomalous small-angle X-ray scattering investigation. *Cryst. Growth Des.,* 2014, **14** (6), P. 2838–2845.

[14] Höche T., Patzig C., Gemming T., Wurth R., Rüssel C, Avramov I., Temporal evolution of diffusion barriers surrounding $ZrTiO_4$ nuclei in lithia aluminosilicate glass-ceramics. *Cryst. Growth Des*., 2012, **12** (3), P. 1556–1563.

[15] Zheng T., Li M.H., Ma Y.P., Jiang H. Kinetic analysis of the crystallization of Y_2O_3 and La_2O_3 doped Li_2O–Al_2O_3–SiO_2 glass. *RSC Adv*., **14** (10), P. 7052–7060.

[16] Li B., Wang S., Fang Y. Effect of Cr_2O_3 addition on crystallization, microstructure and properties of Li_2O–Al_2O_3–SiO_2 glass-ceramics. *J. Alloys Compd*., 2017, **693**, P. 9–15.

[17] Lilensten L., Fu Q., Wheaton B.R., Credle A.J., Stewart R.L., Kohli J.T. Kinetic study on lithium-aluminosilicate (LAS) glass-ceramics containing MgO and ZnO. *Ceram Int*., 2014, **40** (8 PART A), P. 11657–11661.

[18] Alekseeva I.P., Dymshits O.S., Tsenter, M.Y., Zhilin A.A. Influence of various alkali and divalent metal oxides on phase transformations in NiO-doped glasses of the Li_2O–Al_2O_3–SiO_2–TiO_2 system. *J. Non-Cryst. Solids*, 2011, **357**, P. 2209-2214.

[19] Dymshits O., Bachina A., Alekseeva I., Golubkov V., Tsenter M., Zapalova S., Bogdanov K., Danilovich D., Zhilin A. Phase transformations upon formation of transparent lithium alumosilicate glass-ceramics nucleated by yttrium niobates. *Ceram*., 2023, **6**, P. 1490–1507.

[20] Sun T., Zheng C., Zhang F., Zhang J., Han J., Xie J., He J., Jiang H. Mixed CaO/MgO effect on microstructure, mechanical properties and crystallization behaviour of Li_2O–Al_2O_3–SiO_2–ZrO_2–P_2O_5 glass. *J. Non-Cryst. Solids*, 2023, **616**, 122457.

[21] Guo Y., Wang J., Ruan J., Han J., Xie J., Liu C. Microstructure and ion-exchange properties of glass-ceramics containing $ZnAl_2O_4$ and β-quartz solid solution nanocrystals, *J. Eur. Ceram. Soc*., 2021, **41** (10), P. 5331–5340.

[22] Rao C.S., Rao M.C., Srikumar T. Optical absorption studies on lithium aluminosilicate glasses doped with low concentrations of WO_3. *Int. J. Chemtech Res*., 2014, **6** (7), P. 3935–3938.

[23] Dymshits O., Shepilov M., Zhilin A. Transparent glass-ceramics for optical applications. *MRS Bull*., 2017, **42**, P. 200–205.

[24] Dymshits O.S., Alekseeva I.P., Zhilin A.A., Tsenter M.Y., Loiko P.A., Skoptsov N.A., Malyarevich A.M., Yumashev K.V., Mateos X., Baranov A.V. Structural characteristics and spectral properties of novel transparent lithium aluminosilicate glass-ceramics containing (Er,Yb)NbO_4 nanocrystals. *J. Lumin.,* 2015, **160**, P. 337–345.

[25] Loiko P.A., Dymshits O.S., Alekseeva I.P., Zhilin A.A., Tsenter M.Y., Vilejshikova E.V., Yumashev K.V., Bogdanov K.V. Structure and spectroscopic properties of transparent glass-ceramics with (Eu^{3+},Yb^{3+}):$YNbO_4$ nanocrystals. *J. Lumin.,* **2016**, **179**, P. 64–73.

[26] Alekseeva I.P., Bobovich Y.S., Tsenter M.Y., Chuvaeva T.I. Raman spectra of glass ceramics belonging to the Li_2O–Al_2O_3–SiO_2–TiO_2 system and the nature of the phases containing titanium. *J. Appl. Spectrosc*., 1981, **35**, P. 1008–1012.
[27] Schneider C.A., Rasband W.S., Eliceiri K.W. NIH Image to ImageJ: 25 years of image analysis. *Nat. Methods*, 2012, **9** (7), P. 671–675.
[28] Lipson H., Steeple H., in: McMillan (Ed.), Interpretation of X-Ray Powder Patterns, Martins Press, London, N.Y., 1970, p. 344.
[29] Ovono Ovono D., Berre S., Pradeau P., Comte M., Bruno G., Study of the crystallization kinetics of LAS glass by differential scanning calorimetry, X-ray diffraction, and beam bending viscometry. *Thermochim. Acta*, 2012, **527**, P. 158–164.
[30] Dymshits O.S., Zhilin A.A., Petrov V.I., Tsenter M.Ya., Chuvaeva T.I., Golubkov V.V. A Raman spectroscopic study of phase transformations in titanium-containing lithium aluminosilicate glasses. *Glass Phys. Chem*., 1998, **24**, P. 79–96.
[31] Eremeev K., Dymshits O., Alekseeva I., Khubetsov A., Zapalova S., Tsenter M., Basyrova L., Serres J.M., Mateos X., Loiko P., Popkov V., Zhilin A. Effect of redox conditions of glass melting on the structure and the properties of titanium-containing gahnite glass-ceramics. *J. Eur. Ceram. Soc*., 2024, **44**, P. 3362–3380.
[32] Alekseeva I.P., Belyaevskaya N.M., Bobovich Ya.S., Tsenter M.Ya., Chuvaeva T.I. Recording, interpretation, and some examples of application of Raman spectra for glass ceramics activate with titanium (IV) oxide. *Opt. Spectrosc*., 1978, **45**, P. 927–936.
[33] Sprengard R., Binder K., Brandle M., Fotheringham U., Sauer J., Pannhorst W. On the interpretation of the experimental Raman spectrum of β-eucryptite $LiAlSiO_4$ from atomistic computer modeling. *J. Non-Cryst. Solids*, 2000, **274**, P. 264–270.
[34] Shirasuka K., Yanagida H., Yamaguchi G. The preparation of η-alumina and its structure. *Mater. Sci.*, 1976, **84**, P. 610–613.
[35] Basyrova L., Bukina V., Balabanov S., Belyaev A., Drobotenko V., Dymshits O., Alekseeva I., Tsenter M., Zapalova S., Khubetsov A., Zhilin A., Volokitina A., Vitkin V., Mateos X., Serres J.M., Camy P., Loiko P. Synthesis, structure and spectroscopy of Fe^{2+}:$MgAl_2O_4$ transparent ceramics and glass-ceramics. *J. Lumin*., 2021, **236**, 118090.

Accepted 7 December 2024

Information about the authors:

Kristina A. Trukhanova – Nordwestlab LLC, 15.2 Line 26th of Vasilyevsky Island, St. Petersburg, 199106, Russia; ORCID 0000-0001-5587-4037; kristina.truhanova@gmail.com

Olga S. Dymshits – Ioffe Institute, 26 Politekhnicheskaya, St. Petersburg, 194021, Russia; Vavilov State Optical Institute, 36 Babushkina, St. Petersburg, 192171, Russia; ORCID 0000-0003-1980-0561; vodym1959@gmail.com

Irina P. Alekseeva – Vavilov State Optical Institute, 36 Babushkina, St. Petersburg, 192171, Russia; vgolub19@gmail.com

Kirill V. Bogdanov – Saint Petersburg National Research University of Information Technologies, Mechanics and Optics, Kronverkskiy, 49, St. Petersburg, 197101, Russia; ORCID 0000-0003-4243-1354; kirw.bog@gmail.com

Svetlana S. Zapalova – Vavilov State Optical Institute, 36 Babushkina, St. Petersburg, 192171, Russia; zenii99@yandex.ru

Maksim I. Tenevich – Ioffe Institute, 26 Politekhnicheskaya, St. Petersburg, 194021, Russia; ORCID 0000-0003-2003-0672; mtenevich@gmail.com

Anastasia K. Bachina – Ioffe Institute, 26 Politekhnicheskaya, St. Petersburg, 194021, Russia; ORCID 0000-0001-7015-1435; a.k.bachina@yandex.ru

Vadim I. Popkov – Ioffe Institute, 26 Politekhnicheskaya, St. Petersburg, 194021, Russia; ORCID 0000-0002-8450-4278; vip-07@yandex.ru

Aleksandr A. Zhilin – D. V. Efremov Institute of Electrophysical Apparatus, 3 Doroga na Metallostroi, pos. Metallostroi, St. Petersburg, 196641, Russia; ORCID 0000-0002-6681-6577; zhilin1311@yandex.ru

Conflict of interest: the authors declare no conflict of interest.

NANOSYSTEMS:
PHYSICS, CHEMISTRY, MATHEMATICS

Popov P.A., et al. *Nanosystems: Phys. Chem. Math.*, 2025, **16** (1), 67–73.
http://nanojournal.ifmo.ru
DOI 10.17586/2220-8054-2025-16-1-67-73

Original article

Application of the numerical model of temperature-dependent thermal conductivity in $Ca_{1-x}Y_xF_{2+x}$ heterovalent solid solution nanocomposites

Pavel A. Popov[1], Alexandr V. Shchelokov[1], Vasilii A. Konyushkin[2], Andrey N. Nakladov[2], Pavel P. Fedorov[2]

[1]Petrovsky Bryansk State University, Bryansk, Russia

[2]Prokhorov General Physics Institute of the Russian Academy of Sciences, Moscow, Russia

Corresponding author: Pavel P. Fedorov, ppfedorov@yandex.ru

ABSTRACT A series of $Ca_{1-x}Y_xF_{2+x}$ solid solution $x = 0.0005, 0.003, 0.007, 0.013, 0.02, 0.03, 0.04$ single crystals were grown using the Bridgman method. The thermal conductivity of single crystals was measured using the absolute method of longitudinal heat flow in the range of 50 – 300 K. With an increase in the concentration of yttrium fluoride in the solid solution, a transition is observed from the temperature dependence characteristic of single crystals to a monotonically increasing one with increasing temperature, which is characteristic of disordered media. This behavior is associated with the scattering of phonons on nanosized clusters of defects present in the solid solution. Within the framework of a two-component model, including a superposition of thermal resistance coefficients from ordered and disordered media, a system of equations was obtained that provides a quantitative description of the experiment.

KEYWORDS nanocomposite, inorganic fluorides, fluorite, thermal conductivity, phase diagram, heterovalent isomorphism, defect clusters

FOR CITATION Popov P.A., Shchelokov A.V., Konyushkin V.A., Nakladov A.N., Fedorov P.P. Application of the numerical model of temperature-dependent thermal conductivity in $Ca_{1-x}Y_xF_{2+x}$ heterovalent solid solution nanocomposites. *Nanosystems: Phys. Chem. Math.*, 2025, **16** (1), 67–73.

1. Introduction

Solid solutions of yttrium fluoride in calcium fluoride are a classical object of solid state physics and chemistry. The mineral yttrofluorite was discovered more than 100 years ago [1, 2], its research made it possible to formulate the concept of heterovalent isomorphism [3–5]. Further studies of the structure of the $Ca_{1-x}Y_xF_{2+x}$ solid solution [6–22] revealed a complex pattern of association of structural defects, leading to the formation of nanosized clusters coherently embedded in the fluorite lattice [23–25]. This allows us to consider the corresponding solid solution as a unique example of nanosized composites [26, 27].

The phase diagram of the CaF_2–YF_3 system is presented in Fig. 1 [28]. The $Ca_{1-x}Y_xF_{2+x}$ solid solution is characterized by closeness of the liquidus and solidus curves, which makes it possible to grow high-quality single crystals from the melt [29]. The low-temperature decomposition of this solid solution is inhibited.

The $Ca_{1-x}Y_xF_{2+x}$ solid solution is a photonics material, transparent in a wide optical range, from vacuum ultraviolet to mid-IR, differing from pure fluorite in its increased hardness and lack of cleavage [25]. It is a matrix for solid-state lasers, both in the form of single crystals and ceramics [30–51]. In addition, it is characterized by increased ionic conductivity, which determines its use in electrochemical studies [52–54].

Thermal conductivity is the main characteristic that determines the behavior of a material under operating conditions. Preliminary measurements of the thermal conductivity of some single crystals of the $Ca_{1-x}Y_xF_{2+x}$ solid solution were carried out in [55, 56]. Currently, a model has emerged [57], based on the approach formulated in [58, 59], which makes it possible to quantitatively describe the temperature and concentration dependences of the thermal conductivity of such solid solutions.

The purpose of this work was to determine the thermal conductivity of original nanocomposite system, namely, single crystals of the $Ca_{1-x}Y_xF_{2+x}$ solid solution for the missing concentration region and to quantitatively describe the experimental results based on the existing model.

The technique for growing crystals is identical to that used in [56]. The starting materials used were yttrium fluoride of the chemically pure grade, melted under a fluorinating atmosphere of Teflon pyrolysis products, and calcium fluoride – broken optical crystals produced by the State Optical Institute named after S. I. Vavilov. Single crystals with a diameter of 10 mm were grown by the Bridgman method in a seven-channel graphite crucible in a static CF_4 atmosphere (pressure 80 Torr). Drawing speed is 10 mm/h, temperature gradient is 50 ± 10 K/cm. No corrections were made for changes in composition during crystal growth.

© Popov P.A., Shchelokov A.V., Konyushkin V.A., Nakladov A.N., Fedorov P.P., 2025

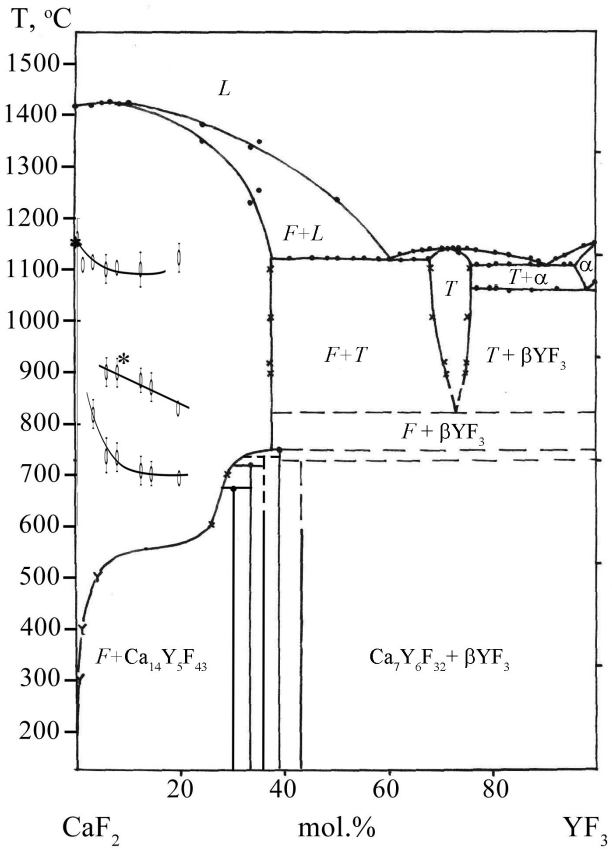

FIG. 1. Phase diagram of the CaF_2–YF_3 system [28]. Phase F denotes the $Ca_{1-x}Y_xF_{2+x}$ solid solution

The objects of the experimental study of thermal conductivity in this work were single-crystal samples of $Ca_{1-x}Y_xF_{2+x}$ with yttrium trifluoride content $x = 0.0005, 0.003, 0.007, 0.013, 0.02, 0.03, 0.04$ cubic structure.

The determination of thermal conductivity in the temperature range 50 – 300 K was carried out using the absolute stationary method of longitudinal heat flow [60]. The error in determining the absolute value of thermal conductivity did not exceed 5 %.

The measurement results in the form of graphs of the temperature dependence of thermal conductivity $k(T)$ are presented in Fig. 2. To complete the picture, the results of previous studies of the thermal conductivity of $Ca_{1-x}Y_xF_{2+x}$ samples with the content of the second component $x = 0.005$ and $x = 0.05 – 0.20$ have been added here (the technique for synthesizing single crystals and measuring thermal conductivity is identical to those used in this work) [56]. The numerical data $k(T)$ for the new samples studied are given in Table 1.

TABLE 1. Smoothed values of thermal conductivity of $Ca_{1-x}Y_xF_{2+x}$ single crystals

YF_3 Content, mol. %	Temperature, K					
	50	100	150	200	250	300
0.05	59.5	29.5	19.2	14.2	11.2	9.3
0.3	26.7	21.9	16.1	12.5	10.2	8.7
0.7	12.5	14.8	12.7	10.7	9.2	7.9
1.3	6.90	9.14	9.02	8.20	7.43	6.8
2	4.70	6.85	7.30	6.97	6.53	6.0
3	3.27	5.20	5.82	5.78	5.51	5.1
4	2.36	3.93	4.65	4.80	4.64	4.45

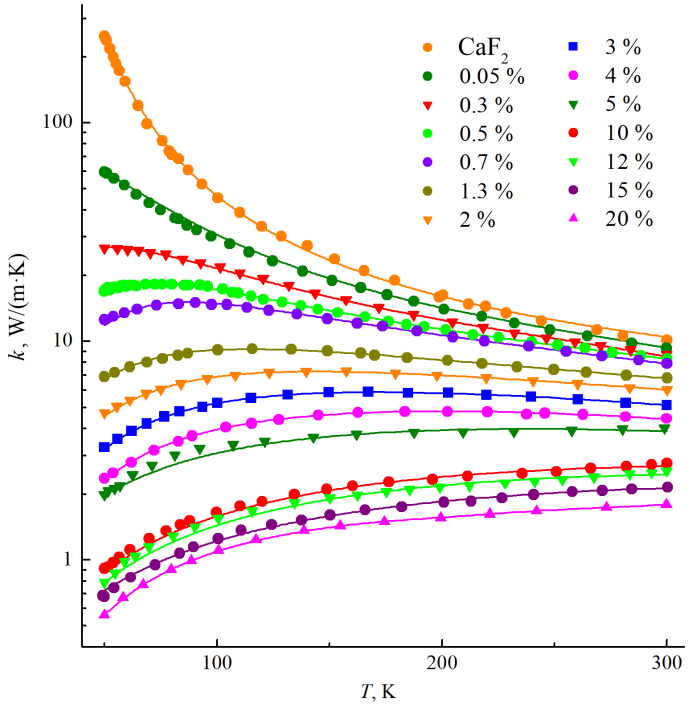

FIG. 2. Temperature-dependent thermal conductivity coefficient for $Ca_{1-x}Y_xF_{2+x}$ solid solution single crystals: markers represent experimental values, and lines are fitted curves calculated by model (1)

As can be seen in Fig. 2, there is a monotonic concentration transition of the nature of the temperature dependence from typical for dielectric single crystals to glass-like. The low-temperature maximum $k(T)$ inherent in ordered media appears ($x = 0.005$, i.e. 0.5 mol %) in the temperature range studied, becomes lower and wider with increasing concentration, shifts towards higher temperatures and completely disappears at $x > 0.05$. This kind of transition has been detected many times for various heterovalent solid solutions of the $M_{1-x}R_xF_{2+x}$ type, where M = Ca, Sr, Ba, Cd, Pb, R=Y, La–Lu (see, for example, [61–63]). It is associated with the formation of nanosize defect clusters in such crystals and corresponding high-intensity phonon scattering.

The $Ca_{1-x}Y_xF_{2+x}$ solid solution is structurally a model for similar compositions with fluorides of rare earth elements of the yttrium subgroup. The most likely type of defect clusters is the so-called hexameric cluster Y_6F_{37}, existing in ordered fluorite-like phases, formed in the system CaF_2–YF_3 [24,64–66]. This point of view is confirmed by the results of precision structural studies of $Ca_{1-x}Y_xF_{2+x}$ solid solution [17,18,20,21] and investigation of its physical properties [22, 67]. The scheme of embedding such a cluster into the fluorite lattice according to the Bevan, Greis and Strahle [23] model is shown in Fig. 3. The size of such clusters with their defective periphery is about 1.5 nm.

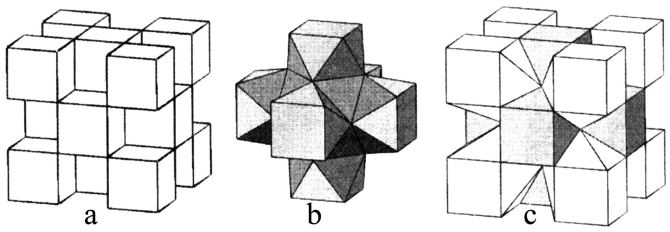

FIG. 3. Fragment of the fluorite lattice (a), the Y_6F_{37} cluster (b), and the Y_6F_{37} cluster incorporated into the fluorite lattice (c)

In application to the obtained experimental values of $k(T)$, we test the relatively simple formulaic expression proposed in [57] for describing the specific thermal resistance $w = 1/k$ of heterovalent solid solutions. This expression looks like:

$$\frac{1}{k} = \frac{1-A}{\beta\sqrt{\frac{k_0}{d}}\cdot\arctan\left(\frac{\sqrt{k_0 d}}{\beta}\right)} + \frac{A}{D+BT+CT^2}. \qquad (1)$$

Here A is the contribution of the thermal resistance associated with the introduction of trivalent rare earth ions and the formation of clusters of defects ("amorphous component"); β is a parameter depending on the type of rare earth dopant; k_0 is the thermal conductivity coefficient of the undoped crystal; d is the concentration of the rare earth dopant; D, B and C are coefficients of the polynomial describing the "amorphous component" of the thermal conductivity coefficient.

In this work, the coefficient k_0 for the thermal conductivity of a nominally pure CaF_2 crystal [68] is taken in accordance with the following expression

$$k_0 = a_1 + a_2 \exp(a_3/T)\, T^{-1}. \tag{2}$$

As can be seen in Fig. 1, the calculated curves have a slight deviation from the experimental $k(T)$ points. The discrepancy in almost all cases does not exceed the experimental error of 5 %. The values of the parameters included in expressions (1) and (2), which do not depend on the concentration of the solid solution, were: $a_1 = 3.38$ W·m^{-1}K^{-1}, $a_2 = 1499$ W·m^{-1}, $a_3 = 104.7$, $\beta = 0.24$. The values of parameters A, B, C and D, directly related to the concentration of yttrium fluoride in the solid solution, are given in Table 2.

TABLE 2. Values of parameters A, B, C and D included in expression (1)

YF_3 Content, mol. %	A	C, W·m^{-1}K^{-3}	B, W·m^{-1}K^{-2}	D, W·m^{-1}K^{-1}
0.0005	0.11	$-1.183 \cdot 10^{-4}$	$2.490 \cdot 10^{-2}$	8.758
0.003	0.155	$-2.852 \cdot 10^{-4}$	$1.036 \cdot 10^{-1}$	1.137
0.005	0.17	$-2.132 \cdot 10^{-4}$	$9.288 \cdot 10^{-2}$	-0.506
0.007	0.21	$-2.514 \cdot 10^{-4}$	$1.087 \cdot 10^{-1}$	-1.881
0.01	0.25	$-3.868 \cdot 10^{-4}$	$1.267 \cdot 10^{-1}$	-2.983
0.013	0.30	$-1.110 \cdot 10^{-4}$	$5.686 \cdot 10^{-2}$	-0.326
0.02	0.40	$-1.009 \cdot 10^{-4}$	$5.154 \cdot 10^{-2}$	-0.362
0.03	0.48	$-8.767 \cdot 10^{-5}$	$4.398 \cdot 10^{-2}$	-0.347
0.04	0.55	$-6.741 \cdot 10^{-5}$	$3.496 \cdot 10^{-2}$	-0.244
0.05	0.60	$-4.006 \cdot 10^{-5}$	$2.355 \cdot 10^{-2}$	0.149
0.1	0.68	$-1.807 \cdot 10^{-5}$	$1.378 \cdot 10^{-2}$	-0.041
0.12	0.70	$-1.728 \cdot 10^{-5}$	$1.288 \cdot 10^{-2}$	-0.038
0.15	0.75	$-1.288 \cdot 10^{-5}$	$1.021 \cdot 10^{-2}$	0.071
0.2	0.77	$-1.638 \cdot 10^{-5}$	$1.032 \cdot 10^{-2}$	-0.014

An increase in the concentration of the solid solution is accompanied by a natural increase in the values of parameter A and their approach to the upper threshold value $A = 1$ (see Fig. 4). To some approximation, the dependence $A(d)$, as in the case of the $Ca_{1-x}Yb_xF_{2+x}$ solid solution [57], can be described by a logarithmic function with a constant component (the parameter d in expression (1) is equal to the value x in the composition formula).

It is not possible to detect clear correlations for parameters B, C and D. To a rough approximation, the decreasing nature of the absolute values of the parameters C and B with increasing Y content, and the weak dependence of $B(d)$ are violated in the region of the lowest concentrations, apparently due to the strong local concentration dependence of the thermal conductivity coefficient. In Fig. 5, this dependence is presented in the form of two isotherms $k(x)$. It can be seen that the new experimental points $k(x)$ for samples with low concentrations fell almost on the interpolation curves proposed earlier [56].

2. Conclusion

In the temperature range 50 – 300 K, the thermal conductivity of the original nanocomposite system, namely, single crystals of the $Ca_{1-x}Y_xF_{2+x}$ solid solution with a low concentration of yttrium fluoride ($x = 0.0005$ – 0.04) was experimentally studied. The inclusion of nanosized clusters in the fluorite lattice leads to a sharp drop in thermal conductivity due to pronounced phonon scattering. We proposed the formula expression for the thermal conductivity coefficient. Testing showed its suitability for describing the dependence of the thermal conductivity coefficient on temperature and concentration for heterovalent $Ca_{1-x}R_xF_{2+x}$ solid solutions, where R is represented by Y and Yb, which differ greatly in mass. In the future, it is planned to search for ways to improve the proposed model based on its application to solid solutions of different compositions with a heterovalent type of ion substitution.

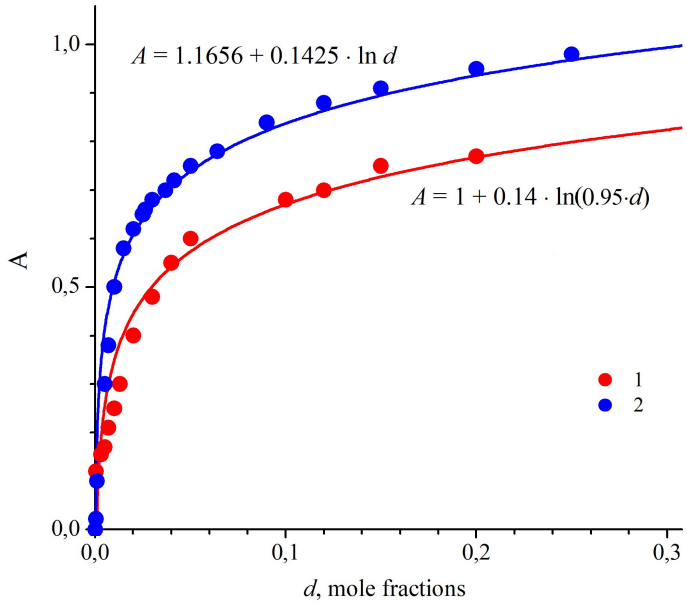

FIG. 4. Parameter A versus YF_3 concentration in $Ca_{1-x}Y_xF_{2+x}$ (1) and $Ca_{1-x}Yb_xF_{2+x}$ (2) solid solutions

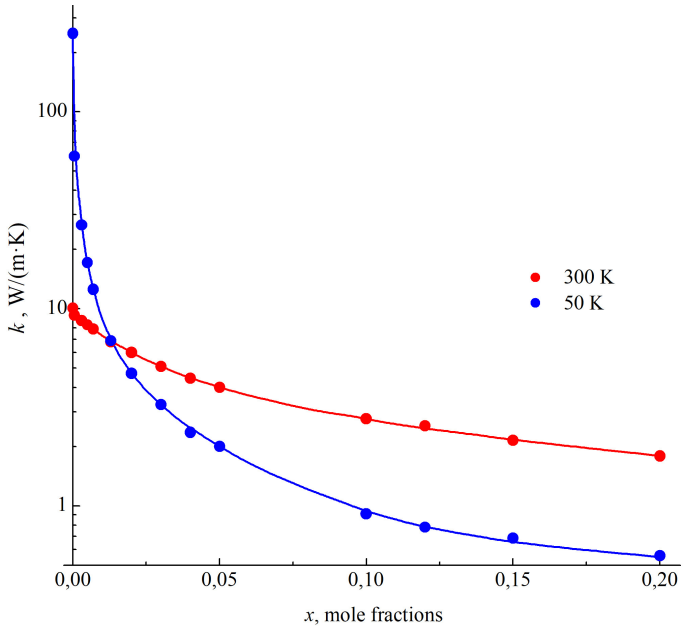

FIG. 5. Dependence of the thermal conductivity of the $Ca_{1-x}Y_xF_{2+x}$ solid solution on the content of the second component

References

[1] Vogt T. Uber die Flusspat – Yttriumfluoritgruppe. *Neues Jahrb. Mineral*, 1914, **2** (1), P. 9–15.

[2] Sobolev B.P. *The Rare Earth Trifluorides. P. 1. The high temperature chemistry of the rare earth trifluorides*. Barcelona, Institut d'Estudis Catalans, 2000.

[3] Goldschmidt V.M., Barth T., Lunde G., Zachariasen W. *Geochemische Verteilungsgesetze der Elemente, VII, Skrift Norske Vid. Acad. Oslo, I, Mat.-Nat. Klasse*, 1926, **1** (2), S. 1–117.

[4] Bokii G.B. *Kristallokhimiya (Crystal Chemistry)*. M.: Nauka, 1971. (in Russian)

[5] Filatov S.K., Krivovichev S.V., Bubnova R.S. *Obschaya kristallokhimiya (General Crystal Chemistry).* St. Petersburg: Izd. SPbGU, 2018. (in Russian)

[6] Hahn H., Seemann W., Kohn H.-L. Zur Mischkristallbildung in den Systemen CaF_2/YF_3, CaF_2/LaF_3, SrF_2/LaF_3 und BaF_2/LaF_3. *Zeitschrift für anorganische und allgemeine Chemie*, 1969, **369** (1–2), P. 48–58.

[7] Alexandrov V.B., Garashina L.S. New data on the structure of CaF_2-TRF_3 solid solutions. *Dokl. Akad. Nauk USSR*, 1969, **189** (2), P. 307–310. (in Russian)

[8] Fedorov P.P. , Izotova O.E., Alexandrov V.B., Sobolev B.P. New phases with fluorite-derived structure in CaF_2–(Y, Ln)F_3 systems. *J. Solid State Chem.*, 1974, **9** (4), P. 368–374.

[9] Osiko V.V., Prokhorov A.M. Investigation of the structure of crystals with an admixture of rare earth elements by spectroscopic methods. In: *Problems of modern crystallography*, M.: Nauka, 1975, P. 280–301.
[10] Cheetham A.K., Fender B.E.F., Steele D., Taylor R.I., Willis B.T.M. Defect structure of fluorite compounds containing excess anions. *Solid State Comm*., 1970, **8**, P. 171–173.
[11] Cheetham A.K., Fender B.E.F., Cooper M.J. Defect structure of calcium fluoride containing excess anions: Bragg scattering. *J. Phys. C.: Solid State Phys*., 1971, **4,** P. 3107–3121.
[12] Allnatt A.R., Yuen P. S. Defect interactions in ionic fluorite structures: Pair clusters in CaF_2 doped by YF_3. *J. Phys. C.: Solid State Phys*., 1975, **8**, P. 2199–2212.
[13] Jacobs P. W.M., Ong S.H. Studies of defect clustering in CaF_2:Y^{3+} by ionic conductivity and thermal depolarization. *J. Phys. Chem. Sol*., 1980, **41**, P. 431–436.
[14] Laval J.P., Frit B. Defect structure of anion-excess fluorite-related $Ca_{1-x}Y_xF_{2+x}$ solid solutions. *J. Solid State Chem*., 1983, **49**, P. 237–246.
[15] Laval J.P., Abaouz A., Frit B., Le Bail A. Short-range order in the ànion-excess fluorite-related $Ca_{0.68}Ln_{0.32}F_{2.32}$ solid solutions: EXAES study of the Eu environment. *J. of Solid State Chemistry*, 1990, **85** (1), P. 133–143.
[16] Catlow C.R.A., Chadwick A.V., Corish J., Moroney L.M., O'Reilly A.N. Defect structure of doped CaF_2 at high temperatures. *Phys. Rev. B*, 1989, **39** (3), P. 1897–1906.
[17] Hofmann M., Hull S., Mclntyre G.J., Wilson C.C. A neutron diffraction study of the superionic transition in $(Ca_{1-x}Y_x)F_{2+x}$. *J. Phys.: Condens. Matter*., 1997, **9**, P. 845–857.
[18] Hull S., Wilson C.C, The defect structure of anion-excess $(Ca_{1-x}Y_x)F_{2+x}$ with $x = 0.06$. *J. Solid State Chem.*, 1992, **100** (1), P. 101–114.
[19] Wang F., Grey C.P. Probing the defect structure of anion-excess $Ca_{1-x}Y_xF_{2+x}$ ($x = 0.03 - 0.32$) with high-resolution 19 F magic-angle spinning nuclear magnetic resonance spectroscopy. *Chem. Mater*., 1998, **10**, P. 3081–3091.
[20] Bendall P.J., Catlow C.R.A., Corish J., Jacobs P.W.M. Jacobs. Defect aggregation in anion-excess fluorites. II. Clusters containing more than two impurity atoms. *J. Solid State Chem*., 1984, **51**, P. 159–169.
[21] Otroshchenko L.P., Aleksandrov V.B., Bydanov N.N., Simonov V.I., Sobolev B.P. Neutron diffraction refinement of the structure of the $Ca_{0.9}Y_{0.1}F_{2.1}$ solid solution. *Crystallography*, 1988, **33** (3), P. 764–765.
[22] Krahl T., Scholz G., Kemnitz E. Solid Solutions CaF_2–YF_3 with Fluorite Structure Prepared on the Sol–Gel Route: Investigation by Multinuclear MAS NMR Spectroscopy. *J. Phys. Chem. C*, 2014, **118** (36), P. 21066–21074.
[23] Bevan D.J.M., Greis O., Strahle J. A new structural principle in anion-excess fluorite-related superlattices. *Acta Cryst*., 1980, **36** (6), P. 889–890.
[24] Greis O., Haschke J.M. *Rare Earth Fluorides. Handbook on the Physics and Chemistry of Rare Earth*. Ed. K.A. Gscheidner & L. Eyring. Amsterdam, New York, Oxford, 1982, **5** (45), P. 387–460.
[25] Sobolev B.P. *The Rare Earth Trifluorides. P. 2. Introduction to Materials Science of Multicomponent Metal Fluoride Crystals*. Barcelona, Institut d'Estudis Catalans, 2001.
[26] Sobolev B.P., Golubev A.M., Erero P. Fluorite phases $M_{1-x}R_xF_{2+x}$ {M – Ca, Sr, Ba; R – rare earth elements) – nanostructured materials. *Crystallography*. 2003, **48** (1), P. 148–169.
[27] Kuznetzov S.V., Osiko V.V., Tkatchenko E.A., Fedorov P.P. Inorganic nanofluorides and related nanocomposites. *Russian Chem. Rev*., 2006, **75** (12), P. 1065–1082.
[28] Alexandrov A.A., Rezaeva A.D., Konyushkin V.A., Nakladov A.N., Kuznetsov S.V., Fedorov P.P. Features of $Ca_{1-x}Y_xF_{2+x}$ solid solution heat capacity behavior: diffuse phase transition. *Nanosystems: Physics, Chemistry, Mathematics*, 2023, **14** (2), P. 279–285.
[29] Kuznetsov S.V., Fedorov P.P. Morphological Stability of Solid-Liquid Interface during Melt Crystallization of Solid Solutions $M_{1-x}R_xF_{2+x}$. *Inorg. Mater.*, 2008, **44** (13), P. 1434–1458. (Supplement)
[30] Bagdasarov Kh.S., Voronko Yu.K., Kaminskii A.A., Krotova L.V., Osiko V.V. Modification of the optical properties of CaF_2-TR^{3+} crystals by yttrium impurities. *Phys. stat. sol*., 1965, **12**, P. 905–912.
[31] Iparraguirre I., Azkargorta J., Fernández J., Balda R., Oleaga A., Kaminskii A.A. Laser spectral dynamics of Nd^{3+} in CaF_2–YF_3 crystals. *J. Optical Soc. America B*, 1999, **16** (9), P. 1439–1446.
[32] Fernández J., Oleaga A., Azkargorta J., Iparraguirre I., Balda R., Voda M., Kaminskii A.A. Nd^{3+} laser spectral dynamics in CaF_2–YF_3–NdF_3 crystals. *Optical Materials*, 1999, **13** (1), P. 9–16.
[33] Kuznetsov S.V., Alexandrov A.A., Fedorov P.P. Optical Fluoride Nanoceramics. *Inorg. Mater.*, 2021, **57** (6), P. 555–578.
[34] Wu Y., Su L., Wang Q., Li H., Zhan Y., Jang D., Qian X., Wang C., Zheng L., Chen H., Xu J., Ryba-Romanowski W., Solarz P., Lisiecki R. Spectroscopic properties of Yb-doped CaF_2–YF_3 solid-solution laser crystal. *Laser Physics*, 2013, **23** (10), 105805.
[35] Su L.B., Wang Q.G., Li H.J., Brasse G., Camy P., Doualan J.L., Braud A., Moncorgé R., Zhan Y.Y., Zheng L.H., Qian X.B., Xu J. Spectroscopic properties and CW laser operation of Nd, Y-codoped CaF_2 single crystals. *Laser Phys. Lett.*, 2013, **10** (3), 035804.
[36] Chen H., Ikesue A., Noto H., Uehara H., Ushinuma Y., Muroga T., Yasuhara R. Nd^{3+} -activated CaF_2 ceramic lasers. *Optics Letters*, 2019, **44** (13), P. 3378–338.
[37] Doualan J.L., Su L.B., Brasse G., Benayad A., Ménard V., Zhan Y.Y., Braud A., Camy P., Xu J., Moncorgé R. Improvement of infrared laser properties of Nd:CaF_2 crystals via codoping with Y^{3+} and Lu^{3+} buffer ions. *J. Opt. Soc. Am. B*, 2013, **30**, P. 3018–3021.
[38] Wang Q., Su L., Ma F., Zhan Y., Jiang D., Qian X., Wang J., Zheng L., Xu J., Ryba-Romanowski W., Solarz P., Lisiecki R. Nd^{3+}:CaF_2 crystal with controlled photoluminescence spectroscopic properties by codoping Y^{3+} ions. *Optical Materials*, 2013, **36**, P. 455–457.
[39] Qin Z.P., Xie G.Q., Ma J., Ge W.Y., Yuan P. , Qian L.J., Su L.B., Jiang D.P., Ma F.K., Zhang Q., Cao Y.X., Xu J. Generation of 103 fs mode-locked pulses by a gain linewidth-variable Nd,Y:CaF_2 disordered crystal. *Optics Letters*, 2014, **39**, 1737.
[40] Li C., Fan M., Liu J., Su L., Jiang D., Qian X., Xu J. Operation of continuous wave and Q-switching on diode-pumped Nd,Y:CaF_2 disordered crystal. *Optics & Laser Technology*, 2015, **69**, P. 140–143.
[41] Sun Z., Mei B., Li W., Liu X., Su L. Synthesis and optical characterizations of Nd, Y:CaF_2 transparent ceramics. *Optical Materials*, 2017, **71**, P. 35–40.
[42] Li W., Huang H., Mei B., Song J., Xu X. Effect of Y^{3+} ion doping on the microstructure, transmittance and thermal properties of CaF_2 transparent ceramics. *J. of Alloys and Compounds*, 2018, **747**, P. 359–365.
[43] Liu X.-Q., Hao Q.-Q., Liu J., Liu D.-H., Li W.-W., Su L.-B. Yb:CaF_2–YF_3 transparent ceramics ultrafast laser at dual gain lines. *Chin. Phys. B*, 2022, **31** (11), 114205.
[44] Tian J., Cao X., Wang W., Liu J., Dong J., Hu D., Wang Q., Xue Y., Xu X., Xu J. Crystal growth, spectral properties and Judd-Ofelt analysis of Pr: CaF_2–YF_3. *Chinese Phys. B*, 2021, **30** (10), 108101.
[45] Li W., Huang H., Mei B., Wang C., Liu J., Wang Sh., Jiang D., Su L. Fabrication, microstructure and laser performance of Yb^{3+} doped CaF_2–YF_3 transparent ceramics. *Ceramics Int.*, 2020, **46** (11), Part B, P. 19530–19536.

[46] Zhang Y., Zhao Q., Shao B., Lü W., Dong X., You H. Facile hydrothermal synthesis and luminescent properties of Eu-doped CaF_2–YF_3 alkaline-earth ternary fluoride microspheres. *RSC Advances*, 2014, **4**, P. 35750–35756.
[47] Jiang D., Zhan Y., Zhang Q., Ma F., Su L., Tang F., Qian X., Xu J. Nd,Y:CaF_2 Laser Crystals: Novel Spectral Properties and Laser Performance from a Controlled Local Structure. *CrystEngComm*, 2015, **17**, P. 7398–7405.
[48] Babu B.H., Billotte Th., Lyu Ch., Poumellec B., Lancry M., Hao X.-T. Study of femtosecond laser writing in the bulk of Nd, Y co-doped CaF_2 crystals. *OSA Continuum*, 2018, **2** (1), P. 151–161.
[49] Liu X., Yang K., Zhao S., Li T., Luan C., Guo X., Zhao B., Zheng L., Su L., Xu J., Bian J. Growth and lasing performance of a Tm, Y: CaF_2 crystal. *Opt. Lett.*, 2017, **42** (13), P. 2567–2570.
[50] Tian J., Cao X., Wang W., Liu J., Dong J., Hu D., Wang Q., Xue Y., Xu X., Xu J. Crystal growth, spectral properties and Judd–Ofelt analysis of Pr: CaF_2–YF_3. *Chinese Phys. B*, 2021, **30** (10), 108101.
[51] Zhu J., Zhang L., Gao Z., Wang J., Wang Zh., Su L., Zheng L., Wang J., Xu J., We Zh. Diode-pumped femtosecond mode-locked Nd, Y-codoped CaF_2 laser. *Laser Phys. Lett*., 2015, **12**, 035801.
[52] Ivanov-Shitz A.K., Murin I.V. *Ionika tverdogo tela. (Solid State Ionics*. St. Petersburg: SPbU, 2010. (in Russian)
[53] Ivanov-Shits A.K., Sorokin N.I., Fedorov P.P., Sobolev B.P. Specific features of ionic transport in nonstoichiometric fluorite-type $Ca_{1-x}R_xF_{2+x}$ (R = La-Lu, Y, Sc) phases. *Solid State Ionics*, 1990, **37**, P. 125–137.
[54] Sobolev B.P., Sorokin N.I., Bolotina N.B. Nonstoichiometric single crystals $M_{1-x}R_xF_{2+x}$ and $R_{1-y}M_yF_{3-y}$ (M = Ca, Sr, Ba, R – rare earth elements) as fluorine-ionic conductive solid electrolytes. In: *Photonic and electronic properties of fluoride materials*. Ed. A. Tressaud, K. Poeppelmeier. Amsterdam e.a.: Elsevier, 2016. P. 465–491.
[55] Mogilevsky B.M., Tumpurova V.F., Chudnovsky A.F. *Eng. Phys. J*., 1974, **27** (2), P. 287–295.
[56] Popov P.A., Fedorov P.P., Osiko V.V. Thermal Conductivity of Single Crystals of the $Ca_{1-x}Y_xF_{2+x}$ Solid Solutions. *Doklady Physics*, 2014, **59** (5), P. 199–202.
[57] Popov P.A., Shchelokov A.V., Fedorov P.P. Numerical model of temperature-dependent thermal conductivity in $M_{1-x}R_xF_{2+x}$ heterovalent solid solution nanocomposites where M stands for alkaline-earth metals and R for rare-earth metals. *Nanosystems: Phys. Chem. Math.*, 2024, **15** (2), P. 255–259.
[58] Liu K., Bian G., Zhang Z., Ma F., Su L. Modelling and analyzing the glass-like heat transfer behavior of rare-earth doped alkaline earth fluoride crystals. *CrystEngComm*, 2022, **24**, 6468.
[59] Liu K., Bian G., Zhang Z., Ma F., Su L. Simulation and demonstration of glass-like heat transfer equations in rare-earth doped alkaline earth fluoride crystals. *Chinese J. of Physics*, 2024, **88**, P. 584–593.
[60] Popov P.A., Sidorov À.À., Kul'chenkov E.A., Anishchenko A.M., Avetisov I.Sh., Sorokin N.I., Fedorov P.P. Thermal conductivity and expansion of PbF_2single crystal. *Ionics*, 2017, **23** (1), P. 233–239.
[61] Popov P.A., Fedorov P.P., Reiterov V.M., Garibin E.A., Demidenko A.A., Mironov I.A., Osiko V.V. Thermal conductivity of single crystals of $Ca_{1-x}Er_xF_{2+x}$ and $Ca_{1-x}Tm_xF_{2+x}$ solid solutions. *Doklady Physics*, 2012, **57** (3), P. 97–99.
[62] Popov P.A., Fedorov P.P., Konyshkin V.A. Heat Conductivity of $Ca_{1-x}R_xF_{2+x}$ (R = La, Ce, or Pr; $0 \leq x \leq 0.25$) Heterovalent Solid Solutions. *Crystallogr. Rep.*, 2015, **60** (5), P. 744–748.
[63] *Popov P.A., Fedorov P.P. Thermal conductivity of fluoride optical materials. Bryansk: "Desyatochka" Group of Companies, 2012. (in Russian)*
[64] Gettmann W., Greis O. Uber fluorit- und tysonitverwandte ordnungsphasen im system CaF_2-YF_3. *J. Solid State Chem*., 1978, **26** (3), P. 255–263.
[65] Greis O. Pulverrontgenographische untersuchungen und einkristal-elektronen-diffraktion an Tveitit $Ca_{13+\delta}(Y,SE)_{6-\delta}F_{44-\delta}$. *Rev. Chim. Miner*., 1978, **15** (6), P. 481–493.
[66] Golubev A.M. *Nanometer-sized clusters in the structures of $Ba_{1-x}R_xF_{2+x}$ fluorite phases and ordered phases with a derivative structure*. Thesis. M. Schubnikov Institute of Crystallography RAS, 2009.
[67] Kazanskii S.A., Ryskin A.I., Nikiforov A.E., Zaharov A.Yu., Ougrumov M.Yu., Shakurov G.S. EPR spectra and crystal field of hexamer rare-earth clusters in fluorites. *Phys. Rev. B*, 2005, **72**, 014127.
[68] Popov P.A., Dukel'skii K.V., Mironov I.A., Smirnov A.N., Smolyanskii P.L., Fedorov P.P., Osiko V.V., Basiev T.T. Thermal conductivity of CaF_2 optical ceramics. *Doklady Physics,* 2007, **52** (1), P. 7–9.

Submitted 27 June 2024; revised 13 August 2024; accepted 25 November 2024

Information about the authors:

Pavel A. Popov – Petrovsky Bryansk State University, 14 Bezhitskaya str., Bryansk, 241036 Russia; ORCID 0000-0001-7555-1390; tfbgubry@mail.ru

Alexandr V. Shchelokov – Petrovsky Bryansk State University, 14 Bezhitskaya str., Bryansk, 241036 Russia; ORCID 0009-0001-4090-2506; alexandershchelokov@mail.ru

Vasilii A. Konyushkin – Prokhorov General Physics Institute of the Russian Academy of Sciences, 38 Vavilova str., Moscow, 119991 Russia; ORCID 0000-0002-6028-8937; vasil@lst.gpi.ru

Andrey N. Nakladov – Prokhorov General Physics Institute of the Russian Academy of Sciences, 38 Vavilova str., Moscow, 119991 Russia; ORCID 0000-0002-4060-8091; andy-nak@yandex.ru

Pavel P. Fedorov – Prokhorov General Physics Institute of the Russian Academy of Sciences, 38 Vavilova str., Moscow, 119991 Russia; ORCID 0000-0002-2918-3926; ppfedorov@yandex.ru

Conflict of interest: the authors declare no conflict of interest.

NANOSYSTEMS:
PHYSICS, CHEMISTRY, MATHEMATICS

Original article

Sudeshna Kar, Yian Tai *Nanosystems: Phys. Chem. Math.*, 2025, **16** (1), 74–88.
http://nanojournal.ifmo.ru
DOI 10.17586/2220-8054-2025-16-1-74-88

Isomeric protected dipeptides generated stable bio-compatible gold nanoparticles

Sudeshna Kar[1,2], Yian Tai[2]

[1]St. Thomas College of Engineering and Technology, Khidirpur, Kolkata, West Bengal 700023, Kolkata, India
[2]National Taiwan University of Science and Technology, 43 Keelung Road, Taipei-106, Taiwan

Corresponding author: Sudeshna Kar, 06.sudeshna@gmail.com; Yian Tai, ytai@mail.ntust.edu.tw

ABSTRACT It has been observed that two isomeric protected dipeptides which show altered nano-morphologies under similar conditions but behave unaltered to form stable gold nano-particles (AuNPs) having similar shape and size; whereas both the peptides showed fluctuating bio-compatibility but after conjugation with AuNP they show stable bio-compatibility. These gold nano conjugates are very stable, even up to 2 months the AuNPs showed no change in size or shape. Using a straightforward and reproducible one-pot synthetic technique, we were able to produce stable biocompatible gold nanoparticles using two isomeric protected dipeptides.

KEYWORDS bio-compatibility, isomeric dipeptides, one-pot synthesis, gold nano-particle, peptide-gold-nano-conjugates

ACKNOWLEDGEMENTS We acknowledge Tzu-Kuei Liu and Ming-Hua Ho of National Taiwan University of Science and Technology, Taiwan, for their generous help in doing the bio-compatibility test.

FOR CITATION Sudeshna Kar, Yian Tai Isomeric protected dipeptides generated stable bio-compatible gold nanoparticles. *Nanosystems: Phys. Chem. Math.*, 2025, **16** (1), 74–88.

Abbreviations

Gold nano-particles (AuNPs), 3-(4,5-dimethylthiazol-2-yl)-2,5-diphenyltetrazolium bromide (MTT), Sodium carbonate (Na_2CO_3)

1. Introduction

Peptides with the same brutto formula but distinct covalent structures are known as isomeric peptides. One of the most prevalent forms of positional isomerism among peptides that has been shown to significantly impact bioactivities is sequence reversal. For instance, it has been noted that alterations in the neurotoxicity of β-amyloid peptide (Aβ), the aggregation of which results in Alzheimer's disease, are brought about by a reversal of its sequence; for example, it has been discovered that the reverse copy of the highly neurotoxic β-amyloid peptide fragment Aβ(25–35), Aβ(35–25) is not neurotoxic [1]. Once more, there has been a noticeable difference in the biological activity of two antimicrobial peptides, Cecropin P (CP1) and its retro analogue, confirming that the peptide sequence determines the bioactivity of these peptides [2].

It has been observed that positional isomerism significantly alters the shape of peptides, which may significantly alter their biological activity [1, 3, 4]. It has been noted that the amino acids primarily responsible for the biological action of antimicrobial peptides are the N-terminal and C-terminal residues [5]. Since dipeptides are the smallest peptide fragments and can be produced at a lower cost than other options, they are our focus since they have demonstrated versatility in the creation of nanomaterials for use in nanobiotechnology [6–16]. In our previous work, it has been determined that the proper pairing of two conformationally rigid amino acids in isomeric dipeptides can result in a notable variation in self-assembly [17]. This can help to construct a variety of nanostructures under the same conditions, potentially modifying their biological activity [17]. These exceptional attributes motivated us to investigate the field of peptide research concerning isomeric peptides.

Peptide-gold nanoparticle (AuNP) conjugates are now a versatile tool for biomedical applications due to recent [18–20]. Peptides and gold nanoparticles are two potential material groups that can operate in accordance to enhance control over their respective biological functions and get beyond the inherent limitations of each material type alone. Gold nanoparticles (AuNPs) derived from self-assembling peptides have garnered significant attention and have been utilised in various scientific disciplines owing to their remarkable stability, biocompatibility, and activity [21, 22]. AuNP can be functionalized with peptides to prevent aggregation and facilitate their use in in-vitro and in-vivo applications [23]. Peptide-coated AuNP's extremely easy manufacturing, great stability, and biocompatibility have made it one of the most widely used biomaterials in recent years. The development of biosensors [24, 25], illness diagnosis [26, 27], and medicine have all benefited greatly from this [28, 29]. Previous studies have shown that smaller AuNP interact with cells more easily than larger nanoparticles, especially those with a diameter of 10 – 20 nm [30–35]. Sequential alterations in peptide-biphenyl hybrid ligands that cap spherical AuNP have been observed to provide a significant difference in biocompatibility

© Sudeshna Kar, Yian Tai, 2025

with the human hepatocellular cancer cell line Hep G2 when used at higher doses [36]. These noteworthy features drove us to study isomeric peptides in the realm of peptide research. As the two isomeric peptides "Boc-m-ABA-Aib-OMe" (Peptide I) and "Boc-Aib-m-ABA-OMe" (Peptide II) (Fig. 1(a, b)) showed different morphologies under identical condition due to different kind of self-assembly [17], we wanted to inspect how they interact with gold nanoparticle by reducing Chloroauric acid ($HAuCl_4$) and then capping the AuNPs. We also focused on the cell viability assay of the gold nanoparticles to see their bio-compatibility; we have created a straightforward, one-pot method to create very stable gold nanoparticles using these tiny protected di-peptides, which may be an effective substitute for chemical processes.

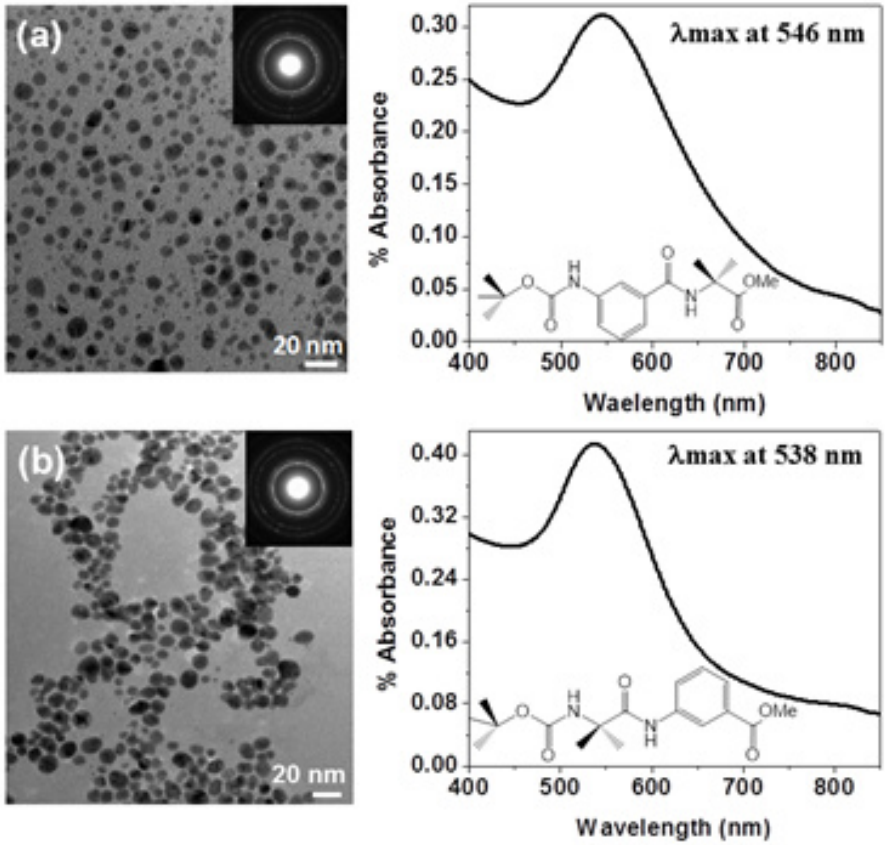

FIG. 1. (a) and (b) show TEM image and UV spectrum of peptide **I** and **II** bound AuNP solutions respectively; In the insets of (a) and (b) SAED pattern depict the polycrystalline nature of the AuNP; In the insets of UV spectra in (a) and (b) chemical structures of peptide **I** and **II** have been shown

2. Materials and methods

At first peptide **I** and **II** were synthesized in solution phase method; next with the help of these two peptide molecules gold nanoparticles were synthesized.

2.1. Methodology

2.1.1. Synthesis of Boc-mABA-OH. The amino acid *m*-aminobenzoic acid (6 g, 43.75 mmol) was suspended in a 1:1 tetrahydrofuran (THF) water mixture. Solid sodium bicarbonate $NaHCO_3$ (11.02 g, 131.25 mmol) was added and Boc-anhydride (10.49 ml, 48.12 mmol) was added to it. The reaction mixture was stirred at room temperature over night. After 24 h, the THF layer should be driven out with the help of vaccum pump. The aqueous layer was cooled in an icebath, acidified with 2 M HCl and extracted with ethylacetate. The organic layer was washed with excess of water and dried over anhydrous sodium sulphate, Na_2SO_4 and evaporated in *vacuo* producing a white solid. Yield: 9.20 g (88.71%).

2.1.2. Synthesis of methyl ester of a-aminoisobutyric acid (Aib-OMe). A mixture of absolute methanol (40 ml) and a-aminoisobutyric acid 1.5 g was cooled in an ice-salt bath for 30 mins. Then thionyl chloride (30 ml) was dropwise added to the reaction mixture with constant stirring and it was slowly allowed to attain room temperature. After stirring the clear mixture for 15 hrs. The excess methanol and thionyl chloride were removed and the residue was treated with ether. The solid methyl ester hydrochloride obtained (1.05 g) was dissolved in water, neutralised with sodium bicarbonate solution and extracted with ethyl acetate. Finally, the liquid ester was obtained by removal of solvent and it was used without further purification.

2.1.3. Synthesis of the peptide Boc-mABA-Aib-OMe (Peptide I) [17]. Boc-*m*ABA-OH was dissolved in dimethylformamide (1.25 g, 5.27 mmol) (DMF; 10 mL). N,N'-Dicyclohexylcarbodiimide, (DCC) (1.62 g, 7.90 mmol), Hydroxybenzotriazole, (HOBT) (1.6 g, 10.54 mmol), and methyl ester of 2-Aminoisobutyric acid Aib-OMe (1.6 g, 10.54 mmol) were then added (0.71 g, 5.27 mmol). During a whole day, the reaction mixture was stirred at room temperature. Filtered, then diluted with ethyl acetate, was the precipitated dicyclohexylurea (DCU) (80 mL). 100 mL of water, 1 M HCl (3×30 mL), 1 M sodium carbonate solution (3×30 mL), and then about 100 mL of water was used to wash the organic layer. A light-yellow gum was produced by drying the solvent over anhydrous sodium sulphate and allowing it to evaporate in vacuum. Silica gel was used as the stationary phase in the purification process, and a solution of ethyl acetate and petroleum ether served as the eluent. MeOH was used to generate single crystals that were stable at room temperature. 1.50 g (84.74 %) in yield. m.p. = 164 °C.

2.1.4. Synthesis of Boc-Aib-OH. The a-amino isobutyric acid (5 g, 48.54 mmol) was suspended in a 1:1 tetrahydrofuran (THF) water mixture. solid $NaHCO_3$ (12.23 g, 145.62 mmol) was added and Boc-anhydride (11.63 mL, 53.39 mmol) was added to it. The reaction mixture was stirred at room temperature over night. After 24 h, the THF layer should be driven out with the help of vaccum pump. The aqueous layer was cooled in an icebath, acidified with 2 M HCl and extracted with ethylacetate. The organic layer was washed with excess of water and dried over anhydrous Na_2SO_4 and evaporated in *vacuo* producing a white solid. Yield: 8.0 g (81.21 %).

2.1.5. Synthesis of methyl m-aminobenzoate (m-ABA-OMe). A mixture of absolute methanol (40 ml) and *m*-amino benzoic acid 1.37 g (10 mmol) was cooled in an ice-salt bath for 30 mins. Then thionyl chloride (30 ml) was dropwise added to the reaction mixture with constant stirring and it was slowly allowed to attain room temperature. After stirring the clear mixture for 15 hrs. the excess methanol and thionyl chloride were removed and the residue was treated with ether. The solid methyl ester hydrochloride obtained (1.03 g) was dissolved in water, neutralised with sodium bicarbonate solution and extracted with ethyl acetate. Finally, the liquid ester was obtained by removal of solvent and it was used without further purification.

2.1.6. Synthesis of the peptide Boc-Aib-mABA-OMe (Peptide II) [17]. Boc-Aib-OH was dissolved in dimethylformamide (0.65 g, 3.25 mmol) (DMF; 10 mL). Upon the addition of methyl ester of meta amino benzoic acid, *m*-ABA-OMe (1.40 g, 6.5 mmol) made from its hydrochloride, N,N'-Dicyclohexylcarbodiimide, DCC (0.97 g, 4.87 mmol), and Hydroxybenzotriazole, HOBT (0.42 g, 3.25 mmol). During a whole day, the reaction mixture was stirred at room temperature. Filtered, then diluted with ethyl acetate, was the precipitated dicyclohexylurea (DCU) (80 mL). 100 mL of water, 1 M HCl (3×30 mL), 1 M sodium carbonate solution (3×30 mL), and then about 100 mL of water was used to wash the organic layer. A light-yellow gum was produced by drying the solvent over anhydrous Na_2SO_4 and allowing it to evaporate in vacuum. Silica gel was used as the stationary phase in the purification process, and a solution of ethyl acetate and petroleum ether served as the eluent. 0.95 g (88.78 %) in yield. M.p = 138 °C.

2.1.7. Synthesis of gold nano particles (AuNPs). Separately, 0.84 mg/5 mL of peptides **I** and **II** were dissolved in 0.001 M chloroauric acid ($HAuCl_4$) solution, and the pH of both solutions was adjusted to ∼7 by adding 5 mL of 1.25 mM sodium hydroxide solution. The solution combinations were ultrasonically treated for five minutes in a special tank. The freshly created AuNPs solutions changed ruby red hue (Fig. A1, Appendix). Fourier transform infrared (FT-IR), X-ray energy dispersive spectrometric analysis (EDX), selected area diffraction pattern (SAED), transmission electron microscopic study (TEM), and proton nuclear magnetic resonance (^{1}H-NMR) spectroscopic investigation were used to describe the AuNP. Prior to performing the studies, we eliminated extra capping agent by ultrasonically dissolving AuNP deposits in extra MeOH and centrifuging the mixture. Every time, we eliminated the supernatant portion and carried out a second round of washing.

2.2. NMR Experiments

A Bruker Avance 300 model spectrometer running at 500 MHz was used to record all of the ^{1}H NMR spectra of the peptides and peptide bound AuNPs. In DMSO-D6, the peptide-bound AuNPs were dissolved.

2.3. FT-IR Spectroscopy

With a spectrophotometer of the Perkin Elmer-782 design, FT-IR spectra of PMM were studied. The KBr disc method was used to conduct the solid-state FT-IR measurements.

2.4. Transmission electron microscopic study

The morphology of the gold nanoparticles was examined using a transmission electron microscopic study (TEM) (AuNP). A drop of the appropriate solution was applied to a copper grid coated with carbon (300 mesh) for the TEM examinations of the peptide-AuNP, which was then slowly evaporated and allowed to dry under vacuum. TEM experiments were performed on these grids using a Philips Tecnai F20 G2 electron microscope. TEM pictures were captured at a 200 kV accelerated voltage. Also, the chosen area diffraction pattern allowed for the observation of the diffraction pattern

of a particular AuNP (SAED). X-ray energy dispersive spectrometry was also used to observe the qualitative elemental analysis (EDX).

2.5. UV-Vis analysis

Gold nanoparticles' surface Plasmon resonance (SPR) band was measured using a UV-Vis spectrophotometer. A JASCO V-670 spectrophotometer was used to record UV absorption spectra (800 – 200 nm).

2.6. In vitro cytotoxicity test using MTT assay

On a culture dish filled with cell medium (a mixture of 90 % Dulbeco's modified eagle's medium, 10 % foetal bouvine serum, and 1 mM sodium pyruvate), osteoblast type 7F2 cells (derived from mouse bone marrow) were sown at a density of 12000 cells per millilitre for 24 hours to allow for cell growth. After the full development of the cells, 450 L of cell media and 50 L of a peptide bound AuNPs solution (5 μg/mL) were added to each well, and the cells were then incubated for 1, 3 and 5 days. Similar experiments were performed with peptide **I** and **II** also with the same concentration (5 μg/mL). For the purpose of observing cell vitality, MTT (3-(4,5-dimethylthiazol-2-yl)-2,5-diphenyltetrazolium bromide) was applied to the cell-well after 1, 3 and 5 days. MTT is converted into a purple formazan product with a maximum absorbance near 570 nm by viable cells with an active metabolism. The MTT tetrazolium's formazan product deposits near the cell surface, inside cells, and in the culture medium as an insoluble precipitate. Before taking readings on absorbance, the formazan is solubilized in DMSO. The quantity of live cells is likely directly correlated with the formazan absorbance at 570 nm using a plate reading spectrophotometer (OD value at 570 nm).

2.7. Zeta potential measurements

According to the manufacturer's instructions, the zeta potentials of solutions of gold nanoparticles in water were measured. A Brookhaven Instruments Company Zeta Potential Analyzer was used for the analysis. Direct placement of gold nanoparticle solutions into a cuvette with a zeta potential electrode within was used. It was believed that only the gold nanoparticles would produce results from the zeta potential experiments. In order to measure the peptides, a zeta potential electrode was placed within a cuvette containing a methanolic solution of both peptides (0.84 mg/5 mL) (Table A1 in Appendix)

3. Results and discussions

Both peptide molecules formed spherical AuNP, as seen in TEM images (Fig. 1(a,b)). AuNP's diameters were in the 10 – 20 nm range, which is ideal for cellular uptake (Fig. 1(a,b)) [13–16]. The polycrystalline character of the AuNP was represented by the SAED pattern (insets of Fig. 1(a,b)). A distinctive peak for spherical AuNP, the surface plasmon resonance (SPR) bands for peptide **I** conjugated AuNP and peptide **II** conjugated AuNP are found at 546 and 538 nm, respectively (Fig. 1(a,c)) [25–28]. Using "Image J" software, we determined the sizes of the spherical gold nanoparticles from a fraction of the TEM pictures. 150 nanoparticles' worth of data was gathered, and the size distribution profile was displayed in origin while the mean standard deviation was computed. The average diameter of spherical AuNPs produced by peptide **I** was predicted to be 4.4 ± 1.2 nm, whereas the average diameter of AuNPs bound to peptide **II** was discovered to be 8.8 ± 2.25 nm. Fig. 2 depict the size distribution profile for peptide bound AuNPs.

In addition to the C, N, and O that the peptide molecules contributed, the Energy dispersive X-ray (EDX) examination also amply demonstrates the existence of gold nanoparticles on the surface of AuNP (Fig. 3).

We carried out Fourier-transform infrared (FT-IR) experiments to investigate the chemical interactions between the peptides and AuNP [25–28]. FT-IR spectrum of Peptide **I** shows a band at 3347.43 cm^{-1} caused by N–H stretching vibrations as well as a broad band at 3251.65 – 3271.6 cm^{-1} (Shoulder band, which is an overtone of the N–H bending vibration). Nevertheless, peptide **I** coupled with gold nanoparticles showed an N–H stretching frequency of 3394.42 and 3347.13 cm^{-1} (Fig. 4).

The interaction of the –NH group in the amide bond with gold can be used to explain the increase in wavenumber. The overtone 3251.65 – 3271.6 cm^{-1} discovered in the single peptide molecule can't be found may be due to interaction of AuNP with peptide **I**. Peak positions did not significantly alter for the C=O stretching frequency range (Fig. 5). A new peak was discovered for peptide **II**-bound AuNP at location 3442.91 cm^{-1} in addition to peak 3324.5, which also revealed a strong interaction between the –NH group in the amide bond and gold (Fig. A2, Appendix). In the range of C=O stretching (Fig. A3, Appendix), no appreciable change in peak position was seen either.

We used a ^{1}H-NMR spectroscopy investigation to further confirm and pinpoint the precise chemical interaction between peptide molecules and AuNP [29]. The signal for the C-terminal amino acid, Aib-NH, appeared at 8.527 ppm and was displaced to 8.306 ppm following conjugation with AuNP, while the peak for the N-terminal amino acid, *m*-ABA-NH, appeared at 9.446 ppm for peptide **I** in D6-dimethyl sulfoxide solvent (Table 1 and Figs. 6 and 7). By interactions with arene-cations (metals), the presence of aromatic rings in the *m*-ABA residue can also help stabilize the nanoparticle [28]. Both a reducing and a capping effect are possible with *m*-ABA [25–31]. Due to this, both the up-field and down-field shifts, which are modest relative to the N–H shifts, were observed in the aromatic C-H area, specifically between 7 ppm and 8 ppm (Figs. 6 and 7).

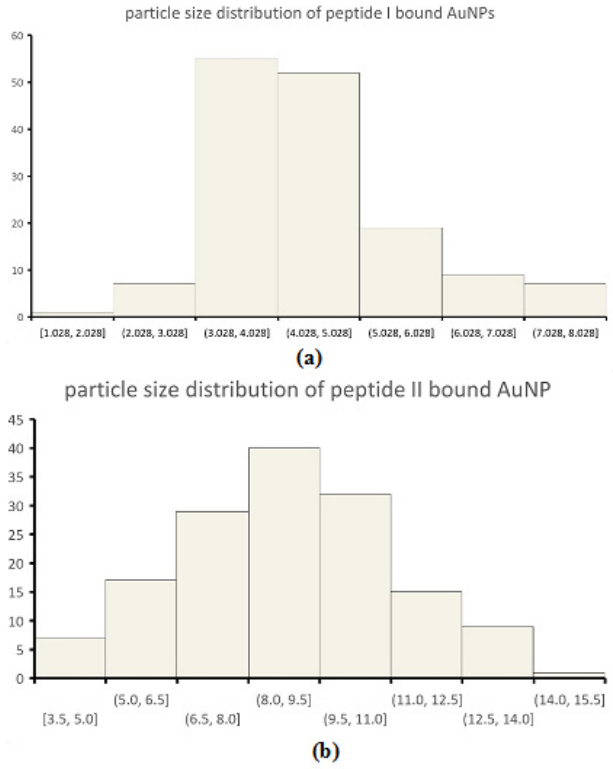

FIG. 2. Particle size distribution of (a) peptide **I** bound AuNPs and (b) Particle size distribution of peptide **II** bound AuNPs

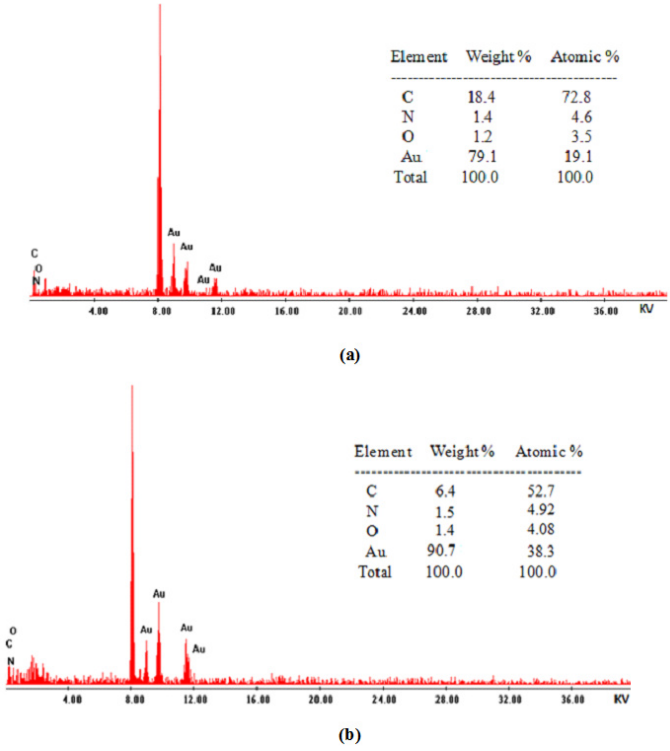

FIG. 3. EDX analysis of AuNPs synthesized by (a) peptide **I** and (b) peptide **II**. EDX analysis clearly indicates the presence of Au nanoparticle along with C, N and O contributed by the peptide molecules on the surface of AuNPs

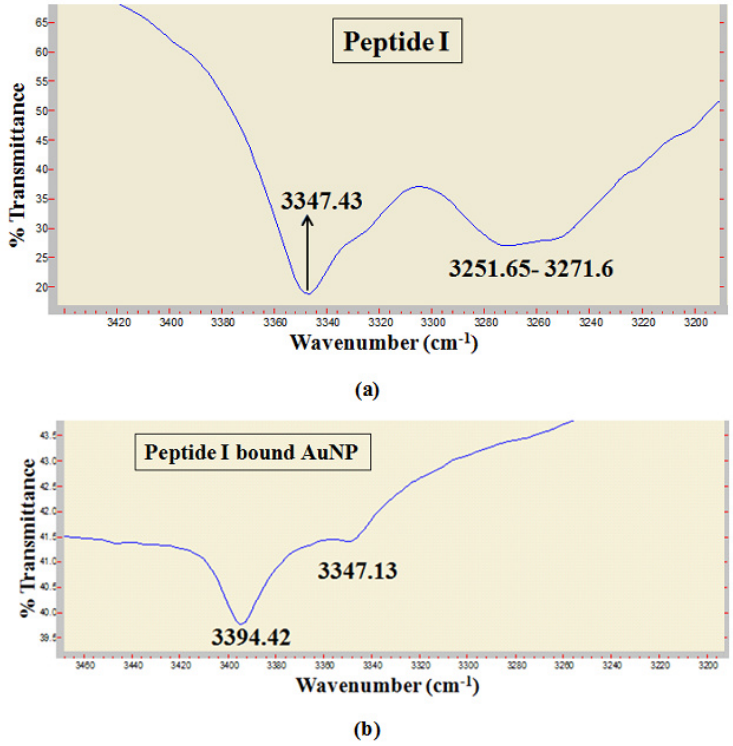

FIG. 4. FT-IR spectra of (a) peptide **I** and (b) peptide **I** bound gold nano-particles (AuNPs) in solid state (3200 – 3430 cm^{-1} range)

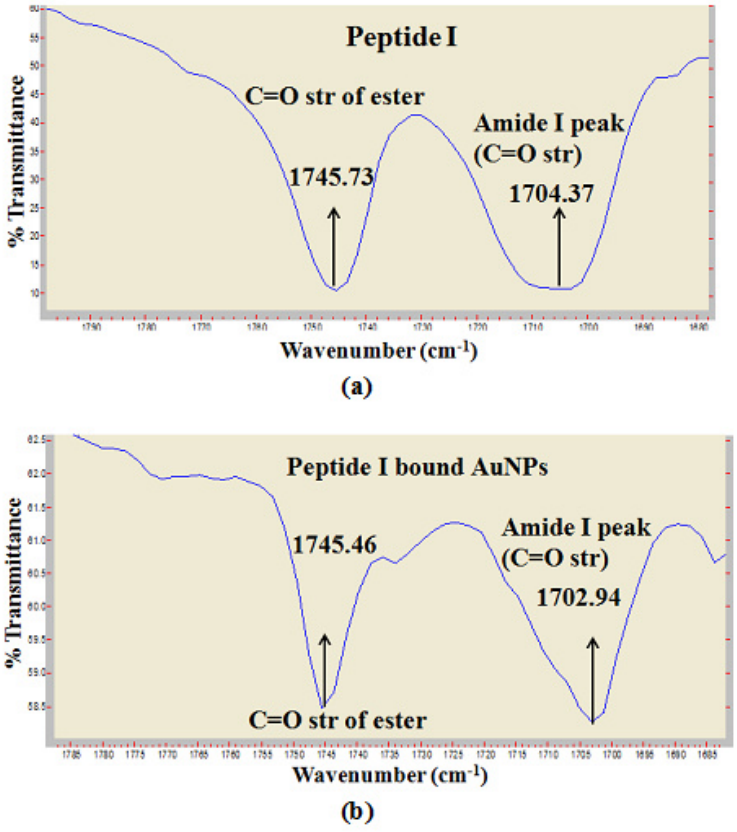

FIG. 5. FT-IR spectra of (a) peptide **I** and (b) peptide **I** bound gold nano-particles (AuNPs) in solid state (1680 – 1780 cm^{-1} range)

TABLE 1. Comparison of ^{1}H NMR Chemical Shift Values (in PPM) of Peptides and Peptide Bound AuNP (In DMSO-D6 (500 MHz))

Functional group	Peptide I	Peptide I AuNP	Peptide II	Peptide II AuNP
***m*ABA-NH**	9.446	9.698	9.685	9.445
Aib-NH	8.527	8.306	8.297	8.527
-OCH$_3$	3.582	3.847	3.847	3.582

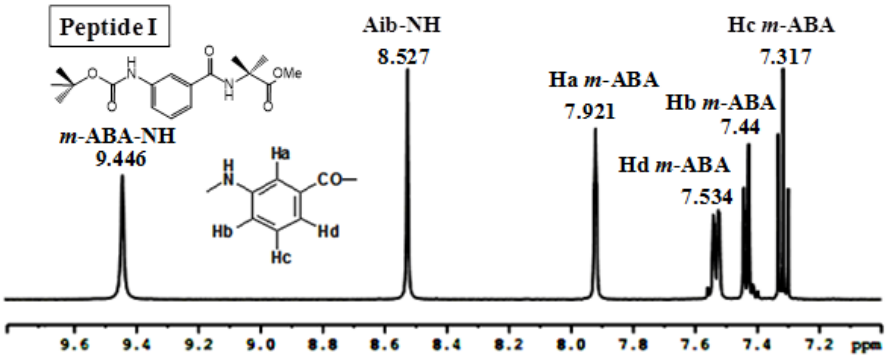

FIG. 6. ^{1}H NMR spectrum of peptide **I** in DMSO-D6 (500 MHz) (7 – 10 ppm region)

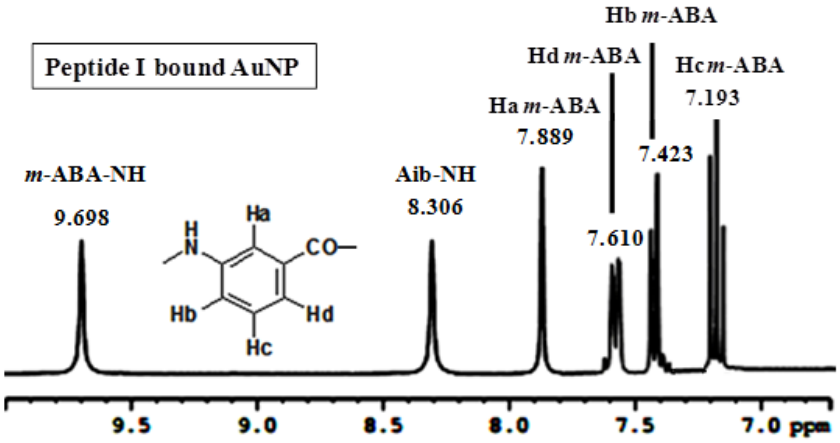

FIG. 7. ^{1}H NMR spectrum of peptide **I** bound AuNPs in DMSO-D6 (500 MHz) (7 – 10 ppm region)

After conjugation with AuNP, the ^{1}H-NMR peak for –OCH$_3$ in peptide **I** changed to 3.847 ppm from 3.582 ppm (Table 1 and Figs. 8 and 9). It follows that oxygen in the –OCH$_3$ group contributes electrons to the reduction of Au^{3+}. Moreover, the Boc-CH3 ^{1}H-NMR signal was at 1.477 ppm prior to conjugation with AuNP and shifted to 1.295 ppm following conjugation (Figs. 8 and 9). After conjugation with AuNP, the peak for C–H of Aib hardly migrated to the up-field area (from 1.444 to 1.375 ppm) (Figs. 8 and 9).

Curiously, the pattern of NMR peak shifts corresponding to individual amino acids differs from that of peptide **I** after binding with AuNP in the instance of peptide **II**, which is a positional isomer of peptide **I** with the position of *m*-ABA and Aib inverted. Whereas Aib-NH occurred at 8.297 ppm for peptide **II** and was pushed down field to 8.527 ppm after conjugation with AuNP, the peak for *m*-ABA-NH appeared at 9.685 ppm for peptide **II** was shifted up field to 9.445 ppm (Table 1 and Figs. A4 and A5 in Appendix). As a result, when peptide **II** is attached to AuNP, *m*-ABA acts as a capping agent, which is seen as an "up field" shift in the aromatic C–H region (between 7 and 8 ppm; Figs. A4 and A5 in Appendix), and Aib acts as a reducing agent, which is visible as a "down field" shift (Figs. A4 and A5, Appendix). After conjugation with AuNP, the ^{1}H-NMR signal for –OCH$_3$ in peptide **II** was moved up field to 3.582 from 3.847 ppm (Table 1 and Figs. A6 and A7 in Appendix). Moreover, the ^{1}H-NMR signal for Boc-CH$_3$ was displaced from 1.377 to

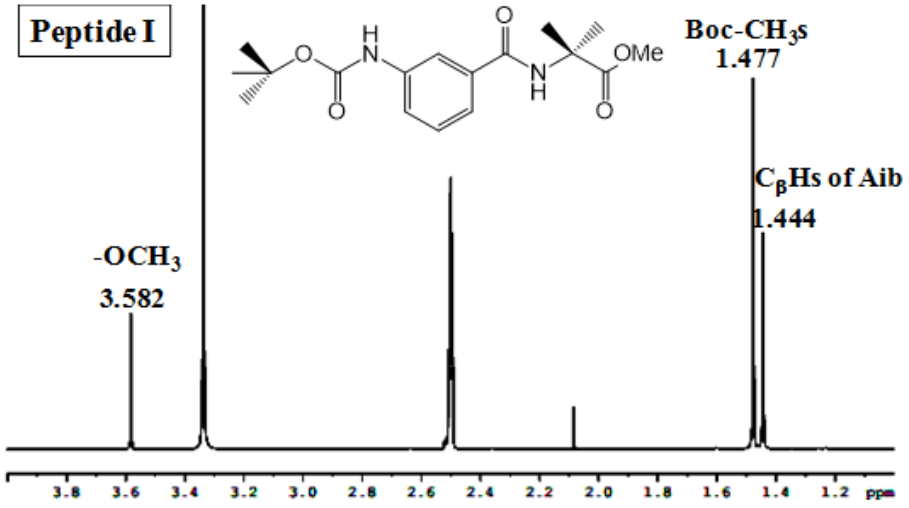

FIG. 8. ^{1}H NMR spectrum of peptide **I** in DMSO-D6 (500 MHz) (1 – 4 ppm region)

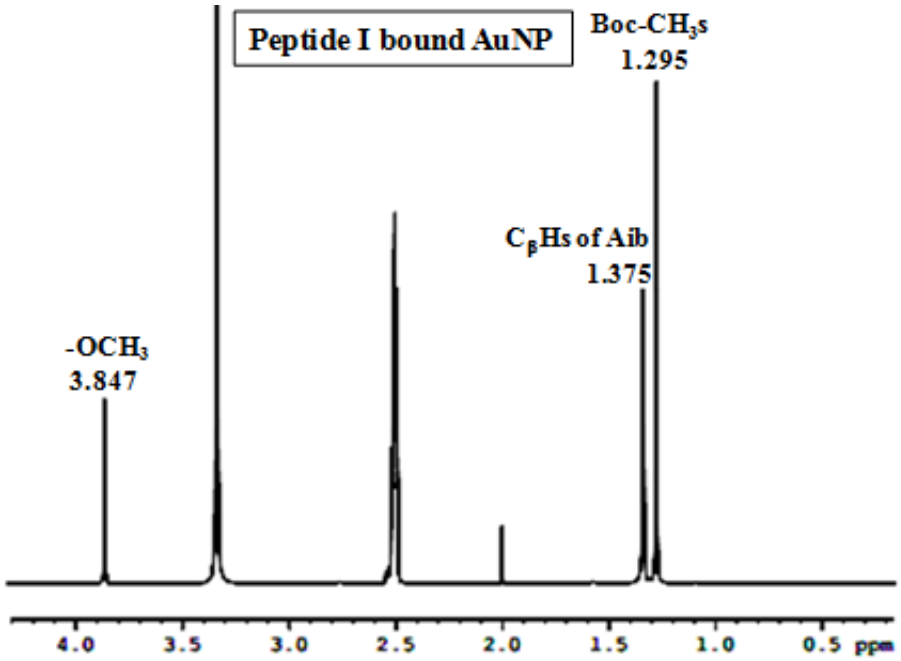

FIG. 9. ^{1}H NMR spectrum of peptide **I** bound AuNPs in DMSO-D6 (500 MHz) (1 – 4 ppm region)

1.476 ppm following conjugation with AuNP (Figs. A6 and A7, Appendix). Together, the results of the ^{1}H-NMR study led us to hypothesis that in these peptide molecules, the N-terminal amino acid is in charge of reducing the Au^{3+} ion by accepting electrons from nitrogen and the C-terminal amino acid is in charge of capping AuNP by donating as well as accepting electrons to gold. The NMR shifts of additional segments or groups connected to the relevant amino acids also reflect this. Hence, during the production of metal nanoparticles, the position of amino acids has a significant impact on the ability to donate and absorb electrons.

The AuNP solutions were kept at room temperature for two months to test their stability. After two months, we found no precipitation or colour change in the solution. UV-Vis absorption spectra of AuNP solutions after two months of storage were gathered and contrasted with those of freshly generated AuNP solutions to ensure that there is no aggregation. Figs. A8(a,c) (Appendix) of the spectra show no discernible change in the plasmon absorption bands, demonstrating the absence of nanoparticle aggregation in the solution [32]. According to TEM images of 2-month-old peptide-bound AuNP, neither the form nor the size of the AuNP had changed (Fig. A8(b,d), Appendix). We can infer that the absence of any free functional groups in the peptide molecules lowers the likelihood that the peptide bound AuNP will aggregate, limiting the interactions between the peptides and promoting the production of stable AuNP. Consequently, we have created a straightforward, one-pot method to create very stable gold nanoparticles using tiny protected di-peptides, which may be an effective substitute for chemical processes.

Following that, cell survival assays were conducted using gold nanoparticles that had been stabilized with peptides **I** and **II** and had similar size and shape. With the MTT assay, we were able to monitor the cell survival of the peptides and peptide-bound AuNP towards osteoblast type 7F2 cells (derived from mouse bone marrow) for up to 5 days [33–36]. Because they allow for bone formation, remodelling, and repair, osteoblasts are crucial. It was shown that cell viability fluctuated when both peptides were present, suggesting that both peptides randomly interact with normal cells (Fig. 10 and Table A2 in Appendix). The isomeric structure of peptides **I** and **II** refers to their comparable content but different sequencing. The fact that both peptides position themselves around each cell in a way that creates an extracellular matrix with a lot of good binding sites may be the cause. Both peptides are small in size, flexible, and interact with cells randomly, which occasionally encourages cell spreading and allows for prolonged cell viability. However, occasionally due to improper orientation of the peptide molecules, proper binding with the cells may not be facilitated and cell spreading may not be permitted. In contrast, MTT results for peptide **I** and peptide **II** bound AuNP were significantly stable when applied to normal bone cells (Fig. 10 and Table A2 in Appendix). After 1, 3, and 5 days, it was shown that cell viability in the presence of peptide **II** bound AuNP was marginally lower than that of peptide **I** bound AuNP. That may be because of the following factors.

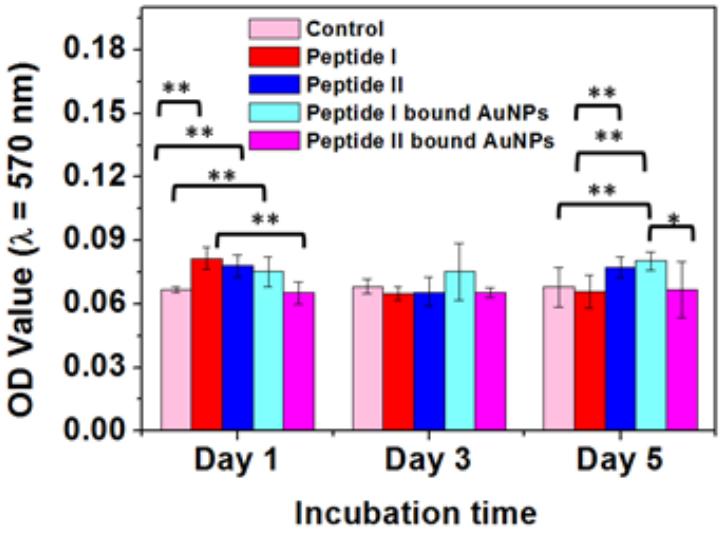

FIG. 10. MTT assay for peptide **I**, **II** and peptide bound AuNP. Methanol water (1:1 v/v) was used as the control system. The absorbance of formazan at 570 nm using a plate reading spectrophotometer (OD value at $l = 570$ nm) is presumably directly proportional to the number of viable cells. (*) means significant difference (0.01 – 0.05) and (**) means very significant difference (0.001 – 0.01)

First, even though the peptide-bound AuNPs' sizes and shapes are relatively similar, their distributions varied slightly. It was discovered that the number density of peptide **II** bound AuNP was lower than that of peptide **I** bound AuNP (Fig. 1). This distributional difference may have an impact on how well the two peptide bound AuNPs are absorbed by cells and affect cell survival. Second, if we look at the schematics for both peptides, we can see that N3 and N4 are separated by a flexible group like $–C(CH_3)_2$, while N1 and N2 are separated by a hard group, the phenyl ring (Fig. 11). The –NH– groups' ability to adhere to the surface of Au may be partially inhibited by these steric effects, which would affect their capacity to be cytotoxic. On the other hand, it is evident that for both peptides, the fluctuation of cell viability decreases after binding with AuNP; this may be because a portion of the peptides' binding sites are involved in capping the AuNP and as a result, fewer binding sites are available to interact with cells. As a result, there is less fluctuation in cell viability since the randomness of the peptides' binding to the cell is reduced. We draw the conclusion that the peptide-bound AuNPs are displaying slight difference in cell viability since we see a noticeable difference in standard deviation values and the pairwise t-test also reveals a significant difference between means.

One of the key physical factors affecting AuNP toxicity is surface charge, as determined by zeta potential [37]. It is crucial to keep in mind that modifying NP surfaces could result in different ionic interactions with biological systems because surface charges can alter [38, 39]. Mean zeta potentials (ζ-potentials) of peptide **I** attached AuNP solutions were determined to be $+12.47 \pm 1.67$ and $+6.97 \pm 1.63$ mV, respectively. Experimental parameters have been mentioned in Table A1 (Appendix).

Without AuNP conjugation, the zeta potentials of peptides **I** and **II** were likewise measured to be -7.17 ± 0.38 and -8.37 ± 0.63 mV, respectively. Two peptides' negative zeta-potentials were changed to positive ones after conjugation with AuNP, probably as a result of the electron-rich groups responsible for showing negative ζ-potential on the peptides being bound to the surface of AuNP. We presume that the conjugates become positively charged because we have already

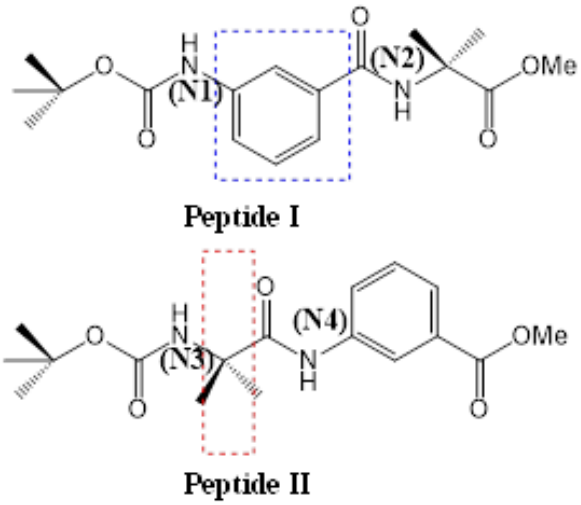

FIG. 11. Schematic representation of peptide **I** and peptide **II**

shown that peptide molecules work as the reducing agent to generate the AuNP by donating electrons from nitrogen and oxygen present in various groups. Spectroscopic studies have already shown that the role of amino acids in reducing Au^{3+} and capping the AuNP has changed because of changes in amino acid position in the peptide sequence. Hence, it stands to reason that this phenomenon will have an impact on how the peptides **I** and **II**, which act as capping agents, are distributed in bulk on the AuNP, changing their +ve ζ-potential. A positive ζ-potential not only offers advantages for improved DNA loading efficiency but may also give the effective accumulation in the target cells since many proteins, DNA, and cell membrane surfaces are somewhat anionic [40]. Because cationic nanoparticles are an easy, safe, and effective route to transport medicinal chemicals, more and more researchers are now using them [41].

4. Conclusion

In conclusion, using a straightforward and reproducible one-pot synthetic technique, we were able to produce stable gold nanoparticles using two isomeric peptides molecules having no free functional group. We demonstrated that despite the similar composition of these isomeric peptides, they show fluctuating cell-viability effects [17], which decreases after conjugation with gold nanoparticles. Moreover, following binding with AuNP, the isomeric peptides exhibits very stable and reliable MTT assay even after prolonged incubation with normal cells, making them more biocompatible. Our spectroscopic investigations show that amino acids' roles in reducing Au^{3+} and capping the AuNP are altered because of changes in amino acid position in the peptide sequence. After all the experiments we performed, it has been observed that two isomeric dipeptides which show altered nano-morphologies under similar conditions but behave unaltered to form AuNPs having similar shape and size; whereas both the peptides showed fluctuating bio-compatibility but after conjugation with AuNP they show stable bio-compatibility. Therefore we can conclude, although two isomeric peptides undergo different self-assembly pattern to develop different morphological pattern but in case of forming gold nanoparticle they behave as individual peptide molecule. These peptides capped nanoparticle may facilitate the binding of other biologically active proteins on their surface by protein-peptide interaction, for model study. Isomeric peptide bound AuNPs may bind with the same protein molecule differently, which there-by can cause different functionality of the same protein molecule which may find its' use in nanomedical devices and therapeutics development. Some crucial benefits of using these peptide-conjugated-gold-nanoparticles might be enhanced specificity, increased penetration, improved solubility and reduced toxicity. By binding with specific bioactive peptides which inhibit any disease can enhance the inhibition process and will minimize off-target effects reducing the risk of damaging healthy cells. The small size of peptide bound AuNPs can allow them to penetrate through blood-brain barrier and reach the brain more effectively, facilitating the delivery of therapeutic agents to the target site; the hydrophobic nature of some neurodegenerative disease-creating peptide-folding makes them especially difficult to dissolve in aqueous solutions, limiting the efficacy of traditional drug delivery methods; these peptide bound AuNPs can be engineered to enhance the solubility of drugs, facilitating their delivery to the target site; these AuNPs can improve the pharmacokinetic and pharmacodynamic properties of therapeutic agents, reducing their toxicity and improving their therapeutic index. Another important aspect of using peptide bound AuNPs is that these are very stable, even up to 2 months the AuNPs showed no change in size or shape. This factor is very important for use of AuNPs in biological field for their efficiency and safety issue.

Appendix

Peptide **I** bound AuNPs Peptide **II** bound AuNPs

FIG. A1. The color of the newly synthesized AuNPs solutions

TABLE A1. Experimental parameters of Zeta potential study

Measurement Parameters:			
		Liquid	= Methanol
Zeta Potential Model	= Smoluchowski	Temperature	= 25.0 °C
Mean Mobility	= 1.01 (μ/s) / (V/cm)	Viscosity	= 0.548 cP
pH	= 7.00	Refractive Index	= 1.324
Conductance	= 248 μS	Dielectric Constant	= 32.63

Instrument Parameters:			
Sample Count Rate	= 375 kcps	Voltage	= 4.00 volts
Ref. Count Rate	= 1263 kcps	Electric Field	= 7.36 V/cm
Wavelength	= 659.0 nm		
Field Frequency	= 2.00 Hz		
Cycles Per Run	= 20		

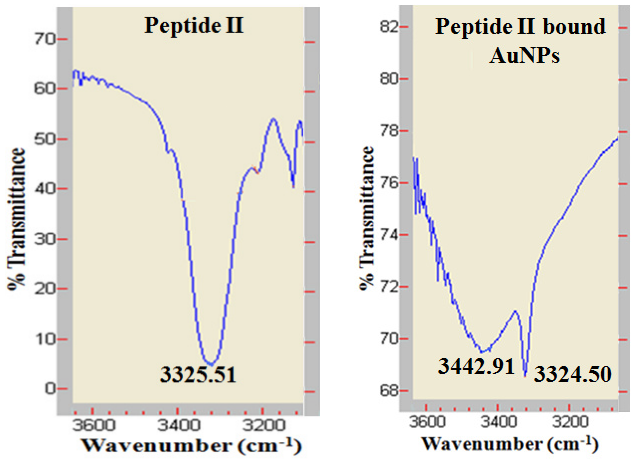

FIG. A2. FT-IR spectra of peptide **II** and peptide **II** bound gold nano-particles (AuNPs) in solid state (3200 – 3600 cm^{-1} range)

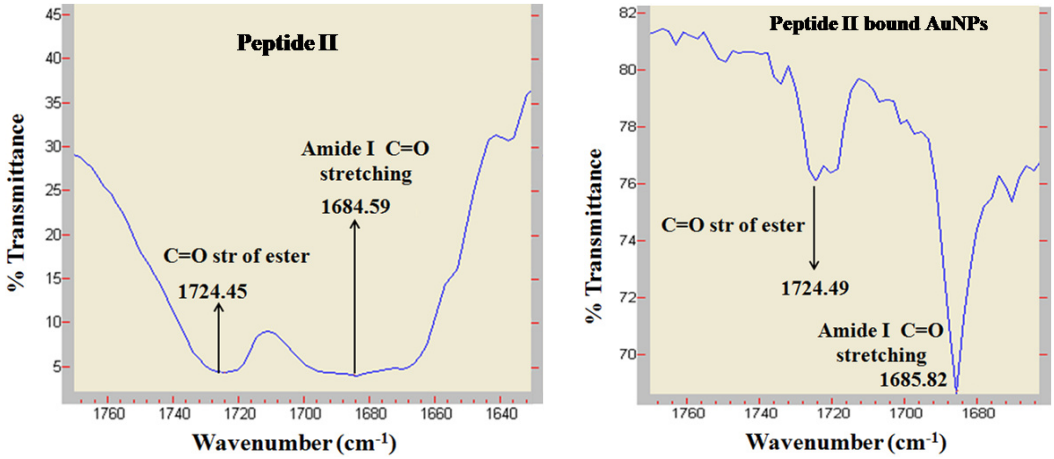

FIG. A3. FT-IR spectra of peptide **II** and peptide **II** bound gold nano-particles (AuNPs) in solid state (1640 – 1760 cm^{-1} range)

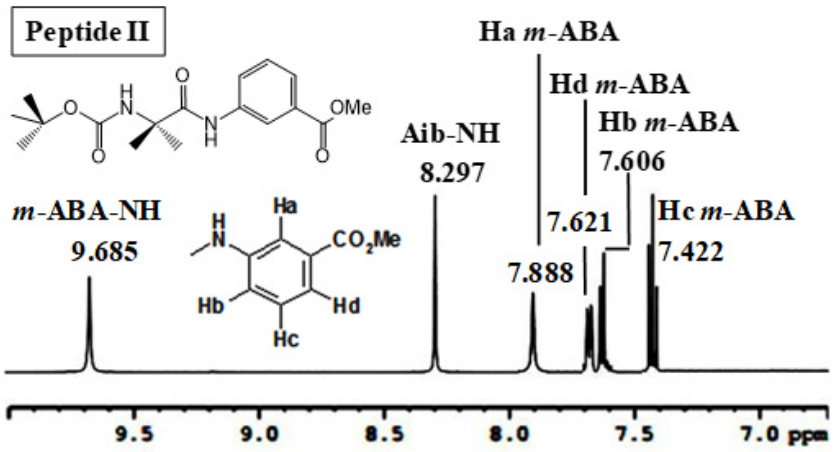

FIG. A4. ^{1}H NMR spectrum of peptide **II** in DMSO-D6 (500 MHz) (7 – 10 ppm region)

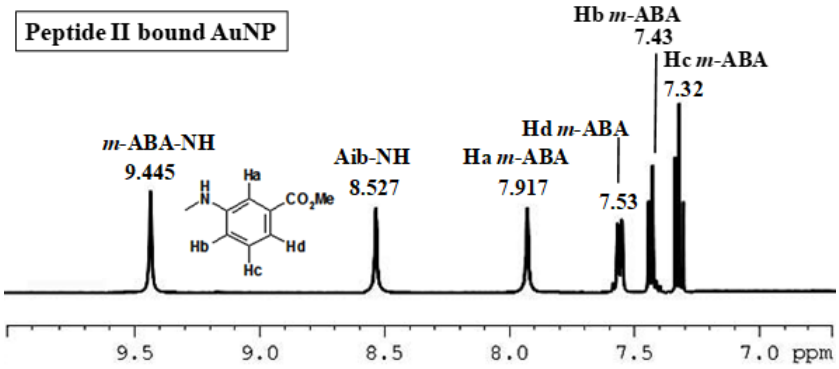

FIG. A5. ^{1}H NMR spectrum of peptide **I** bound AuNPs in DMSO-D6 (500 MHz) (7 – 10 ppm region)

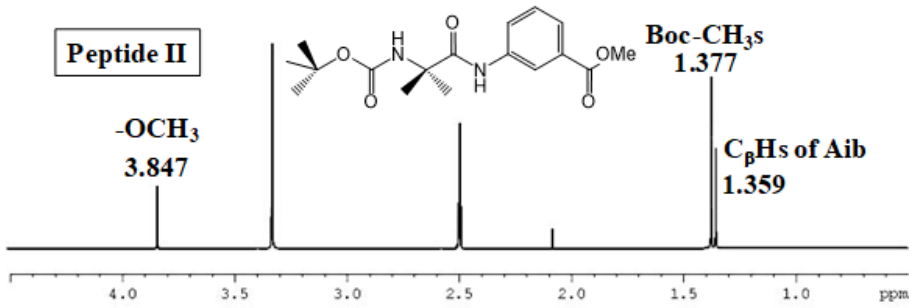

FIG. A6. ^{1}H NMR spectrum of peptide **II** in DMSO-D6 (500 MHz) (1 – 4 ppm region)

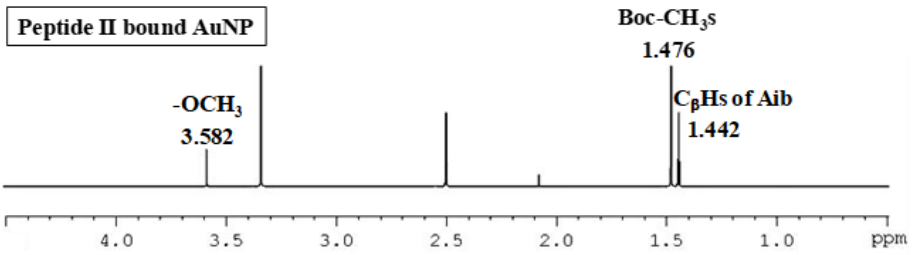

FIG. A7. ^{1}H NMR spectrum of peptide **II** bound AuNPs in DMSO-D6 (500 MHz) (1 – 4 ppm region)

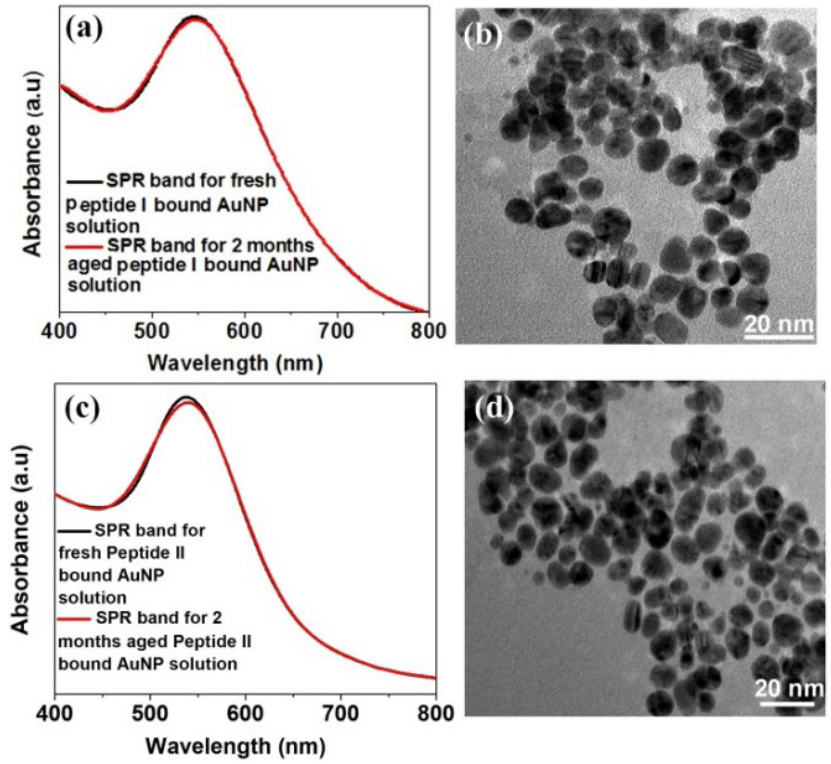

FIG. A8. (a) surface plasmon resonance band for freshly prepared peptide **I** bound AuNP solution and 2 months aged peptide **I**/AuNP solution are shown in the UV spectrum; (b) TEM image of 2 months aged peptide **I**/AuNP; (c) surface plasmon resonance band for freshly prepared peptide **II** bound AuNP solution and 2 months aged peptide **II**/AuNP solution are shown in the UV spectrum; (d) TEM image of 2 months aged peptide **II**/AuNP

TABLE A2. Statistical results of MTT test

Sample	Control	Peptide I	Peptide II	Peptide I AuNP	Peptide II AuNP
Day 1	0.067 ±0.002	0.082 ± 0.005	0.078 ± 0.006	0.075 ± 0.008	0.065 ± 0.007
Day 3	0.068 ±0.003	0.065 ±0.003	0.066 ± 0.007	0.075 ± 0.014	0.065 ± 0.002
Day 5	0.068 ± 0.010	0.066 ± 0.008	0.077 ± 0.005	0.08 ± 0.005	0.067 ± 0.013

References

[1] Butterfield D.A., Hensley K., Harris M., Mattson M., Carney J. β-Amyloid Peptide Free Radical Fragments Initiate Synaptosomal Lipoperoxidation in a Sequence-Specific Fashion: Implications to Alzheimer's Disease. *Biochem. Biophys. Res. Commun.*, 1994, **200**, P. 710–715.

[2] Vunnam S., Juvvadi P., Merrifield R.B. Synthesis and antibacterial action of cecropin and proline-arginine-rich peptides from pig intestine. *J. Pept. Res.*, 1997, **49**, P. 59–66.

[3] Marqusee S., Baldwin R.L. Helix stabilization by Glu-...Lys+ salt bridges in short peptides of de novo design. *Proc. Natl. Acad. Sci. U. S. A.*, 1987, **84**, P. 8898–8902.

[4] Bond, J.P., Deverin, S.P., Inouye, H., El-Agnaf O.M.A., Teeter M.M., Kirschnera D.A. *J. Struct. Biol.*, 2003, **141**, P. 156–170.

[5] Soares J.W., Mello C.M. Antimicrobial Peptides: a Review of How Peptide Structure Impacts Antimicrobial Activity. *Proceedings of SPIE*, 2004, **5271**, P. 20–27.

[6] Yang Z.M., Gu H., Zhang Y., Wang L., Xu B. Small molecule hydrogels based on a class of antiinflammatory agents. *Chem. Commun.*, 2004, **9**, P. 208–209.

[7] Reches M., Gazit E. Formation of closed-cage nanostructures by self-assembly of aromatic dipeptides. *Nano Lett.*, 2004, **4**, P. 581–585.

[8] Yan X., Zhu P., Li J. Self-assembly and application of diphenylalanine-based nanostructures. *Chem. Soc. Rev.*, 2010, **39**, P. 1877–1890.

[9] Wang W., Yang Z., Patanavanich S., Xu B., Chau Y. Controlling self-assembly within nanospace for peptidenanoparticle fabrication. *Soft Matter*, 2008, **4**, P. 1617–1620.

[10] Toledano S., Williams R.J., Jayawarna V., Ulijn R.V. Enzyme-Triggered Self-Assembly of Peptide Hydrogels via Reversed Hydrolysis. *J. Am. Chem. Soc.*, 2006, **128**, P. 1070–1071.

[11] Reches M., Gazit E. Enzyme-Triggered Self-Assembly of Peptide Hydrogels via Reversed Hydrolysis. *Nat. Nanotechnol.*, 2006, **1**, P. 195–200.

[12] Laromaine A., Koh L., Murugesan M., Ulijn R.V., Stevens M.M. Protease-Triggered Dispersion of Nanoparticle Assemblies. *J. Am. Chem. Soc.* , 2007, **129**, P. 4156–4157.

[13] Reches M., Gazit E. Casting metal nanowires within discrete self-assembled peptide nanotubes. *Science*, 2003, **300**, P. 625–627.

[14] Amdursky N., Koren I., Gazit E., Rosenman G. Adjustable Photoluminescence of Peptide Nanotubes Coatings. *J. Nanosci. Nanotechnol.*, 2011, **11**, P. 9282–9286.

[15] Carny O., Gazit E. Creating prebiotic sanctuary: Self-assembling supramolecular peptide structures bind and stabilize RNA. *Origins Life Evol. Biospheres*, 2011, **41**, P. 121–132.

[16] Yemini M., Reches M., Rishpon J. Gazit E. Novel electrochemical biosensing platform using self-assembled peptide nanotubes. *Nano Lett.*, 2005, **5**, P. 183–186.

[17] Kar S., Tai Y. Marked difference in self-assembly, morphology and cell viability of positional isomeric dipeptides generated by reversal of sequence. *Soft Matter.*, 2015, **11**, P. 1345–1351.

[18] Goddard Z.R, Beekman A.M., Cominetti M.M.D., O'Connell M.A., Chambrier I., Cook M.J., Marín M.J., Russell D.A., Searcey M. Peptide directed phthalocyanine-gold nanoparticles for selective photodynamic therapy of EGFR overexpressing cancers. *RSC Med. Chem.*, 2021, **12**, P. 288–292.

[19] Rai A., Ferreira L. Biomedical applications of peptide decorated gold nanoparticles. *Critical Reviews in Biotechnology*, 2021, **41**, P. 186–215.

[20] Kumar A., Ma H., Zhang X., Huang K., Jin S., Liu J., Wei T., Cao W., Zou G., Liang X.J. Gold nanoparticles functionalized with therapeutic and targeted peptides for cancer treatment. *Biomaterials*, 2012, **33**, P. 1180–1189.

[21] Bucci R., Maggioni D., Locarno S., Ferretti A.M., Gelmi M.L., Pellegrino S. Exploiting ultrashort a,b-peptides in the colloidal stabilization of gold nanoparticle. *Langmuir*, 2021, **37**, P. 11365–11373.

[22] Li Y., Tang Z., Prasad P.N., Knecht M.R., Swihart M.T. Peptide-mediated synthesis of gold nanoparticles: effects of peptide sequence and nature of binding on physicochemical properties. *Nanoscale*, 2014, **6**, P. 3165–3172.

[23] Kalimuthu K., Lubin B.C., Bazylevich A., Gellerman G., Shpilberg O., Luboshits G., Firer M.A. Gold nanoparticles stabilize peptide-drug-conjugates for sustained targeted drug delivery to cancer cells. *Nanobiotechnol.*, 2018, **16**, 34.

[24] Zhao X.R., Chen Y.L., Wang L., Wang W.F., Chen X.G. Highly sensitive fluorescence detection of trypsin based on gold nanoparticle probe. *Anal. Methods*, 2016, **8**, P. 393–400.

[25] Chandrawati R., Stevens M.M. Controlled assembly of peptide-functionalized gold nanoparticles for label-free detection of blood coagulation factor XIII activity. *Chem. Commun.*, 2014, **50**, P. 5431–5434.

[26] Liu X., Wang Y., Chen P., McCadden A., Palaniappan A., Zhang J., Liedberg B. Peptide functionalized gold nanoparticles with optimized particle size and concentration for colorimetric assay development: detection of cardiac Troponin I. *ACS Sens.*, 2016, **1**, P. 1416–1422.

[27] Liu L., Xia N., Liu H., Kang X., Liu X., Xue C., He X. Highly sensitive and label-free electrochemical detection of microRNAs based on triple signal amplification of multifunctional gold nanoparticles enzymes and redox-cycling reaction. *Biosens. Bioelectron.*, 2014, **53**, P. 399–405.

[28] Sun L., Liu D. Functional gold nanoparticle-peptide complexes as cell-targeting agents. *Langmuir*, 2008, **24**, P. 10293–10297.

[29] Morais T., Soares M.E., Duarte J.A., Soares L., Maia S., Gomes P., Pereira E., Fraga S., Carmo H., Bastos M.D.L. Effect of surface coating on the biodistribution profile of gold nanoparticles in the rat. *Eur. J. Pharm. Biopharm.*, 2012, **80**, P. 185–193.

[30] Nel A., Xia T., Mädler L., Li N. Toxic potential of materials at the nano level. *Science*, 2006, **311**, P. 622–627.

[31] Balasubramanian S.K., Yang L., Yung L.Y., Ong C.N., Ong W.Y., Yu L.E. Characterization, purification and stability of gold nanoparticles. *Biomaterials.*, 2010, **31**, P. 9023–9030.

[32] Pan Y., Neuss S., Leifert A., Fischler M., Wen F., Simon U., Schmid G., Brandau W., Jahnen-Dechent W. Size-dependent cytotoxicity of gold nanoparticles. *Small*, 2007, **3**, P. 1941–1949.

[33] Zhang G., Yang Z., Lu W., Zhang R., Huang Q., Tian M., Li L., Liang D., Li C. Influence of anchoring ligands and particle size on the colloidal stability and in vivo biodistribution of polyethylene glycol-coated gold nanoparticles in tumor-xenografted mice. *Biomaterials.*, 2009, **30**, P. 1928–1936.

[34] Sonavane G., Tomoda K., Makino K. Biodistribution of colloidal gold nanoparticles after intravenous administration: Effect of particle size. *Colloids and Surfaces B: Biointerfaces.*, 2008, **66**, P. 274–280.

[35] De. Jong W.H., Hagens W.I., Krystek P., Burger M.C., Sips A.J., Geertsma R.E. Paticle size-dependent organ distribution of gold nanoparticles after intravenous administration. *Biomaterials*, 2008, **29**, P. 1912–1919.

[36] Connolly M., Pérez Y., Mann E., Herradón .B, Fernández-Cruz M.L., Navas J.M. Peptide-biphenyl hybrid-capped AuNP, P. stability and biocompatibility under cell culture conditions. *Nanoscale Research Letters*, 2013, **8**, P. 315–323.

[37] Oberdorster G., Oberdorster E., Oberdorster J. Nanotoxicology: an emerging discipline evolving from studies of ultrafine particles. *Environ. Health Perspect.*, 2005, **113**, P. 823–839.

[38] Tedesco S., Doyle H., Redmond G., Sheehan D. Gold nanoparticles and oxidative stress in Mytilus edulis. *Marine Environmental Research*, 2008, **66**, P. 131–133.

[39] Schaeublin N.M., Braydich-Stolle L.K., Schrand A.M., Miller J.M., Hutchison J., Schlagera J.J., Hussain S.M. Surface charge of gold nanoparticles mediates mechanism of toxicity. *Nanoscale*, 2011, **3**, P. 410–420.

[40] Feng S., Ruanb G., Lic Q. Fabrication and characterizations of a novel drug delivery device liposomes-in-microsphere (LIM). *Biomaterials*, 2004, **25**, P. 5181–5189.

[41] Honary S., Zahir F. Effect of zeta potential on the properties of nano-drug delivery systems-A review (Part 2). *Tropical J. of Pharmaceutical Research*, 2013, **12**, P. 265–273.

Submitted 2 September 2024; revised 12 December 2024; accepted 23 December 2024

Information about the authors:

Sudeshna Kar – Assistant Professor, Department of Basic Science and Humanities (Chemistry), St. Thomas College of Engineering and Technology, 4, Diamond Harbour Rd, Alipore Body Guard Lines, Khidirpur, Kolkata, West Bengal 700023, Kolkata, India; ORCID 0000-0002-0469-3399; 06.sudeshna@gmail.com

Yian Tai – Professor, Department of Chemical Engineering, National Taiwan University of Science and Technology, 43 Keelung Road, Taipei-106, Taiwan; ORCID 0000-0001-7000-6086; ytai@mail.ntust.edu.tw

Conflict of interest: The authors do not have other competing interests to declare.

Declaration: No part of the manuscript has been published before.

Associated Content: Supporting Information: Detailed synthesis and characterization of peptides and gold nanoparticles. NMR, FT-IR, Mass spectra, UV, EDX analysis (PDF).

NANOSYSTEMS:
PHYSICS, CHEMISTRY, MATHEMATICS

Salman Basha Sheik, et al. *Nanosystems: Phys. Chem. Math.*, 2025, **16** (1), 89–104.
http://nanojournal.ifmo.ru
DOI 10.17586/2220-8054-2025-16-1-89-104

Original article

Experimental studies on thermal and physical characteristics of mono and hybrid nanofluids

Salman Basha Sheik[1,2,a], Praveena Devi Nagireddy[1,b], Kiran Kumar Kupireddi[3,c]

[1]SR University, Warangal, India

[2]Sasi Institute of Technology and Engineering, Tadepalligudem, India

[3]NIT, Warangal, India

[a]sheiksalmanbasha@gmail.com, [b]n.praveenadevi@sru.edu.in, [c]kiran@nitw.ac.in

Corresponding author: Salman Basha Sheika, sheiksalmanbasha@gmail.com

ABSTRACT This research paper aims to present experimental findings on important thermophysical properties such as thermal conductivity, viscosity, and density of selected nanofluids. Ethylene glycol is considered as the base fluid, and multi-walled carbon nanotubes, zinc oxide, aluminum oxide nanoparticles are used in the present study. The nanopartices are chosen due to their remarkable thermal and physical properties. The results indicate that the thermal conductivity of the ethylene glycol increases in a linear manner when Al_2O_3, MWCNT, and ZnO nanoparticles are dispersed in the base fluid. Particle concentration varied from 0.1 to 0.3 vol %. The highest increment noted is 39 % at the highest concentrations. The viscosity of the nanoparticles containing ethylene glycol improves with temperature, and Al_2O_3 and MWCNT have the highest improvement. Thus, the density analysis shows that the nanofluids with 0.1 and 0.2 vol % nanoparticles dispersed in ethylene glycol and having 0.2 vol % have less fluctuation compared to nanofluids with 0.3 vol %, which may affect various characteristics of the coolant considerably. This shows how nanofluids can help in managing the thermal conditions of automobiles and electronic gadgets.

KEYWORDS hybrid Nanofluids, thermal conductivity, viscosity, density, automobile

FOR CITATION Salman Basha Sheik, Praveena Devi Nagireddy, Kiran Kumar Kupireddi Experimental studies on thermal and physical characteristics of mono and hybrid nanofluids. *Nanosystems: Phys. Chem. Math.*, 2025, **16** (1), 89–104.

1. Introduction

Nanofluids are suspended with small particles having high heat conductivity, and these particles may be metal oxides or carbon nanotubes. The concept of nanofluids is comparatively recent and originated in the last decade, mainly with the first research focused on the introduction of nanoparticles into basic fluids. Nanofluid as a term was first used in the 1990s by Dr. W. Yu and colleagues at the Argonne National Laboratory. During the beginning of the 2000s, the primary focus in the field of nanofluids was to determine potential applications of the nanofluids and to develop methods to control problems such as instability and sedimentation. Thermal conductivity is a significant parameter, especially in heat transfer applications of nanofluids. It improves heat exchange between hot cores and coolants, productivity, stability, and prevents hot spots in the cooling systems, prolonging the life span of the engine elements. This paper discussed the thermal efficiency of mono- and hybrid nanofluids using ethylene glycol as a base fluid with different concentrations. Nanofluids having metallic particles with dimensions less than 100 nm inspired considerable interest due to their enhancement of heat transfer. Some of the materials used due to their unique thermal conduction include aluminum oxide (Al_2O_3), zinc oxide (ZnO), and multi-walled carbon nanotubes (MWCNTs). Nanoadditives have been incorporated into the engine coolants to increase their thermal effectiveness, so smaller radiators can be employed; thus, there is less weight and less fuel consumption. The study was focused on the utilization of nanofluid in cool blends of the engine by applying an accurate proportion of nanofluid to the basic fluid with the help of an ultrasonic wave device. The analysis of the results revealed that these nanoparticles, which include Al_2O_3, ZnO, and MWCNTs, are capable to increase the rates of heat transfer. This effect is illustrated when the nanofluid, which consists of ethylene glycol, has a volumetric fraction of 0.1 to 0.5 vol %. For high-efficiency engines, it is vital to provide an adequate rate of cooling, as overstress can bring about problems such as excessive heat, which affects the viscosity of oils, and the failure of different engine parts, among others. Thus, the various parameters of the radiator have to be chosen adequately in order to achieve consistently high efficiency in the engine's operation, especially if a new type of radiator design is to be developed.

The advantages were demonstrated with the new use of hybrid nanofluids as prominent in heat transfer systems, implying their importance in enhancing the heat transfer industry. Ethylene glycol plays another role in heat transfer, as this fluid, when mixed with silicon carbide nanoparticles as the base fluid, has the effect of improving thermal conductivity, thus increasing the efficiency of heat dissipation [1]. The study [2] showed that the thermal conductivity of multi-walled

© Salman Basha Sheik, Praveena Devi Nagireddy, Kiran Kumar Kupireddi, 2025

carbon nanotubes-dispersed ethylene glycol increases significantly, which in turn considerably enhances the heat transfer coefficient in solar thermal applications. Ethylene glycol is very important for increasing the boiling point of water and thus improving the efficiency of heat transfer in radiators, as shown by nanofluid studies [3]. Hybrid nanofluids are valuable because they raise heat transfer efficiency, decrease entropy generation, and offer ecologically sound means of transferring heat; hence, they find application in various heat transport processes [4]. Both types of nanofluids also show enhanced thermal and viscous properties; therefore, they are optimal for the improvement of heat transfer in heat exchangers, reduction of weight fractions, and increase in system efficiency [5, 6].

MWCNTs, Al_2O_3, and ZnO are widely used materials in nanofluids that affect heat transfer efficiently in numerous applications. These nanoparticles, when incorporated in nanofluids, enhance the thermal attributes and thus are applicable for heat transfer fluids in the aerospace and automobile industries, as well as renewable energy [7]. A study on the convective heat transfer coefficient and thermo-physical properties of Al_2O_3 nanoparticles in ethylene glycol has been presented for the possibility of increasing the enhanced heat transfer rates. Also, the enhancement of heat transfer coefficient is observed when ZnO nanoparticles are suspended in ethylene glycol using the base fluid ratio as follows: therefore, it can be concluded that ZnO/Ethylene glycol can be a good solution to control overheating problems in different industries. Additionally, the adjustable heat transport rate in ethylene glycol with ZnO and MWCNT hybrid nanofluid has revealed the best improvement out of all feasible nanofluid pairs, which is consistently essential in modernized heat transfer technologies [8–10].

The term nanofluid refers to a liquid enhanced with nanoparticles; the thermal conductivity of a heat exchanger is enhanced with the application of hybrid nanofluids, besides improving the mixing ratio of the nanoparticles [11]. Nanofluids enhance the base fluid's thermo-physical characteristics and heat transfer coefficients, making them useful for applications like heat exchangers, heat sinks, heat pipes, solar panels, and air conditioning [12]. On the method of preparing hybrid nanofluids, one-step and two-step methods are common, and in terms of durability, they apply the use of surfactant addition, surface treatment, and pH modification [13]. The preparation of hybrid nanofluids includes the addition of surfactant to improve stability, and the main focus will be on the preparation technique, which is important for the enhancement of the thermophysical property and heat transfer performance of the nanofluids [14]. Ultrasonication is widely used in the preparation of nanofluids since it enhances dispersion and thus leads to higher stable fluids, reduced particle size, higher thermal conductivity, and lower viscosity values [15].

For the preparation of nanofluid, it has been established that the duration of ultrasonication increases with an increase in dispersion, thermal conductivity, and density, as well as decreases with an increase in viscosity. Thus, the enhancement of thermal conductivity by ultrasonication for alumina-water nanofluids is favorable for heat transfer since it enhances stability [16]. The flowing drag coefficients of the nanofluids and the heat transfer coefficients are the viscosity and the coefficient of thermal conductivity, which are imperative in the design of the nanofluid system [17]. The viscosity of nanofluid is useful in convective thermal transport, and through the functioning of the ANSYS-based model, very accurate results are obtained for heat transport systems [18]. Nanofluid density influences heat transfer characteristics such as Reynolds number, Nusselt number, pressure loss, and the Darcy friction factor in heat transfers [19]. The study of thermal conductivity of nanofluids also focuses on hybrid nanofluids since they possess special thermo-physical properties significant for heat transfer [20].

Al_2O_3 and MWCNT hybrid nanofluids enhance the thermal conductivity of radiator coolant in response to temperature and volume fraction changes. The maximum gain with 0.5 % vol % was 11 % at 60°C. These improved thermophysical properties of nanofluid are important in solar applications since heat transfer is improved [21]. Therefore, nanofluids, when focused on the radiator coolant, prove to have a lower total outlet temperature as opposed to conventional coolants. The thermal conductivity of the nanofluid is higher than that of other fluids and enhances with an increase in temperature, especially for high-rpm engines. This leads to small radiators, better configuration and design, and lower pumping energy for better engine performance [22]. Rahul Ghimire et al. investigated the thermal characteristics of Al_2O_3 and ethylene glycol/water nanofluids in a vehicle radiator's flat tube using single and multiphase simulations and revealed that the later technique was more accurate [23]. Kumar et al. investigated the thermal conductivity of concentrated polyester oil with nanoparticles prior to and during ball-milling. They applied the Taguchi methods for designing parameters and realized an enhancement of the thermal conductivity of 0.020 W/m-K and a reduction in the friction coefficient [24]. Srimanickam et al. have made a comparison of water and nanofluid thermal efficiency with the help of Al_2O_3 nanoparticles. They identified a maximum improvement of 79.4 %, which is similar to any volume flow rate of water. Nanoparticles of Al_2O_3 enhanced thermal conductivity by 1.988 %, which is enabled the diurnal average thermal efficiency [25].

Raviteja Surakasi et al. have identified the role of TiO_2 nanoparticles as vital in environmental purification and water treatment. The zeta potential of TiO_2 nanofluids with pure CNTs was lower at the start, but SM-CNTs were more stable in coolants. Oxidized CNTs also maintained a constant zeta potential for two months [26]. Similar to the Alniacar study, Karar Mahdi Al-Araji et al. noted that by employing a nanofluid that is affected by the conductivity coefficient and the viscous coefficient, it is possible to enhance the thermal improvement value by more than 50 percent. Being inexpensive and highly effective, Al_2O_3 nanoparticles are widely employed [27]. In the preparation of nanofluids, Sanjeev Kumar Gupta et al. proposed two ways of sonicating, magnetically stirring, and homogenizing the base fluids with nanoparticles effectively and at a relatively low cost. To address the problems of nanoparticle deposition and buildup,

this method optimizes the flow through the solar collectors and enhances the heat transmission rate with an increase in the concentration of the nanoparticles [28]. Serdar Mart et al. indicated that there is a possibility of enhancing the engine coolant's cooling capacity by up to 17.46 % when Al_2O_3 nanoparticles are incorporated. In this aspect, the density of Jews also decreased to 46 % from the original design. The study provided a comparative analysis between the cooling power per unit area, velocity, and flow rate of the clearance fluid for the engine radiator and the nanofluid to show the prospect of nanofluids as coolants for automobile engines [29]. In their study, Reza Aghayari et al. found that the Timofeeva, Drew, and Passman theoretical models present the thermal conductivity and viscosity of nanofluid. They concluded that employing Fe_2O_3/water nanofluid raised the values of Nusselt number, heat rate, and friction factor to the highest expressional thermal efficiency factor of 3.25 [30].

A study carried out by Akshata Pattanshetti et al. revealed that the nanocomposite films, the garlic powder, and the garlic microparticles exhibited substantial antibacterial effects in Gram-positive and Gram-negative bacteria species. The 3 % MWCNT film exhibited the steepest increase in antibacterial activity, and the GMs presented the optimum antibacterial efficacy because of the high SV ratio [31]. Abu Raihan Ibna Ali et al. also discovered that appropriate stability is the primary issue with nanofluid, which is critical for heat transfer. However, for the synthesis of nanoparticles and the required stability, further research has to be conducted on identifying the optimal sonication and magnetic stirring times, the concentration of the surfactant, and the mixture of nanoparticles [32]. CuO nanofluid, as per the research done by N. Sadashiv Vele et al., has excellent heat transfer characteristics and lower pressure losses compared to Al_2O_3 nanofluids. The study therefore recommends studying the Brownian motion of nanoparticles to improve their heat transmissivity. Further studies are necessary in order to better understand the mechanism by which hybrid nanofluids enhance heat transfers in practical applications [33].

Zafar Said et al. found that Al_2O_3-DW/EG nanoparticles with a 1:1 nanoparticle to AG surfactant mass ratio were the most stable sample, while TiO_2-DW/EG nanofluids with a 0.3 % volume fraction and no surfactant added were the most stable. High volume concentrations negatively affected nanosuspension stability. Al_2O_3-based nanoparticles indicated reduced corrosion at acid electrolyte and an elevated Nusselt number at 1 L min^{-1}1 [34]. The ZnO water nanofluids have a bright future in the automotive industry as well as in heat exchanger systems due to their improved heat transfer characteristics, light-weight radiators, and lesser fuel consumption", said Muhammad Qasim et al. Muhammad Qasim et al. have found that ZnO water nanofluids are promising for use in the automobile industry and heat exchangers because of enhanced heat transfer properties, lightweight radiators, and reduced petrol consumption. This is because a 0.2 % by volume concentration of such particles has resulted in decreased pressure drop and friction factor [35].

2. Selection of nanomaterials and base fluid

Aluminum oxide (Al_2O_3) nanoparticles are smaller than 100 nm. It has a huge surface area-to-volume ratio, which makes it of great importance in uses such as catalytic agents, circuits, medicine, and the environment. Multi-walled carbon nanotubes (MWCNTs) are long and thin carbon cylinders that have high mechanical, electrical, thermal, and optical properties. They are very strong and have high mechanical strength, which makes them among the hardest-known compounds. However, MWCNTs present brilliant electric conductivity, so they are useful for electronic in addition to energy applications. Zinc oxide nanoparticles (ZnO NPs) may be described as structures comprising zinc oxides that are very small and typically have sizes within the nanometer spectrum, which is between 1 and 100 nanometers. They possess some special characteristics, for instance, high photocatalytic activity, in which a material can decompose organic molecules in a solution with UV light. Also, ZnO nanoparticles have bactericidal properties, which make them an effective factor in the inhibition of bacterial as well as fungal development. This has made it compulsory to incorporate them in quite many consumer goods, like textile antimicrobial coatings, packaging, and medical devices, among others. The nanomaterials Alumina, MWCNTs, and ZnO nanomaterials are purchased from Nano Research Lab, Jharkhand.

Ethylene glycol is a clear, colorless, tasteless liquid often used as a capability of polymers. This molecule consists of two hydroxyl groups; hence, it is a dihydric alcohol. One of the main uses of this substance is in motor vehicle cooling systems as antifreeze in car radiators. As for the freezing point, it is considerably low, due to which ethylene glycol can remain in the liquid state even at extremely low temperatures. The positioning of this property is useful in ensuring that the radiator does not freeze during the winter period. However, the potency of the poison that it has is something to be worried about. Ingestion of ethylene glycol causes deep poisoning because the compound gets metabolized in the body to produce toxic products, which leads to kidney damage, neurological complications, and death. Considering the fact that ethylene glycol is toxic, it is important to avoid contamination by handling and disposing of products that contain the substance. This is in essence necessary to prevent any form of pollution to the environment or harm to any living species. That is why ethylene glycol is considered dangerous but remains indispensable as an industrial material with critical uses that are not limited to automotive ones. Some of these applications include the production of polyester fibers, plastics, and as a solvent across various industries. Some thermo-physical properties of the nanomaterials and the base fluid are listed in Table 1.

TABLE 1. Thermo-physical properties of Nanoparticles and Base fluid

Name of the material	Molecular Mass (g/mol)	Thermal conductivity (W/m-K)	Specific Heat (J/Kg k)	Density g/cm^3)	Boiling Point (°C)	Melting Point (°C)
Al_2O_3	101.96	17.65	525	3.97	2977	2055
MWCNTs	120.1	2586	550	2.1	4027	3550
ZnO	81.38	49	494	6	2360	1975
Ethylene Glycol	62.08	0.253	2093	1.11	197.3	−12.9

2.1. Characterization of nanoparticles using XRD and UV

2.1.1. UV and XRD analysis of Al_2O_3 nanoparticles. UV-Vis spectroscopy is indispensable for the characterization of Al_2O_3 nanoparticles due to its importance for the understanding of the optical, electronic, and surface characteristics of nanoparticles. It can be used for finding absorption characteristics, transparency, band gap energy, size-dependent characteristics, defects and impurities, SPR, concentration and stability investigations, interaction with other materials, and surface functionalization. UV-Vis spectroscopy is especially helpful in determining UV protection, coatings, and transparent ceramics in electronic and optoelectronic devices, surface plasmon resonance, and composites. It is also used in defect sensing, impurity analysis, and surface plasmon resonance experiments. In conclusion, UV-Vis spectroscopy plays a key role in controlling and improving the Al_2O_3 nanoparticle properties essential for their application in modern high-tech applications in optics, electronics, catalysis, and material science.

The UV-Vis absorption spectrum of synthesized Al_2O_3 nanoparticles presented in Fig. 1 revealed considerably high light absorption capability, with a with a marked "band edge" peak at around 400 nm. It ranges from 400 nm to 600 nm, and the graph steadily drops as the wavelength increases. The spectrum also looks to extend down to the longer wavelengths, which is another way of saying that it is quite broad. The high value and the decrease rate demonstrate high purity as well as crystallinity on the basis of absorbance and crystallinity, whereas the same sample contains numerous different peaks that determine less impurity or secondary phase. Thus, a large absorption tail points to the existence of different sizes of nanoparticles or variations in the surface states, which is quite typical for nanoscale materials. From the UV-Vis absorption properties, there could be applications in ultra-violet protection coatings, sensors, and optical apparatus. Further characterization and comparison of these nanoparticles with doped or modified Al_2O_3 nanoparticles will help to elucidate their optical properties.

The X-ray diffraction pattern for Al_2O_3 nanoparticles illustrated in Fig. 2 has diffraction peaks. These peaks can be used for the comparison with the standard diffraction pattern proves that the sample is crystalline. The peaks width gives information about the crystallite size, while the broader peaks suggest a small crystallite size. The crystallite size of Al_2O_3 nanoparticles was calculated using the Scherrer formula, $D = \dfrac{K\lambda}{\beta \cos\theta}$ where, K is the shape factor (0.9), λ is the X-ray wavelength (1.5406 Å), β is the full width at half-maximum (FWHM), and θ is the Bragg angle. The estimated size was approximately 33 nm.

2.1.2. XRD analysis of MWCNTs. The X-ray diffraction (XRD) pattern of the Multi-Walled Carbon Nanotubes (MWCNTs), as shown in Fig. 3, has specific features that include a prominent (002) peak at 2θ = 26 °C, signifying the presence of graphical carbon. The other two peaks can be indexed to the (100) and (004) crystallography planes of graphite. The peak at $2\theta = 26^\circ$ represents the highest intensity, which demonstrates high graphitization. The broadening of the first peak indicates that the MWCNTs possess nanoscopic characteristics and structure the irregularity. Based on background noise and a broad shoulder at $2\theta \approx 25^\circ$, there is usually amorphous carbon and a wide peak at $2\theta = 20^\circ$ to 30°.

The XRD analysis of multi-walled carbon nanotubes showed a very prominent peak at $2\theta = 26^\circ$ and indicated a high degree of graphite formation as well as the presence of graphitic carbon. The crystallite size calculated through the Scherrer formula was approximately 10.2 nm, confirming the nanoscale features of MWCNTs.

2.1.3. UV analysis of ZnO nanoparticles. The optical properties of the ZnO nanoparticles have been characterized using UV-Vis spectroscopy. From Fig. 4 one can conclude that there is a strong absorption peak around 350–380 nm. This is because the semiconductor is showing the band-gap transition.

2.2. Characterization of nanoparticles using SEM and TEM

2.2.1. TEM analysis of Al_2O_3 nanoparticles. Further tests resulted for the presented Al_2O_3 nanoparticles from the Nano Research Lab in Jamshedpur. As shown in Fig. 5, the morphology of the synthesized Al_2O_3 nanoparticles was spherical, as revealed by TEM. In the case of the synthesized nanoparticles, the degree of purity can be marked as very high; their composition is 99.9 %. The synthesized nanoparticles have particle sizes below 50 nm, and most of them are in the

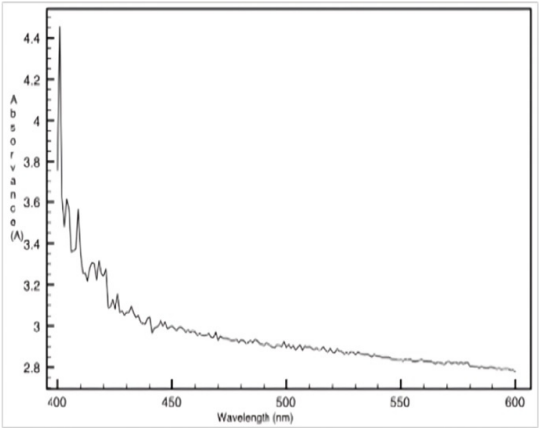

FIG. 1. UV Spectroscopy of Al_2O_3 nanoparticles

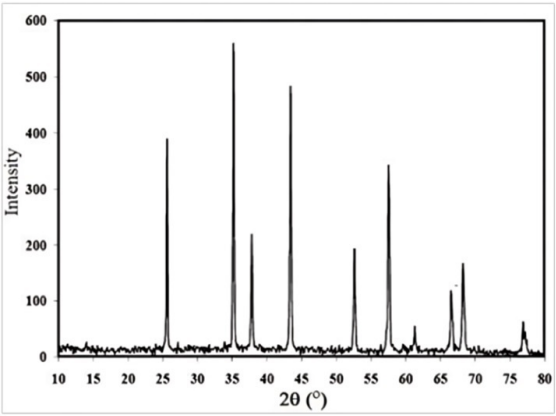

FIG. 2. XRD Analysis of Al_2O_3 nanoparticles

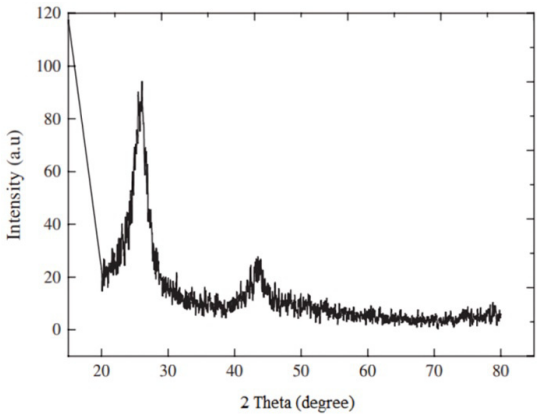

FIG. 3. XRD analysis of MWCNTs

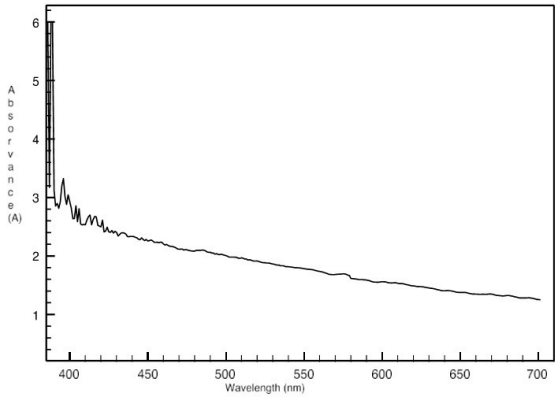

FIG. 4. UV Spectroscopy of ZnO nanoparticles

range of 30–50 nm. Aluminum oxide nanoparticles are also uniform in shape and size and have a fairly high purity level, according to the obtained results. Due to this, these nanoparticles are preferable for use in settings that require frequent supplies of high-quality nanomaterials.

2.2.2. SEM analysis of MWCNTs. In the SEM image of MWCNTs shown in Fig. 6, it can be observed that they have a very high entangled fibrous structure interconnected in various forms and different diameters. The image retains a sort of purity in that both it and its neighboring pixels are free from blemishes and contamination, therefore the higher purity value. The MWCNTs produced in this study have a good dispersion and no obvious agglomeration, and their size is generally in the range of a few nanometers to tens of nanometers, which meets the requirements of various applications.

SEM data showed that the outer diameter ranged from 10 to 20 nm. With an interlayer spacing of 0.34 nm, the average number of layers was estimated to be around 44. The internal channel diameter, calculated by subtracting the wall thickness from the outer diameter, ranged from 0 to 0.28 nm, emphasizing their nanoscale features.

2.2.3. TEM analysis of ZnO nanoparticles. The TEM analysis of ZnO nanoparticles synthesized and offered by the Nano Research Lab as mentioned in Fig. 7, declared an average particle size of 30–50 nm with a 99.9 % adsorption and hence a nearly spherical morphology, which makes them more useful in advanced applications.

3. Synthesis of Nanofluids

3.1. Estimation of Nanofluid volume concentration

In this experiment, Al_2O_3, MWCNTs, and ZnO nanofluids were prepared. The weight of the nanoparticles for a particular volume concentration can be expressed using the formula [12].

$$\Phi = \frac{\left[\frac{w_{np}}{\rho_{np}}\right]}{\left[\frac{w_{np}}{\rho_{np}} + \frac{w_{bf}}{\rho_{bf}}\right]} \cdot 100 \tag{1}$$

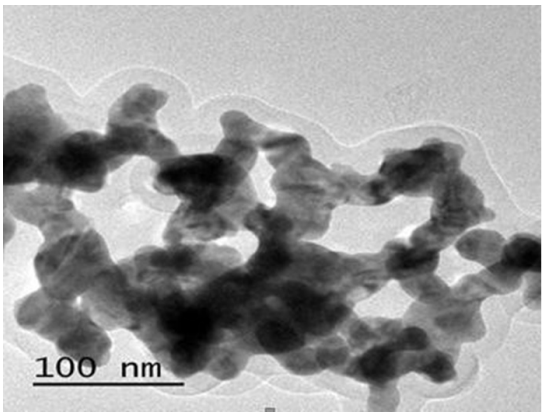

FIG. 5. TEM Photograph of Al_2O_3 nanoparticles

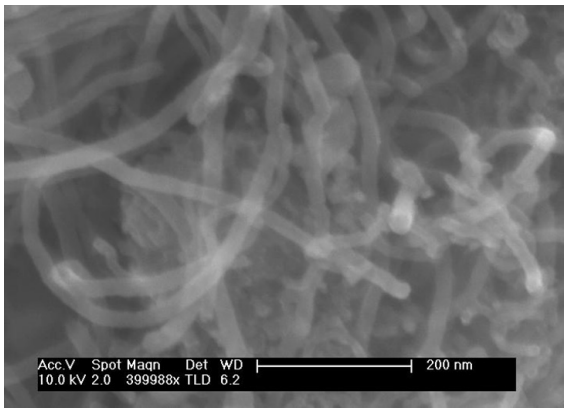

FIG. 6. SEM Analysis of MWCNTs

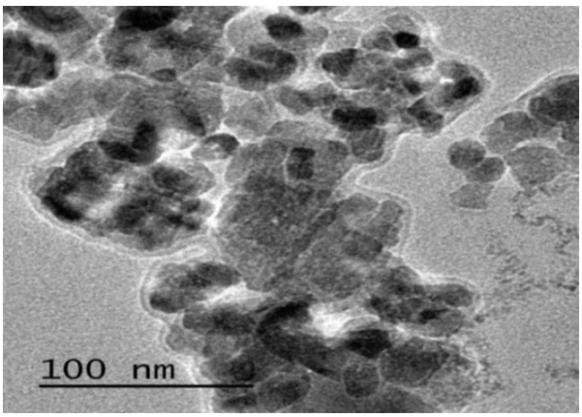

FIG. 7. TEM Analysis of ZnO Nanoparticles

Where, np represents nanoparticles and bf represents base fluid.

3.2. Estimation of Hybrid Nanofluid volume concentration

Hybrid nanofluids, which consist of a combination of different nanoparticles like aluminum oxide (Al_2O_3) and multi-walled carbon nanotubes (MWCNTs), are being extensively studied due to their improved thermal properties and possible use in numerous heat transfer systems. The procedure for synthesizing nanofluids will significantly determine the development of a stable hybrid nanofluid. Evidently, the ultrasonication process has been found to be most effective in forming nanofluids, as identified by R. M. Mostafizur [21]. The nanofluids were synthesized at room temperature following a two-phase dehydration-rehydration technique. The prediction of hybrid nanofluid volume concentration by the proposed quantity (50:50) of multi-walled carbon nanotubes (MNCNT) and aluminum oxide (Al_2O_3) nanoparticles was evaluated by the equation.

$$\Phi = \left[\frac{\left[\frac{W_{MWCNT}}{\rho_{MWCNT}}\right] + \left[\frac{W_{Al2O3}}{\rho_{Al2O3}}\right]}{\left[\frac{W_{MWCNT}}{\rho_{MWCNT}}\right] + \left[\frac{W_{Al2O3}}{\rho_{Al2O3}}\right] + \left[\frac{W_{bf}}{\rho_{bf}}\right]} \right] \cdot 100 \tag{2}$$

The focus and control of nanoparticle volume are important characteristics in the field of nanotechnology. Thus, it aids in the determination of the distribution, activity, and interconnection of the nanoparticles in a certain environment. The volume concentration of the nanoparticles with their respective weights is presented in Table 2.

3.3. Mixing of nano powder in the base fluid

The flowchart of the method used in the preparation of nanofluid is shown below in Fig. 8. The aim of the work is to obtain steady nanofluids of ZnO, MWCNTs, and Al_2O_3 nanoparticles suspended in ethylene glycol (EG) using ultrasonication and probe sonication, each process taking 2 hours for the nanoparticles to be well dispersed in the base fluid. This involves determining the mass of the nanoparticles, pouring the ethylene glycol into the beakers, and then adding the nanoparticles to the ethylene glycol. The ultrasonication technique also controls the temperature of the solutions, while probe sonication exposes the samples to more hours of sonication – 2 hours, to be precise. Subsequently, the resultant

TABLE 2. Volume concentration of the nanoparticles along with their associated weight

S.No.	Nanoparticles	Volume Concentration (%)	Weight Concentration(grams)
1	Aluminium Dioxide(Al_2O_3)	0.1	0.4
2		0.2	0.7
3		0.3	1
4	Multi-Wall Carbon Nanotubes (MWCNT)	0.1	0.2
5		0.2	0.4
6		0.3	0.6
7	Zinc Oxide (ZnO)	0.1	0.6
8		0.2	1
9		0.3	1.7
10	Al_2O_3 + MWCNT	0.25	0.6
11		0.35	0.84
12		0.45	1.08

samples will cool and be transferred to containers that are airtight to avoid the penetration of air after the process of sonication.

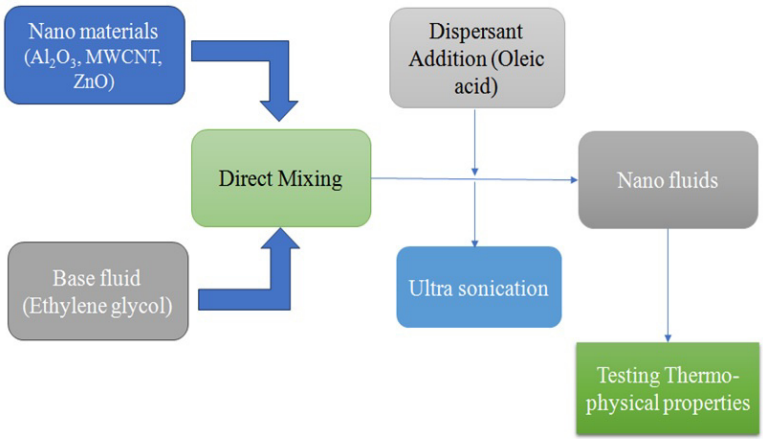

FIG. 8. Flow chart for the preparation of nanofluids

3.3.1. Dispersant for stability. Oleic acid ($C_{18}H_{34}O_2$) can be blended with various kinds of ethylene glycol, and thus the stability of the nanofluids containing ZnO, MWCNTs, and Al_2O_3 nanoparticles would greatly increase. Oleic acid works as an emulsifying agent and prevents the aggregation of the particles, thus allowing an even distribution of the nanoparticles.

The procedure entails measuring the necessary quantity of nanoparticles, transferring the ethylene glycol into beakers, introducing the nanoparticle suspensions, incorporating oleic acid, and agitating the mixes. The ultrasonication procedure entails immersing the suspensions in an ultrasonicator bath and subjecting them to sonication for duration of 1 hour. Following the sonication process, the prepared nanofluids with different concentrations (0.1, 0.2, and 0.3 wt %) samples are allowed to cool and then stored in containers.

4. Experimentation

4.1. Experimental measurement of viscosity

Viscosity, which is a measure of the fluid's resistance to change in shape and form, plays a significant role in the hydrodynamic and thermal characteristics of the nanofluids used in automobile heat transfer systems. It affects the Reynolds number, the coefficient of heat transfer, and the stability of the nanofluid; the nanoparticles should be uniformly distributed

to obtain optimum results. Therefore, studies on the viscosity of nanofluids (ethylene glycol) with dispersed nanoparticles like Al_2O_3, MWCNT, and ZnO are of immense importance in materials science and fluent dynamics. The fluids of these nanocomposite materials express distinctly different rheological parameters that impact their viscous and flow characteristics.

One of the traditional viscometers, namely the Redwood viscometer, has been used to measure the viscosity of petroleum products, including nanofluids such as Al_2O_3, ZnO, and MWCNT dispersed in the base fluid, ethylene glycol. This method is easily understood, inexpensive, and ideal for obtaining viscosity values in the field or within industries.

4.1.1. Theoretical estimation of viscosity. The Einstein model is an effective method that can be used for the prediction of the viscosity of nanofluids. It is for suspensions only and offers a means by which the viscosity of a dilute suspension of spherical particles in a liquid can be approximated. The model hereby adopted accepts the premise that the viscosity of a fluid loaded with particles or droplets is presumed to have the ability to be determined with the aid of the volume fractions or concentrations of the particles and the base fluid viscosity. From the formula, one is in a position to estimate the volume fraction of nanoparticles contained in a nanofluid. It is presumed that the nanoparticles in the model have a low volume fraction, that they form a stable suspension, and that the particle size and shape do not change significantly. It is most accurate where the concentration is low and where the effects of interactions between particles and their packing are negligible. Application of nanoparticles to the base fluid can easily be explained by the Einstein model, depending on the concentration of the nanoparticles.

$$\mu_{nf} = \mu_{bf}(1 + 2.5\emptyset) \tag{3}$$

4.2. Experimental measurement of density

The investigation of density for these nanofluid systems in ethylene glycol is necessary to enhance their description. Nanofluids cover nanoparticles suspended in a base fluid such as ethylene glycol, and it is not unusual for the density of the new fluids to be significantly different than that of the base fluid solely due to the nanoparticles. Higher accuracy density values provide significant information about the dispersion quality, stability, and movement of nanofluids. The density of nanofluids in ethylene glycol is measured by an instrument known as a densitometer, as depicted in Fig. 9, since it is not uncommon for nanofluids to exhibit some rather strange density trends in terms of the nanoparticles they contain. The instruments, such as the densitometer, can correctly read the density of the liquid and, hence, the buoyancy or mass of the sample, depending on the volume or displacement formulas formulated. It involves the generation of the required nanoparticles, their dispersion in ethylene glycol, and putting the samples in the densitometer.

4.2.1. Theoretical estimation of density. The Pak and Cho model [37] is an empirical model to predict the density of nanofluids that confines the former output, which is a developer of densities and volume fractions of the base fluid and nanoparticles. The density of the nanofluid according to the given model can be expressed through the contributions of the base fluid and nanoparticles. The formula for calculating the density of a nanofluid is:

$$\rho_{nf} = (1 - \emptyset)\,\rho_{bf} + \emptyset\rho_{np} \tag{4}$$

When the volume fraction of nanoparticles is low, the Pak and Cho model becomes useful for estimating the density of nanofluids in practical applications. This is a viable and simple way of determining the density of these nanofluids; therefore, it can help in many applications of nanofluids in different areas.

4.3. Experimental measurement of thermal conductivity

The C-Therm Analyzer Setup (ASTM D7984) is a valuable equipment to determine the thermal conductivity of nanofluids, as it allows doing that quickly and accurately and provides pleasing versatility given the ability to work with rather various samples. So it is useful in deciding the heat transfer coefficient, materials to be used, and overall performance. The C-Therm analyzer works on the modified transient plane source (MTPS) method, which shows a high degree of accuracy and reliability. It is non-destructive; hence, the same sample can be tested over and over again, which gives more accurate results. The analyzer is also usable for different types of samples and gives immediate results at stable temperatures. It again necessitated a low sample volume, which can prove advantageous in cases where a large amount of money is invested or a small amount of nanomaterial is available. In this study, some of the processes that have been carried out are sample preparation, calibration, measurement, and obtaining the value of thermal conductivity. The advantages of having accurate thermal conductivity include better thermal control, improved nanofluid composition, and standardization.

4.3.1. Theoretical estimation of thermal conductivity. The current experimental data demonstrates that the thermal conductivity of nanofluids is influenced by the thermal conductivities of both the base fluids and particles. Many mathematical models have been derived by Maxwell et al. (1956), Hamilton and Crosser et al. (1962), Masuda et al. (1993), and H. S. Chen et al. (2007) to enable the comparison of experimental data with theoretical data.

This model considers the thermal conductivity of the base fluid and the dispersed nanoparticles, as well as their volume fractions, in order to compute the overall thermal conductivity of nanofluids. Maxwell's model demonstrates that the thermal conductivity of suspensions with spherical particles increases as the volume percentage of the solid particles

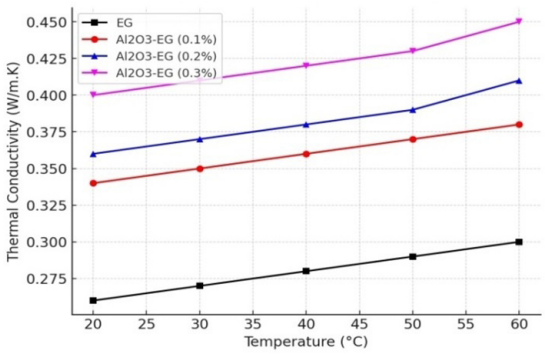

FIG. 9. Thermal conductivity Vs Temperature Al_2O_3/EG

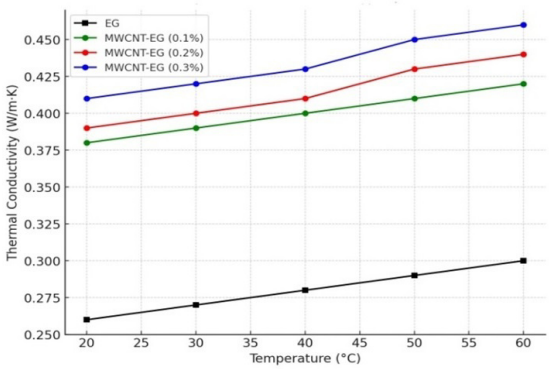

FIG. 10. Thermal conductivity Vs Temperature MWCNT/EG

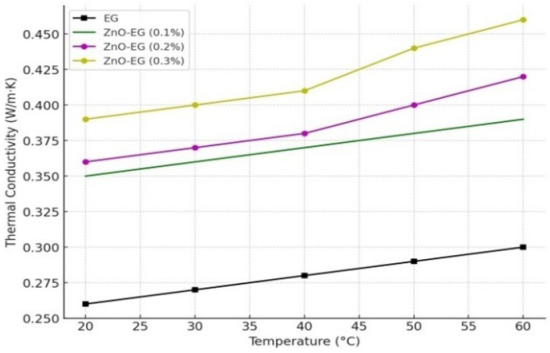

FIG. 11. Thermal conductivity Vs Temperature ZnO/EG

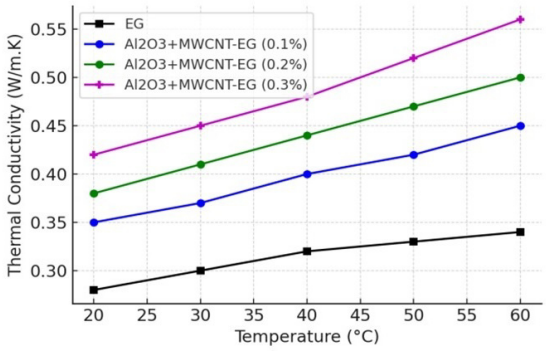

FIG. 12. Thermal conductivity Vs Temperature Al_2O_3 + MWCNT /EG

increases. The thermal conductivity of suspensions containing non-spherical particles is influenced by factors beyond only the volume fraction of the particles. The Maxwell model is the most appropriate mathematical model for determining the effective thermal conductivity of solid-liquid mixtures containing nanoparticles [36].

$$k_{nf} = \frac{k_p + 2k_f + 2\emptyset(k_p - k_f)}{k_p + 2k_f - \emptyset(k_p - k_f)} x k_f \tag{5}$$

5. Results and discussions

5.1. Thermal conductivity

Experiments on heat transfer using a C-thermal analyzer are comprised of ethylene glycol containing some nanoparticles. The C-thermal analyzer is used primarily in computing thermal conductivity values for nanofluids by means of the transient plane source (TPS) technique. A well-controlled heat pulse is produced during an electrical power supply, providing such sensors as those placed between two samples, termed a plane source. When producing heat within itself led to non-permanent thermal reactions, those were captured at that moment in the shape of sharp flats or rectangles made up of common materials; in reference to them, such materials would have high degrees of heat transfer. The speed at which those reactions spread out through these sample materials depends on the thermal conduction rate. While the heat pulse traverses the sample, the device monitors the temporal temperature variations on both sides of the sensor. By closely monitoring these temperature swings, it is feasible to determine the thermal conductivity of the material.

The findings of this study are shown in Figs. 9–12, along with a comprehensive report. The impact of temperature on the thermal conductivity of ethylene glycol with nanoparticles is demonstrated in the following study.

The thermal conductivity of ethylene glycol, when mixed with nanoparticles of Al_2O_3, MWCNT, and ZnO, rises as the quantities of the nanoparticles are raised while keeping the temperature constant. More precisely, when the volumetric concentrations increase from 0.1 to 0.2 vol % and 0.3 vol %, the thermal conductivity improvement reaches a maximum of 39.09 %.

The thermal conductivity increases linearly as the volumetric concentration percentage increases, while keeping the temperature constant. Furthermore, within the temperature range of 20 °C to 60 °C, the thermal conductivity of ethylene glycol with these nanoparticles increases in a nearly linear fashion. At lower temperatures, the rise in thermal conductivity is less significant compared to the rise observed at higher temperatures within the range of 20 °C to 60 °C.

While the experimental results show an increase in thermal conductivity within thestudied temperature range of 20 °C to 60 °C and nanoparticle concentrations from 0.1 vol % to 0.3 vol %, extrapolation to higher temperatures and concentrations requires caution. At highertemperatures, changes in the base fluid properties (e.g., viscosity reduction) and potential-nanoparticle agglomeration could lead to non-linear effects. Similarly, at concentrationsexceeding 0.3 vol %, increased inter-particle interactions and aggregation might diminish the thermal conductivity or even destabilize the nanofluid. These factors need to be accounted for in theoretical models or further experimental investigations.

TABLE 3. Comparison of theoretical and experimental thermal conductivity

(a) Comparison of theoretical and experimental thermal conductivity of Al_2O_3/EG

S. No.	Samples	Maxwell model (W/m·K)	Experimental value (W/m·K)	% Deviation
1	EG+Al_2O_3 0.1 vol%	0.3333	0.333	0.09
2	EG+Al_2O_3 0.2 vol%	0.372	0.367	1.36
3	EG+Al_2O_3 0.3 vol%	0.40	0.394	1.5

(b) Comparison of theoretical and experimental thermal conductivity of MWCNT/EG

S. No.	Samples	Maxwell model (W/m·K)	Experimental value (W/m·K)	% Deviation
1	EG+MWCNT0.1 vol%	0.384	0.382	0.52
2	EG+MWCNT0.2 vol%	0.403	0.391	2.91
3	EG+MWCNT0.3 vol%	0.412	0.399	3.15

(c) Comparison of theoretical and experimental thermal conductivity of ZnO/EG

S. No.	Samples	Maxwell model (W/m·K)	Experimental value (W/m·K)	% Deviation
1	EG+ZnO 0.1 vol%	0.342	0.343	0.2
2	EG+ZnO 0.2 vol%	0.375	0.361	3.70
3	EG+ZnO 0.3 vol%	0.41	0.379	7.38

(d) Comparison of theoretical and experimental thermal conductivity of Al_2O_3+ MWCNT/EG

S. No.	Samples	Maxwell model (W/m·K)	Experimental value (W/m·K)	% Deviation
1	EG+Al_2O_3/MWCNT 0.1 vol%	0.414	0.413	0.24
2	EG+Al_2O_3/MWCNT 0.2 vol%	0.458	0.436	4.80
3	EG+Al_2O_3/MWCNT 0.3 vol%	0.546	0.4972	8.65

From the obtained theoretical results of thermal conductivity at 20 °C represented in Tables 3(a-d), show that for all the volumetric concentrations, ethylene glycol shows a better result at 0.1 vol % and 0.2 vol % for all nanofluids, and ethylene glycol with ZnO and Al_2O_3+MWCNT at 0.3 vol % shows a higher percentage deviation due to the agglomerations formed with the increase in mass concentration of the compositions.

The findings of the experiments shown in Fig. 13 indicated that for all nanofluid concentrations at 20 °C, the thermal conductivity calculated exceeded the predicted values of the Maxwell model. In particular, the improvements varied between a low of 2 % and a high of 12 % across types and amounts of the nano injection. A small increase of 2–8 % was recorded for single-component nanofluids like EG + Al_2O_3 and EG + ZnO while double-phase nanofluids comprised of EG and Al_2O_3 and MWCNT recorded the largest increase of up to 12 %. This demonstrates the significance of nanoparticle concentration and synergism in tailoring thermal conductivity for advanced heat transfer applications.

5.2. Viscosity

Experimentation is carried out for the estimation of viscosity using a Redwood viscometer. Data on the variation of the viscosity of ethylene glycol with nanoparticles is presented in Tables 4(a–d) with regards to its correlation with temperature. The tables below provide the results of the dependency of the EG-nanoparticle solution's viscosity at different

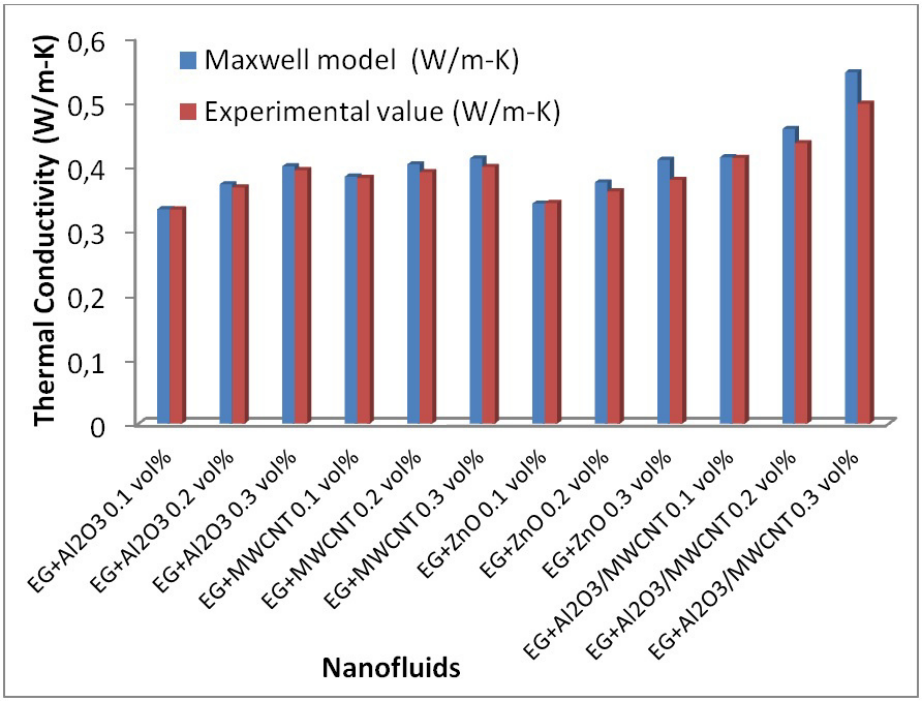

FIG. 13. Thermal conductivity of Nanofluids

concentrations on the nanoparticle type and temperature: 30 °C and 60 °C. Furthermore, this document also contains theoretical viscosities, and the percentage deviation from experimental values. The comparison of the experimental and calculated values of viscosity is represented in Fig. 14.

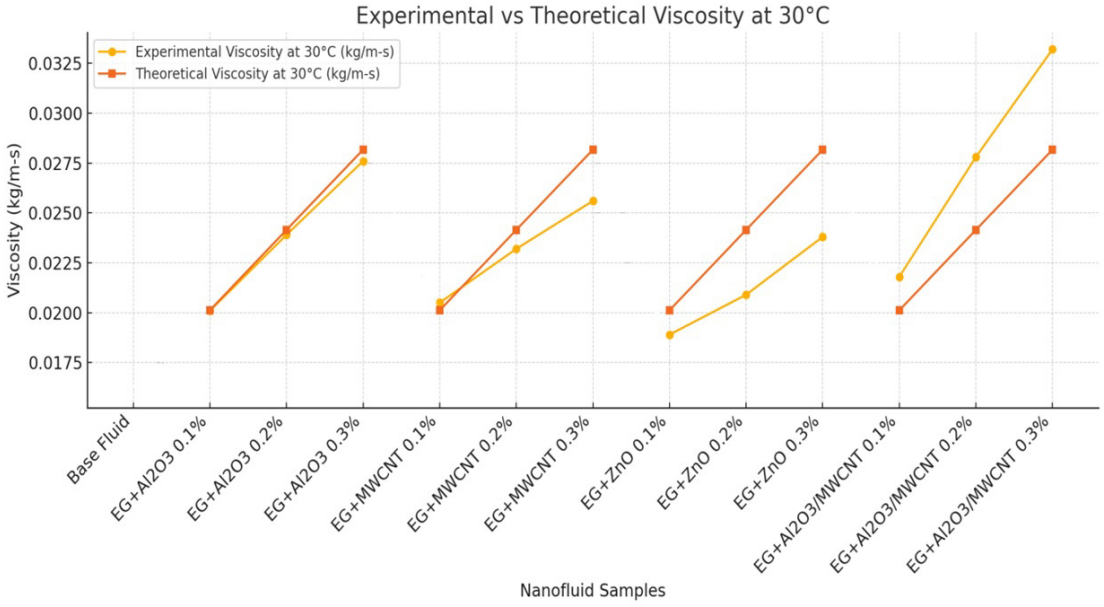

FIG. 14. Viscosity of Nanofluids

It is established that there was a significant and rapid rise in viscosity based on the results obtained. When increasing the temperature, the intermolecular bond interaction diminishes, and subsequently, the viscosity of ethylene glycol-containing nanoparticles decreases. Thus, it is seen that the viscosity has a very significant change or a steep fall with the increase in temperature. In the case of ethylene glycol, the viscosity increases with an increase in nanoparticles, and the maximum viscosity enhancement is 39.24 %. The above observations were all made at a constant temperature. Due to the higher inter-particle interaction, there is a direct relationship between the viscosity of the substance and the concentration of nanoparticles. The results imply that nanoparticle concentration affects the degree of viscous behavior, and a sharp increase can be seen when transitioning from a volume concentration of 0.1 % to 0.2 %.

TABLE 4. Viscosity of EG

(a) Viscosity of EG with Al_2O_3 nanoparticles

S. No.	Nanofluid Samples	Viscosity at 30 °C μ (kg/m-s)	Viscosity at 60 °C μ (kg/m-s)	Theoretical Viscosity at 30 °C μ (kg/m-s)	% deviation
1	Base fluid	1.61×10^{-2}	1.15×10^{-2}	1.61×10^{-2}	0
2	EG+Al_2O_3 0.1 vol%	2.01×10^{-2}	1.45×10^{-2}	2.012×10^{-2}	−0.09
3	EG+Al_2O_3 0.2 vol%	2.39×10^{-2}	1.58×10^{-2}	2.415×10^{-2}	−1.03
4	EG+Al_2O_3 0.3 vol%	2.76×10^{-2}	1.96×10^{-2}	2.817×10^{-2}	−2.02

(b) Viscosity of EG with MWCNT nanoparticles

S. No.	Nanofluid Samples	Viscosity at 30 °C μ (kg/m-s)	Viscosity at 60 °C μ (kg/m-s)	Theoretical Viscosity at 30 °C μ (kg/m-s)	% deviation
1	Base fluid	1.61×10^{-2}	1.15×10^{-2}	1.61×10^{-2}	0
2	EG+MWCNT 0.1 vol%	2.05×10^{-2}	1.52×10^{-2}	2.012×10^{-2}	1.88
3	EG+MWCNT 0.2 vol%	2.32×10^{-2}	1.76×10^{-2}	2.415×10^{-2}	−3.93
4	EG+MWCNT 0.3 vol%	2.56×10^{-2}	1.92×10^{-2}	2.817×10^{-2}	−9.12

(c) Viscosity of EG with ZnO nanoparticles

S. No.	Nanofluid Samples	Viscosity at 30 °C μ (kg/m-s)	Viscosity at 60 °C μ (kg/m-s)	Theoretical Viscosity at 30 °C μ (kg/m-s)	% deviation
1	Base fluid	1.61×10^{-2}	1.15×10^{-2}	1.61×10^{-2}	0
2	EG+ZnO 0.1 vol%	1.89×10^{-2}	1.42×10^{-2}	2.012×10^{-2}	−6.06
3	EG+ZnO 0.2 vol%	2.09×10^{-2}	1.65×10^{-2}	2.415×10^{-2}	−13.45
4	EG+ZnO 0.3 vol%	2.38×10^{-2}	1.75×10^{-2}	2.817×10^{-2}	−15.51

(d) Viscosity of EG with Al_2O_3 + MWCNT nanoparticles

S. No.	Nanofluid Samples	Viscosity at 30 °C μ (kg/m-s)	Viscosity at 60 °C μ (kg/m-s)	Theoretical Viscosity at 30 °C μ (kg/m-s)	% deviation
1	Base fluid	1.61×10^{-2}	1.15×10^{-2}	1.61×10^{-2}	0
2	EG+Al_2O_3/ MWCNT 0.1 vol%	2.18×10^{-2}	1.92×10^{-2}	2.012×10^{-2}	8.34
3	EG+Al_2O_3/ MWCNT 0.2 vol%	2.78×10^{-2}	2.58×10^{-2}	2.415×10^{-2}	15.11
4	EG+Al_2O_3/ MWCNT 0.3 vol%	3.32×10^{-2}	4.15×10^{-2}	2.817×10^{-2}	17.85

Fluids based on ethylene glycol (EG) appear to be thickening with the addition of nanoparticles such as Al_2O_3, MWCNTs, and ZnO, where stronger increases are seen with higher concentrations and Al_2O_3/MWCNT mixtures because of the synergetic effect. Remembering also that high shear viscosity has an apparent relation with fluid temperature: As the temperature rises, viscosity decreases; however, that would be an oversimplification, as higher concentrations bring forth agglomeration, and that makes the results deviate away from the prediction. This emphasizes the significance of the status of the particles and the interplay between them in determining the nature of the fluid.

5.3. Density

A densitometer is one of the most effective tools to determine the density of liquids, especially nanofluids with ethylene glycol as the base fluid. The functioning of this device is based on Archimedes' principle, which states that the upward thrust that is exerted by fluid in which an object is fully or partly immersed is equal to the weight of the fluid displaced by the body. Density is experimented with by carrying out trials using the densitometer at room temperature.

TABLE 5. Comparison of Theoretical and Experimental Density results

(a) Comparison of Theoretical and Experimental Density results of Al_2O_3/EG

S. No.	Samples	Theoretical value (kg/m^3)	Experimental value (kg/m^3)	% Deviation
1	EG+Al_2O_3 0.1 vol%	1396	1391.2	0.34
2	EG+Al_2O_3 0.2 vol%	1482	1462.5	1.31
3	EG+Al_2O_3 0.3 vol%	1596	1565.3	1.92

(b) Comparison of Theoretical and Experimental Density results of MWCNT/EG

S. No.	Samples	Theoretical value (kg/m^3)	Experimental value (kg/m^3)	% Deviation
1	EG+MWCNT 0.1 vol%	1199	1189.3	0.80
2	EG+MWCNT 0.2 vol%	1288	1273.1	1.15
3	EG+MWCNT 0.3 vol%	1377	1351.8	1.83

(c) Comparison of Theoretical and Experimental Density results of ZnO and ethylene glycol

S. No.	Samples	Theoretical value (kg/m^3)	Experimental value (kg/m^3)	% Deviation
1	EG+ZnO 0.1 vol%	1599	1592.9	0.38
2	EG+ZnO 0.2 vol%	1765	1752.1	0.73
3	EG+ZnO 0.3 vol%	1862	1821.9	2.19

(d) Comparison of Theoretical and Experimental Density results of Al_2O_3 + MWCNT and ethylene glycol

S. No.	Samples	Theoretical value (kg/m^3)	Experimental value (kg/m^3)	% Deviation
1	EG+Al_2O_3/ MWCNT 0.1 vol%	1132	1125.2	0.60
2	EG+Al_2O_3/ MWCNT 0.2 vol%	1186	1169.9	1.35
3	EG+Al_2O_3/ MWCNT 0.3 vol%	1286	1237.1	3.80

The test for the density of a solution of ethylene glycol at increasing volumetric proportions of aluminum dioxide, multi-wall carbon nanotubes, and zinc oxide is conducted with the help of a densitometer. It also has Ethylene Glycol impact density, Aluminium Dioxide, Multi-Wall Carbon Nanotubes, and Zinc Oxide presented in tabular forms 5 (a-d) compared with the theoretical model.

By comparing all the theoretical values and experimental values of density, the results shown in Fig. 15 indicated that with 0.1 vol % and 0.2 vol % nanoparticles in ethylene glycol, the percentage deviation is less when compared to 0.3 vol % nanofluids. This percentage deviation is caused by the fact that with the increase in volume concentration, there is a chance to form agglomerated particles, which may cause a reduction in some coolant properties.

5.4. Correlation between thermal conductivity, viscosity, and density

Thermal conductivity increases nearly in linear fashion with nanoparticle concentration and temperature, achieving a maximum enhancement of 39 % at 0.3 vol % concentration and 60 °C. Viscosity exhibits a significant rise with increased nanoparticle concentration but decreases with temperature due to weakened intermolecular forces. The maximum observed increase in viscosity is 39.24 %. Finally, density shows minor deviations from theoretical predictions, with higher concentrations leading to marginal increases in density due to nanoparticle agglomeration. These properties collectively demonstrate the potential of the studied nanofluids in applications requiring efficient thermal management. High thermal conductivity and controllable viscosity ensure enhanced heat transfer, while density stability supports consistent performance.

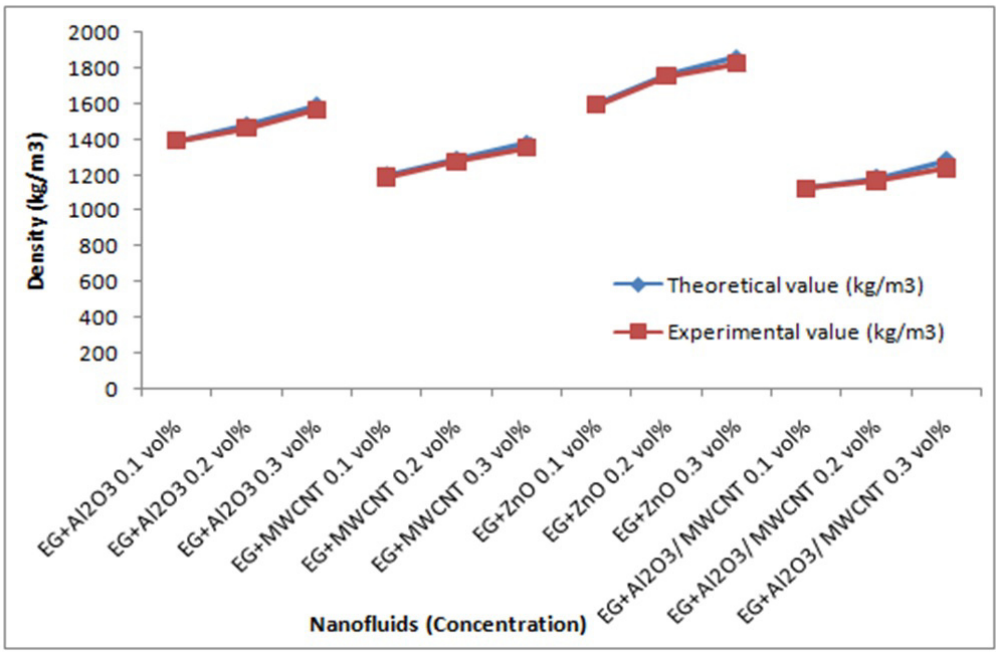

FIG. 15. Density of Nanofluids

The remarkable thermophysical properties of the studied nanofluids make them optimal. The improved thermal conduction in the core industry results in the use of small and lightweight radiators that have high efficiency in cooling, thus improving fuel economy and reducing emissions. With stable viscosity and density over temperature ranges, effective and reliable engine cooling systems would be assured. In cars and in electronics industries, a high rate of heat dissipation avoids overheating of miniaturized electronic devices. Better thermal management increases the lifetime and good efficiency of high-end devices like CPUs or GPUs.

6. Conclusions

The thermal conductivity of ethylene glycol increases linearly with the addition of Al_2O_3, MWCNT, and ZnO nanoparticles, reaching a maximum of 39.09 % when volumetric concentrations increase from 0.1 to 0.3 vol % and linearly within the temperature range of 20 °C to 60 °C.

This linear increase in thermal conductivity as temperature increases, especially at 60 °C, shows the great possibility of nanofluids for thermal management in automobiles as well as in electronic appliances.

The study shows that as temperature increases, the viscosity of ethylene glycol-containing nanoparticles increases because of a weak interaction between the particles. It does this at lower temperatures, though at higher temperatures the viscosity decreases up to a maximum of 39.24 %.

It was observed that high concentrations of nanoparticles raised the viscosity of the solution, for instance, when going from 0.1 % to 0.2 %. EG+ZnO nanofluid and EG+MWCNT/ Al_2O_3at 0.2 and 0.3 vol % show the maximum deviation in viscosity. It is expected to have this deviation due to experimental errors and the agglomeration of hybrid nanofluids.

The incorporation of Al_2O_3 and MWCNT nanoparticles into the base fluid EG raises the fluid's viscosity, with a minor effect on Al_2O_3 and a greater effect on MWCNT nanoparticles. It is observed that the mix of Al_2O_3 and MWCNT has the highest increment in viscosity of the composites.

The density study shows that nanoparticles in EG (ethylene glycol) with 0.1 and 0.2 vol % exhibit a lower percentage deviation than nanofluids with 0.3 vol %, which may reduce the coolant's physical properties.

References

[1] Xianjun Hou., Chen Chu., Hua Jiang., Mohamed Kamal, Ahmed Ali., Karl D., Dearn. Enhancing Heat Transfer Behaviour of Ethylene Glycol by the Introduction of Silicon Carbide Nanoparticles: An Experimental and Molecular Dynamics Simulation Study. *Molecules*, 2023, **28**(7), 3011 p.

[2] Srinivas Vadapalli, Jaikumar Sagari, Haricharan Alapati, Vishnuvardhan Reddy, Kalamalla, Ravi Su. Heat transfer enhancement of mono ethylene glycol – water based solar thermic fluids dispersed with multiwalled carbon nano tubes in a coiled tube heat exchanger. *Journal of Enhanced Heat Transfer*, 2023, **30**(5), P. 1–22.

[3] R. Prasanna Shankara, N.R. Banapurmath, Abhinandan D'Souza, A.M. Sajjan, N.H. Ayachit, T.M. Yunus Khan, Irfan Anjum Badruddin, Sarfaraz Kamangar. An insight into the performance of radiator system using ethylene glycol-water based graphene oxide nanofluids. *Alexandria Engineering Journal*, 2022, **61**(7), P. 5155–5167.

[4] Tanveer A., Aneja M., Ashraf M.B., Nawaz R. Bioconvection heat and mass transfer across a nonlinear stretching sheet with hybrid nanofluids, joule dissipation, and entropy generation. *Z. Angew. Math. Mech.*, 2024, **104**, P. e202300550.

[5] Shihao Wu., Genghao Xu., Haosen Lin., Wensheng Xiao., Lei Ma. Heat transfer and flow characteristics of CuO-Al_2O_3 hybrid nanofluids in slotted finned channels. *Journal of Physics: Conference Series*, 2024, **2683**, P. 012035.

[6] Firas Aziz, Ali Adnan, M. Alsaffawi. Friction Factor and Heat Transfer Enhancement of Hybrid Nanofluids in a Heated Circular Tube. *International Journal of Heat and Technology*, 2023, **41**(5), P. 1383–1388.

[7] Tarun Sharma., Pooja Sharma. Heat transfer analysis of Cu–H_2O/Al_2O_3–H_2O nanofluid flow in wavy/microchannels: A review. *Modern Physics Letters B*, 2024, P. 2430001.

[8] Kusammanavar, Basavaraj., K., Elangovan., Shiva, Shankar., S., Satyanarayan. Effects of Al_2O_3 Concentration in Ethylene Glycol on Convection Heat Transfer Coefficient. *International Journal of Vehicle Structures and Systems*, 2023, **15**(3), P. 345.

[9] Elbadawy I., Alali F., Farrokhi Javad, Derakhshandeh Ali, Dinc Mohamed, Abouelela Wael, Al-Kouz. Effect of Al_2O_3, SiO_2, and ZnO Nanoparticle Concentrations Mixed with EG–Water on the Heat Transfer Characteristics through a Microchannel. *Processes*, 2023, **11**(7), P. 2015.

[10] Preeti Prashar, Odelu Ojjela. Numerical investigation of ZnO–MWCNTs/ethylene glycol hybrid nanofluid flow with activation energy. *Indian Journal of Physics*, 2021, **96**(7), P. 2079–2092.

[11] Gabriela Huminic, Angel Huminic, A. Hybrid nanofluids for heat transfer applications – A stateoftheart review. *International Journal of Heat and Mass Transfer*, 2018, **125**, P. 82–103.

[12] Muneeshwaran M., Srinivasan G., Muthukumar P., Wang C. Role of hybrid-nanofluid in heat transfer enhancement – A review. *International Communications in Heat and Mass Transfer*, 2021, **125**, P. 105341.

[13] Urmi W., Shafiqah A., Rahman M., Kadirgama K., Maleque M. Preparation Methods and Challenges of Hybrid Nanofluids: A Review. *Journal of Advanced Research in Fluid Mechanics and Thermal Sciences*, 2021, **78**(2), P. 56–66.

[14] Babar H., Ali H. Towards hybrid nanofluids: Preparation, thermophysical properties, applications, and challenges. *Journal of Molecular Liquids*, 2019, **281**, P. 598–633.

[15] Sandhya M., Ramasamy D., Sudhakar K., Kadirgama K., Harun W. Ultrasonication an intensifying tool for preparation of stable nanofluids and study the time influence on distinct properties of graphene nanofluids – A systematic overview. *Ultrasonics Sonochemistry*, 2021, **73**, P. 105479.

[16] Mahbubul I., Shahrul I., Khaleduzzaman S., Saidur R., Amalina M., Turgut A. Experimental investigation on effect of ultrasonication duration on colloidal dispersion and thermophysical properties of alumina–water nanofluid. *International Journal of Heat and Mass Transfer*, 2015, **88**, P. 73–81.

[17] Yang L., Xu J., Du K., Zhang X. Recent developments on viscosity and thermal conductivity of nanofluids. *Powder Technology*, 2017, **317**, P. 348–369.

[18] Baghban A., Jalali A., Shafiee M., Ahmadi M., Chau K. Developing an ANFIS-based swarm concept model for estimating the relative viscosity of nanofluids. *Engineering Applications of Computational Fluid Mechanics*, 2018, **13**, P. 26–39.

[19] Sahaluddin M., Alade I., Oyedeji M., Aliyu U. A machine learning-based model to estimate the density of nanofluids of nitrides in ethylene glycol. *Journal of Applied Physics*, 2020, **127**, P. 205105.

[20] Adun H., Wole-Osho I., Okonkwo E., Bamisile O., Dagbasi M., Abbasoğlu S. A neural network-based predictive model for the thermal conductivity of hybrid nanofluids. *International Communications in Heat and Mass Transfer*, 2020, **119**, P. 104930.

[21] Mostafizur R.M., Rasul M.G., Nabi M.N., Gopalan Saianand. Properties of Al_2O_3-MWCNT/radiator coolant hybrid nanofluid for solar energy applications. *7th International Conference on Advances on Clean Energy Research*, ICACER 2022, Barcelona, Spain, *Energy Reports8*, 2022, P. 582–591.

[22] Aditi Zoya Farooque, Nathi Ram Chauhan. Comparative study of Nano-fluids as Coolants in a Car Radiator, IOP Conf. Series: *Materials Science and Engineering*, 2022, **1228**, P. 012011.

[23] Rahul Ghimire, Pankaj Mehta, Nischal Aryal, Daya Ram Sah, Surya Prasad Adhikari. Thermal Performance of Car Radiator Operated by Al_2O_3 – Ethylene Glycol/Water-Based Nanofluids: A Computational Fluid Dynamics Study. *Journal of Thermal Science and Engineering Applications*, 2022, **15**(1), P. 011012.

[24] V.P. Suresh Kumar, N. Manikandan, N. Nagaprasad, Jule LetaTesfaye, Ramasamy Krishnaraj. Analysis of the Performance Characteristics of ZnO Nanoparticles' Dispersed Polyester Oil. *Advances in Materials Science and Engineering*, 2022, P. 1–10.

[25] Srimanickam B., Elangovan M., Sachin Salunkhe, Emad Abouel Nasr, Hussein H.M. A., Ragavanantham Shanmugam. Experimental Studies on Water-Based Al_2O_3 Nanofluid to Enhance the Performance of the Hybrid Collector. *Advances in Materials Science and Engineering*, 2022, P. 1–10.

[26] Raviteja Surakasi, Srujana Sripathi, Sarada Purnima Nadimpalli, Ibtain Afzal, Bharat Singh, Manoj Tripathi, and Rahel Alemu Hafa. Synthesis and Characterization of TiO_2-Water Nanofluids. *Adsorption Science and Technology*, 2022, P. 1–9.

[27] Karaar Mahdi Al-Araji, Dhafer Manea Hachim, Almoussawi M A. Nano-Fluids as a Coolant for Automotive Engine Radiators: Review Study. *Al-Furat Journal of Innovations in Mechanical and Sustainable Energy Engineering (FJIMSE)* Published by Al-Furat Al-Awsat Technical University (ATU) / Iraq, 2021, **1**(2), P. 64–78.

[28] Sanjeev Kumar Gupta, Sangam Dixit. Progress and application of nanofluids in solar collectors: An overview of recent advances. *Materials Today: Proceedings*, 2021, **44**(1), P. 250–259.

[29] Serdar Mart, Halit Yasar, Ufuk Durmaz, Adnan Topuz, Alper Yeter, Tahsin Engin. An Experimental Study on Cooling Performance of a Car Radiator Using Al_2O_3 – Ethylene Glycol / Water Nanofluid. *Thermal Science*, 2021, **25**(1), P. 801–809.

[30] Reza Aghayari, Heydar Maddah, Seyed Mohsen Pourkiaei, Mohammad Hossein Ahmadi, Lingen Chen, Mahyar Ghazvini. Theoretical and experimental studies of heat transfer in a double-pipe heat exchanger equipped with twisted tape and nanofluid. *Eur. Phys. J. Plus*, 2020, **135**, P. 252.

[31] Akshata Pattanshetti, N. Pradeep, V. Chaitra, V. Uma. Synthesis of multi-walled carbon nanotubes (MWCNTs) from plastic waste and analysis of garlic coated gelatin/MWCNTs nanocomposite flms as food packaging material, *SNApplied Sciences*, 2020, **2**, P. 730.

[32] Abu Raihan Ibna Ali, Bodius Salam. A review on nanofuid: preparation, stability, thermophysical properties, heat transfer characteristics and application. *SN Applied Sciences*, 2020, **2**, P. 1636.

[33] Nand Kumar Sadashiv Vele, R.K. Patil. Review On Heat Transfer Enhancement In Car Radiator Using Nano Fluids. *Proceedings of the International Conference on Industrial Engineering and Operations Management*, Bangkok, Thailand, March 5-7, 2019.

[34] Zafar Said, M. El Haj Assad, Ahmed Amine Hachicha, Evangelos Bellos, Mohammad Ali Abdelkareem, Duha Zeyad Alazaizeh, Bashria A.A. Yousef, 2019, *Renewable and Sustainable Energy Reviews*, 2019, **112**, P. 183–194.

[35] Muhammad Qasim, Muhammad Sajid Kamran, Muhammad Ammar, Muhammad Ali Jamal, Muhammad Yasar Javaid. Heat Transfer Enhancement of an Automobile Engine Radiator using ZnO Water Base Nanofluids, *Journal of Thermal Science*, 2020, **29**(4), P. 1010–1024.

[36] Choi S.U.S., Eastman J.A. Enhancing thermal conductivity of fluids with nanoparticles. *ASME International Mechanical Engineering Congress and Exposition*, San Francisco, CA, 1995.

[37] Pak B.C., Cho Y.I. Hydrodynamic and heat transfer study of dispersed fluids with submicron metallic oxide particles. *Experimental Heat Transfer*, 1998, **11**(2), P. 151–170.

Submitted 9 August 2024; revised 23 December 2024, 8 February 2025; accepted 9 February 2025

Information about the authors:

Salman Basha Sheik – Research Scholar, Department of Mechanical Engineering, SR University, Warangal, India, 506371; Assistant Professor, Department of Mechanical Engineering, Sasi Institute of Technology and Engineering, Tadepalligudem, 534101; ORCID 0009-0006-4685-6004; sheiksalmanbasha@gmail.com

Praveena Devi Nagireddy – Assistant Professor, Department of Mechanical Engineering, SR University, Warangal, India, 506371; ORCID 0000-0001-8816-7419; n.praveenadevi@sru.edu.in

Kiran Kumar Kupireddi – Professor, Department of Mechanical Engineering, National Institute of Technology Warangal, Warangal, India, 506004; ORCID 0000-0002-2681-2010; kiran@nitw.ac.in

Conflict of interest: the authors declare no conflict of interest.

NANOSYSTEMS:
PHYSICS, CHEMISTRY, MATHEMATICS

Original article

Sumina A.A.. et al. *Nanosystems: Phys. Chem. Math.*, 2025, **16** (1), 105–115.
http://nanojournal.ifmo.ru
DOI 10.17586/2220-8054-2025-16-1-105-115

Nickel-copper-containing alloy catalysts for furfural hydroconversion: the influence of composition and physicochemical features on the distribution of reaction products in various modes

Anastasiya A. Sumina[a], Svetlana A. Selishcheva[b], Olga A. Bulavchenko[c], Vadim A. Yakovlev[d]

Federal Research Center Boreskov Institute of Catalysis SB RAS, Novosibirsk, Russia

[a]sumina@catalysis.ru, [b]svetlana@catalysis.ru, [c]obulavchenko@catalysis.ru, [d]yakovlev@catalysis.ru

Corresponding author: Svetlana A. Selishcheva, svetlana@catalysis.ru

PACS 82.45.Jn

ABSTRACT In this work, nickel-copper-containing alloy catalysts with different contents of nickel oxide were prepared and used in the furfural hydroconversion to 2-methylfuran and furfuryl alcohol. The most active catalyst (7Ni19Cu61Fe13Al) was chosen. We selected the reaction conditions, providing a high yield of 2-methylfuran (81 wt. %) at 100 % furfural conversion in a batch reactor: $T = 200$ °C, $P(H_2) = 5.0$ MPa, reaction time 4 h. The selected catalyst was studied by a complex of physicochemical methods; we determined the phase and surface composition, the morphology of the active component, and the possible cause of catalyst deactivation during the reaction due to the irreversible sorption of reactants and reaction products, as well as their polymeric structures on the catalyst surface. We have demonstrated the possibility of obtaining 2-methylfuran for the 7Ni19Cu61Fe13Al catalyst with a selectivity of 70 % at 87 % conversion of furfural in a flow-type reactor without solvent at $LHSV = 6$ h^{-1}, $T = 200$ °C, $P(H_2) = 5.0$ MPa.

KEYWORDS hydroconversion, furfural, catalysis, value-added chemicals, batch reactor, flow-type reactor

ACKNOWLEDGEMENTS The work was supported by the Ministry of Science and Higher Education of the Russian Federation within the governmental order for Boreskov Institute of Catalysis (project FWUR-2024-0043).

FOR CITATION Sumina A.A.. Selishcheva S.A.. Bulavchenko O.A.. Yakovlev V.A. Nickel-copper-containing alloy catalysts for furfural hydroconversion: the influence of composition and physicochemical features on the distribution of reaction products in various modes. *Nanosystems: Phys. Chem. Math.*, 2025, **16** (1), 105–115.

1. Introduction

Currently, due to the depletion of fossil resources, there is an increasing relevance in the search for new alternative sources used to produce raw materials. One of the sources for obtaining valuable chemical compounds are hemicelluloses, which are extracted during the processing of plant materials [1]. Hemicelluloses are of particular interest to the industry due to their low content of heavy metals, sulfur, and nitrogen, making them safer to process.

Furfural is obtained through the acid hydrolysis of hemicelluloses (Fig. 1a), and its world production in 2021 exceeded 300,000 tons [2]. Furfural is a platform for the synthesis of various chemicals due to its reactive aldehyde groups and conjugated double bonds [3]. Furfural derivatives are widely used to produce organic solvents, pharmaceuticals, agrochemicals, perfumes, biofuels, fuel additives, and synthetic resins or rubber [4]. One of the most interesting and common methods for processing furfural is hydroconversion, as the products obtained have a high value added [5]. For example, 2-methylfuran (2-MF), which is used in the fuel industry as an octane-boosting additive due to its high octane number (101) [6], as well as in medicine and pharmaceuticals as a precursor in the production of dietary supplements and drugs. The hydroconversion of furfural to 2-MF can proceed in two ways: through the intermediate formation of furfuryl alcohol (FA) or directly through the hydrogenolysis of the C=O double bond (Fig. 1b) [7, 8].

Traditional catalysts for the furfural hydroconversion to target products (2-MF, FA) are high-percentage copper-chromium ones [10], as well as catalysts based on noble metals [11, 12]. However, despite their high activity, these systems have several disadvantages. Use of chromium catalysts can contribute to toxic emissions due to the tendency of Cr^{6+} compounds to dissolve in many organic and inorganic solvents, including furfural [13, 14]. During the catalyst preparation stage, substances containing Cr^{6+} are used, and Cr^{6+} is also present in the fresh oxide catalyst (for example, in the following compounds: $CuCrO_4$, $CuCrO_4{\cdot}Cu(OH)_2$, $2CuCrO_4 \cdot 3Cu(OH)_2{\cdot}H_2O$) [15, 16]. During preliminary calcination or reduction in the preparation stage, the transition of chromium from the $+6$ state to the $+3$ state may be incomplete, which subsequently leads to contamination of the target products. Additionally, in some cases, these catalysts deactivate quickly, necessitating the use of high hydrogen pressure. In the case of noble metal catalysts, the primary limiting factor is their high cost [17].

© Sumina A.A.. Selishcheva S.A.. Bulavchenko O.A.. Yakovlev V.A., 2025

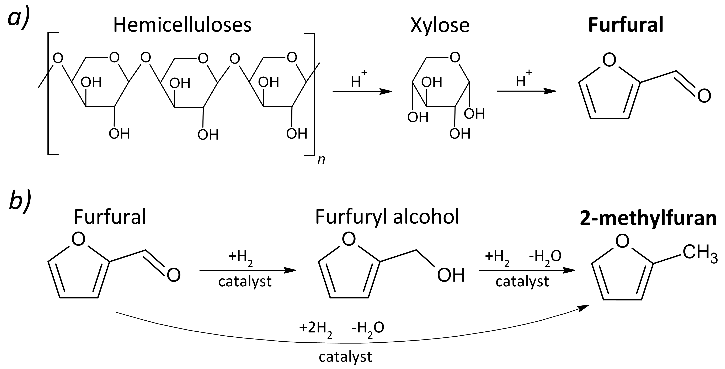

FIG. 1. a) The scheme for obtaining furfural from hemicelluloses [9]; b) The scheme of furfural hydroconversion over catalysts

Transition-based chromium-free systems can act as an alternative to the above-mentioned catalysts. Copper is one of the most active metals in the hydroprocessing of organic substances, particularly in the conversion of furfural into various C5-C6 organic compounds [18, 19]. Yunlong Yao et al. found that the Zn-modified Cu-containing catalyst demonstrated good results in the hydrogenation of furfural (100 % conversion) to FA ($\sim$ 100 % yield) under the following reaction conditions: 120 °C, 2.0 MPa, 0.2 g catalyst, 100 mL/min H_2, WHSV 0.3 h^{-1}) [20]. However, such systems are not suitable for obtaining 2-MF with high selectivity.

Doping of copper systems with nickel and cobalt accelerates furfural conversion and increases 2-MF yield [21, 22]. Munsuree Kalong et al. [23] describe monometallic copper samples supported on alumina, as well as the systems doped with nickel and cobalt. The conversion of furfural in the batch reactor reached 100 % of all samples over a reaction time of 2 hours. However, the nickel-promoted catalyst proved to be the most efficient. The maximum 2-MF yield obtained was 47 – 50 % at a reaction time of 2 hours. The authors concluded that doping with nickel enhances the activity of the catalyst and accelerates the reaction rate. In the work [24], the authors studied Ni–Fe catalysts obtained by co-precipitation; a 2-MF yield of up to 80 % was achieved, with complete conversion of furfural and a reaction time of 10 hours in the batch reactor over the catalyst. Apparently, high yields were due to the presence of fine metallic nickel particles and strong acid sites on the catalyst surface, represented by metal oxides, which promote the activation of the aldehyde group and the reduction of the C=O bond. Acidic sites on iron oxide are often employed to activate oxygen in molecules of aldehydes, acids, and alcohols [25], as well as in the Fischer–Tropsch process for the adsorption and activation of carbon monoxide molecules [26].

It should be noted that the high content of transition metals promotes the hydrogenation of the furan ring, resulting in the formation of tetrahydrofurfuryl alcohol (THFA), 1-pentanol, pentanal, 2-methyltetrahydrofuran (2-MTHF), etc. [27, 28]. However, at low concentrations, such additives enable the successful hydrogenation of the aldehyde group of furfural while preserving the structure of the furan ring [29].

The work [30] examined CuFeAl catalysts, which were prepared by the fusion method. Metallic copper serves as the active component of such systems. The modifying additives of aluminum and iron form a matrix for the active component, promote the formation of fine particles of copper, prevent its sintering, and prolong the service life of the catalyst. Nevertheless, this system is effective to produce FA; a higher content of a more active component is necessary in the catalyst to obtain 2-MF. The addition of nickel to the composition of such a system can improve the 2-MF selectivity. Previously, NiCu-containing catalysts were studied in the hydroconversion processes of bio-oil [31], as well as in its model compounds (anisole, guaiacol) [32], and in the hydrotreatment of vegetable oils [33].

In this work, we considered high-percentage NiCu-containing alloy catalysts with different contents of nickel oxide (5 – 10 wt.%) for the hydroconversion of furfural into FA and 2-MF. We tested the obtained catalysts in both a batch reactor with diluted feedstock and a flow-type reactor with pure furfural. The first method is well-studied and found in many works; however, the second method is less commonly used but more applicable for transition to industrial conditions. We studied the physicochemical properties of such systems and selected the optimal metal content in the catalyst to ensure maximum selectivity for the desired product (2-MF).

2. Experimental

We used the salt fusion method for the preparation of catalysts for the hydroconversion of furfural. We mixed the calculated weights of aqueous nitrates of iron, aluminum, copper, and nickel in a quartz bowl and heated on an electric stove to $\sim$ 300 °C. Next, the catalyst was calcined in a muffle furnace at a temperature of 450 °C for an hour. As a result, three catalysts were obtained: 5Ni19Cu63Fe13Al (5Ni), 7Ni19Cu61Fe13Al (7Ni), and 10Ni18Cu60Fe12Al (10Ni); value indicates metal oxide content (wt. %) in the sample.

The study of samples of the H_2-TPR method was carried out on a Chemosorb device (JSC Modern Laboratory Equipment, Moscow, Russia).

The XRD, in situ XRD, XPS, HRTEM, CHNS methods, textural characteristics of the reduced catalysts, the amount of chemisorbed CO on reduced catalysts at 250 °C, and qualitative and quantitative analysis of liquid products were previously described in [19].

Furfural (GOST 10930-74) was used for hydroconversion experiments and was pre-purified in a vacuum distillation unit. Isopropyl alcohol (GOST 9805-84) was used as a solvent to carry out the process in a batch reactor.

The furfural hydroconversion was carried out in a batch reactor with a volume of 300 cm^3. The reactor is equipped with a mechanical stirrer with a magnetic drive, a thermocouple, and a pressure sensor, as well as a control system for stirring speed, temperature, and pressure. Reduction conditions: $T = 250$ °C, hydrogen flow = 100 ml/min, $t = 1$ h; reaction conditions: $P(H_2) = 5$ MPa, mixing speed = 1800 rpm, $T = 160 - 250$ °C, $t = 4$ h.

The furfural hydroconversion in a flow-type unit was carried out using a reactor with a volume of 10 cm^3, into which we placed a catalyst weighing 1 g (fraction size 0.25 – 0.50 mm) mixed with quartz in a volume ratio of 1:4. We used crystalline purified quartz with a fraction size of 0.25 – 0.50 mm. Reduction conditions: $T = 250$ °C, hydrogen flow = 100 ml/min, $t = 1$ h; reaction conditions: $P(H_2) = 5$ MPa, $T = 200$ °C, LHSV = $1 - 8$ h^{-1}.

The thermal analysis was carried out using an STA 449 C Jupiter synchronous thermal analysis instrument from NETZSCH (Selb, Germany). For the study, the sample was placed in a crucible corundum. The rate of air supply to the sample chamber was 30 ml/min. The sample was heated at a rate of 10 °C/min to 1000 °C. The experimental data were analyzed using the NETZSCH Proteus Thermal Analysis software package (Selb, Germany).

3. Results and discussion

3.1. Characterization of fresh catalysts

We determined the reduction temperature of the obtained fresh catalysts using temperature-programmed reduction with hydrogen (H_2-TPR). The results showed that there are two regions of hydrogen uptake for all samples (Fig. 2). The first region is in the low-temperature range (200 – 330 °C), where copper and nickel oxide particles are reduced. The second region is in the high-temperature range (500 – 850 °C), where iron oxide is gradually reduced to metal.

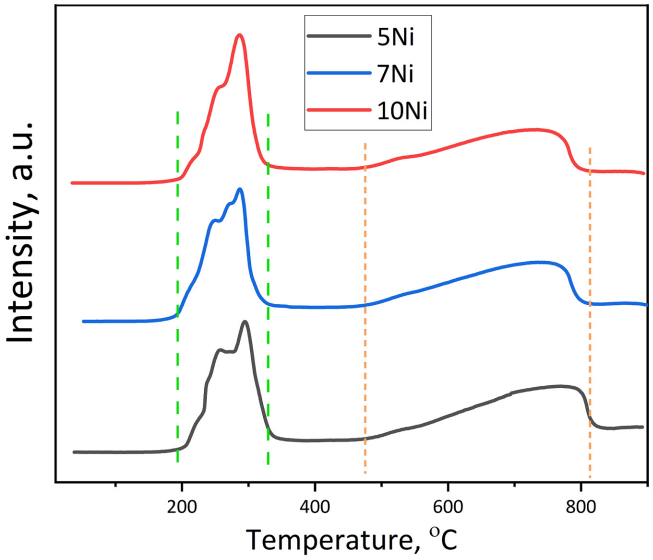

FIG. 2. H_2-TPR profiles of studied catalysts

Based on the data obtained from the H_2-TPR analysis, we chose a reduction temperature of 250 °C, which would reduce fine copper and nickel oxides.

The study of unreduced catalysts to determine their phase composition was carried out using X-ray diffraction analysis (XRD). For three catalyst samples (5Ni, 7Ni, and 10Ni) the X-ray patterns are similar (Fig. 3). The main peaks correspond to reflections from hematite (Fe_2O_3), and the CuO reflection is also observed (the peak with a maximum at $2\theta = 38.8°$ corresponds to the CuO reflection [111]). In the domain $2\theta = 35 - 37°$, there is a superposition of reflections [110] and [11-1] of CuO and [110] of Fe_2O_3. The absence of reflections corresponding to NiO and Al_2O_3 can be explained by their X-ray amorphous state.

The composition of the catalyst surface layer was studied using X-ray photoelectron spectroscopy (XPS). We examined three catalyst samples (5Ni, 7Ni, and 10Ni) after reduction at 250 °C.

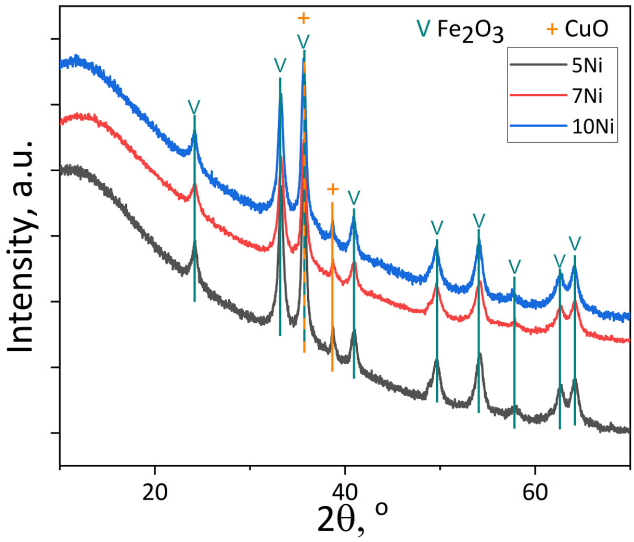

FIG. 3. X-ray patterns of unreduced catalysts

Figure 4a shows the Ni2p spectra of the studied catalysts. In the Ni2p spectra, we observed a reverse orbital splitting, and two groups of peaks associated with the $Ni2p_{3/2}$ and $Ni2p_{1/2}$ levels. In the spectra of the studied catalysts, a peak for the $Ni2p_{3/2}$ bond was found in the region of 852.8 eV, along with a peak for plasma losses in the region of 858.9 eV. Additionally, the presence of a peak in the region of 855.3 eV, accompanied by "main" satellite peaks in the regions of 857.1 and 862.0 eV, is typical for Ni^{2+} compounds. Thus, after reduction treatment, a portion of the nickel is in the metallic state (38 – 43 %), while the remainder is in the Ni^{2+} state as nickel oxide (NiO) [34, 35].

Figure 4b presents the spectra of the Cu2p catalysts. We observe back-orbital splitting, and two groups of peaks associated with the levels of $Cu2p_{3/2}$ (in the regions of 932.6 and 946.0 – 949.3 eV) and $Cu2p_{1/2}$. The shape of the spectra allows us to assert that almost all copper in the near-surface layer of the catalyst is in the reduced state [36–38].

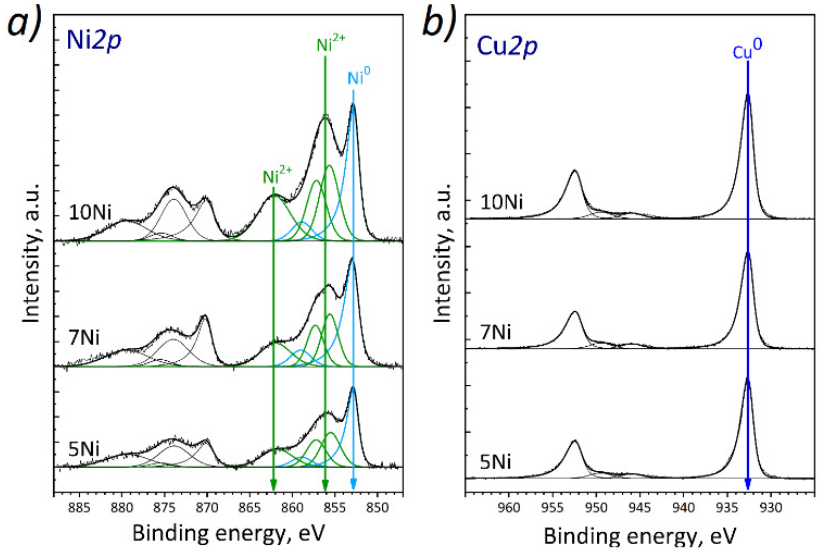

FIG. 4. Spectra a) Ni2p; b) Cu2p of the studied catalysts

According to XPS data, aluminum is completely in the oxide form (Al_2O_3). Furthermore, it was found that iron is predominantly in the Fe^{3+}/Fe^{2+} state, which likely corresponds to partially reduced iron oxide (Fe_3O_4), in which most of the iron cations are in the Fe^{2+} state [39, 40].

To determine the textural characteristics of the catalysts, we employed N_2 physical adsorption (BET) and CO chemisorption methods. Table 1 presents the results of the study on the fresh samples in oxide form and reduced catalysts. It should be noted that the textural characteristics of the samples determined by using the BET method are practically identical. However, based on the CO chemisorption data for pre-reduced samples (at 250 °C), it can be inferred that the catalyst with 7 wt.% nickel oxide content may exhibit higher activity in the target process compared to the other samples. Apparently, in this case, the optimal Cu/Ni ratio is achieved, which promotes the formation of a larger number of

active centers on the catalyst surface. Nickel doping of the 20Cu66Fe14Al catalyst increased the amount of adsorbed CO from 31 μmol/g_{cat} [30] to 85 μmol/g_{cat}. Thus, we can assume that the main adsorption centers for the 7Ni sample are predominantly nickel particles.

TABLE 1. Textural characteristics of catalysts in oxide[1] and reduced[2] forms

Catalyst	A^1_{BET}, m^2/g	$V_{pore\Sigma}{}^1$, cm^3/g	Amount of adsorbed CO[2], μmol/g
5Ni	50	0.11	58
7Ni	55	0.10	85
10Ni	53	0.11	49

The data obtained from the H_2-TPR and CO chemisorption methods correlate with each other: the optimal reduction temperature for the catalysts is 250 °C, at which finely dispersed nickel oxide particles transition to a metallic state and copper oxide is completely reduced.

3.2. Catalytic performance in a batch reactor

To compare the obtained catalysts, we studied them during the hydrogenation of furfural in a batch reactor and established correlations between the product composition, reaction temperature, catalyst composition, and mass of the loaded catalyst.

FA is the main product for the 5Ni catalyst; its weight content at low temperatures (160 °C) is 98 % (Fig. 5a). As the temperature rises (200 – 250 °C), 2-MF begins to form, with a maximum yield of 32 % at 250 °C. In addition, under these conditions, small quantities of by-products (2-MTHF and THFA) are formed (4 wt.%) (Fig. 5a).

The formation of 2-MF requires more stringent hydrogenation conditions, such as the presence of a catalyst with a higher nickel oxide weight content. Over the 7Ni catalyst, the hydrogenation of furfural is faster compared to the 5Ni catalyst; at 200 °C, the yield of 2-MF increases to 20 %, though by-products (THFA and 2-MTHF) are also formed. At higher reaction temperatures (250 °C), the content of the target product (2-MF) increases to 67 %.

Further, increases in the mass content of nickel oxide in the catalyst lead to greater formation of by-products. For example, over the 10Ni catalyst at 200 °C, the yield of by-products (THFA and 2-MTHF) doubles compared to the 7Ni sample. As the reaction temperature rises to 250 °C, the yield of 2-MF decreases to 48 %, while the yield of FA almost doubles (from 23 to 40 %).

The data obtained for the hydroconversion of furfural correlate with the CO chemisorption results: the most active catalyst in the target process is 7Ni.

Based on the dependencies obtained, we selected the reaction conditions to achieve 100 % selectivity for FA under relatively mild conditions (H_2 5.0 MPa, 160 °C, mass of 7Ni catalyst is 0.3 g, reaction time 4 h). Additionally, we determined that the optimal temperature for the hydroconversion of furfural to 2-MF is 200 °C.

To increase the yield of the desired product (2-MF) at this temperature, we increased the catalyst loading to 1 g.

Comparing the three catalysts (Fig. 5b), we observed a greater reaction depth for the sample with a nickel oxide mass content of 7 %. 2-MF was obtained in high yield, with relatively low concentrations of side products. The 7Ni catalyst was chosen for further study, as it exhibits the highest activity in the target process and demonstrates a high yield of 2-MF (81 %, 1 g of catalyst, 200 °C, 4 hours).

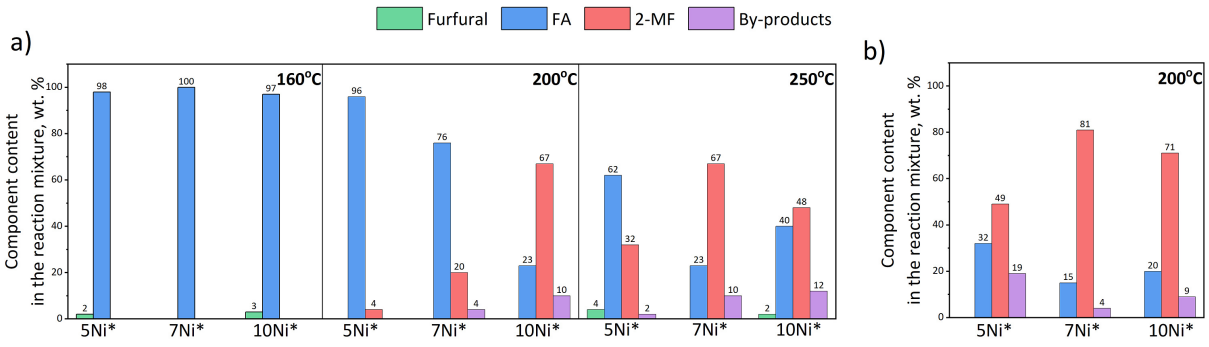

FIG. 5. The composition of the reaction mixture in the furfural hydroconversion over catalysts with different nickel contents. Reaction conditions: batch reactor, $P(H_2) = 5$ MPa, V(furfural) $= 4.8$ ml, V(i-PrOH) $= 55.2$ ml, $t = 4$ h, a) $m_{cat} = 0.3$ g; b) $m_{cat} = 1.0$ g; * by-products – 2-MTHF, THFA

3.3. Study of the 7Ni catalyst morphology and phase composition by HRTEM and XRD in situ methods

We used high-resolution transmission electron microscopy (HRTEM) and in situ X-ray diffraction (XRD) methods for a detailed study of the surface morphology and phase composition of the reduced 7Ni catalyst.

Figure 6 shows the in-situ X-ray diffraction patterns of the catalyst during stepwise reduction. In the temperature range of 30 – 175 °C, we do not observe any changes in the diffraction pattern. At a temperature of 200 °C, intense reflections of Cu appear at $2\theta = 43.2°$ and $50.3°$.

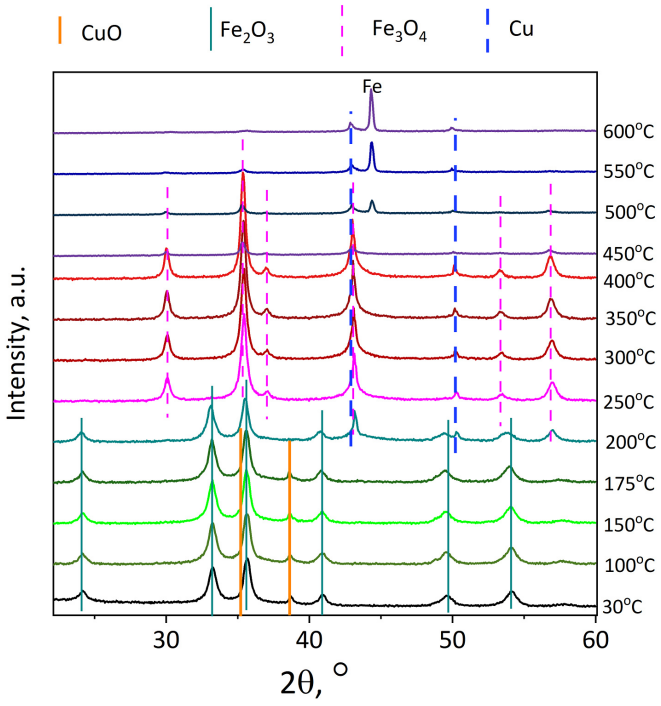

FIG. 6. In situ H_2 XRD patterns for the 7Ni catalyst

With a further increase in temperature to 250 °C, the reflections of CuO and Fe_2O_3 disappear. Peaks corresponding to reflections of iron oxide Fe_3O_4 and metallic copper appear. When the reduction temperature reaches 450 °C, there is a significant decrease in the intensity of the Fe_3O_4 reflections and a reduction in the corresponding lattice parameter (from 8.38 to 8.21 Å). Presumably, it is observed due to aluminum being incorporated into the lattice of iron oxide. The spinel Fe_2AlO_4 forms, and a narrow peak appears at 44.6°, corresponding to the metallic iron reflection. The diffraction pattern at 550 – 600 °C predominantly shows reflections from Cu and Fe.

Based on the HRTEM data for the 7Ni catalyst reduced at 250 °C and passivated with ethyl alcohol, we can identify several structural features of this sample. Copper is represented by a metallic phase (10 – 50 nm) covered with an oxide layer (Fig. 7b). Aluminum and iron exist in the form of individual oxide phases (Fig. 7a), sized 2 – 3 nm and 10 – 20 nm, respectively; these oxides create a matrix over which the copper and nickel phases are distributed. Nickel is primarily represented by an oxide phase, sized 2 – 3 nm, distributed over the surface of the iron and aluminum oxides (Fig. 7b). Additionally, nickel forms a core-shell structure with copper, where the core is nickel oxide, and the shell is copper oxide; the total size of such particles varies from 3 to 5 nm (Fig. 7c).

Summarizing the data obtained for the 7Ni catalyst in both oxidized and reduced forms, we can draw a conclusion about its phase composition and morphology. The fresh sample contains individual oxide phases of all metals. During reduction (250 °C), copper is completely converted into a metallic form, while nickel is partially reduced to metal, and iron and aluminum remain in oxide form (Fe_3O_4 and Al_2O_3, respectively). Based on the obtained data, we assume that the active component of the 7Ni catalyst is represented by finely dispersed metal particles of copper and nickel.

3.4. Study of spent 7Ni catalyst

At relatively high temperatures and due to the high activity of the catalyst, furfural and its hydroconversion products can polymerize on the catalyst surface, resulting in the formation of polymer structures that deactivate the active sites.

To confirm the theory of catalyst deactivation during the reaction, a complex of physicochemical methods was used to examine the spent 7Ni sample. The HRTEM results indicate that carbonization occurs on the catalyst surface. Mostly, amorphous carbon is located on the particles of iron and aluminum oxide, forming filament-like structures with a metal-containing center (Fig. 8a). Additionally, carbon is adsorbed on the catalyst surface, leading to its gradual deactivation (Fig. 8b–c). The average particle size of the catalyst does not significantly increase, indicating that dispersity is preserved

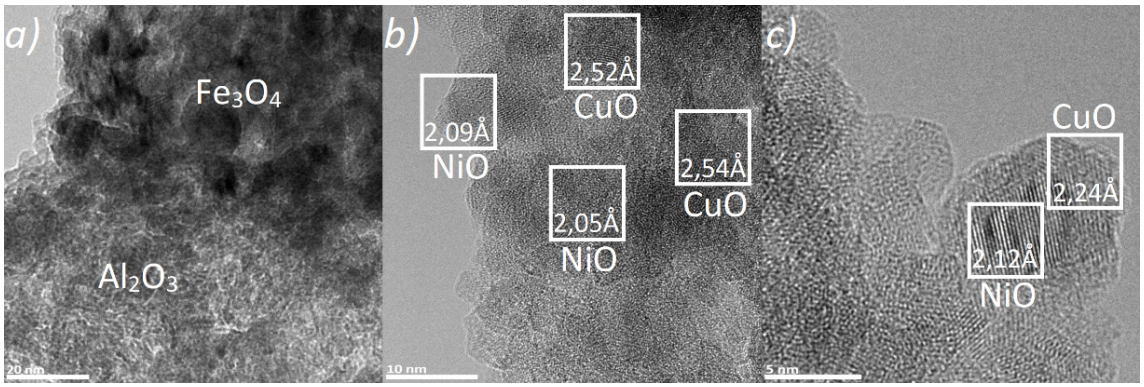

FIG. 7. HRTEM images: a) phases of hematite and aluminum oxide; b) individual phases of copper oxide (2.52, 2.54 Å are the interplanar distances corresponding to the [002] and [−111] reflections, respectively) and nickel oxide (2.05, 2.09 Å are the interplanar distances corresponding to the [200] reflection); c) NiCu-O core-shell structure (2.12, 2.24 Å – interplanar distances corresponding to reflections [200] of NiO and [200] of CuO, respectively)

during the reaction. On the surface of the spent sample, all metals are present in their oxide forms: Cu_2O, NiO, Fe_3O_4, and Al_2O_3 (Fig. 8d).

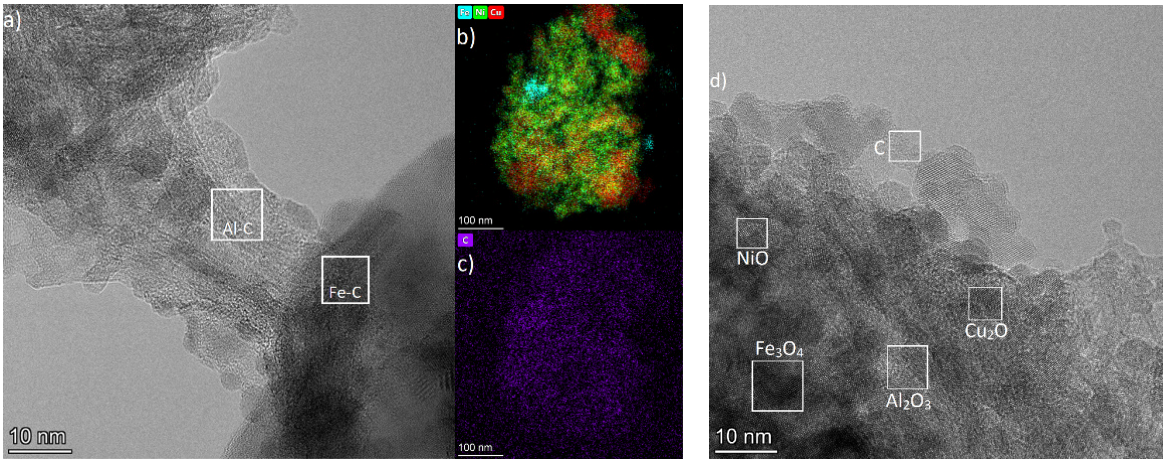

FIG. 8. a) HRTEM image of filament-like C–Al and Fe–Al structures; mapped HRTEM images for b) iron, copper, nickel; c) carbon; d) HRTEM image of nickel, copper, aluminum, ferric oxide, and amorphous carbon

CHNS analysis of the spent 7Ni catalyst sample showed that the mass content of carbon in the catalyst reaches 4.7 wt.%.

A spent sample of the 7Ni catalyst was studied using thermal analysis (Fig. 9) to determine the content of adsorbed water and organic compounds. The TG curve indicates that mass loss of the sample occurs in four steps. Analyzing the DTG curve, the temperatures at which changes in the rate of weight loss occur were identified. The maximum values on the DTG are illustrated by extremum points. The first extremum is detected at approximately 99 °C, which corresponds to the evaporation of adsorbed water (4.4 wt.%). Additionally, two more regions of mass loss are observed at 239 °C (2.6 wt.%) and 435 °C (0.9 wt.%), where reagents and products from two different groups of active sites of the catalyst are likely desorbed. With a further increase in temperature, high-molecular compounds (0.7 wt.%) evaporate.

Based on the data obtained for the spent 7Ni catalyst, we can draw conclusions about the nature of deactivation in such systems. During the reaction, products and reagents are adsorbed on the surface of active centers, leading to their polymerization and the formation of high-molecular compounds. To reduce the amount of carbon deposits on the catalyst surface and prevent its deactivation, it is necessary to either increase the hydrogen pressure in the system or to preliminarily purify the raw material before the experiment (furfural is prone to polymerization during long-term storage). These methods for reducing carbonaceous deposits are widely used in industry for hydroconversion processes involving furfural. Additionally, the catalyst can be regenerated after the reaction in a stream of hydrogen at the reduction temperature. For example, in the work [42], a copper-zinc catalyst was studied during the hydroconversion of furfural in a batch reactor. The catalyst maintains its activity over 6 cycles of reaction and regeneration.

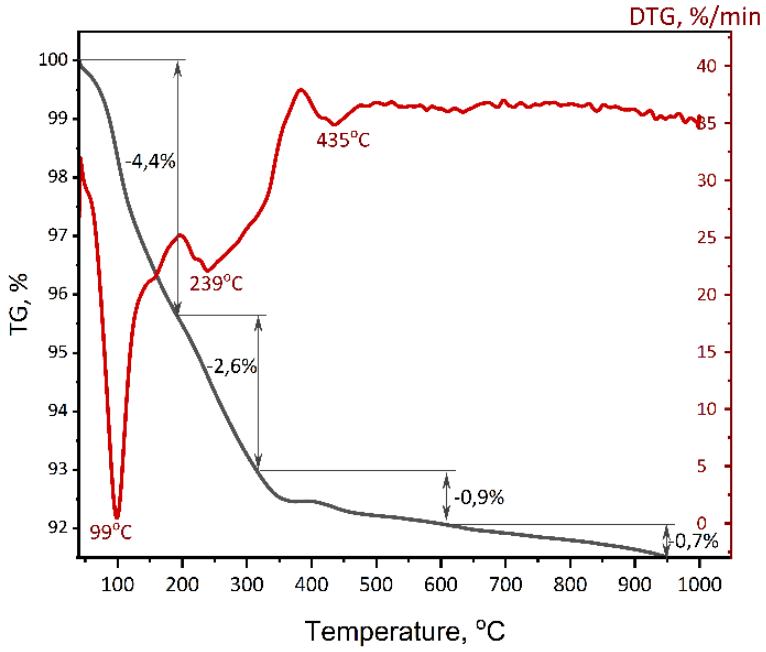

FIG. 9. TG and DTG curves for the spent 7Ni catalyst

3.5. Testing the selected catalyst in a flow type reactor

To understand how the selected 7Ni catalyst will behave under near-industrial conditions, we conducted a series of experiments in a flow-type reactor. The reaction conditions were established based on experiments conducted in a batch reactor (flow reactor, $P(H_2) = 5.0$ MPa, $T = 200$ °C, $m_{\text{cat}} = 1.0$ g, catalyst fraction $= 0.25 - 0.50$ mm, catalyst:quartz $= 1 : 4$ (vol.)). By varying the liquid hourly space velocity (LHSV, 1 – 8 h^{-1}), we obtained different ratios of products; however, the conversion of furfural and selectivity to 2-MF were identified as the most important parameters (Fig. 10).

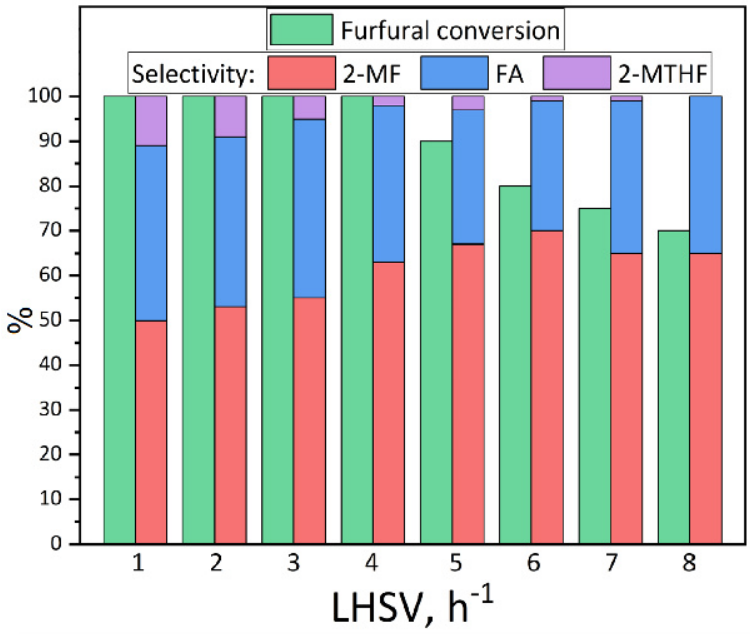

FIG. 10. Diagram of dependencies of furfural conversion and product selectivity on LHSV. Reaction conditions: flow reactor, $P(H_2) = 5.0$ MPa, $T = 200$ ° C, $m_{\text{cat}} = 1.0$ g, catalyst fraction $= 0.25 - 0.50$ mm, catalyst:quartz $= 1 : 4$ (vol.)

Based on the data obtained for furfural conversion and 2-MF selectivity, we chose a deliberately high LHSV value (6 h^{-1}), which allows for a faster evaluation of catalyst performance under severe conditions. Regarding the lower LHSV

values in the range of 1 to 4, there is a complete furfural conversion but low selectivity for 2-MF. It is due to the reaction of furan ring hydrogenation, resulting in the formation of 2-MTHF and THFA. At higher LHSV values, the conversion of furfural decreases significantly due to a reduction in contact time. Thus, we obtained the dependence of furfural conversion and 2-MF selectivity on the reaction time at LHSV $= 6$ h^{-1}. During the first 4 hours of the reaction in flow mode, the catalyst retains its activity (furfural conversion of 80 – 90 %, selectivity for 2-MF of 75 – 80 %). However, after 4 hours, there is a decrease in selectivity to 60 – 65 %, while maintaining furfural conversion.

As a result, it can be noted that the activity of the 7Ni catalyst does not fall over time, and furfural conversion is maintained at 80 – 90 % for 5 hours. During the reaction, there is a trend toward a decrease in selectivity for 2-MF; however, selectivity for FA rises (Fig. 11). It is possible that during the reaction, the nickel centers, on which hydroconversion to 2-MF partially depends, become deactivated [7,43]. Copper centers may also become deactivated, but their quantity is higher than that of nickel centers due to the higher copper content in the catalyst. Thus, by choosing the optimal reaction conditions over this catalyst, it is possible to achieve a high yield of both FA and 2-MF.

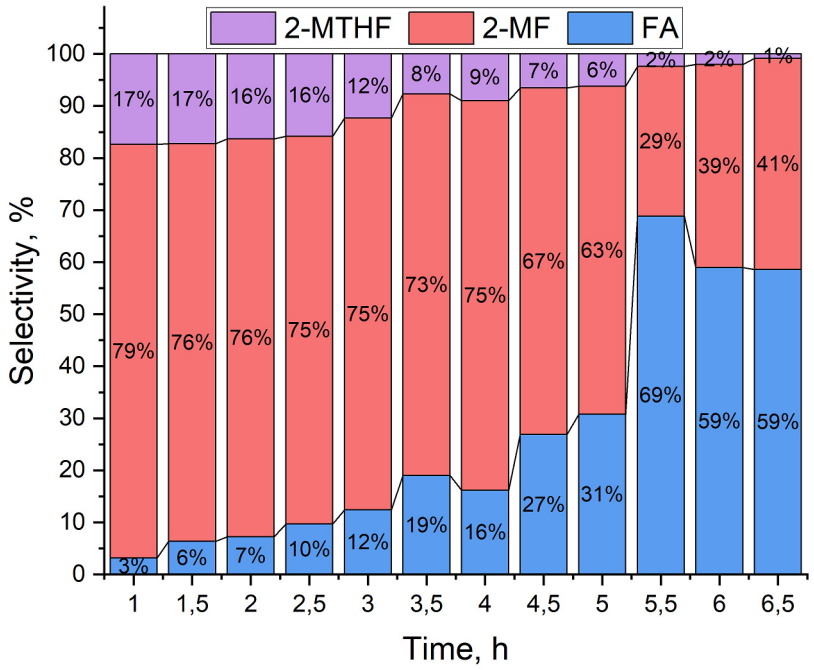

FIG. 11. Diagram of dependencies 2-MF, FA, and 2-MTHF selectivity on time. Reaction conditions: flow reactor, LHSV $= 6$ h^{-1}, $P(H_2) = 5.0$ MPa, $T = 200$ °C, $m_{\text{cat}} = 1.0$ g, catalyst fraction $= 0.25$ – 0.50 mm, catalyst:quartz $= 1 : 4$ (vol.)

The work [44] also studied the gas-phase hydroconversion of furfural in a flow reactor over copper-zinc catalysts. The reaction was carried out in the gas phase at a temperature of 200 °C, and as a result, the yield of 2-MF reached 95 % with 100 % conversion of furfural. Due to the lower LHSV (1.5 h^{-1}) compared to our work, the catalyst retained its activity after 10 hours of reaction. This process was also studied in liquid phase mode in work [45]. Hydroconversion of furfural took place at 180 °C and elevated hydrogen pressure (1 MPa) over a cobalt-containing catalyst. As a result, the conversion of furfural was 100 %, and the yield of 2-MF was 94 %, with a relatively low value of LHSV $= 0.5$ h^{-1} (calculated from the approximation that the bulk density of the catalyst is 1 g/cm^3).

Thus, the advantage of our method lies in higher LHSV values and, consequently, higher productivity. However, the service life of the catalyst is reduced due to carbonization of the active sites. Possible ways to reduce the carbonization of the catalyst include increasing the flow rate and pressure of hydrogen [46], as well as prepurifying the feedstock used in furfural refineries.

4. Conclusions

New NiCu-containing catalysts with different nickel oxide contents were prepared by the alloy method for furfural hydroconversion to 2-MF and FA. As a result of testing the obtained systems in a batch reactor in the target process, the 7Ni19Cu61Fe13Al (7Ni) catalyst was chosen as the most active. 100 % conversion of furfural and 81 % yield of 2-MF are achieved over 7Ni catalyst.

Analysis of the most active 7Ni catalyst by a complex of physicochemical methods showed that the fresh sample contains individual oxide phases of all metals. When this catalyst is reduced (250 °C), copper is completely converted into a metallic form, nickel is partially reduced to metal, and iron and aluminum are oxides (Fe_3O_4 and Al_2O_3, respectively).

The active component of the catalyst is represented by metallic copper (10 – 50 nm) and nickel (3 – 5 nm), which do not form joint phases. During the reaction, the catalyst is deactivated due to the irreversible sorption of reagents and reaction products on the surface, as well as their polymerization on the catalyst active sites. The total carbon content after the reaction in a batch reactor was 4.7 wt.%.

The selected 7Ni catalyst was tested in a flow reactor in solvent-free furfural hydroconversion. We have shown the possibility of obtaining 2-MF with a selectivity of 75 – 80 % at 80 – 90 % furfural conversion for 4 hours. After that, the trend in selectivity changes: for FA it rises to 55 – 60 %, and for 2-MF it decreases to 35 – 40 % while maintaining the furfural conversion. Compared to other catalysts used in this process, 7Ni demonstrates good results at a higher LHSV, and therefore has higher productivity.

References

[1] Dietrich K., Dumont M.-J., Del Rio L.F., Orsat V. Producing PHAs in the Bioeconomy – Towards a Sustainable Bioplastic. *Sustainable Production and Consumption*, 2017, **9**, P. 58–70.

[2] Nhien L.C., Long N.V.D., Lee M. Novel hybrid reactive distillation with extraction and distillation processes for furfural production from an actual xylose solution. *Energies*, 2021, **14** (4), 1152.

[3] Xu C., Paone E., Rodríguez-Padrón D., Luque R., Mauriello F. Recent Catalytic Routes for the Preparation and the Upgrading of Biomass Derived Furfural and 5-Hydroxymethylfurfural. *Chemical Society Reviews*, 2020, **49** (13), P. 4273–4306.

[4] Zhang X., Xu S., Li Q., Zhou G., Xia H. Recent advances in the conversion of furfural into bio-chemicals through chemo-and bio-catalysis. *RSC advances*, 2021, **11** (43), P. 27042–27058.

[5] Wang Y., Zhao D., Rodríguez-Padrón D., Len C. Recent Advances in Catalytic Hydrogenation of Furfural. *Catalysts*, 2019, **9** (10), 796.

[6] Li S., Li N., Li G., Wang A., Cong Y., Wang X., Zhang T. Synthesis of Diesel Range Alkanes with 2-Methylfuran and Mesityl Oxide from Lignocellulose. *Catalysis Today*, 2014, **234**, P. 91–99.

[7] Sitthisa S., Sooknoi T., Ma Y., Balbuena P.B., Resasco D.E. Kinetics and Mechanism of Hydrogenation of Furfural on Cu/SiO_2 Catalysts. *J. of Catalysis*, 2011, **277** (1), P. 1–13.

[8] Srivastava S., Jadeja G.C., Parikh J. Copper-Cobalt Catalyzed Liquid Phase Hydrogenation of Furfural to 2-Methylfuran: An Optimization, Kinetics and Reaction Mechanism Study. *Chemical Engineering Research and Design*, 2018, **132**, P. 313–324.

[9] Seo G. Hydrogenation of Furfural over Copper-Containing Catalysts. *J. of Catalysis*, 1981, **67** (2), P. 424–429.

[10] Dutta S., De S., Saha B., Alam M.I. Advances in conversion of hemicellulosic biomass to furfural and upgrading to biofuels. *Catalysis Science & Technology*, 2012, **2** (10), P. 2025–2036.

[11] Šivec R., Huš M., Likozar B., Grilc M. Furfural Hydrogenation over Cu, Ni, Pd, Pt, Re, Rh and Ru Catalysts: Ab Initio Modelling of Adsorption, Desorption and Reaction Micro-Kinetics. *Chemical Engineering J.*, 2022, **436**, 135070.

[12] Wang Z., Wang X., Zhang C., Arai M., Zhou L., Zhao F. Selective Hydrogenation of Furfural to Furfuryl Alcohol over Pd/TiH_2 Catalyst. *Molecular Catalysis*, 2021, **508**, 111599.

[13] Dong F., Zhu Y., Zheng H., Zhu Y., Li X., Li Y. Cr-free Cu-catalysts for the selective hydrogenation of biomass-derived furfural to 2-methylfuran: The synergistic effect of metal and acid sites. *J. of Molecular Catalysis A: Chemical*, 2015, **398**, P. 140–148.

[14] Wang S., Zhao G., Lan T., Ma Z., Wang H., Liu Y., Lu Y. Gas-phase hydrogenation of furfural to furfuryl alcohol: A promising Cu/SiO_2 catalyst derived from lamellar Cu-based hydroxy double salt. *Fuel*, 2024, **372**, 132095.

[15] Tyuryaeva I.Ya., Chistyakova G.A. *Catalysts for basic organic synthesis*, GIPH 68, Leningrad, 1967, 85.

[16] Chistyakova G.A., Zubritskaya N.G. Hydrogenation catalysts based on metal chromites. *GIPH collection*, 1973, **68**, P. 5–13.

[17] Demirbas A. Progress and Recent Trends in Biofuels. *Progress in Energy and Combustion Science*, 2007, **33** (1), P. 1–18.

[18] Zhao Y., Tao L. Towards catalytic reactions of Cu single-atom catalysts: Recent progress and future perspective. *Chinese Chemical Letters*, 2024, **35** (2), 108571.

[19] Selishcheva S., Sumina A., Gerasimov E., Selishchev D., Yakovlev V. High-Loaded Copper-Containing Sol-Gel Catalysts for Furfural Hydroconversion. *Int. J. of Molecular Sciences*, 2023, **24** (8), 7547.

[20] Yao Y., Yu Z., Lu C., Sun F., Wang Y., Sun Z., Wang A. Highly efficient Cu-based catalysts for selective hydrogenation of furfural: A key role of copper carbide. *Renewable Energy*, 2022, **197**, P. 69–78.

[21] Şebin M.E., Akmaz S., Koc S.N. Hydrogenation of Furfural to Furfuryl Alcohol over Efficient Sol-Gel Nickel-Copper/Zirconia Catalyst. *J. of Chemical Sciences*, 2020, **132** (1), 157.

[22] Akmaz S., Algorabi S., Koc S.N. Furfural Hydrogenation to 2-methylfuran over Efficient Sol-gel Copper-cobalt/Zirconia Catalyst. *The Canadian J. of Chemical Engineering*, 2021, **99** (S1), S562–S574.

[23] Kalong M., Hongmanorom P., Ratchahat S., Koo-amornpattana W., Faungnawakij K., Assabumrungrat S., Srifa A., Kawi S. Hydrogen-Free Hydrogenation of Furfural to Furfuryl Alcohol and 2-Methylfuran over Ni and Co-Promoted $Cu/\gamma\text{-}Al_2O_3$ Catalysts. *Fuel Processing Technology*, 2021, **214**, 106721.

[24] Wang Y., Hu D., Guo R., Deng H., Amer M., Zhao Z., Xu H., Yan K. Facile Synthesis of Ni/Fe_3O_4 Derived from Layered Double Hydroxides with High Performance in the Selective Hydrogenation of Benzaldehyde and Furfural. *Molecular Catalysis*, 2022, **528**, 112505.

[25] Rajabi F., Arancon R.A.D., Luque R. Oxidative Esterification of Alcohols and Aldehydes Using Supported Iron Oxide Nanoparticle Catalysts. *Catalysis Communications*, 2015, **59**, P. 101–103.

[26] Wang C., Zhang J., Gao X., Zhao T. Research Progress on Iron-Based Catalysts for CO_2 Hydrogenation to Long-Chain Linear α-Olefins. *J. of Fuel Chemistry and Technology*, 2023, **51** (1), P. 67–85.

[27] Sunyol C., Owen R.E., González M.D., Salagre P., Cesteros Y. Catalytic hydrogenation of furfural to tetrahydrofurfuryl alcohol using competitive nickel catalysts supported on mesoporous clays. *Applied Catalysis A: General*, 2021, **611**, 117903.

[28] Li Z., Zhu M., Chen X., Mei H. Catalytic performance of Ni/Al_2O_3 catalyst for hydrogenation of 2-methylfuran to 2-methyltetrahydrofuran. *J. of Fuel Chemistry and Technology*, 2018, **46** (1), P. 54–58.

[29] Xu C., Paone E., Rodríguez-Padrón D., Luque R., Mauriello F. Recent Catalytic Routes for the Preparation and the Upgrading of Biomass Derived Furfural and 5-Hydroxymethylfurfural. *Chemical Society Reviews*, 2020, **49** (13), P. 4273–4306.

[30] Selishcheva S.A., Smirnov A.A., Fedorov A.V., Bulavchenko O.A., Saraev A.A., Lebedev M.Yu., Yakovlev V.A. Highly Active CuFeAl-Containing Catalysts for Selective Hydrogenation of Furfural to Furfuryl Alcohol. *Catalysts*, 2019, **9** (10), 816.

[31] Yakovlev V.A., Khromova S.A., Sherstyuk O.V., Dundich V.O., Ermakov D.Yu., Novopashina V.M., Lebedev M.Yu., Bulavchenko O.A., Parmon V.N. Development of New Catalytic Systems for Upgraded Bio-Fuels Production from Bio-Crude-Oil and Biodiesel. *Catalysis Today*, 2009, **144** (3–4), P. 362–366.
[32] Khromova S.A., Smirnov A.A., Bulavchenko O.A., Saraev A.A., Kaichev V.V., Reshetnikov S.I., Yakovlev V.A. Anisole Hydrodeoxygenation over Ni–Cu Bimetallic Catalysts: The Effect of Ni/Cu Ratio on Selectivity. *Applied Catalysis A: General*, 2014, **470**, P. 261–270.
[33] Selishcheva S.A., Lebedev D.Yu., Reshetnikov S.I., Trusov L.I., Yakovlev V.A. Kinetics of the Hydrotreatment of Rapeseed Oil Fatty Acid Triglycerides under Mild Conditions. *Catalysis in Industry*, 2014, **6** (1), P. 60–66.
[34] Alders D., Voogt F.C., Hibma T., Sawatzky G.A. Nonlocal screening effects in 2p X-ray photoemission spectroscopy of NiO (100). *Physical Review B*, 1996, **54** (11), 7716.
[35] Van Veenendaal M.A., Sawatzky G.A. Nonlocal screening effects in 2p X-ray photoemission spectroscopy core-level line shapes of transition metal compounds. *Physical Review Letters*, 1993, **70** (16), 2459.
[36] Batista J., Pintar A., Mandrino D., Jenko M., Martin V. XPS and TPR examinations of γ-alumina-supported Pd-Cu catalysts. *Applied Catalysis A: General*, 2001, **206** (1), P. 113–124.
[37] Bukhtiyarov V.I., Kaichev V.V., Prosvirin I.P. X-ray photoelectron spectroscopy as a tool for in-situ study of the mechanisms of heterogeneous catalytic reactions. *Topics in Catalysis*, 2005, **32**, P. 3–15.
[38] McIntyre N.S., Cook M.G. X-ray photoelectron studies on some oxides and hydroxides of cobalt, nickel, and copper. *Analytical chemistry*, 1975, **47** (13), P. 2208–2213.
[39] Descostes M., Mercier F., Thromat N., Beaucaire C., Gautier-Soyer M. Use of XPS in the determination of chemical environment and oxidation state of iron and sulfur samples: constitution of a data basis in binding energies for Fe and S reference compounds and applications to the evidence of surface species of an oxidized pyrite in a carbonate medium. *Applied Surface Science*, 2000, **165** (4), P. 288–302.
[40] Tan B.J., Klabunde K.J., Sherwood P.M. X-ray photoelectron spectroscopy studies of solvated metal atom dispersed catalysts. Monometallic iron and bimetallic iron-cobalt particles on alumina. *Chemistry of Materials*, 1990, **2** (2), P. 186–191.
[41] Fairley N., Carrick A., Fairley N. *Recipes for XPS Data Processing*. The Casa cookbook. Acolyte Science, Knutsford, 2005.
[42] Niu H., Luo J., Li C., Wang B., Liang C. Transfer hydrogenation of biomass-derived furfural to 2-methylfuran over CuZnAl catalysts. *Industrial & Engineering Chemistry Research*, 2019, **58** (16), P. 6298–6308.
[43] Srivastava S., Jadeja G.C., Parikh J. Copper-Cobalt Catalyzed Liquid Phase Hydrogenation of Furfural to 2-Methylfuran: An Optimization, Kinetics and Reaction Mechanism Study. *Chemical Engineering Research and Design*, 2018, **132**, P. 313–324.
[44] Yang X., Xiang X., Chen H., Zheng H., Li Y. W., Zhu Y. Efficient Synthesis of Furfuryl Alcohol and 2-Methylfuran from Furfural over Mineral-Derived Cu/ZnO Catalysts. *ChemCatChem*, 2017, **9** (15), P. 3023–3030.
[45] Liu P., Sun L., Jia X., Zhang C., Zhang W., Song Y., Li C. Efficient one-pot conversion of furfural into 2-methyltetrahydrofuran using non-precious metal catalysts. *Molecular Catalysis*, 2020, **490**, 110951.
[46] Forzatti P., Lietti L. Catalyst deactivation. *Catalysis Today*, 1999, **52** (2-3), P. 165–181.

Submitted 25 April 2024; revised 16 October 2024; accepted 10 December 2024

Information about the authors:

Anastasiya A. Sumina – Federal Research Center Boreskov Institute of Catalysis SB RAS, Lavrentiev Ave. 5, Novosibirsk 630090, Russia; ORCID 0009-0006-4393-7866; sumina@catalysis.ru

Svetlana A. Selishcheva – Federal Research Center Boreskov Institute of Catalysis SB RAS, Lavrentiev Ave. 5, Novosibirsk 630090, Russia; ORCID 0000-0003-2768-9680; svetlana@catalysis.ru

Olga A. Bulavchenko – Federal Research Center Boreskov Institute of Catalysis SB RAS, Lavrentiev Ave. 5, Novosibirsk 630090, Russia; ORCID 0000-0001-5944-2629; obulavchenko@catalysis.ru

Vadim A. Yakovlev – Federal Research Center Boreskov Institute of Catalysis SB RAS, Lavrentiev Ave. 5, Novosibirsk 630090, Russia; ORCID 0000-0001-5015-3521; yakovlev@catalysis.ru

Conflict of interest: the authors declare no conflict of interest.

NANOSYSTEMS:
PHYSICS, CHEMISTRY, MATHEMATICS

Kagilev A.A., et al. *Nanosystems: Phys. Chem. Math.*, 2025, **16** (1), 116–122.
http://nanojournal.ifmo.ru
DOI 10.17586/2220-8054-2025-16-1-116-122

Original article

Synthesis, structure and noncovalent interactions of mesityl(phenyl)phosphine oxide glycolate based hydrogen-bonded nanosized organic framework

Alexey A. Kagilev[1,a], Ilyas F. Sakhapov[1,b], Zufar N. Gafurov[1,c], Artyom O. Kantyukov[1,2,d], Ilya K. Mikhailov[1,e], Daut R. Islamov[3,f], Alexander V. Gerasimov[2,g], Oleg A. Filippov[4,h], Aidar T. Gubaidullin[1,j], Olga S. Soficheva[1,k], Oleg G. Sinyashin[1,l], Dmitry G. Yakhvarov[1,2,m]

[1]Arbuzov Institute of Organic and Physical Chemistry, FRC Kazan Scientific Center, Russian Academy of Sciences, 420088, Kazan, Russian Federation

[2]A.M. Butlerov Institute of Chemistry, Kazan Federal University, 420008, Kazan, Russian Federation

[3]Laboratory for Structural Studies of Biomacromolecules, FRC Kazan Scientific Center, Russian Academy of Sciences, 420111, Kazan, Russian Federation

[4]A.N. Nesmeyanov Institute of Organoelement Compounds, Russian Academy of Sciences, 119991, Moscow, Russian Federation

[a]al-kagilev@mail.ru, [b]ilyas.sakhapov@iopc.ru, [c]gafurov.zufar@iopc.ru, [d]kant.art@mail.ru, [e]tiimhailovilya@gmail.com, [f]daut1989@mail.ru, [g]Alexander.Gerasimov@kpfu.ru, [h]h-bond@ineos.ac.ru, [j]aidar@iopc.ru, [k]myaolechka@yandex.ru, [l]oleg@iopc.ru, [m]yakhvar@iopc.ru

Corresponding author: D. G. Yakhvarov, yakhvar@iopc.ru

PACS 61.46.–w

ABSTRACT The reaction of glyoxylic acid monohydrate with mesityl(phenyl)phosphine in air led to the formation of mesityl(phenyl)phosphine oxide glycolate. The synthesized mesityl(phenyl)phosphine oxide glycolate has been characterized by various analytical methods including X-ray crystal structure analysis. The analysis of intermolecular interactions in the crystal revealed interesting modes of the noncovalent bonding between pairs of molecules. These intermolecular interactions cause the formation of one-dimensional cylindrical channels with diameter of 1 nm (10 Å) and provide the crystal with the properties of precise nano-sized crystalline porous material which can be served as the component for precise nanofiltration membranes improving the properties of amorphous polymers which suffer from disordered pore structures and reduced selectivity towards separating molecules.

KEYWORDS phosphine, phosphine oxide, glycolate, X-ray diffraction, noncovalent bonding

ACKNOWLEDGEMENTS This research was funded by the grant of the Ministry of Science and Higher Education of the Russian Federation for large scientific projects of the priority areas of scientific and technological development (Nr. 075-15-2024-646).

FOR CITATION Kagilev A.A., Sakhapov I.F., Gafurov Z.N., Kantyukov A.O., Mikhailov I.K., Islamov D.R., Gerasimov A.V., Filippov O.A., Gubaidullin A.T., Soficheva O.S., Sinyashin O.G., Yakhvarov D.G. Synthesis, structure and noncovalent interactions of mesityl(phenyl)phosphine oxide glycolate based hydrogen-bonded nanosized organic framework. *Nanosystems: Phys. Chem. Math.*, 2025, **16** (1), 116–122.

1. Introduction

Covalent and noncovalent interactions, including hydrogen bonds, are objects of extensive study in the global scientific literature [1–7]. The significant interest in utilizing hydrogen bonding to construct ordered crystalline networks has prompted extensive research into hydrogen-bonded organic frameworks (HOFs). These frameworks rely on the assembly of organic building blocks through hydrogen-bonding interactions, enabling the formation of two-dimensional (2D) and three-dimensional (3D) crystalline nanosized networks [8]. Such a hydrogen-bonded nanocrystalline structures has gained a great attention during the past decade mostly due to their applications in the fields of catalysis, energy, biochemistry as well as the storage and separation of fine chemicals [4, 9–14]. Due to the weakness of single hydrogen bond, the stability of HOF can be significantly improved by creating multiple intermolecular forces including $\pi\cdots\pi$ and $CH\cdots\pi$ interactions. Whereas, examples of C–H$\cdots$C contacts are rather unusual and are rarely invoked in the description of nanomolecular aspects of crystal structures [15–19]. At the same time, these types of weak hydrogen bonds play an important role in the formation of some intricate 3D supramolecular networks [20]. Nevertheless, one of the basic

© Kagilev A.A., Sakhapov I.F., Gafurov Z.N., Kantyukov A.O., Mikhailov I.K., Islamov D.R., Gerasimov A.V., Filippov O.A., Gubaidullin A.T., Soficheva O.S., Sinyashin O.G., Yakhvarov D.G., 2025

hydrogen bonding synthesizer motifs used to design HOFs is O–H$\cdots$O interaction involving carboxylic acid group (–COOH), which presence, however, often causes polymorphism due to the flexibility of hydrogen bonds [13]. It should be also noted, that examples of phosphorus-based HOFs are rather uncommon in published literature, although P = O groups of phosphine oxides are also known to form stable hydrogen bonds with diverse substance classes [21–24]. The interest of our research group is focused on the synthesis of organophosphorus compounds, including unsymmetrically substituted phosphines and phosphine oxides [25], which are commonly applied in asymmetric synthesis, both as chiral ligands [26–28] and as organocatalysts [29–33].

2. Experimental

2.1. Materials and measurements

Diethyl ether was dried by standard method and freshly distilled before use. Glyoxylic acid monohydrate was purchased from Sigma-Aldrich and used as received without further purification. Mesityl(phenyl)phosphine was prepared according to the published procedure [34]. NMR spectra were recorded using a Bruker MSL-400 spectrometer. ^{1}H and ^{13}C$\{^{1}$H$\}$ chemical shifts are reported in parts per million (ppm) downfield of tetramethylsilane and were calibrated against the residual resonance of the deuterated solvent, whereas ^{31}P and ^{31}P$\{^{1}$H$\}$ NMR spectra are referenced to an external 85 % H_3PO_4 sample (0 ppm). Elemental analysis was performed on a EuroVector CHNS-O Elemental Analyser EA3000.

Data set for single crystal of mesityl(phenyl)phosphine oxide glycolate was collected on a Rigaku XtaLab Synergy S instrument with a HyPix detector and a PhotonJet microfocus X-ray tube using Cu Kα (1.54184 Å) radiation at low temperature (100.0(2) K). Images were indexed and integrated using the CrysAlisPro data reduction package. Data were corrected for systematic errors and absorption using the ABSPACK module: numerical absorption correction based on Gaussian integration over a multifaceted crystal model and empirical absorption correction based on spherical harmonics according to the point group symmetry using equivalent reflections. The GRAL module was used for analysis of systematic absences and space group determination. The structure was solved by direct methods using SHELXT [35] and refined by the full-matrix least-squares on F^2 using SHELXL [36]. Non-hydrogen atoms were refined anisotropically. The hydrogen atoms were inserted at the calculated positions and refined as riding atoms. A solvent mask was calculated and 156 electrons were found in a volume of 756Å^3 in one void per unit cell. This is consistent with the presence of 0.5 [CH_3OH] per asymmetric unit which account for 162 electrons per unit cell. The figures were generated using Mercury 4.1 program [37]. CCDC 2093649 contains the supplementary crystallographic data for this paper. These data can be obtained free of charge via [38].

The powder diffractograms were obtained on a Bruker D8 Advance automatic X-ray diffractometer equipped with a Vario attachment and a Vantec linear coordinate detector. Cu Kα1 radiation (λ 1.54063 Å), monochromatized with a bent Johansson monochromator, 40 kV, 40 mA X-ray tube mode was used. The experiments were performed at room temperature in Bragg-Brentano geometry with a flat sample. The sample was applied to the surface of a standard silicon plate reducing background scattering. The diffractograms were recorded in the range of scattering angles 2–80°, step 0.008°, time of the spectrum acquisition at the point 0.1–0.5 sec. The results of 8 scans were summed up, so that the total set time was equal to 1.2 sec per step. The data have been processed using the EVA software package [39].

Simultaneous thermal analysis was carried out using Simultaneous Thermal Analyzer – STA 449 F1 Jupiter® (Netzsch). All studies were carried out in an argon atmosphere with a flow rate of 75 ml/min and a heating rate of 10 °C/min. The measurements were taken in the temperature range from 40 to 350 °C. For experiments, 5.6 mg sample was placed in aluminium crucibles (40 μL) with lids having 3 holes, each of 0.5 mm in diameter.

The interactions in the crystal were analyzed with the CrystalExplorer program [40]. There are 15 neighbors for single molecule of **1**. Due to the symmetry of the crystal, there are only nine unique modes of the interaction between pairs of molecules. The energies of the pairwise interaction were computed under the approach parametrized in the CrystalExplorer [41] on the B3LYP/6-31G(d,p) level and provided in Table 1.

2.2. Preparation of mesityl(phenyl)phosphine oxide glycolate (1)

A solution of glyoxylic acid monohydrate (100 mg, 1.0 mmol) in 10 mL of diethyl ether was added to a solution containing mesityl(phenyl)phosphine (0.2 mL, 1.0 mmol) in 10 mL of diethyl ether. After the addition of glyoxylic acid monohydrate, the flask was opened to air and stirred for 24 hours at room temperature, after which the formation of a white precipitate was observed. The resulting precipitate was filtered, washed with diethyl ether and dried under vacuum. The yield was 223 mg (70 %).

^{1}H NMR (400.17 MHz, DMSO-D_6, 300 K):δ (ppm) = 2.28 (s, 3H, p-CH_3 of Mes), 2.47 (s, 6H, o-CH_3 of Mes), 3.62 (s, 1H, PCOH), 5.27 (d, $^{2}J_{PH}$ = 6.1 Hz, 1H, PCH), 6.91 (s, 2H, m-H of Mes), 7.40–7.51 (m, 2H, o-H of Ph), 7.80–7.83 (m, 3H, m-. p-H of Ph). ^{13}C$\{^{1}$H$\}$ NMR (100.62 MHz, DMSO-D_6, 300 K): δ = 20.05 (s, p-CH_3 of Mes), 22.68 (s, o-CH_3 of Mes), 72.89(s, PCH), 127.99 (d, $^{3}J_{PC}$ = 11.8 Hz, m-CH of Mes), 130.53 (d, $^{3}J_{PC}$ = 11.6 Hz, m-CH of Ph), 131.02 (d, $^{1}J_{PC}$ = 12.5 Hz, i-C of Ph), 135.69 (s, o-CH of Ph), 141.35 (s, p-CH of Ph), 143.93 (d, $^{1}J_{PC}$ = 10.2 Hz, i-C of Mes), 170.36 (d, $^{2}J_{PC}$ = 10.6 Hz, COOH). ^{31}P$\{^{1}$H$\}$ NMR (161.70 MHz, DMSO-D_6, 300 K):δ (ppm) = 39.27 (s).

Anal. (%) calcd. for $C_{17}H_{19}O_4P$ (318.29): C, 64.15; H, 6.02. Found: C, 64.10; H, 6.01.

3. Results and discussion

In this article, we report on the synthesis, crystal structure analysis and hydrogen bonding motifs of a mesityl(phenyl)phosphine oxide glycolate **1** which forms hydrogen-bonded nanosized organic framework (Fig. 1).

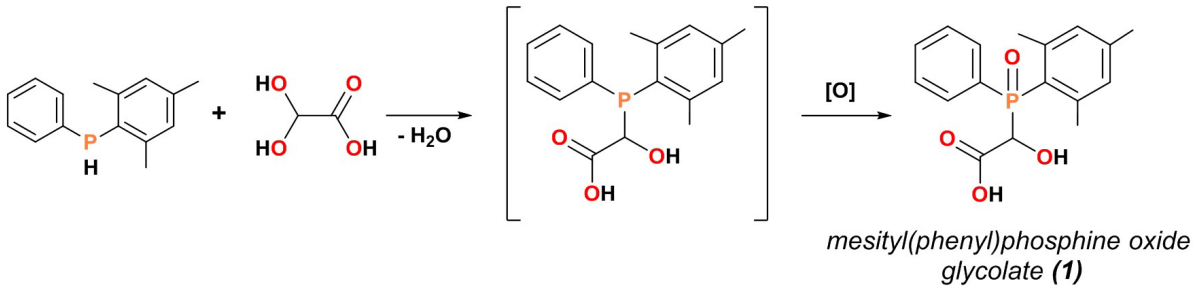

FIG. 1. Scheme 1. Synthesis of mesityl(phenyl)phosphine oxide glycolate **1**

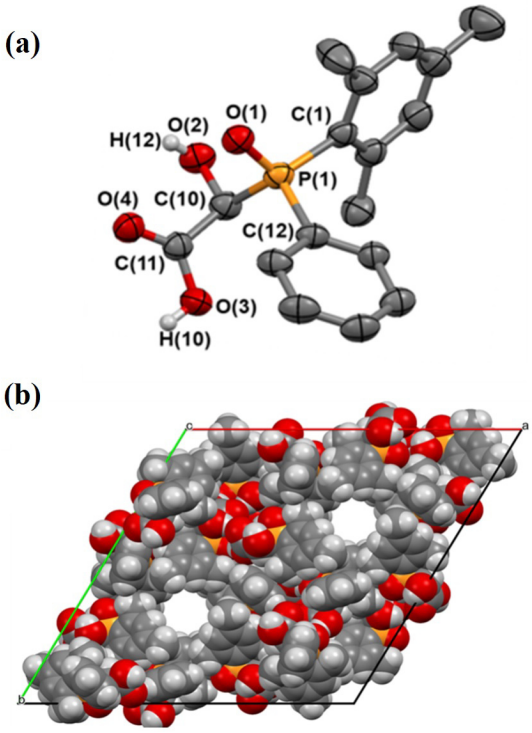

FIG. 2. The solid-state molecular structure of mesityl(phenyl)phosphine oxide glycolate (thermal ellipsoids at the 50 % probability level, hydrogen atoms except those of the -OH groups are omitted for clarity) (a); its crystal packing featuring one-dimensional channels along the c axis (b)

The ^{31}P NMR spectrum recorded after stirring the reaction mixture containing mesityl(phenyl)phosphine and glyoxylic acid monohydrate in 1:1 ratio in diethyl ether as a solvent for 24 h showed a signal at $\delta_P = -8.70$ ppm attributed to mesityl(phenyl)phosphine glycolate. However, the generated species rapidly oxidizes in air with formation of a new signal at $\delta_P = 39.27$ ppm, which was ascribed to mesityl(phenyl)phosphine oxide glycolate (Scheme 1). After 6 days, the formed precipitate was redissolved in DMSO-D_6 and was analysed by ^{1}H, ^{31}P$\{^{1}$H$\}$, ^{13}C NMR spectroscopy, which revealed the formation of **1** as analytically pure product. The thermophysical properties of **1** were investigated using synchronous thermal analysis. The results are shown in Fig. S1. The mass loss of the sample in the temperature range 40–164 °C does not exceed 3.3 % and is related to solvent removal. Subsequent steps of the mass loss are related to the thermal decomposition of the sample and are accompanied by exo-effects. In addition to the exo-effects of decomposition, the DSC curve clearly captures the endo-effect of melting with an onset temperature of 164 °C and a peak temperature of 172 °C.

The molecular structure of **1** was studied by X-ray diffraction analysis (Fig. 2a). According to powder X-ray diffraction data, the obtained mesityl(phenyl)phosphine oxide glycolate is a crystalline solid substance with well-formed crystallites and almost no amorphous component (see Fig. S2). Thus, mesityl(phenyl)phosphine oxide glycolate crystallizes

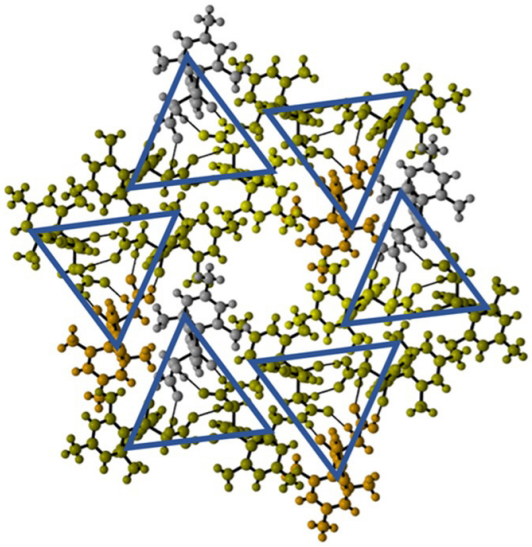

FIG. 3. Schematic representation of molecular model of a fragment of mesityl(phenyl)phosphine oxide glycolate crystal packing showing its honeycomb network

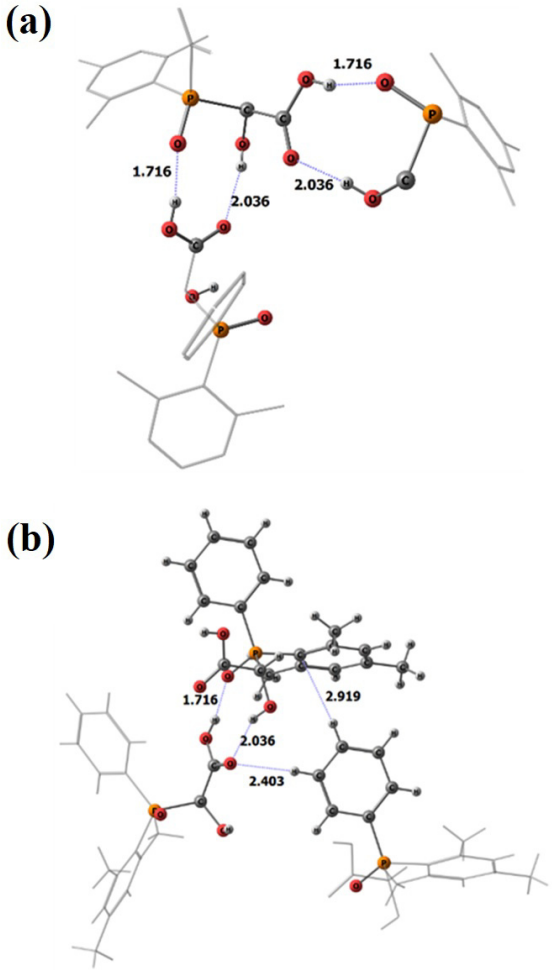

FIG. 4. Fragments of crystal packing showing two equivalent cyclic hydrogen bonds formed by each molecule of **1**, hydrogen atoms, except participated in the target hydrogen bonds are removed, carbon skeleton shown as a wireframe

TABLE 1. The results of the interaction energy analysis. Distances between centres of the interacting molecules are in Å, energies are in kJ/mol

#	distance	E_{ele}	E_{pol}	E_{disp}	E_{rep}	E_{tot}	Main interaction	type
1	8.02	−112.1	−27.6	−23.3	135.7	−75.4	OH$\cdots$O	Intra-rod
2	7.00	−11.1	−3.7	−42.2	26.3	−35.0	$CH_3 \cdots \pi^{Mes}$	Inter-rod
3	6.33	−7.6	−1.6	−54.5	36.3	−34.3	$CH_3 \cdots \pi^{Ph}$	Inter-rod
4	9.09	−5.4	−1.7	−26.1	16.2	−19.6	$CH^{Ph} \cdots \pi^{Mes}$	Intra-rod
5	7.84	−5.5	−1.8	−14.6	2.5	−18.3	$CH_3 \cdots \pi^{Ph}$	Inter-rod
6	9.58	−6.3	−1.7	−9.0	13.7	−7.3	$CH^{Ph} \cdots O^{carboxylic}$	Intra-rod
7	11.20	−0.4	−0.3	−8.8	2.7	−6.7	vdW	Inter-rod
8	11.64	−2.3	−0.3	−1.1	0.0	−3.6	vdW	Inter-rod
9	12.11	−0.5	−0.1	−2.1	0.0	−2.5	vdW	Inter-rod

in a trigonal crystal system (space group R-3 (no. 148)) with one molecule in the asymmetric part of unit cell. The phosphorus atom displays the typical for phosphine oxides tetrahedral configuration, the Newman projection along the C(10)–P(1) bond shows that mesityl group locates in *trans*-position to the C(10)–C(11) bond, while phenyl group in *gauche*-position [torsion angles C(1)P(1)C(10)C(11) 173.26°, C(12)P(1)C(10)C(11) −54.44°]. Tetrahedral phosphorus atom of phosphine oxide with three different substituents (phenyl, mesityl and glycolate) is chiral, and actual crystal structure is a racemic. Expectedly, the P(1)–C(1) bond distance (1.826 Å), is longer than that of the P(1)–C(12) bond (1.799 Å), while the P(1)–C(10) distance is 1.863 Å. The H(10) and H(12) atoms engage into O–H$\cdots$O hydrogen bonds with O(1') and O(4') atoms on adjacent molecules in the lattice respectively [d(O(3)$\cdots$O(1')) = 2.521 Å, d(O(2)$\cdots$O(4')) = 2.791 Å]. The O$\cdots$H$\cdots$O angles are in the range of 152.6°–166.5°. Interestingly, these intermolecular interactions together with C–H$\cdots$C contacts (*vide infra*) causes the formation of one-dimensional cylindrical channels with diameter of ∼10 Å(cylindrical approximation) in the crystal, these channels are directed along the *c* crystallographic axis (Fig. 2b, 8.5 % of unit cell volume, see Fig. S3 for details).

The analysis of the interaction energies in the framework of CrystalExplorer package helps us to understand the peculiarities of the formed structure. Obviously, the strongest interaction in the crystal is a cyclic hydrogen bonds of HOC–P=O group with carboxylate fragment. Each molecule of **1** bind two neighbours via this motif. Energy of each cyclic hydrogen bonding interaction is 75.4 kJ/mol, and it is also electrostatic (Table 1), verifying the nature of this interaction [20, 42]. Actually, this type of interaction is responsible for the formation of helical chains (rods) of H-bonded molecules along the c axis. The formed rods are additionally stabilized by $CH^{Ph} \cdots$O=C and $CH^{Ph} \cdots CC^{Mes}$ hydrogen bonds with 7.3 and 19.6 kJ/mol energies. Notable that there are two types of rods each formed exclusively by single enantiomer. In the packing these enantiomerically pure rods are alternating, finally forming a honeycomb-like structure of racemate (Fig. 3).

After the rods formation there are no available OH groups to form an interrod connection, so the rods packing driven by weaker interactions. Nevertheless, their energetic impact is still high, being 35 kJ/mol. The one of *o*-CH_3^{Mes} form dimer with another molecule of 1, additionally stabilized by the same Me group protons interaction with the carboxylic OH oxygen atom, and the second *o*-CH_3^{Mes} interacts with the *o*-CH^{Ph}, *m*-C^{Mes}, with some additional stabilization due to $CH^{Mes} \cdots$Ph hydrogen bond (Fig. 4b). Notably the shortest intermolecular distance from p-CH_3^{Mes} to any carbon atom is 3.1 Å, making the CH_3 group in the p-position of mesityl substituent almost non-interacting and turned inside the channel. It is worth noting that the interaction of the two adjacent mesityl(phenyl)phosphine oxide glycolates responsible for the interrod interaction in the crystal (see Fig. S4a). Also, the interaction energy between the two mesityl(phenyl)phosphine oxide glycolates is due to a Van der Waals dimer (E_{int} = −18.3 kJ/mol, of which only −5.5 kJ/mol is electrostatic) where $CH_3^{Mes} \cdots$Ph interaction (2.86 Å) could be revealed (see Fig. S4b, S5 and Table 1 for details).

4. Conclusion

In summary, the unsymmetrically substituted organophosphorus compound mesityl(phenyl)phosphine oxide glycolate (**1**) has been synthesised from glyoxylic acid monohydrate and mesityl(phenyl)phosphine using *one pot* condensation approach with good yield of 70 %. The structure characterization of **1** by means of single crystal X-ray analysis revealed the one-dimensional cylindrical channels with diameter of *ca.* ∼1 nm (10 Å) in the crystal. Channels are formed by honeycomb like aggregation of six three-pointed star shaped spiral rods. Each rod formed by single enantiomer via strong cyclic hydrogen bonds, whereas CH_3 groups of mesityl fragment are responsible for the joining of the alternating

enantiomerically pure rods into a racemic pack providing precise nano-sized channels. Such crystalline porous materials with precise nano-sized pores could overcome the limitations of traditional nanofiltration (NF) membranes, which are typically composed for amorphous polymers and suffer from disordered pore structures and reduced solvent permeability. Incorporating these crystalline materials into NF membranes, we offer a promising solution to enhance both permeability and selectivity, potentially revolutionizing molecular separation processes.

References

[1] de Silva P., Corminboeuf C. Simultaneous Visualization of Covalent and Noncovalent Interactions Using Regions of Density Overlap. *J. Chem. Theory Comput.*, 2014, **10**, P. 3745–3756.

[2] Johnson E.R., Keinan S., Mori-Sánchez P., Contreras-García J., Cohen A.J., Yang W. Revealing Noncovalent Interactions. *J. Am. Chem. Soc.*, 2010, **132**, P. 6498–6506.

[3] Andrezálová L., Országhová Z. Covalent and noncovalent interactions of coordination compounds with DNA: An overview. *Journal of Inorganic Biochemistry*, 2021, **225**, P. 111624.

[4] Gao X., Zou X., Ma H., Meng S., Zhu G. Highly Selective and Permeable Porous Organic Framework Membrane for CO_2 Capture. *Advanced Materials*, 2014, **26**, P. 3644–3648.

[5] Hobza P., ŘezáčJ. Introduction: Noncovalent Interactions. *Chem. Rev.*, 2016, **116**, P. 4911–4912.

[6] Kollman P.A. Noncovalent interactions. *Acc. Chem. Res.*, 1977, **10**, P. 365–371.

[7] Vyas V.S., Vishwakarma M., Moudrakovski I., Haase F., Savasci G., Ochsenfeld C., Spatz J.P., Lotsch B.V. Exploiting Noncovalent Interactions in an Imine-Based Covalent Organic Framework for Quercetin Delivery. *Advanced Materials*, 2016, **28**, P. 8749–8754.

[8] Li P., Ryder M.R., Stoddart J.F. Hydrogen-Bonded Organic Frameworks: A Rising Class of Porous Molecular Materials. *Acc. Mater. Res.*, 2020, **1**, P. 77–87.

[9] Shah M., McCarthy M.C., Sachdeva S., Lee A.K., Jeong H.-K. Current Status of Metal–Organic Framework Membranes for Gas Separations: Promises and Challenges. *Ind. Eng. Chem. Res.*, 2012, **51**, P. 2179–2199.

[10] Caro J., Noack M. Zeolite membranes – Recent developments and progress. *Microporous and Mesoporous Materials*, 2008, **115**, P. 215–233.

[11] Zhu X., Tian C., Mahurin S.M., Chai S.-H., Wang C., Brown S., Veith G.M., Luo H., Liu H., Dai S. A Superacid-Catalyzed Synthesis of Porous Membranes Based on Triazine Frameworks for CO2 Separation. *J. Am. Chem. Soc.*, 2012, **134**, P. 10478–10484.

[12] Carta M., Malpass-Evans R., Croad M., Rogan Y., Jansen J.C., Bernardo P., Bazzarelli F., McKeown N.B. An Efficient Polymer Molecular Sieve for Membrane Gas Separations. *Science*, 2013, **339**, P. 303–307.

[13] Chen L., Zhang B., Chen L., Liu H., Hu Y., Qiao S. Hydrogen-bonded organic frameworks: design, applications, and prospects. *Mater. Adv.*, 2022, **3**, P. 3680–3708.

[14] Yang J., Wang J., Hou B., Huang X., Wang T., Bao Y., Hao H. Porous hydrogen-bonded organic frameworks (HOFs): From design to potential applications. *Chemical Engineering Journal*, 2020, **399**, P. 125873.

[15] Arduengo A.J.I., Gamper S.F., Tamm M., Calabrese J.C., Davidson F., Craig H.A. A Bis(carbene)-Proton Complex: Structure of a C-H-C Hydrogen Bond. *J. Am. Chem. Soc.*, 1995, **117**, P. 572–573.

[16] Gronert S., Keeffe J.R. Identity Hydride-Ion Transfer from C?H Donors to C Acceptor Sites. Enthalpies of Hydride Addition and Enthalpies of Activation. Comparison with C$\cdots$H$\cdots$C Proton Transfer. An ab Initio Study. *J. Am. Chem. Soc.*, 2005, **127**, P. 2324–2333.

[17] Krishnamohan Sharma C.V., Broker G.A., Rogers R.D. Polymorphous One-Dimensional Tetrapyridylporphyrin Coordination Polymers Which Structurally Mimic Aryl Stacking Interactions. *Journal of Solid State Chemistry*, 2000, **152**, P. 253–260.

[18] Duarte M.T., Piedade M.F.M., Robalo M.P., Teixeira A.P.S., Garcia M.H. A supramolecular zigzag chain of organometallic dipoles mediated by PF6-anions. *Acta Crystallogr C Cryst Struct Commun*, 2005, **61**, P. m386–m389.

[19] Das S., Bharadwaj P.K. Self-Assembly of a Luminescent Zinc(II) Complex: a Supramolecular Host–Guest Fluorescence Signaling System for Selective Nitrobenzene Inclusion. *Inorg. Chem.*, 2006, **45**, P. 5257–5259.

[20] Chakravorty S., Platts J.A., Das B.K. Novel C–H$\cdots$C contacts involving 3,5-dimethylpyrazole ligands in a tetracoordinate Co(ii) complex. *Dalton Trans.*, 2011, **40**, P. 11605.

[21] Kharel S., Bhuvanesh N., Gladysz J.A., Blümel J. New hydrogen bonding motifs of phosphine oxides with a silanediol, a phenol, and chloroform. *Inorganica Chimica Acta*, 2019, **490**, P. 215–219.

[22] Tupikina E.Yu., Bodensteiner M., Tolstoy P.M., Denisov G.S., Shenderovich I.G. P=O Moiety as an Ambidextrous Hydrogen Bond Acceptor. *J. Phys. Chem. C*, 2018, **122**, P. 711–1720.

[23] Kostin M.A., Pylaeva S.A., Tolstoy P.M. Phosphine oxides as NMR and IR spectroscopic probes for the estimation of the geometry and energy of PO$\cdots$H–A hydrogen bonds. *Phys. Chem. Chem. Phys.*, 2022, **24**, P. 7121–7133.

[24] Kostin M.A., Alkhuder O., Xu L., Krutin D.V., Asfin R.E., Tolstoy P.M. Complexes of phosphine oxides with substituted phenols: hydrogen bond characterization based on shifts of P-O stretching bands. *Phys. Chem. Chem. Phys.*, 2024, **26**, P. 10234–10242.

[25] Gafurov Z.N., Zueva E.M., Yakhvarov D.G. Sustainable Synthesis, NMR and Computational Study of Isobutylmesitylphosphine. *Chemistry Select*, 2021, **6**, P. 1833–1837.

[26] Jerphagnon T., Renaud J.-L., Bruneau C. Chiral monodentate phosphorus ligands for rhodium-catalyzed asymmetric hydrogenation. *Tetrahedron: Asymmetry*, 2004, **15**, P. 2101–2111.

[27] Imamoto T., Crépy K.V.L., Katagiri K. Optically active 1,1'-di-tert-butyl-2,2'-dibenzophosphetenyl: a highly strained P-stereogenic diphosphine ligand. *Tetrahedron: Asymmetry*, 2004, **15**, P. 2213–2218.

[28] Cheng X., Horton P.N., Hursthouse M.B., Hii K.K. Aminohydroxy phosphine oxide ligands in ruthenium-catalysed asymmetric transfer hydrogenation reactions. *Tetrahedron: Asymmetry*, 2004, **15**, P. 2241–2246.

[29] Methot J.L., Roush W.R. Nucleophilic Phosphine Organocatalysis. Adv Synth Catal, 2004, 346, P. 1035–1050.

[30] Seayad J., List B. Asymmetric organocatalysis. *Org. Biomol. Chem.*, 2005, **3**, P. 719.

[31] Connon S.J. Chiral Phosphoric Acids: Powerful Organocatalysts for Asymmetric Addition Reactions to Imines. *Angew Chem Int Ed*, 2006, **45**, P. 3909–3912.

[32] Benaglia M., Rossi S. Chiral phosphine oxides in present-day organocatalysis. *Org. Biomol. Chem.*, 2010, **8**, P. 3824.

[33] Adams H., Collins R.C., Jones S., Warner C.J.A. Enantioselective Preparation of P-Chiral Phosphine Oxides. *Org. Lett.*, 2011, **13**, P. 6576–6579.

[34] Gafurov Z.N., Musin L.I., Sakhapov I.F., Babaev V.M., Musina E.I., Karasik A.A., Sinyashin O.G., Yakhvarov D.G. The formation of secondary arylphosphines in the reaction of organonickel sigma-complex [NiBr(Mes)(bpy)], where Mes = 2,4,6-trimethylphenyl, bpy = 2,2'-bipyridine, with phenylphosphine. *Phosphorus, Sulfur, and Silicon and the Related Elements*, 2016, **191**, P. 1475–1477.

[35] Sheldrick G.M. SHELXT– Integrated space-group and crystal-structure determination. *Acta Crystallogr A Found Adv*, 2015, **71**, P. 3–8.
[36] Sheldrick G.M. A short history ofSHELX. *Acta Crystallogr A Found Crystallogr*, 2007, **64**, P. 112–122.
[37] Macrae C.F. Edgington P.R., McCabe P., Pidcock E., Shields G.P., Taylor R., Towler M., Van De Streek J. Mercury: visualization and analysis of crystal structures. *J Appl Crystallogr*, 2006, **39**, P. 453–457.
[38] www.ccdc.cam.ac.uk/conts/retrieving.html (or from the Cambridge Crystallographic Data Centre, 12 Union Road, Cambridge CB2 1EZ, UK; fax: (+44) 1223-336-033; or deposit@ccdc.cam.uk)
[39] EVA v.11.0.0.3. User Manual. SOCABIM, 2005.
[40] Spackman P.R., Turner M.J., McKinnon J.J., Wolff S.K., Grimwood D.J., Jayatilaka D., Spackman M.A. CrystalExplorer: a program for Hirshfeld surface analysis, visualization and quantitative analysis of molecular crystals. *J Appl Crystallogr*, 2021, **54**, P. 1006–1011.
[41] Mackenzie C.F., Spackman P.R., Jayatilaka D., Spackman M.A. CrystalExplorermodel energies and energy frameworks: extension to metal coordination compounds, organic salts, solvates and open-shell systems. *IUCrJ*, 2017, **4**, P. 575–587.
[42] Grossmann G., Krüger K., Ohms G., Fischer A., Jones P.G., Goerlich J., Schmutzler R. Phosphorus Nuclear Magnetic Shielding Anisotropy and Crystal Structure of (1-Hydroxyalkyl)dimethylphosphine Sulfides. *Inorg. Chem.*, 1997, **36**, P. 770–775.

Submitted 30 December 2024; revised 11 February 2025; accepted 12 February 2025

Information about the authors:

Alexey A. Kagilev – Arbuzov Institute of Organic and Physical Chemistry, FRC Kazan Scientific Center, Russian Academy of Sciences, 420088, Kazan, Russian Federation; ORCID 0000-0002-5603-1311; al-kagilev@mail.ru

Ilyas F. Sakhapov – Arbuzov Institute of Organic and Physical Chemistry, FRC Kazan Scientific Center, Russian Academy of Sciences, 420088, Kazan, Russian Federation; ORCID 0000-0002-7440-1486; ilyas.sakhapov@iopc.ru

Zufar N. Gafurov – Arbuzov Institute of Organic and Physical Chemistry, FRC Kazan Scientific Center, Russian Academy of Sciences, 420088, Kazan, Russian Federation; ORCID 0000-0001-6615-8968; gafurov.zufar@iopc.ru

Artyom O. Kantyukov – Arbuzov Institute of Organic and Physical Chemistry, FRC Kazan Scientific Center, Russian Academy of Sciences, 420088, Kazan, Russian Federation; A.M. Butlerov Institute of Chemistry, Kazan Federal University, 420008, Kazan, Russian Federation; ORCID 0000-0002-2285-300X; kant.art@mail.ru

Ilya K. Mikhailov – Arbuzov Institute of Organic and Physical Chemistry, FRC Kazan Scientific Center, Russian Academy of Sciences, 420088, Kazan, Russian Federation; ORCID 0000-0001-9373-2996; tiimhailovilya@gmail.com

Daut R. Islamov – Laboratory for Structural Studies of Biomacromolecules, FRC Kazan Scientific Center, Russian Academy of Sciences, 420111, Kazan, Russian Federation; ORCID 0000-0002-5988-1012; daut1989@mail.ru

Alexander V. Gerasimov – A.M. Butlerov Institute of Chemistry, Kazan Federal University, 420008, Kazan, Russian Federation; ORCID 0000-0003-4213-9724; Alexander.Gerasimov@kpfu.ru

Oleg A. Filippov – A.N. Nesmeyanov Institute of Organoelement Compounds, Russian Academy of Sciences, 119991, Moscow, Russian Federation; ORCID 0000-0002-7963-2806; h-bond@ineos.ac.ru

Aidar T. Gubaidullin – Arbuzov Institute of Organic and Physical Chemistry, FRC Kazan Scientific Center, Russian Academy of Sciences, 420088, Kazan, Russian Federation; ORCID 0000-0002-8114-7025; aidar@iopc.ru

Olga S. Soficheva – Arbuzov Institute of Organic and Physical Chemistry, FRC Kazan Scientific Center, Russian Academy of Sciences, 420088, Kazan, Russian Federation; ORCID 0000-0003-3107-5251; myaolechka@yandex.ru

Oleg G. Sinyashin – Arbuzov Institute of Organic and Physical Chemistry, FRC Kazan Scientific Center, Russian Academy of Sciences, 420088, Kazan, Russian Federation; ORCID 0000-0002-2241-9764; oleg@iopc.ru

Dmitry G. Yakhvarov – Arbuzov Institute of Organic and Physical Chemistry, FRC Kazan Scientific Center, Russian Academy of Sciences, 420088, Kazan, Russian Federation; A.M. Butlerov Institute of Chemistry, Kazan Federal University, 420008, Kazan, Russian Federation; ORCID 0000-0002-3906-8841; yakhvar@iopc.ru

Conflict of interest: the authors declare no conflict of interest.

NANO
ФИХМ

NANOSYSTEMS:

PHYSICS, CHEMISTRY, MATHEMATICS

INFORMATION FOR AUTHORS

The journal publishes research articles and reviews, and also short scientific papers (letters) which are unpublished and have not been accepted for publication in other magazines. Articles should be submitted in English. All articles are reviewed, then if necessary come back to the author to completion.

The journal is indexed in Web of Science Core Collection (Emerging Sources Citation Index), Chemical Abstract Service of the American Chemical Society, Zentralblatt MATH and in Russian Scientific Citation Index.

Author should submit the following materials:

1. Article file in English, containing article title, the initials and the surname of the authors, Institute (University), postal address, the electronic address, the summary, keywords, MSC or PACS index, article text, the list of references.
2. Files with illustrations, files with tables.
3. The covering letter in English containing the article information (article name, MSC or PACS index, keywords, the summary, the literature) and about all authors (the surname, names, the full name of places of work, the mailing address with the postal code, contact phone number with a city code, the electronic address).
4. The expert judgement on possibility of publication of the article in open press (for authors from Russia).

Authors can submit a paper and the corresponding files to the following addresses: nanojournal.ifmo@gmail.com, popov1955@gmail.com.

Text requirements

Articles should be prepared with using of text editors MS Word or LaTex (preferable). It is necessary to submit source file (LaTex) and a pdf copy. In the name of files the English alphabet is used. The recommended size of short communications (letters) is 4-6 pages, research articles– 6-15 pages, reviews – 30 pages.

Recommendations for text in MS Word:

Formulas should be written using Math Type. Figures and tables with captions should be inserted in the text. Additionally, authors present separate files for all figures and Word files of tables.

Recommendations for text in LaTex:

Please, use standard LaTex without macros and additional style files. The list of references should be included in the main LaTex file. Source LaTex file of the paper with the corresponding pdf file and files of figures should be submitted.

References in the article text are given in square brackets. The list of references should be prepared in accordance with the following samples:

[1] Surname N. *Book Title*. Nauka Publishing House, Saint Petersburg, 2000, 281 pp.
[2] Surname N., Surname N. Paper title. *Journal Name*, 2010, **1** (5), P. 17-23.
[3] Surname N., Surname N. Lecture title. In: Abstracts/Proceedings of the Conference, Place and Date, 2000, P. 17-23.
[4] Surname N., Surname N. Paper title, 2000, URL: http://books.ifmo.ru/ntv.
[5] Surname N., Surname N. Patent Name. Patent No. 11111, 2010, Bul. No. 33, 5 pp.
[6] Surname N., Surname N. Thesis Title. Thesis for full doctor degree in math. and physics, Saint Petersburg, 2000, 105 pp.

Requirements to illustrations

Illustrations should be submitted as separate black-and-white files. Formats of files – jpeg, eps, tiff.

NANOSYSTEMS:

PHYSICS, CHEMISTRY, MATHEMATICS

Журнал зарегистрирован
Федеральной службой по надзору в сфере связи, информационных технологий и массовых коммуникаций
(свидетельство ПИ № ФС 77 - 49048 от 22.03.2012 г.)
ISSN 2220-8054

Учредитель: федеральное государственное автономное образовательное учреждение высшего образования
«Национальный исследовательский университет ИТМО»

Издатель: федеральное государственное автономное образовательное учреждение высшего образования
«Национальный исследовательский университет ИТМО»

Отпечатано в Учреждении «Университетские телекоммуникации»
Адрес: 197101, Санкт-Петербург, Кронверкский пр., 49

Подписка на журнал НФХМ
На второе полугодие 2025 года подписка осуществляется через
ОАО «АРЗИ», подписной индекс Э57385